



**UNIVERSITÀ DI PISA**

**DIPARTIMENTO DI INGEGNERIA DELL'INFORMAZIONE**

**ELETTRONICA, INFORMATICA, TELECOMUNICAZIONI**

# **STATISTICAL ANALYSIS OF HIGH RESOLUTION SAR GROUND CLUTTER DATA**

**Fulvio Gini, Maria S. Greco, F. Lombardini**

**Pisa, November 2005**

This work has been funded by USARDSG grant N62558-04-P-6114 on “Statistical analysis and modeling of high resolution ground radar clutter and targets”

Report Documentation Page				Form Approved OMB No. 0704-0188	
Public reporting burden for the collection of information is estimated to average 1 hour per response, including the time for reviewing instructions, searching existing data sources, gathering and maintaining the data needed, and completing and reviewing the collection of information. Send comments regarding this burden estimate or any other aspect of this collection of information, including suggestions for reducing this burden, to Washington Headquarters Services, Directorate for Information Operations and Reports, 1215 Jefferson Davis Highway, Suite 1204, Arlington VA 22202-4302. Respondents should be aware that notwithstanding any other provision of law, no person shall be subject to a penalty for failing to comply with a collection of information if it does not display a currently valid OMB control number.					
1. REPORT DATE <b>NOV 2005</b>		2. REPORT TYPE		3. DATES COVERED <b>00-00-2005 to 00-00-2005</b>	
4. TITLE AND SUBTITLE <b>Statistical Analysis of High Resolution SAR Ground Clutter Data</b>				5a. CONTRACT NUMBER	
				5b. GRANT NUMBER	
				5c. PROGRAM ELEMENT NUMBER	
6. AUTHOR(S)				5d. PROJECT NUMBER	
				5e. TASK NUMBER	
				5f. WORK UNIT NUMBER	
7. PERFORMING ORGANIZATION NAME(S) AND ADDRESS(ES) <b>Universita di Pisa,Dipartimento di Ingegneria Dell'Informazione,Elettronica, Informatica, Telecomunicazioni,Via G. Caruso 16 - 56122 - Pisa ,</b>				8. PERFORMING ORGANIZATION REPORT NUMBER	
9. SPONSORING/MONITORING AGENCY NAME(S) AND ADDRESS(ES)				10. SPONSOR/MONITOR'S ACRONYM(S)	
				11. SPONSOR/MONITOR'S REPORT NUMBER(S)	
12. DISTRIBUTION/AVAILABILITY STATEMENT <b>Approved for public release; distribution unlimited</b>					
13. SUPPLEMENTARY NOTES <b>U.S. Government or Federal Rights License</b>					
14. ABSTRACT <b>see report</b>					
15. SUBJECT TERMS					
16. SECURITY CLASSIFICATION OF:			17. LIMITATION OF ABSTRACT <b>Same as Report (SAR)</b>	18. NUMBER OF PAGES <b>184</b>	19a. NAME OF RESPONSIBLE PERSON
a. REPORT <b>unclassified</b>	b. ABSTRACT <b>unclassified</b>	c. THIS PAGE <b>unclassified</b>			

## ABSTRACT

*The work described in this technical report deals with the problem of providing a statistical model of the backscattering from ground surfaces for high-resolution Synthetic Aperture Radar (SAR) systems. We report here the results of our research activity. In particular, the statistical analysis of amplitude, texture and speckle of high-resolution X-band MSTAR data of two different vegetated areas, grass field, and tree area. The analysis of the data has been performed focusing on the possible statistical differences and similarities in the statistical behavior of clutter due to changes of vegetation and terrain structure.*

*The report is also devoted to the description of the analysis of clutter on many more data files, with particular attention to the range and cross-range correlation functions and Power Spectral Density (PSD). Also, speckle analysis is also extended to other SAR data sets in X- and L-band, at coarser resolution than MSTAR, including data from AIRSAR.*

<b>CHAPTER 1 - STATISTICAL ANALYSIS OF MSTAR CLUTTER DATA.....</b>	<b>1</b>
<b>1.1 INTRODUCTION .....</b>	<b>1</b>
<b>1.2 STATISTICAL ANALYSIS OF GRASS FIELD .....</b>	<b>13</b>
1.2.1 HB06171 File .....	13
1.2.2 HB06172 File .....	22
1.2.3 HB06173 File .....	32
1.2.4 HB06174 File .....	39
1.2.5 HB06176 File .....	46
1.2.6 HB06177 File .....	51
1.2.7 HB06188 File .....	60
1.2.8 Conclusions .....	67
<b>1.3 TERRAIN WITH DENSE VEGETATION AND TREES .....</b>	<b>68</b>
1.2.1 HB06202 file.....	68
1.2.2 Texture and speckle estimation and statistical analysis .....	77
1.2.3 Statistic analysis of the patches of HB06202 file.....	86
1.2.4 Conclusions .....	100
<b>CHAPTER 2 - FREQUENCY ANALYSIS.....</b>	<b>102</b>
<b>2.1 FREQUENCY ANALYSIS OF GRASS FIELD CLUTTER.....</b>	<b>103</b>
2.1.1 HB06171 File .....	103
<b>2.2 FREQUENCY ANALYSIS OF THE CLUTTER OF DENSE VEGETATED AREAS .....</b>	<b>114</b>
2.2.1 Periodogram of file HB06202 .....	114
2.2.2 Correlations of HB06202 file: wood and trees.....	118
<b>2.3 THEORETICAL TEXTURE CORRELATION MODELS.....</b>	<b>125</b>
<b>2.4 RESULTS .....</b>	<b>126</b>
<b>2.5 CONCLUSIONS .....</b>	<b>138</b>
<b>CHAPTER 3 - EXTENDED SPECKLE ANALYSIS .....</b>	<b>140</b>
<b>3.1 INTRODUCTION .....</b>	<b>140</b>
<b>3.2 STATISTICAL MODELS .....</b>	<b>141</b>
<b>3.3 PHASE UNIFORMITY TEST AND SNR ESTIMATION.....</b>	<b>142</b>
<b>3.4 FIRST DATA SET.....</b>	<b>142</b>
<b>3.5 SECOND DATA SET.....</b>	<b>152</b>
<b>3.6 THIRD DATA SET .....</b>	<b>157</b>
<b>3.7 FOURTH DATA SET .....</b>	<b>161</b>
<b>3.8 CONCLUSIONS .....</b>	<b>166</b>
<b>APPENDIX A .....</b>	<b>168</b>
<b>A.1 GOODNESS-OF-FIT TEST .....</b>	<b>168</b>
A.1.1 Kolmogorov-Smirnov Test .....	169
A.1.2 Variants of Kolmogorov-Smirnov test.....	174
A.1.3 Remarks.....	177
<b>REFERENCES.....</b>	<b>178</b>





# CHAPTER 1

## STATISTICAL ANALYSIS OF MSTAR CLUTTER DATA

### 1.1 Introduction

In a SAR image each pixel corresponds to a pair of voltages for phase and quadrature channels. These measured values represent the effects of the scene on the transmitted wave. The measured voltages should be converted to “geophysical” units corresponding to the complex reflectivity RCS (radar cross section), or backscattering coefficient of the scene. Then the measurements made by the SAR are fundamentally determined by electromagnetic scattering processes. SAR images may be considered in terms of solution of Maxwell’s equations for the propagation geometry and the scattering scene. However, both on theoretical and practical grounds, this viewpoint provides only a partial contribution to the understanding of the available information. From the point of view of electromagnetic theory, two approaches are relevant. The first of these is the *Forward Problem*, in which the properties of the scattering medium and the incoming wave are specified and used to predict the scattered field. Solutions to this problem are currently available only by imposing considerable restrictions on the scattering medium, for example, by assuming that all length scales in the medium are large (or small) relative to the wavelength, or that only surface (not volume) scattering is occurring (or viceversa), or that occultation (shadowing) effects can be ignored. Even with such restrictions, full wave solutions are in most cases unavailable.

Much more important is the *Inverse Problem*. Methods to solve the Inverse Problem are mathematically complicated and difficult. However, the real source of the difficulty in the Inverse Problem is not only the mathematics but that there is rarely enough information to provide a unique solution. In other words, the number of parameters needed to characterize the target in the scattering model exceeds the number of independent measurements available at the sensor [Oli98].

These approaches to describe information in SAR images through electromagnetic theory have the apparent advantage that they map the observed signal onto physical properties of the scene, such a dielectric constant, geometrical factors (e.g. size, height, and roughness), and polarizability. In other words, they provide a link between observations and measurable quantities on the ground (this is often very difficult to turn into practice because of the problem of providing measurements that are truly representative of the scattering medium). Typically, both the Forward and Inverse Problems require some a priori knowledge before they can be invoked, such as knowledge that the region is woodland or ocean or ice.

The primary geophysical quantity determining the SAR data is the complex radar reflectivity of the scene. Qualitatively, this concept expresses the fact that when an electromagnetic wave scatters from position  $(x,y)$  on Earth's surface, the physical properties of the terrain cause changes both phase  $\Phi(x,y)$  and amplitude  $A(x,y)$  of the transmitted wave. In fact, the SAR measures the pair  $(A\cos\phi, A\sin\phi)$  in the in-phase and quadrature channels of the receiver. This estimate of the local reflectivity at each pixel can also be represented by the complex number  $Ae^{j\phi}$ ; in this form, the SAR data are known as the *complex image*. From the complex image, a variety of other products can be formed, for example, images of the real part  $A\sin\phi$  (the quadrature component), the amplitude  $A$ , the phase  $\phi$ , the intensity  $I=A^2$ , or the log-intensity  $\log(I)$  (intensity is synonymous of power or energy). The log-image is also sometimes referred to as the “dB” image, since for calibrated data each pixel corresponds to a linearly scaled estimate of the backscattering coefficient  $\sigma^\circ$  in dB. For a properly calibrated system, these are all true measurements of the scattering properties of Earth's surface (except for those effects caused by system noise), but visually they produce quite different representations. For example, the real and the imaginary images show some structure, but appear extremely noisy, the phase image is noise-like and shows no structure, while the amplitude, intensity, and log-images, though noisy, are clearly easier to interpret. In Fig.1.1, as an example, we can observe a dB image relative to MSTAR data.



**Figure 1.1** - SAR image, file HB06209, MSTAR data.

The noise characterizing SAR images is known as speckle. The speckle is different from electrical thermal noise but it is a real electromagnetic measurement.

With distributed targets, we can think that each resolution cell contains a number of discrete scatters. When radar wave interacts with the target, each scatterer contributes to the returned wave with a phase and amplitude change, so the total returned wave is:

$$Ae^{j\phi} = \sum_{k=1}^N A_k e^{j\phi_k} \quad (1.1)$$

This summation is over the number of scatterers illuminated by the beam. The individual scattering amplitude is not observable because the individual scatters are on much smaller scales than the resolution of the SAR, and there are normally many such scatters per resolution cell.

An immediate conclusion from (1.1) is that the observed signal will be affected by interference effects as a consequence of the phase differences between scatterers. In fact, speckle can be understood as an interference phenomenon in which the principal source of the noise-like quality of the observed data is the distribution of the phase term  $\phi_k$ . Hence, scatterers at different parts of the resolution cell will contribute very different phases to signal return even if their scattering behavior is identical. As a result, we can in practice think of the phase  $\phi_k$  as being uniformly distributed in  $[-\pi, \pi]$  and independent of the amplitude  $A_k$ .

By considering large number of statistically identical scatterers, the analysis reveals that:

- The in-phase and quadrature components  $z_1 = A \cos \phi$  and  $z_2 = A \sin \phi$  will be independent and identically distributed Gaussian random variables, with zero mean and variance  $\sigma^2/2$ .
- The in phase and quadrature components will have a joint probability density function (PDF) given by:

$$p_{z_1, z_2}(z_1, z_2) = \frac{1}{\pi \sigma^2} \exp\left(-\frac{z_1^2 + z_2^2}{\sigma^2}\right) \quad (1.2)$$

- The phase observed will be uniformly distributed over  $[-\pi, \pi]$ .
- The amplitude A will have a Rayleigh distribution:

$$p_A(A) = \frac{2A}{\sigma^2} \exp\left(-\frac{A^2}{\sigma^2}\right) \quad A \geq 0 \quad (1.3)$$

with mean value  $\frac{\sqrt{\pi\sigma^2}}{2}$  and standard deviation  $\sqrt{\left(1-\frac{\pi}{4}\right)\sigma^2}$ .

- The observed intensity or power  $I = A^2$  will have a negative exponential distribution:

$$P_I(I) = \frac{1}{\sigma^2} \exp\left(-\frac{I}{\sigma^2}\right) \quad I \geq 0 \quad (1.4)$$

- The log intensity  $D = \ln I$  has a Fischer-Tippet distribution:

$$P_D(D) = \frac{e^D}{\sigma^2} \exp\left(-\frac{e^D}{\sigma^2}\right) \quad (1.5)$$

whose mean value and variance are  $\ln\sigma^2 - \gamma_E$  and  $\pi^2/6$ , respectively. The symbol  $\gamma_E$  denotes Euler's constant whose approximate value is 0.57722. The distributions in equations (1.1)-(1.5) are of fundamental importance in handling SAR data. Notice that, with the exception of the phase distribution; they are completely characterized by a single parameter  $\sigma^2$  which carries all the available information about the illuminated area. From (1.4) we can see that  $\sigma^2$  corresponds to the *average intensity*.

By analyzing an SAR image as that in figure 1.2 in the wooded region, it is apparent that there are fluctuations in addition to speckle. Physically this appears to correspond to strong returns from the crowns of trees with shadows behind them. If we disregard the deterministic positions of these light and dark fluctuations, we can treat this type of natural clutter as a noise-like *texture*. Note that texture is a consequence of fluctuation in the RCS.

Let us now identify measures that can provide discrimination between such classes of texture. Typically, in SAR images the brightness of the field is the same as the wood, a discriminating feature could then be the contrast ( $=\sqrt{\text{var } I}/\langle I \rangle$ ), which takes different values for the field and woodland regions. Generally, the result for the field region is close to unity, as expected for pure speckle, while the woodland region has increased fluctuations. Urban areas typically display even stronger contrast. Another distinguishing characteristic can be spatial size of the forms that appear in the image. In the field region, only speckle fluctuations

are observed. The woodland sample also includes variation on a scale consistent with tree size and separation. Generally, images with different vegetation present different statistics characteristics [Oli98].

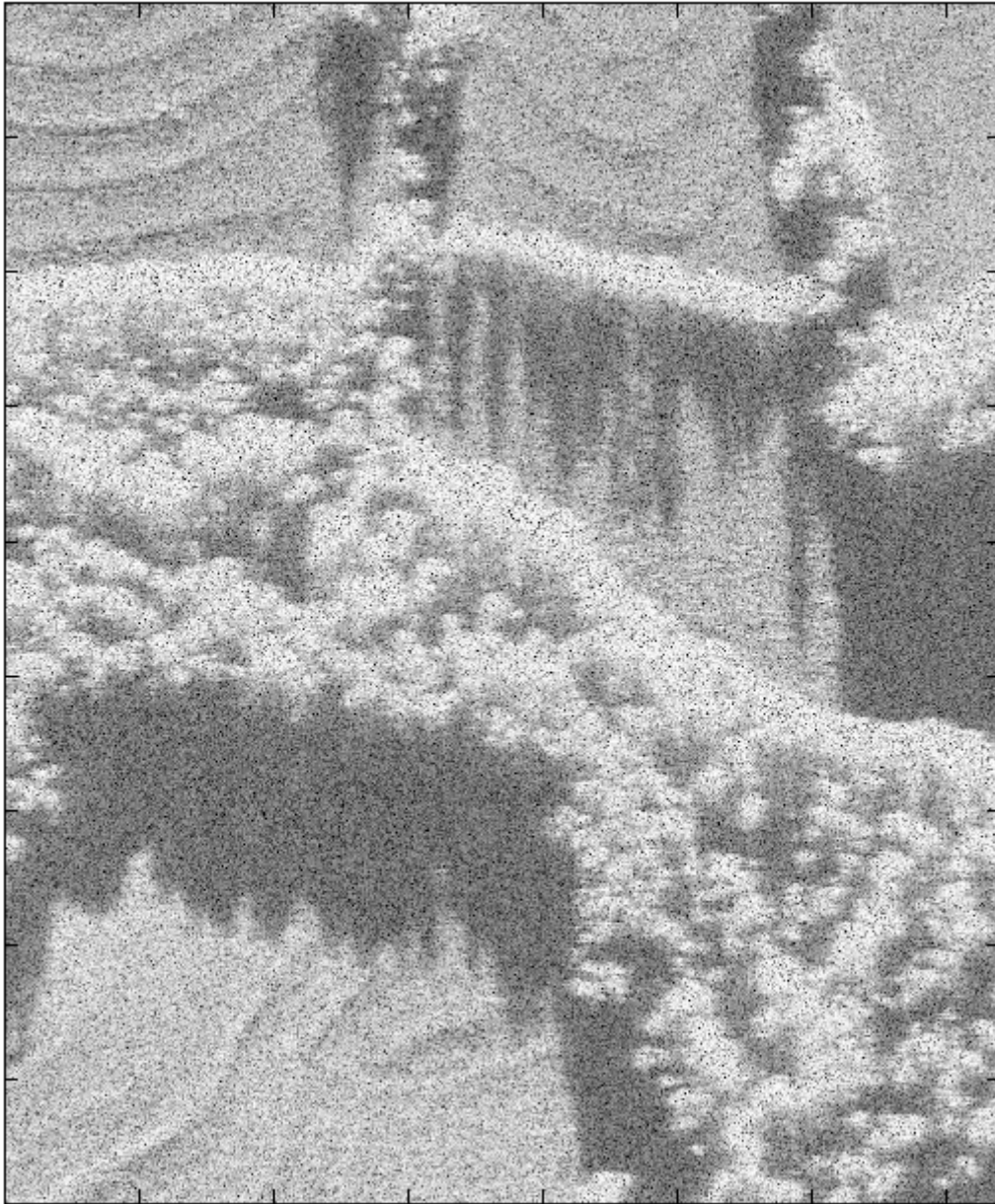


**Figure 1.2** - SAR image, file HB06198, MSTAR data.

Many distributions have been proposed in the literature to model the amplitude probability density function (APDF) of ground SAR data. In this work, we compare the histogram or empirical APDF of the data with Log-normal (LN), Weibull (W), K, and

Generalized K (GK) PDFs. The expressions of these PDFs and their moments are reported below (see also [Gre04], [Far97]), where  $R = \|z[i]\|$  denotes the clutter amplitude:

**Log-normal (LN):**

$$\text{PDF} \quad p_r(r) = \frac{1}{r\sqrt{2\pi\sigma^2}} \exp\left(-\frac{1}{2\sigma^2}[(\ln r - \ln \delta)^2]\right) u(r) \quad (1.6)$$

$$\text{Moments} \quad E\{R^n\} = \delta^n \exp(n^2 \sigma^2 / 2) \quad n=1,2,2\dots \quad (1.7)$$

where  $\delta$  is the scale parameter and  $\sigma$  is the shape parameter.

**Weibull (W):**

$$\text{PDF} \quad p_R(r) = \frac{c}{b^c} r^{c-1} \exp\left[-(r/b)^c\right] u(r) \quad (1.8)$$

$$\text{Moments} \quad E\{R^n\} = b^n \Gamma\left(\frac{n}{c} + 1\right) \quad n=1,2,2\dots \quad (1.9)$$

where  $c$  is the shape parameter and  $b$  the scale parameter. Rayleigh model is a particular case of Weibull for  $c=2$ , while for  $c=1$  we have the exponential negative probability density function (PDF).

**K Model:**

$$\text{PDF} \quad P_R(r) = \frac{\sqrt{2\nu/\mu}}{2^{\nu-1}\Gamma(\nu)} \left(\sqrt{\frac{2\nu}{\mu}} r\right)^\nu K_{\nu-1}\left(\sqrt{\frac{2\nu}{\mu}} r\right) u(r) \quad (1.10)$$

$$\text{Moments} \quad E\{R^n\} = \left(\frac{2\mu}{\nu}\right)^{\frac{n}{2}} \frac{\Gamma\left(\nu + \frac{n}{2}\right) \Gamma\left(1 + \frac{n}{2}\right)}{\Gamma(\nu)} \quad n=1,2,3,\dots \quad (1.11)$$



where:  $\Gamma(\cdot)$  is the Gamma function,  $K_{v-1}$  is the Bessel function of third kind and order  $v-1$ ,  $v$  is shape parameter,  $\mu$  is scale parameter.

**K-Generalized Model (lognormal texture, LNT):**

$$\text{PDF} \quad p_R(r) = \frac{r}{\sqrt{2\pi\sigma^2}} \int_0^\infty \frac{2}{\tau^2} \exp\left[\frac{r^2}{\tau} - \frac{1}{2\sigma^2} \left[\ln\left(\frac{\tau}{2m}\right)\right]^2\right] d\tau \quad (1.12)$$

$$\text{Moments} \quad E\{R^n\} = (2m)^{\frac{n}{2}} \Gamma\left(1 + \frac{n}{2}\right) \exp\left(\frac{n^2\sigma^2}{8}\right) \quad n=1,2,3,\dots \quad (1.13)$$

**K-Generalized Model (Gamma Generalized texture, GK):**

$$\text{PDF} \quad p_R(r) = \frac{2br}{\Gamma(\nu)} \left(\frac{\nu}{\mu}\right) \int_0^\infty \tau^{\nu b-2} \exp\left[\frac{r^2}{\tau} - \left(\frac{\nu}{\mu}\tau\right)^b\right] d\tau \quad (1.14)$$

$$\text{Moments} \quad E\{R^n\} = \left(\frac{\mu}{\nu}\right)^{\frac{n}{2}} \frac{\Gamma\left(\nu + \frac{n}{2b}\right) \Gamma\left(1 + \frac{n}{2}\right)}{\Gamma(\nu)} \quad n=1,2,3,\dots \quad (1.15)$$

In the past, the most popular model for clutter analysis was the Gaussian. According to it,  $r(n)$  is a stationary Gaussian complex process,  $r(n) = r_I(n) + jr_Q(n)$  with  $r_I(n)$  and  $r_Q(n)$  the in-phase and quadrature component respectively, both with zero mean value. This model is a consequence of the Central Limit Theorem which supposes a large number of scatterers in the resolution cell and no dominant scatterers.

In SAR systems with a very high resolution, the number of scatterers cannot be considered infinite and sometimes dominant scatterers can be present, then the hypotheses of the central limit theorem are not verified; the Gaussian complex model is inadequate and for the description of clutter amplitude we cannot apply the Rayleigh PDF.

A model that in the last 15 years became popular in the description of clutter data, particularly for real aperture radars, is the compound-Gaussian model. According to it, the samples of clutter complex envelope can be written as the product of two uncorrelated processes, that is:

$$r(n) = \sqrt{\tau(n)}x(n) \quad (1.16)$$

where  $x(n)$  is a stationary Gaussian complex process called *speckle*, and  $x(n) = x_I(n) + jx_Q(n)$ , where  $x_I(n)$  and  $x_Q(n)$  are respectively the in-phase and quadrature components.  $x_I(n)$  and  $x_Q(n)$  satisfy the following equations:

$$E\{x_I(n)\} = E\{x_Q(n)\} = 0 \quad (1.17)$$

$$E\{x_I^2(n)\} = E\{x_Q^2(n)\} = \frac{1}{2}. \quad (1.18)$$

Therefore

$$E\{x(n)^2\} = 1 \quad (1.19)$$

The amplitude of the speckle is Rayleigh-distributed.

$\tau(n)$  is a real positive process called *texture* and represents the varying RCS (Radar Cross Section) in the SAR image. If the PDF of clutter and texture are known, we can obtain the distribution of the clutter amplitude through the expression:

$$|r(n)| = R = \sqrt{\tau(n)}|x(n)| \quad (1.20)$$

$$f_R(r) = \int_{-\infty}^{+\infty} f_R(r|\tau) \cdot f_\tau(\tau) d\tau \quad (1.21)$$

It is worth noticing that in this analysis we consider terrain images for which the clutter processes are not variable with time but with space. The  $n$  index generally denotes the time lags. For our data  $n$  denotes the space position.

Weibull, K and Generalized-K models are particular cases of the compound-Gaussian model<sup>1</sup>. The speckle is always Gaussian distributed, while each different model is characterized by the distribution of the texture.

Texture can be characterized by the Gamma ( $\Gamma$ ) PDF [Gin02]:

$$p_{\tau}(\tau) = \frac{1}{\Gamma(\nu)} \left( \frac{\nu}{\mu} \right)^{\nu} \tau^{\nu-1} e^{-(\nu/\mu)\tau} \quad \tau \geq 0 \quad (1.22)$$

where  $\Gamma(\cdot)$  is the gamma function,  $\mu$  the mean value,  $\mu = E\{\tau\}$ ;  $\nu$  is the order parameter ( $\nu$  is a measure of Gaussian deviation); in other words  $\nu$  is a measurement of the non-homogeneity of the texture. The variance of  $\tau$  is related to  $\nu$  by  $\text{var}\{\tau\} = \mu^2 / \nu$ .

Experimental values of  $\nu$  are generally larger than 0.1. When  $\nu \rightarrow \infty$ ,  $\text{var}\{\tau\} \rightarrow 0$  and the clutter becomes Gaussian-distributed; this situation corresponds to a homogeneous scene.

In this condition (Gamma distributed texture and Gaussian distributed speckle), the clutter amplitude  $r$  is distributed by a K PDF, whose analytic expression is reported in eq. (1.5). In the case of Gaussian PDF for speckle and Generalized-Gamma PDF for the texture, we obtain a clutter amplitude modeled as GK (Generalized-K). This PDF is expressed by eq. (1.9). The Generalized Gamma ( $G\Gamma$ ) PDF is given by [Gin00]:

$$p_{G\Gamma}(\tau) = \frac{\nu b}{\mu \Gamma(\nu)} \left( \frac{\nu \tau}{\mu} \right)^{\nu b - 1} \exp \left[ - \left( \frac{\nu}{\mu} \tau \right)^b \right] u(\tau) \quad (1.23)$$

where  $u(\cdot)$  is step function,  $\Gamma(\cdot)$  is the Gamma function,  $\mu$  is scale parameter,  $\nu$  is the shape parameter and  $b$  is the power parameter.

In the case of Gaussian PDF for speckle and Lognormal PDF for texture, we obtain a clutter amplitude distribution modeled as GK “with Lognormal texture”; analytic expression is reported in (1.7).

---

<sup>1</sup> The Lognormal is not a compound-Gaussian model.

Characteristic parameters of Lognormal, Weibull, K, GK with Lognormal texture and GK with Gamma Generalized texture PDFs, have been estimated through moments method, by equating the expressions of theoretical moments with the corresponding estimates obtained by the expression:

$$\hat{E}\{R^n\} = \hat{m}_R(n) = \sum_{i=1}^N |r(i)|^n \quad (1.24)$$

where  $N$  is the number of samples for the considered image (as instance,  $N=2626048$  for the HB06171 file). Characteristic parameters of GK with  $G\Gamma$  texture PDF have been estimated by the following method [Gin00]:

$$\hat{\Lambda} = \arg \min_{\Lambda} \sum_{n=1}^5 \left| \frac{\hat{m}_R(n) - m_R(n)}{m_R(n)} \right|^2 \quad (1.25)$$

where  $\Lambda$  is the vector of parameters to be estimated.

The data we processed have been obtained by Sandia National Laboratory with Starlos SAR on September, 05, 2005 at Huntsville, Alabama (USA). This sensor operates in X-band (central frequency 9.6 GHz). Principal characteristics of this radar are reported in Table 1.1.

The dataset consists of 50 files; each file presents a header in which some information on the radar characteristics is reported: frequency, resolution, etc.

Each file, after the header, contains modulus and phase of the data. The modulus is used for visualization of images. These images represent different type of terrain.

<b>Data Collectors</b>	Sandia National Lab
<b>Date of the acquisition</b>	05/09/1995
<b>site</b>	Huntsville, Alabama (USA)
<b>Sensor name</b>	Twin Otter
<b>Range resolution</b>	0.3047 m
<b>Cross range resolution</b>	0.3047 m
<b>Range pixel spacing</b>	0.2021048 m
<b>Cross range pixel spacing</b>	0.203125 m
<b>Additive Noise</b>	-32 to -34 dB
<b>Multiplicative Noise</b>	-10 dB
<b>Central frequency</b>	9.60 GHz
<b>Bandwidth</b>	0.591 GHz
<b>Dynamic Range</b>	64 dB
<b>Azimuth Beamwidth</b>	8.8°
<b>Elevation Beamwidth</b>	6.8°
<b>Polarization</b>	HH
<b>Bits per pixel</b>	16
<b>Radar position</b>	bottom

**Table 1.1** – MSTAR radar characteristics

We have classified the files by observing SAR images and by noting presence and absence of natural or man-made objects. This classification is based on visual inspection. We have recognized four terrain types:

1. grass field
2. land with dense vegetation
3. land with sparse vegetation
4. land characterized by object man-made (farm-house) and vegetation

This classification is purely visual and it is not rigorous (we can find some man-made object in areas classified as “land with dense vegetation”).

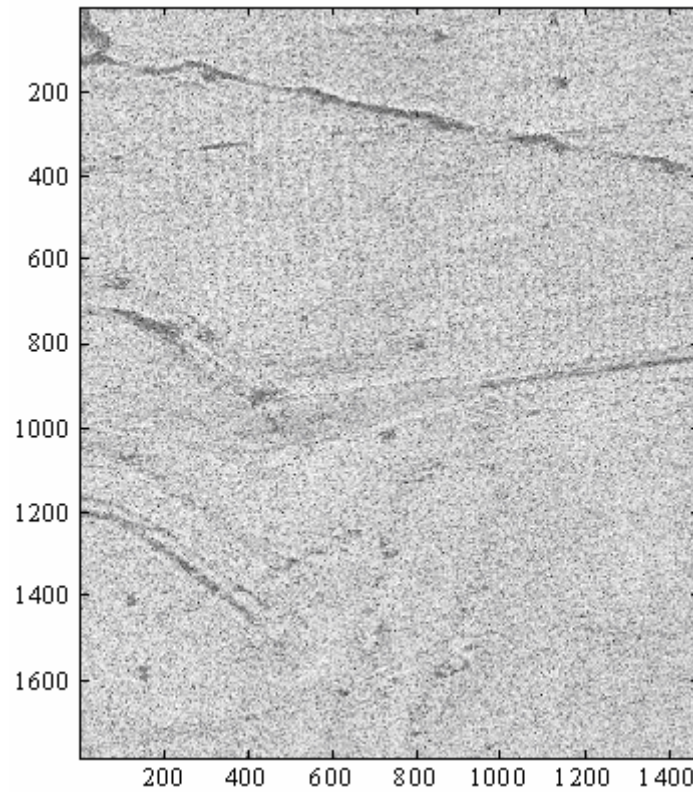
The modulus of data is saved in matrices with variable dimensions. All the matrices have the same number of rows (1784), while the columns vary from a minimum length of 1472 to a maximum length of 1478.

We have analyzed grass field first, in particular 7 files, cut in patches obtained from the original images. Later we will consider the file HB06202 which is relative to dense vegetation terrain.

## 1.2 Statistical analysis of grass field

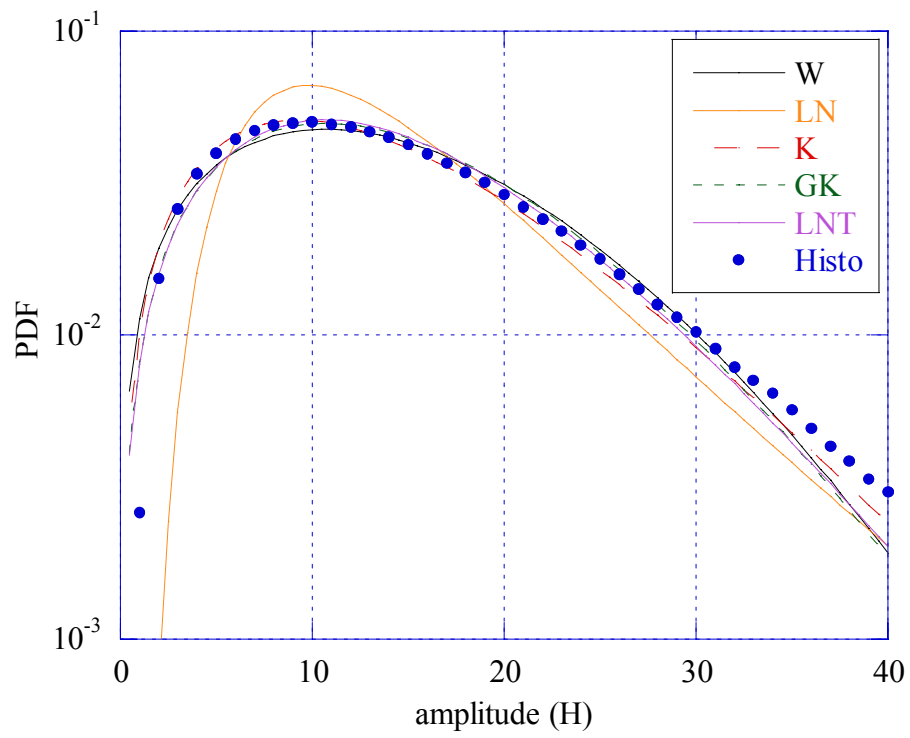
### 1.2.1 HB06171 File

Statistical analysis of this file has been performed on the overall image and on two patches obtained by the original image. The size of the large image is 1784x1472 pixels. The two patches have size (1,892)x(1,1472) and (893,1784)x(1,1472) respectively, where in  $(x,y)$   $x$  is the first pixel and  $y$  the last one in range and cross-range. The whole image is reported in Fig. 1.2.

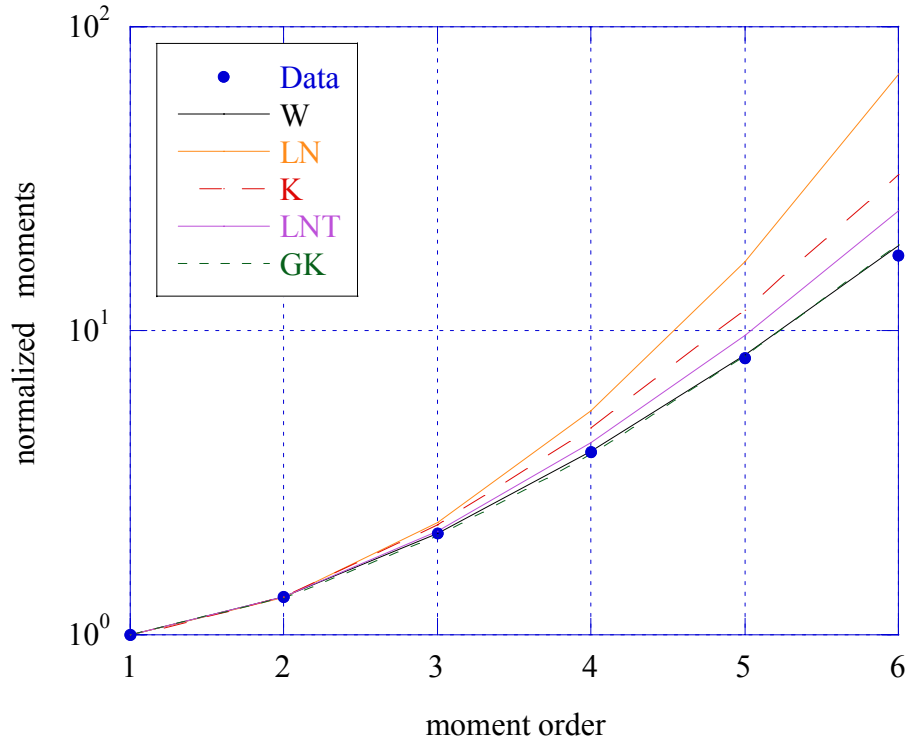


**Figure 1.3** - Grass field of HB06171 file.

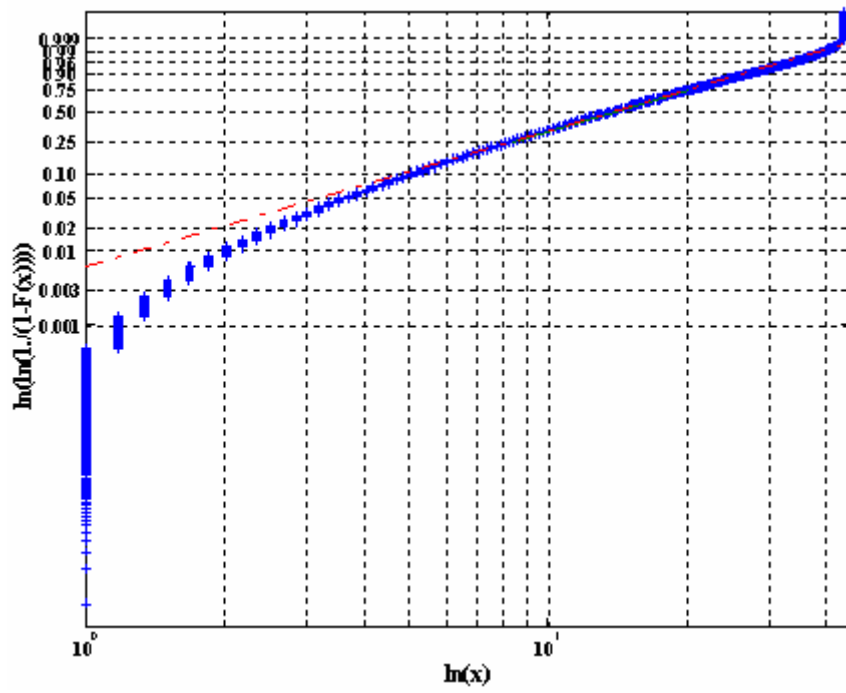
In the following, we show the results of the statistical analysis. Fig. 1.4 shows plots of the PDFs for the overall image. Histogram has been calculated on 101 bins (intervals); Fig. 1.5 and Fig. 1.6 show the normalized moments and the “Weibull paper” [Far97].



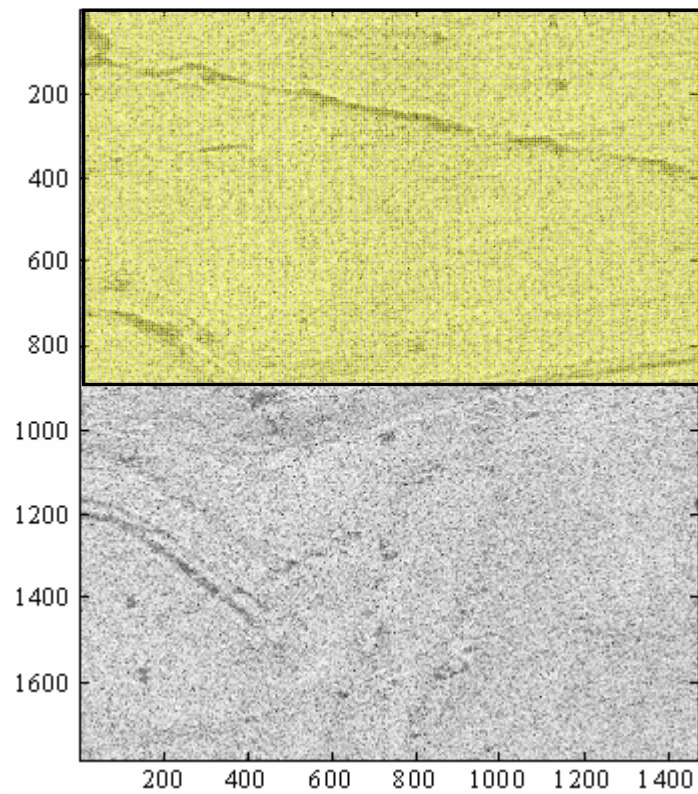
**Figure 1.4** - Amplitude PDF of clutter data for the image (1784x1472).



**Figure 1.5** - Normalized moments for the image (1784x1472).



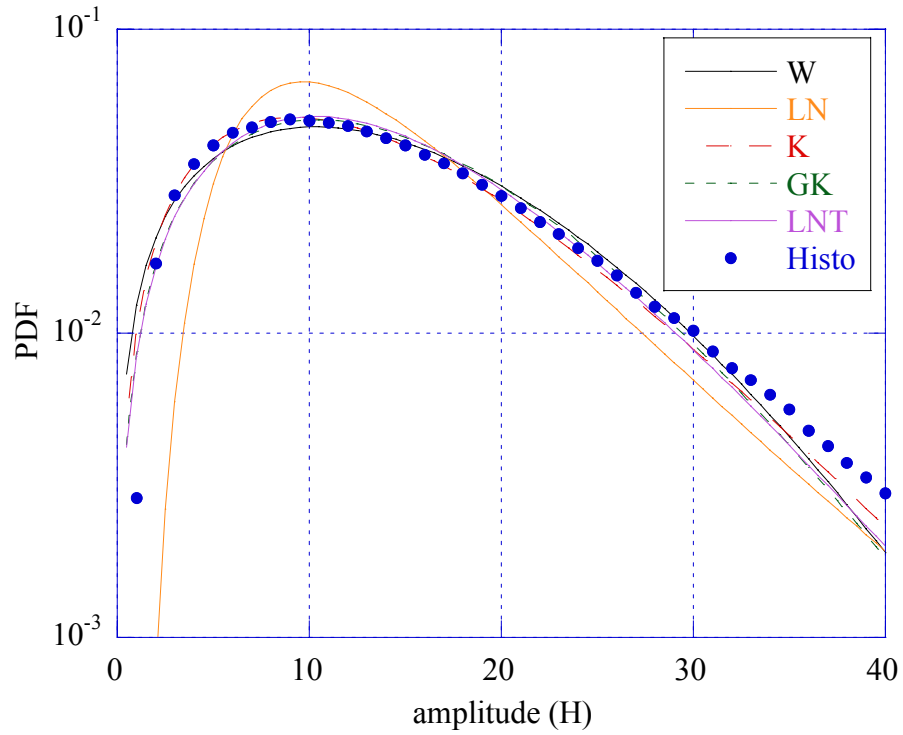
**Figure 1.6** - Weibull paper for the image (1784x1472).



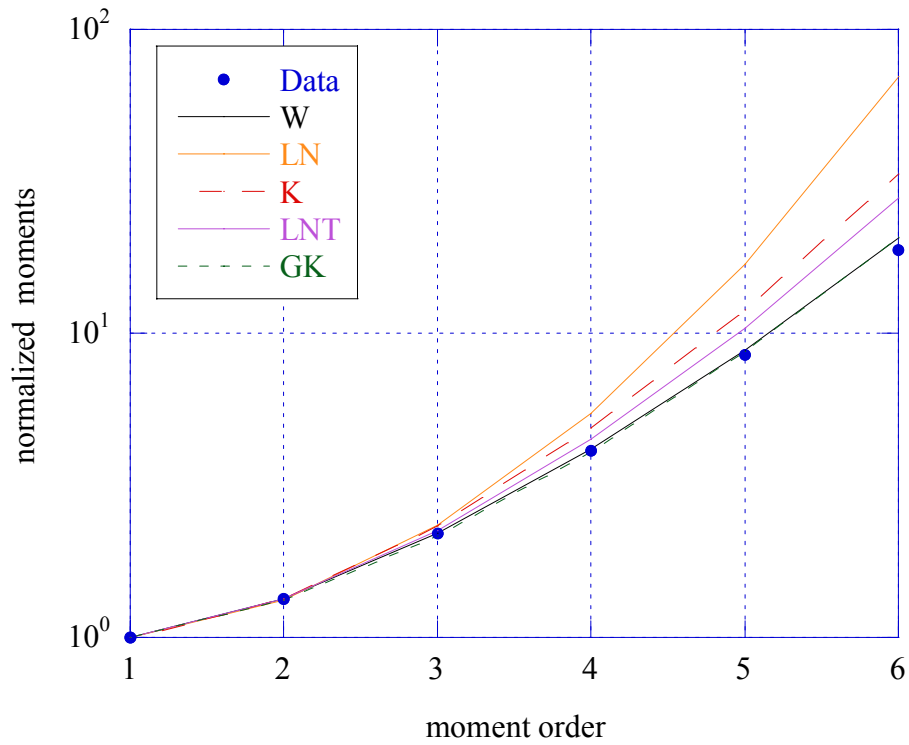
**Figure 1.7** - Grass field in the upper patch (1,892)x(1,1472).



Figure 1.7 shows the image of the upper patch considered in the statistical analysis and Figs. 1.8-1.10 the results of statistical analysis for this patch  $(1,892) \times (1,1472)$ .



**Figure 1.8** - Amplitude PDF of clutter data for the patch  $(1,892) \times (1,1472)$ .



**Figure 1.9** - Normalized moments for the patch  $(1,892) \times (1,1472)$ .

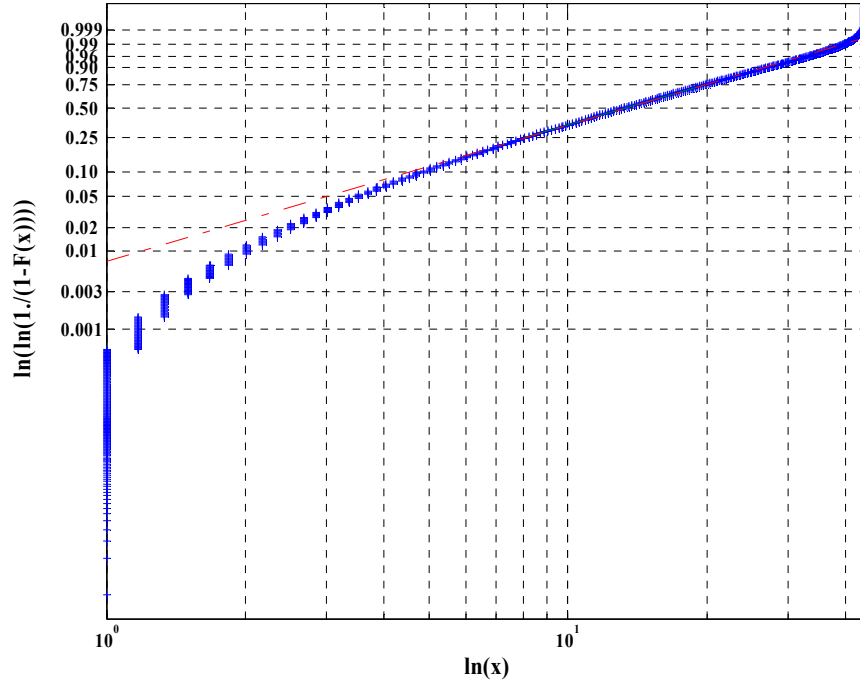


**Figure 1.10** - Weibull paper for the patch  $(1,892) \times (1,1472)$ .

We also report the results for the lower patch in Fig. 1.11-1.14. The results are very similar for the whole image and the two patches due to the homogeneity of the MSTAR data in this area.

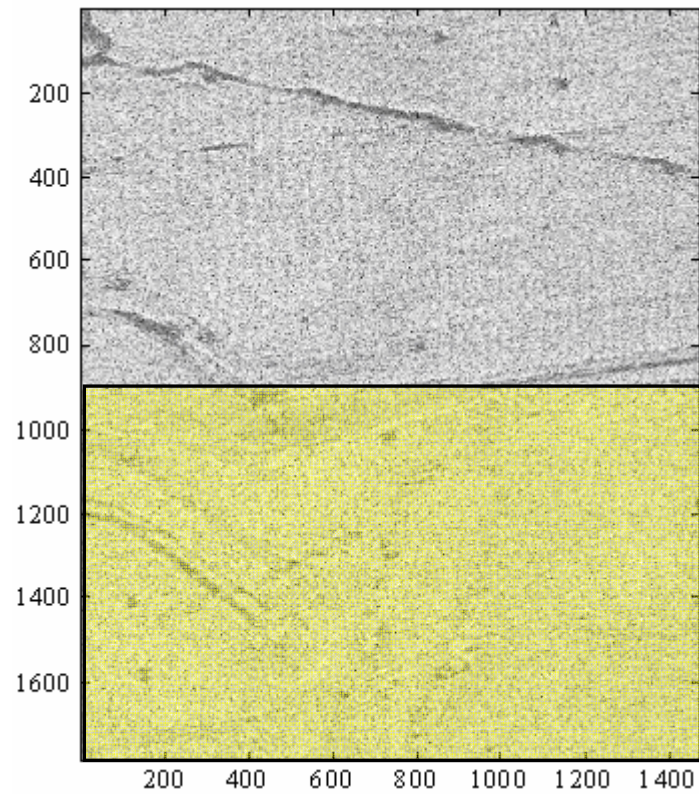


**Figure 1.11** - Grass field in the lower patch  $(893,1784) \times (1,1472)$ .

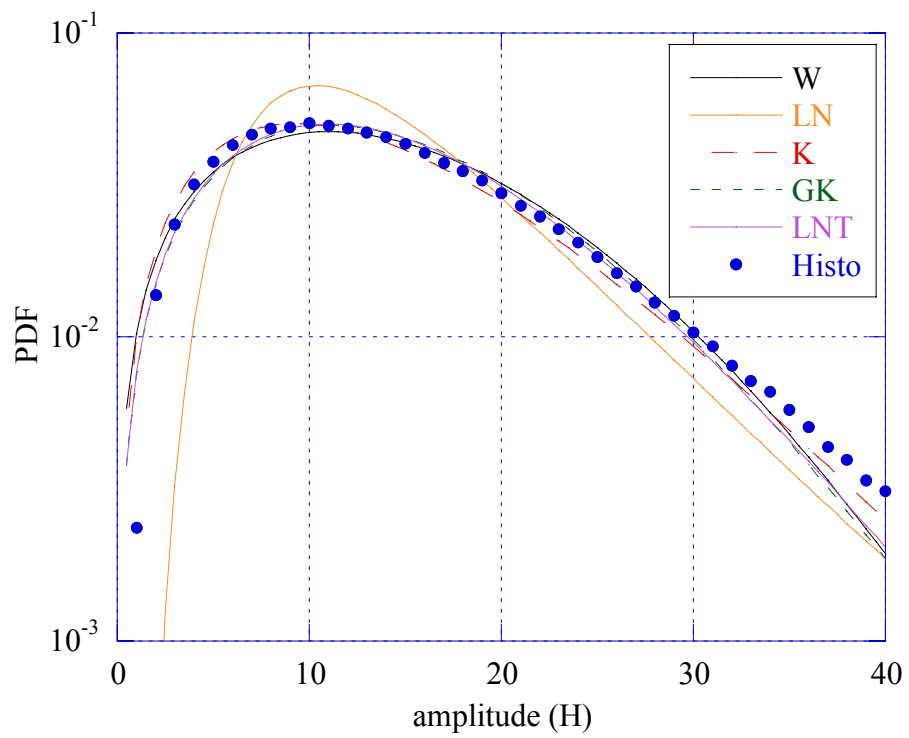


**Figure 1.12** - Amplitude PDF of clutter data for the patch  $(893,1784) \times (1,1472)$ .

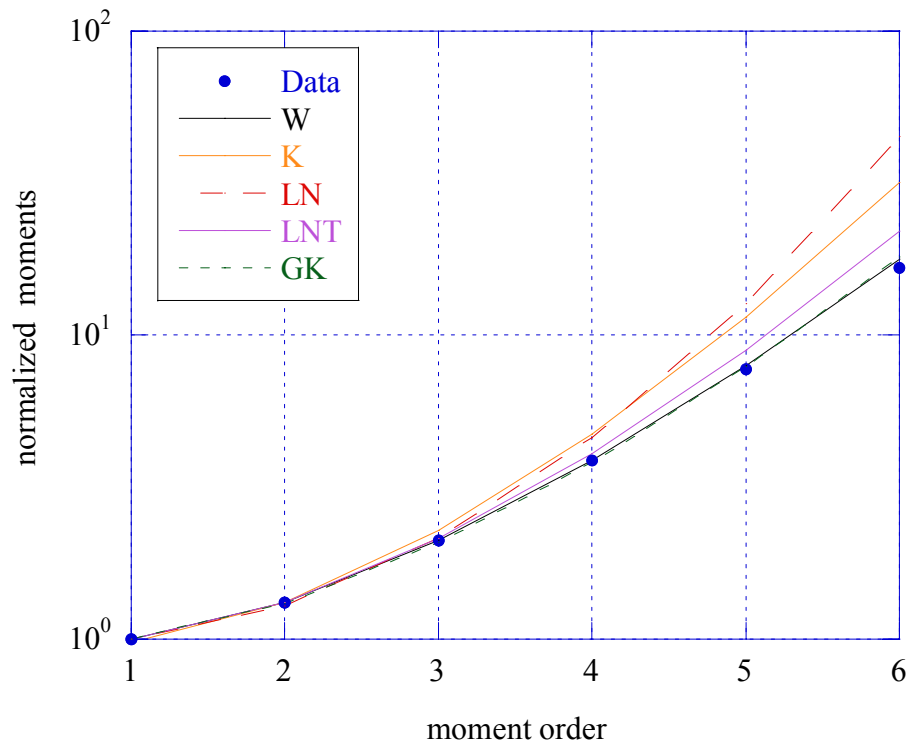


**Figure 1.13** - Normalized moments for the patch  $(893,1784) \times (1,1472)$ .

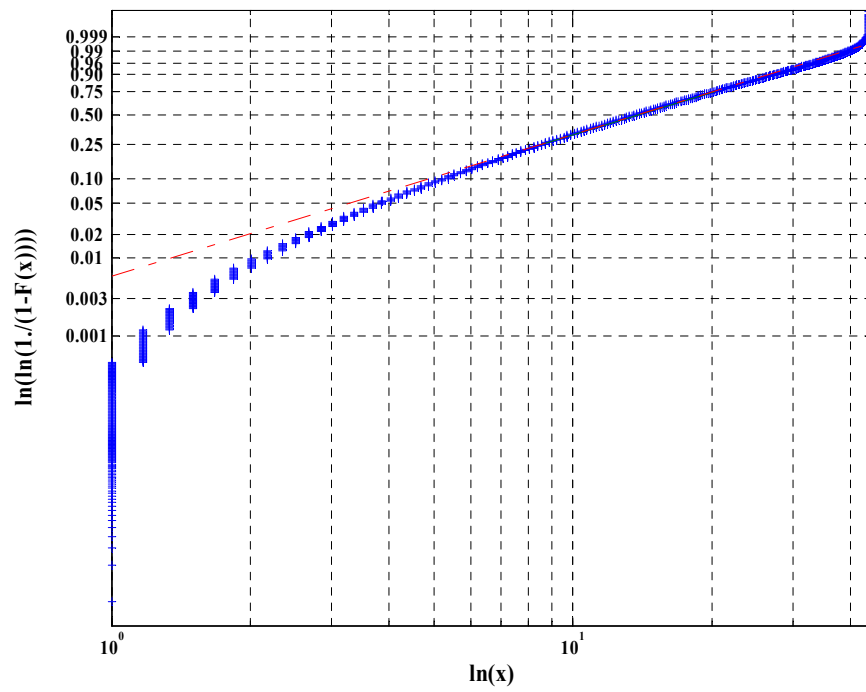


**Figure 1.14** - Weibull paper for the patch  $(893,1784) \times (1,1472)$ .

In Table 1.2 we report the parameters' values estimated by the Method of Moments (MoM) for the whole image and the two patches.

Size of patch	Weibull		Lognormal		K		GK			LNT	
	$\hat{c}$	$\hat{b}$	$\hat{\delta}$	$\hat{\sigma}$	$\hat{\nu}$	$\hat{\mu}$	$\hat{\nu}$	$\hat{\mu}$	$\hat{b}$	$\hat{\sigma}^2$	$\hat{m}$
(1784x1472)	1.66	15.66	11.93	0.57	2.86	135.47	0.35	150.84	4.72	0.33	114.83
(1,892)x(1,1472)	1.63	15.42	11.70	0.58	2.86	132.96	0.28	124.28	5.33	0.36	110.64
(893,1784)x(1,1472)	1.69	15.90	12.19	0.55	2.86	137.99	0.36	151.71	5.02	0.29	119.12

**Table 1.2** - Parameter values of models tested on *HB06171* file.

Due to the homogeneity of the image, the statistical differences between whole image and two patches are negligible, as also evidenced by the PDF parameters, reported in Table 1.2.

All the models, but the log-normal, show a good fitting with the histogram. Some deviation is present only on the tail. Similar conclusions can be drawn observing the plots of moments, where the best models seem to be K, W and LNT. Looking at the values of the PDF parameters, we can conclude that the clutter of this image is not spiky. In fact, the average value of Weibull shape parameter  $c$  is close to 2, meaning that the clutter is almost Rayleigh distributed.<sup>2</sup>

As a deeper analysis, we applied two goodness-of-fit test, Kolmogorov-Smirnov and Kuiper tests. Details on the mathematical theory and practical implementation of these tests are described in Appendix A.

The results are reported in Tables 1.2 and 1.3 relating to the whole images and the two patches. It is apparent that both tests provide very similar results for all the models, and then they do not help us in identifying the best fitting. We report in red the model that exhibits the smallest distance to the data distribution.

<sup>2</sup> We use Weibull shape parameter  $c$  to measure the spikiness of the clutter because the meaning of this parameter is very easy to understand.

<b>1784x1472</b>	<b>W</b>	<b>LN</b>	<b>K</b>	<b>GK</b>	<b>LNT</b>
<b>Prob</b>	100 %	97 %	100 %	100 %	100 %
<b>d</b>	$1.48*10^{-2}$	$6.71*10^{-2}$	$2.25*10^{-2}$	$1.57*10^{-2}$	$1.23*10^{-2}$
<b>(893,1784)x (1,1472)</b>					
	100 %	92 %	100 %	100 %	100 %
	$1.55*10^{-2}$	$7.66*10^{-2}$	$2.86*10^{-2}$	$1.70*10^{-2}$	$1.17*10^{-2}$
<b>(1,892)x(1,1472)</b>					
	100	94 %	100 %	100 %	100 %
	$1.44*10^{-2}$	$7.30*10^{-2}$	$1.70*10^{-2}$	$1.70*10^{-2}$	$1.44*10^{-2}$

**Table 1.3** - Results of Kolmogorov test -Smirnov for all models utilized.

<b>1784x1472</b>	<b>W</b>	<b>LN</b>	<b>K</b>	<b>GK</b>	<b>LNT</b>
<b>Prob</b>	100 %	97 %	100 %	100 %	100 %
<b>d</b>	$2.84*10^{-2}$	$11.10*10^{-2}$	$2.20*10^{-2}$	$2.61*10^{-2}$	$2.4*10^{-2}$
<b>(893,1784)x (1,1472)</b>					
	100 %	93 %	100 %	100 %	100 %
	$2.92*10^{-2}$	$12.20*10^{-2}$	$2.87*10^{-2}$	$2.78*10^{-2}$	$2.10*10^{-2}$
<b>(1,892)x(1,1472)</b>					
	100	94 %	100 %	100 %	100 %
	$2.44*10^{-2}$	$9.30*10^{-2}$	$2.70*10^{-2}$	$2.70*10^{-2}$	$1.90*10^{-2}$

**Table 1.4** - Results of Kuiper test for all models utilized.

### 1.2.2 HB06172 File

The Figure 1.15 shows the image considered for statistical analysis.

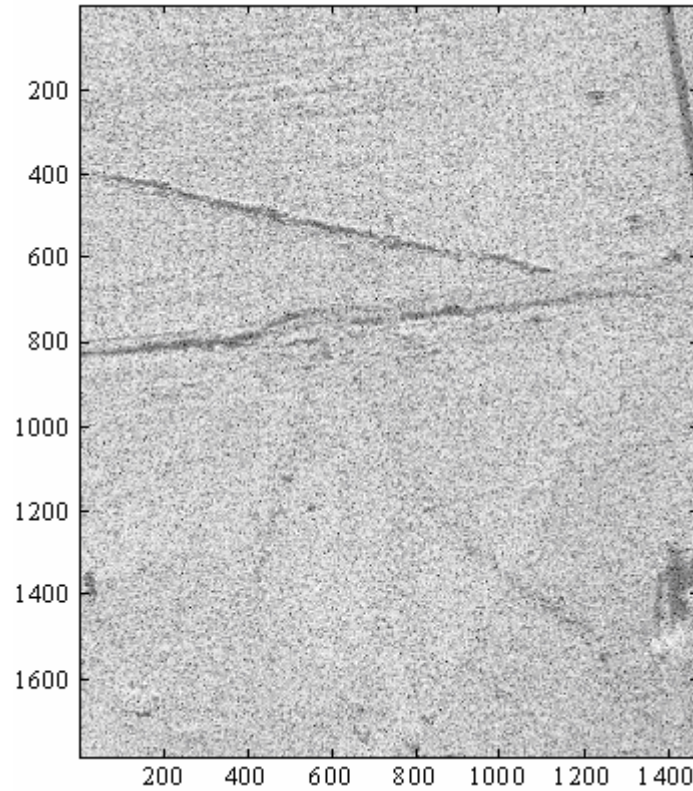


**Figure 1.15** - Grass field for the HB06172 file.

The analysis has been carried out on the total image, on the homogeneous upper patch  $(1,1000) \times (1,1472)$ , on the lower patch  $(1000,1784) \times (1,1472)$  where we observe a deformation of the terrain, and on the central patch  $(700,900) \times (1,1472)$  where the deformation is well evident.

In Figs 1.16-1.18 we show the results relating to the whole image and in Figs 1.19-1.30 the results of the patches.

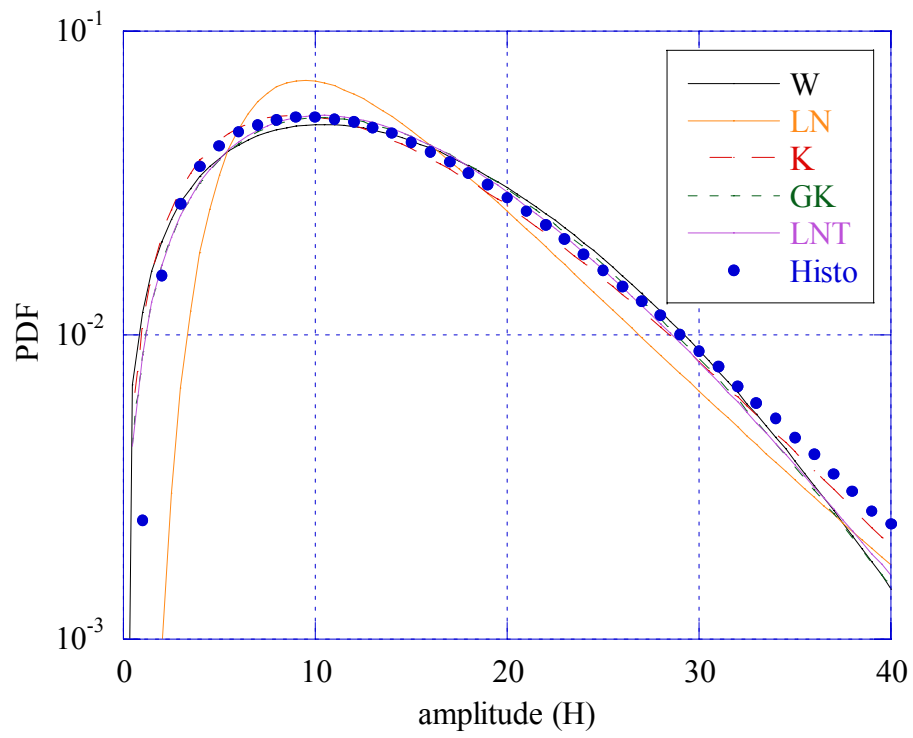


**Figure 1.16** - Amplitude PDF of clutter data for the overall image (1784x1472).

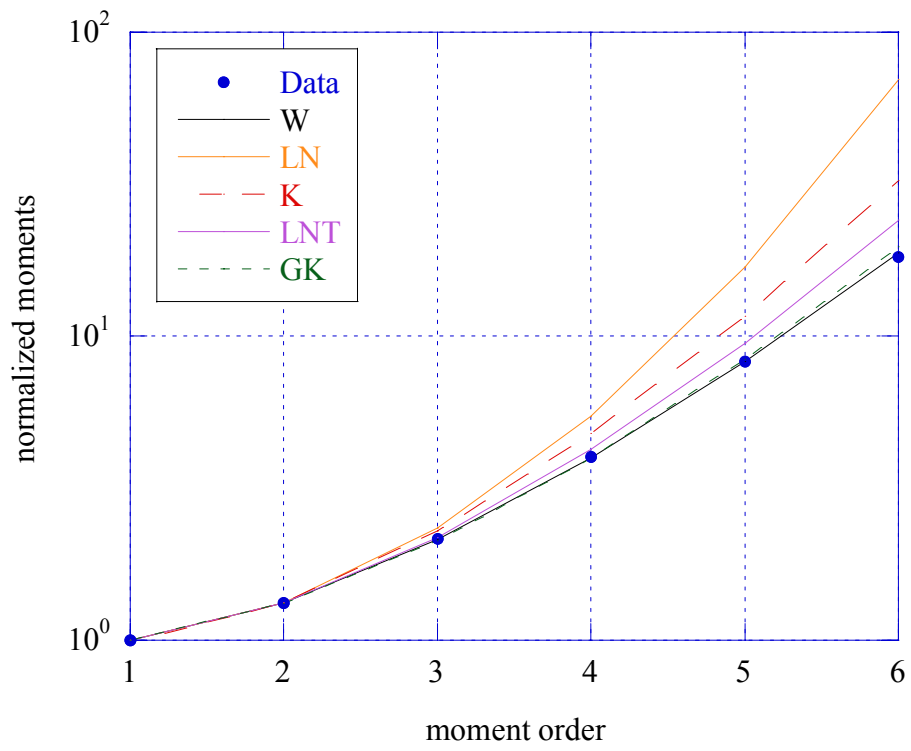


**Figure 1.17** - Normalized moments for the overall image (1784x1472).



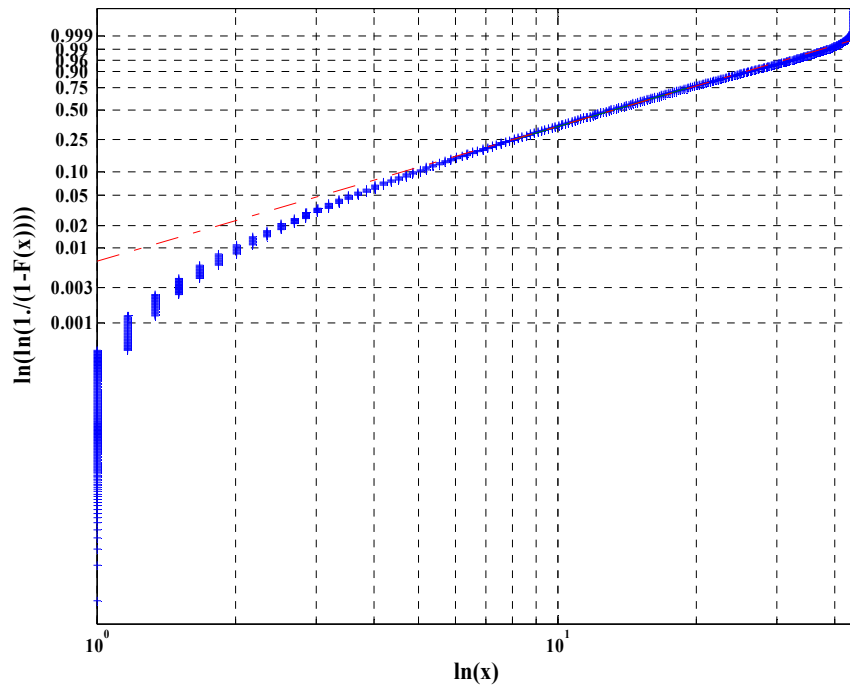


**Figure 1.18** - Weibull paper for the overall image (1784x1472).

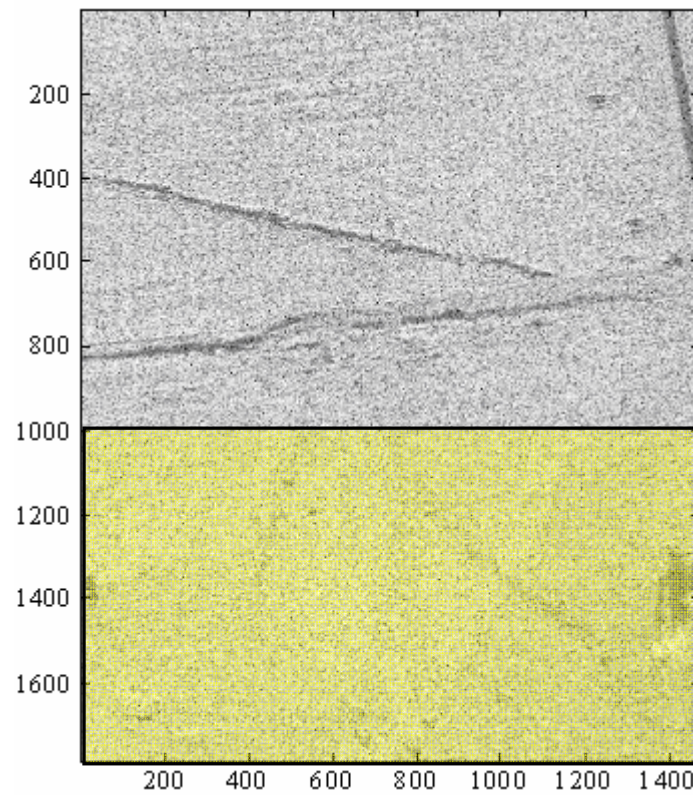


**Figure 1.19** - Image with the lower patch (1000,1784)x(1,1472).

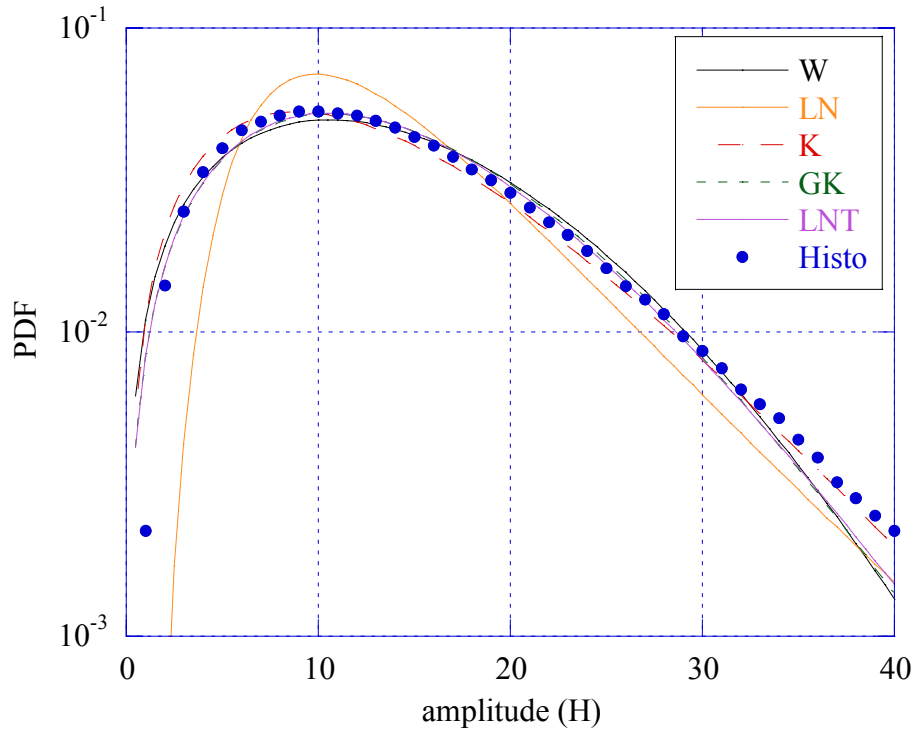


**Figure 1.20** - PDFs of the clutter for the patch  $(1000,1784) \times (1,1472)$ .

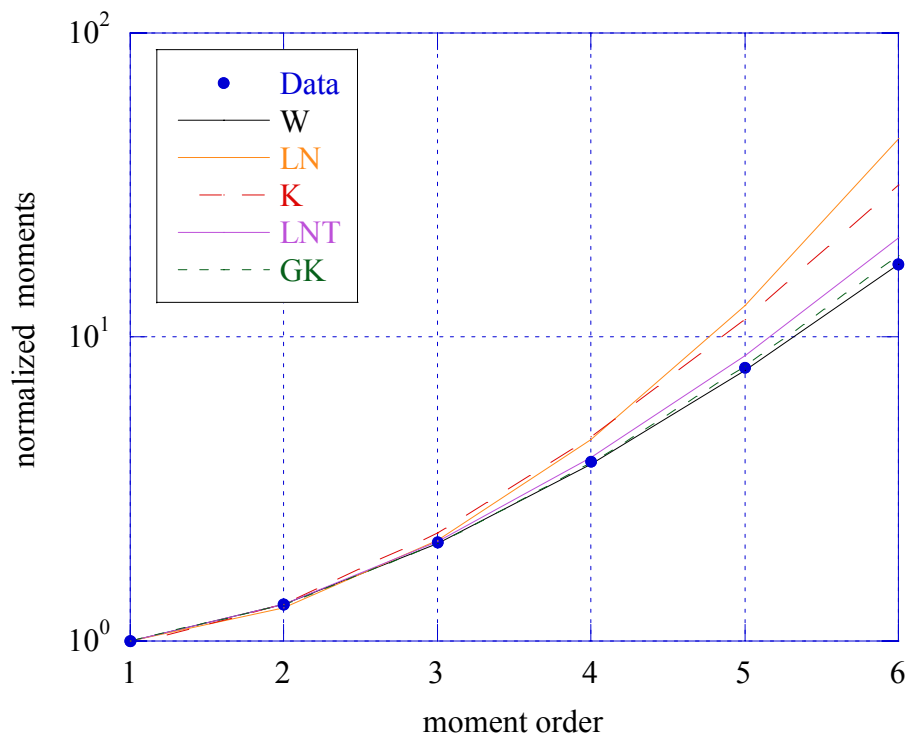


**Figure 1.21** - Normalized moments for the patch  $(1000,1784) \times (1,1472)$ .

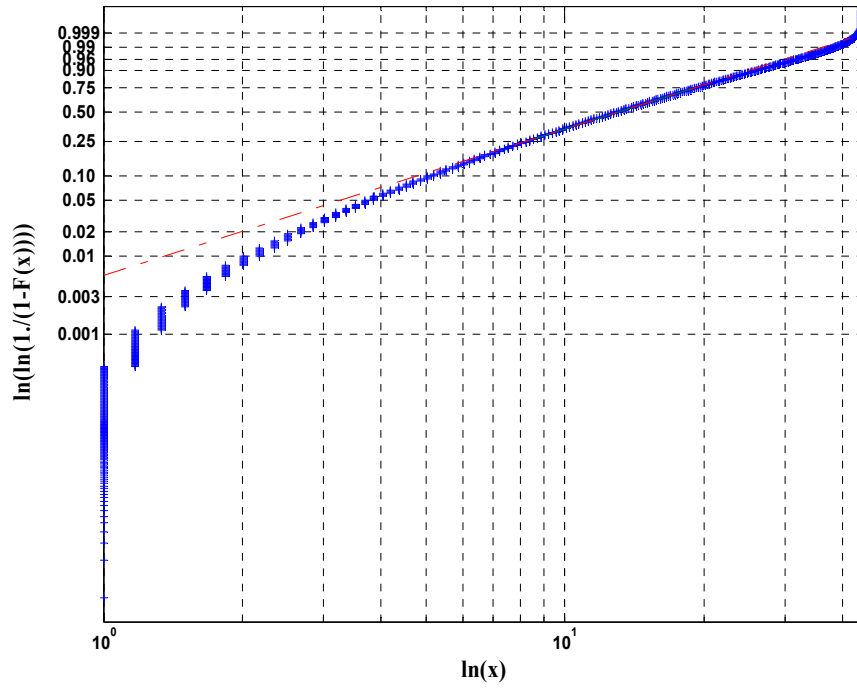


**Figure 1.22** - Weibull paper for the patch (1000,1784)x(1,1472).

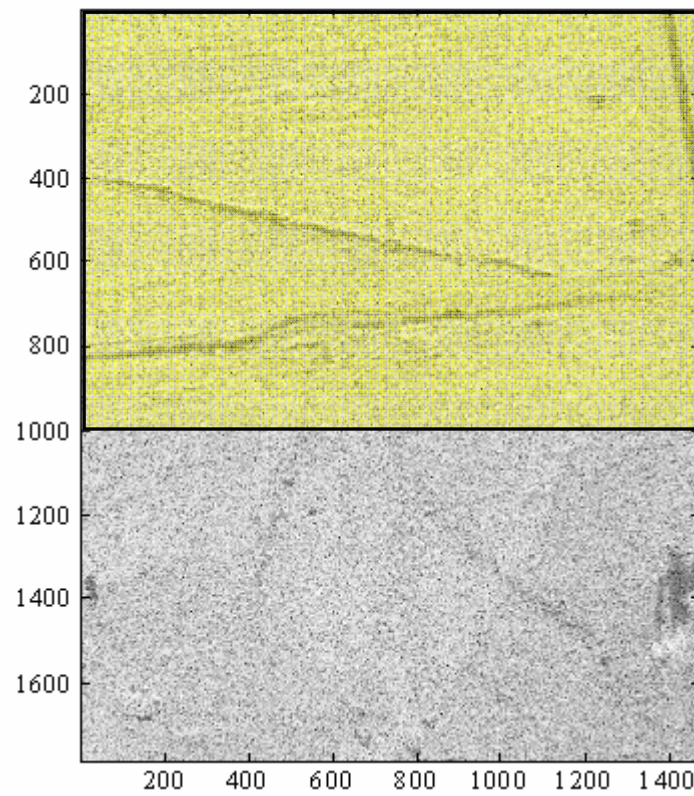


**Figure 1.23** - Image with the upper patch (1,1000)x(1,1472).

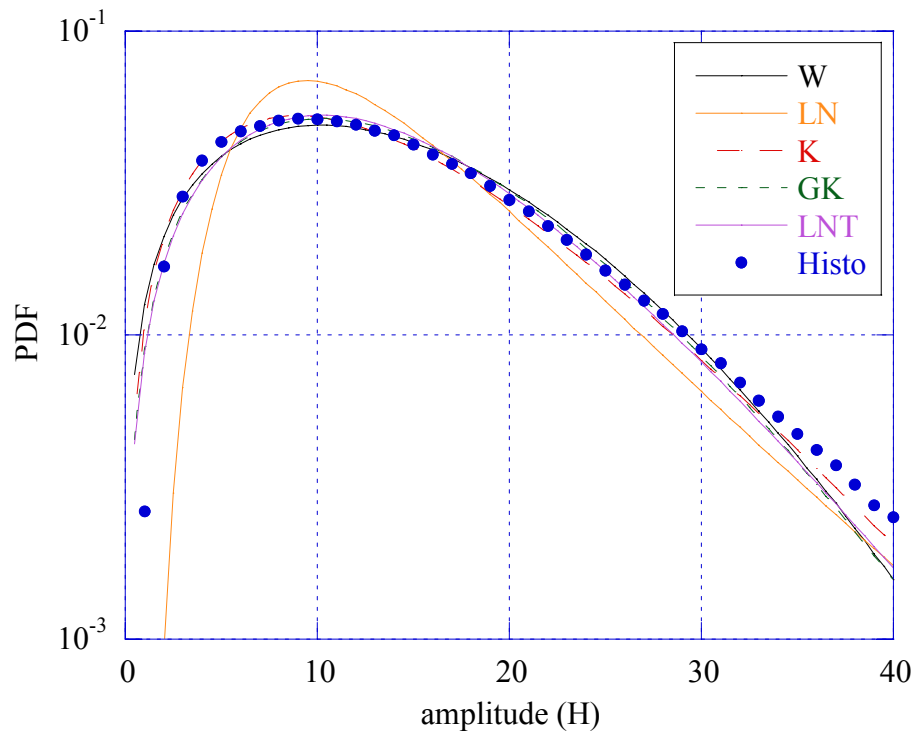


**Figure 1.24** - PDF of clutter for the patch  $(1,1000) \times (1,1472)$ .

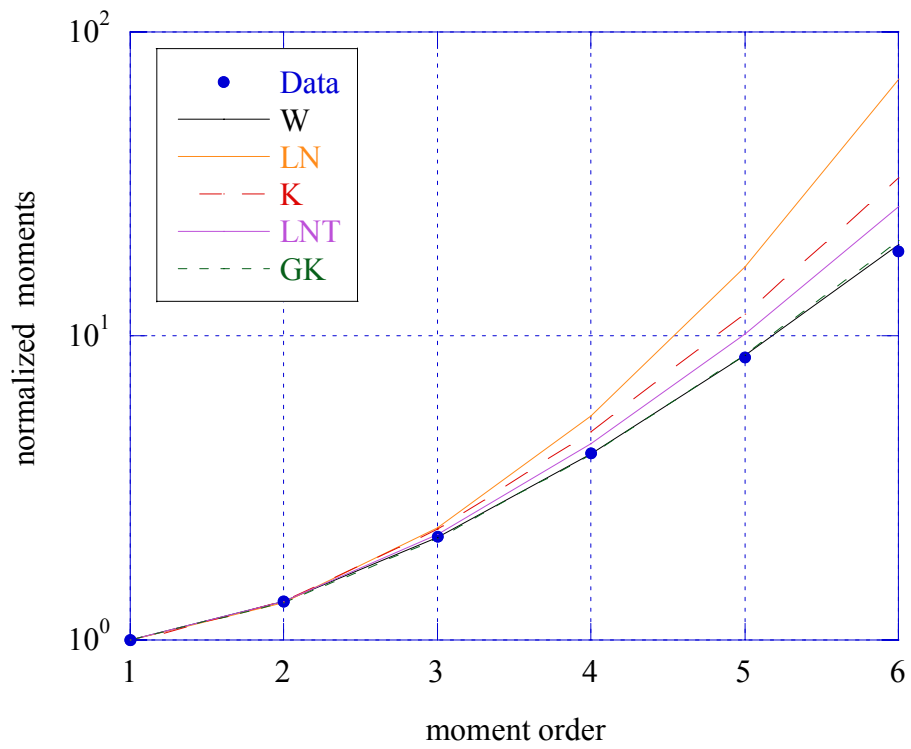


**Figure 1.25** - Normalized moments for the patch  $(1,1000) \times (1,1472)$ .

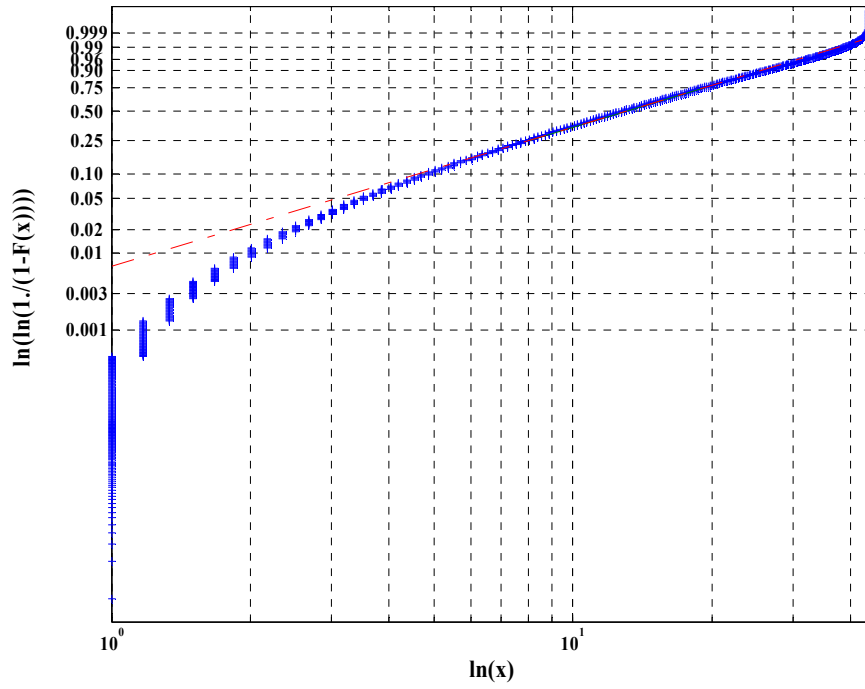


**Figure 1.26** - Weibull paper for the patch  $(1,1000)x(1,1472)$ .

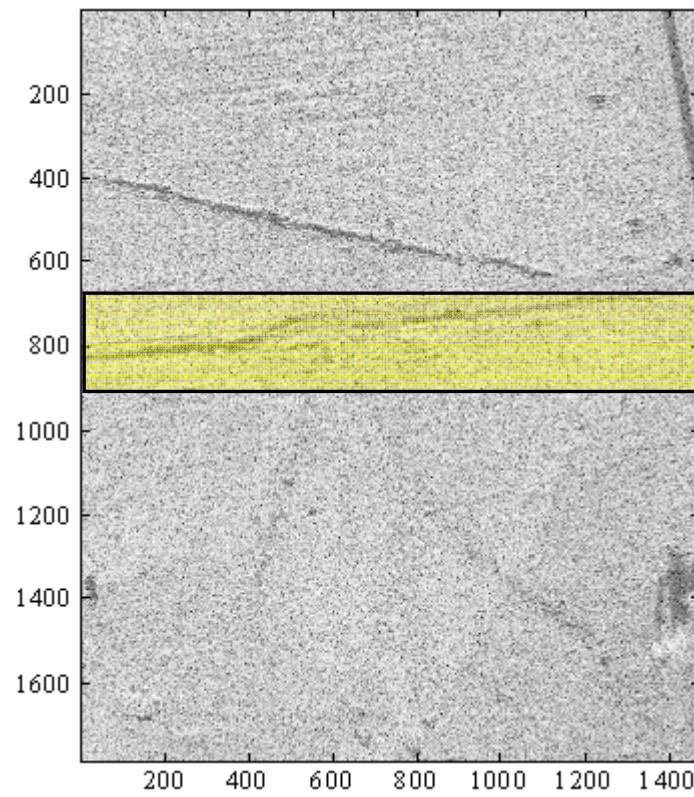


**Figure 1.27** - Image with the central patch  $(700,900)x(1,1472)$ .

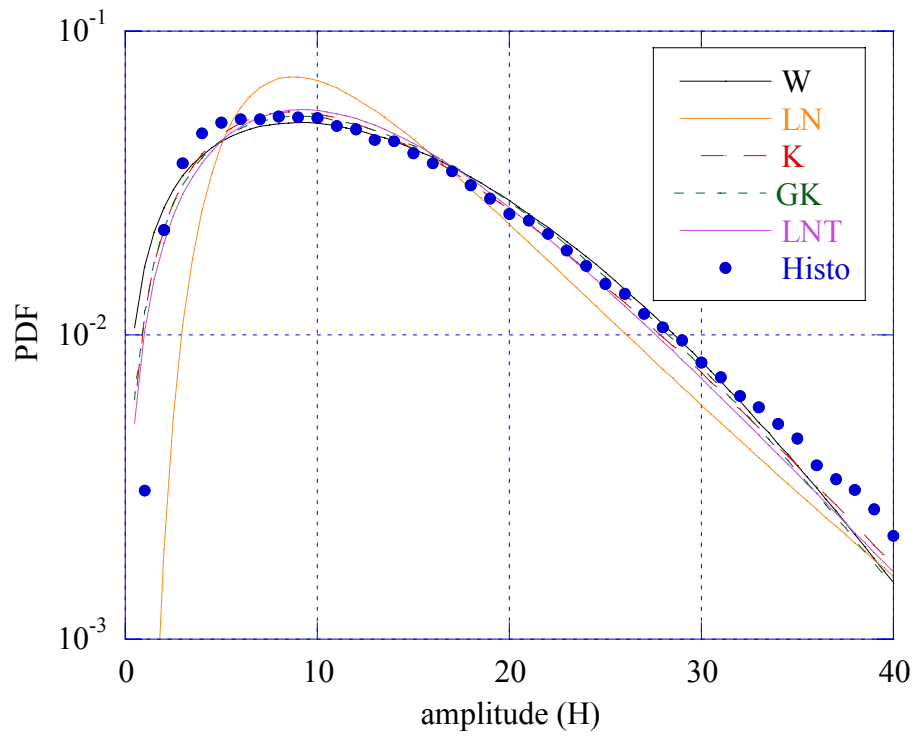


**Figure 1.28** - PDF of clutter for the patch  $(700,900) \times (1,1472)$ .

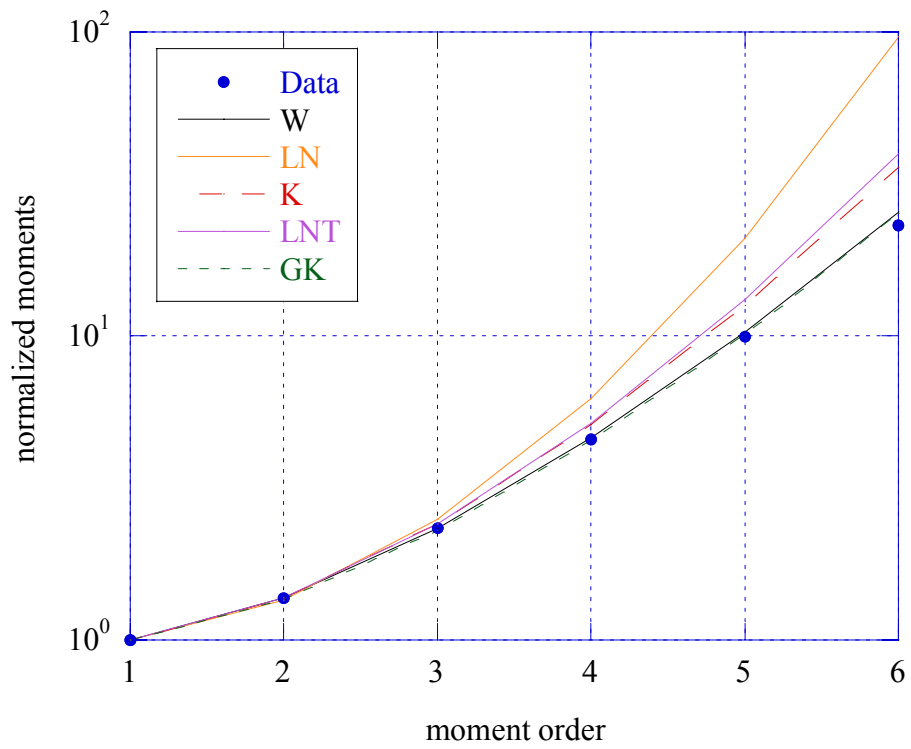


**Figure 1.29** - Normalized moments for the patch  $(700,900) \times (1,1472)$ .

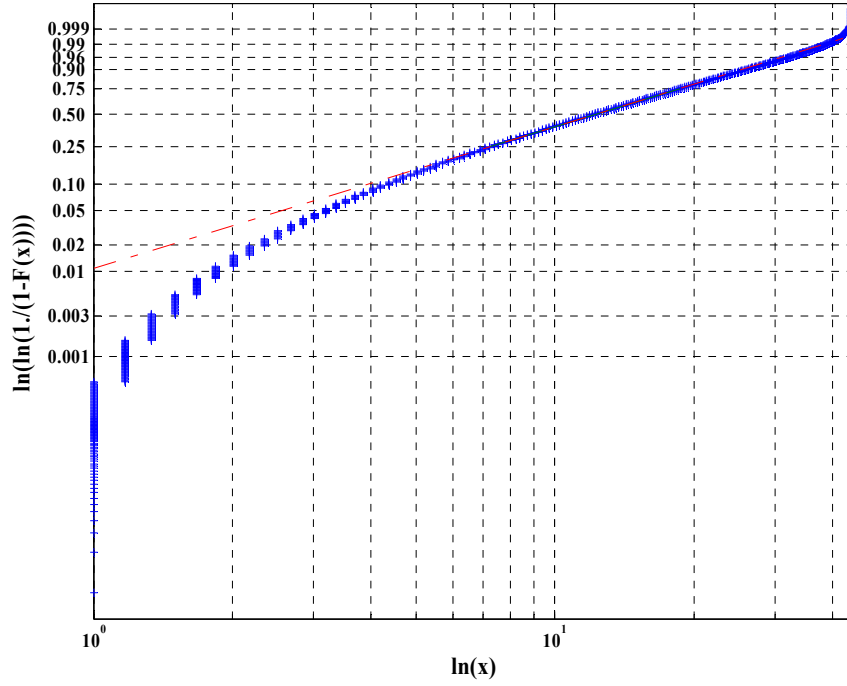


**Figure 1.30** - Weibull paper for the patch  $(700,900) \times (1,1472)$ .

Again, the statistical differences between whole image and the three patches are negligible, as also evidenced by the PDF parameters reported in Table 1.5. We can only observe that the central patch is a little bit spikier than the other two.

All the models, but the log-normal, show a good fitting with the histogram. The results of KS and Kuiper tests are reported in Tables 1.5 and 1.6. Both tests provide very similar results for all the models.

Size of patch	Weibull		Lognormal		K		GK			LNT	
	$\hat{c}$	$\hat{b}$	$\hat{\delta}$	$\hat{\sigma}$	$\hat{\nu}$	$\hat{\mu}$	$\hat{\nu}$	$\hat{\mu}$	$\hat{b}$	$\hat{\sigma}^2$	$\hat{m}$
(1784x1472)	1.66	15.06	11.47	0.57	2.86	125.28	0.28	112.95	5.64	0.33	106.30
(1,1000)x(1,1472)	1.64	15.04	11.47	0.57	2.86	126.14	0.25	107.44	5.83	0.36	105.44
(1000,1784)x(1,1472)	1.69	15.09	11.57	0.55	2.86	124.21	0.36	140.87	4.76	0.29	107.43
(700,900)x(1,1472)	1.54	14.27	10.62	0.62	2.18	118.50	0.19	86.65	5.98	0.48	92.05

**Table 1.5** - Parameter estimates of models tested on *HB06172* file.

<b>1784x1472</b>	<b>W</b>	<b>LN</b>	<b>K</b>	<b>GK</b>	<b>LNT</b>
<b>Prob</b>	100 %	96 %	100 %	100 %	100 %
<b>d</b>	$1.54 \cdot 10^{-2}$	$6.34 \cdot 10^{-2}$	$2.53 \cdot 10^{-2}$	$1.36 \cdot 10^{-2}$	$1.01 \cdot 10^{-2}$
<b>(700,900)x (1,1472)</b>					
	100 %	91 %	100 %	100 %	100 %
	$1.85 \cdot 10^{-2}$	$7.76 \cdot 10^{-2}$	$1.05 \cdot 10^{-2}$	$1.67 \cdot 10^{-2}$	$2.25 \cdot 10^{-2}$
<b>(1,1000)x(1,1472)</b>					
	100	96 %	100 %	100 %	100 %
	$1.51 \cdot 10^{-2}$	$7.00 \cdot 10^{-2}$	$1.95 \cdot 10^{-2}$	$1.43 \cdot 10^{-2}$	$1.25 \cdot 10^{-2}$
<b>(1000,1784)x(1,1472)</b>					
	100 %	95 %	100 %	100 %	100 %
	$1.70 \cdot 10^{-2}$	$7.15 \cdot 10^{-2}$	$2.39 \cdot 10^{-2}$	$1.31 \cdot 10^{-2}$	$0.99 \cdot 10^{-2}$

**Table 1.6** - Results of Kolmogorov -Smirnov test.

<b>1784x1472</b>	<b>W</b>	<b>LN</b>	<b>K</b>	<b>GK</b>	<b>LNT</b>
<b>Prob</b>	100 %	99 %	100 %	100 %	100 %
<b>d</b>	$2.05 \cdot 10^{-2}$	$10.05 \cdot 10^{-2}$	$2.27 \cdot 10^{-2}$	$2.20 \cdot 10^{-2}$	$1.96 \cdot 10^{-2}$
<b>(700,900)x (1,1472)</b>					
	100 %	93 %	100 %	100 %	100 %
	$2.34 \cdot 10^{-2}$	$11.32 \cdot 10^{-2}$	$2.02 \cdot 10^{-2}$	$2.64 \cdot 10^{-2}$	$10.00 \cdot 10^{-2}$
<b>(1,1000)x(1,1472)</b>					
	100 %	97 %	100 %	100 %	100 %
	$2.93 \cdot 10^{-2}$	$11.32 \cdot 10^{-2}$	$2.71 \cdot 10^{-2}$	$2.31 \cdot 10^{-2}$	$2.38 \cdot 10^{-2}$
<b>(1000,1784)x(1,1472)</b>					
	100 %	97 %	100 %	100 %	100 %
	$2.24 \cdot 10^{-2}$	$11.13 \cdot 10^{-2}$	$4.12 \cdot 10^{-2}$	$2.16 \cdot 10^{-2}$	$1.85 \cdot 10^{-2}$

**Table 1.7** - Results of Kuiper test.



### 1.2.3 HB06173 File

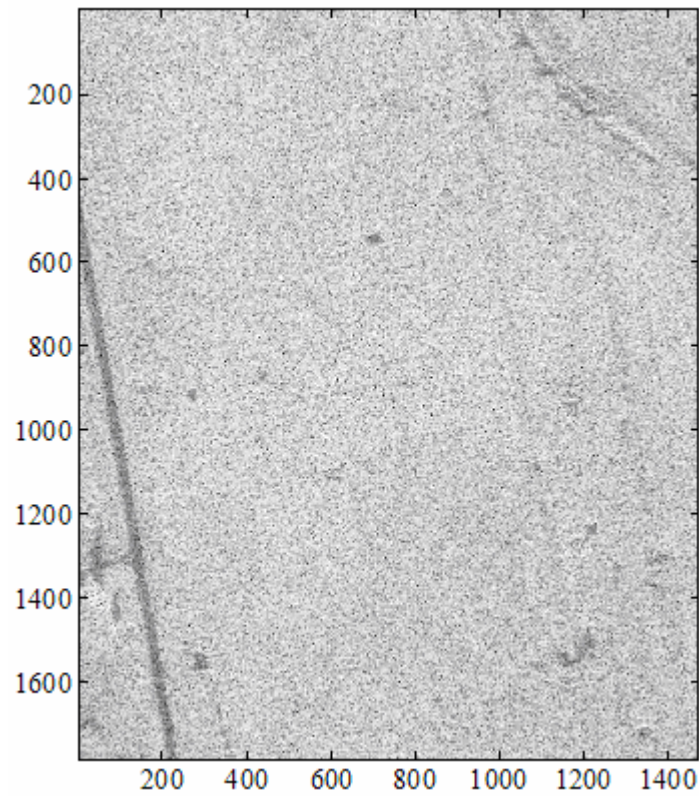


**Figure 1.31** - Grass field for the HB06173 file.

The analysis has been carried out on the overall image (Fig. 1.31), on the patch  $((400,1784) \times (1,300))$  which contains a man-made object (maybe a street), and on the patch  $((800,1200) \times (600,1000))$  which encloses a very homogeneous region of terrain. All the statistical results are summarized in Figs. 1.32-1.42 and in Tables 1.8-1.9. They are very similar to those of the previous file.

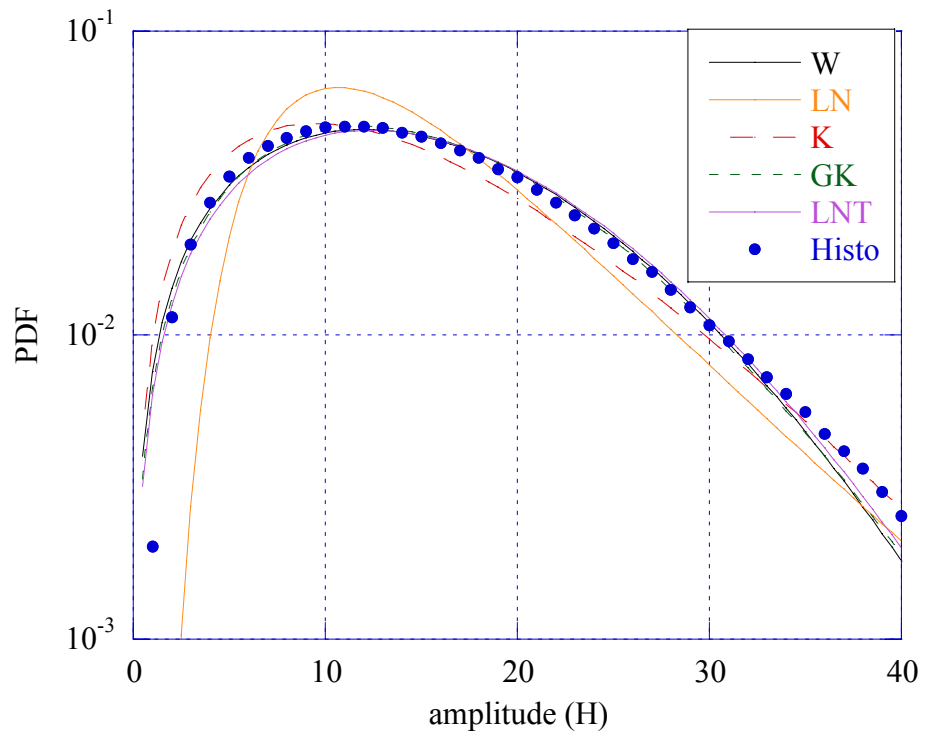


**Figure 1.32** - PDFs of clutter for the whole image (*1784x1474*).

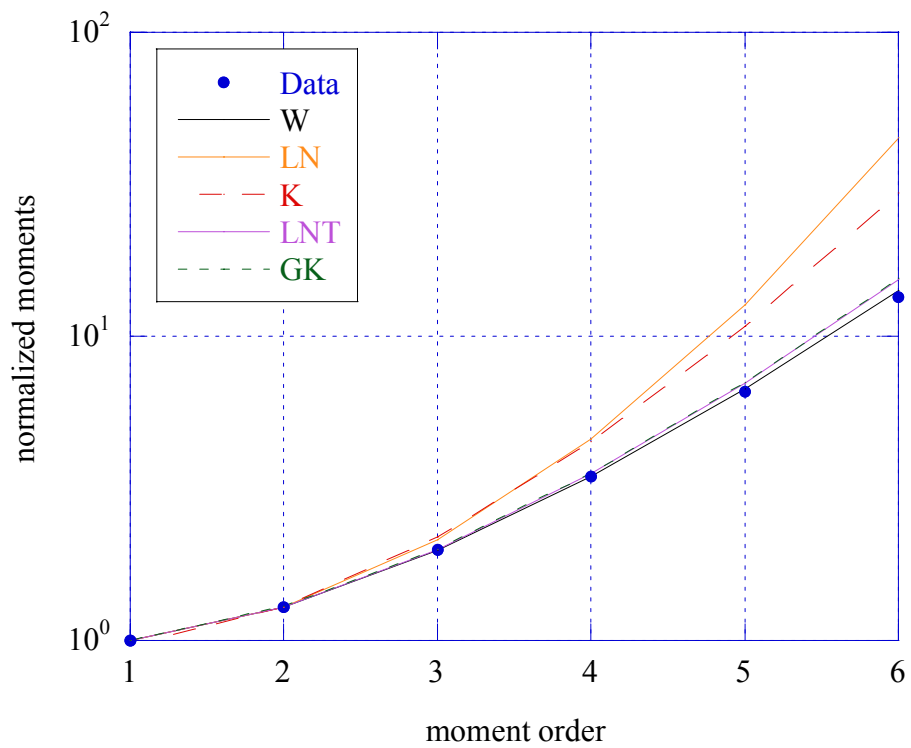


**Figure 1.33** - Normalized moments for the whole image (*1784x1474*).

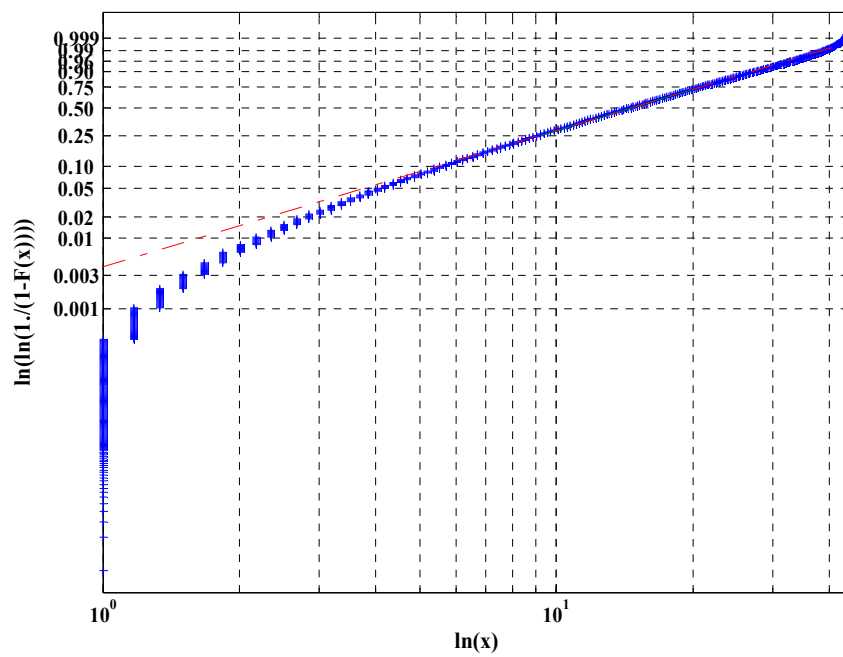


**Figure 1.34** - Weibull paper for whole image (1784x1474).

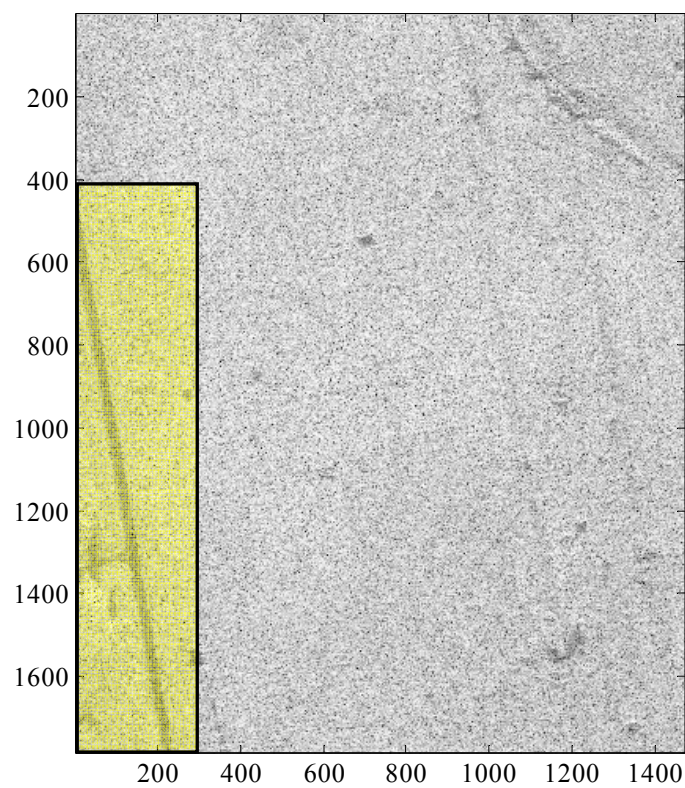


**Figure 1.35** - Terrain image with the patch (400,1474)x(1,300).

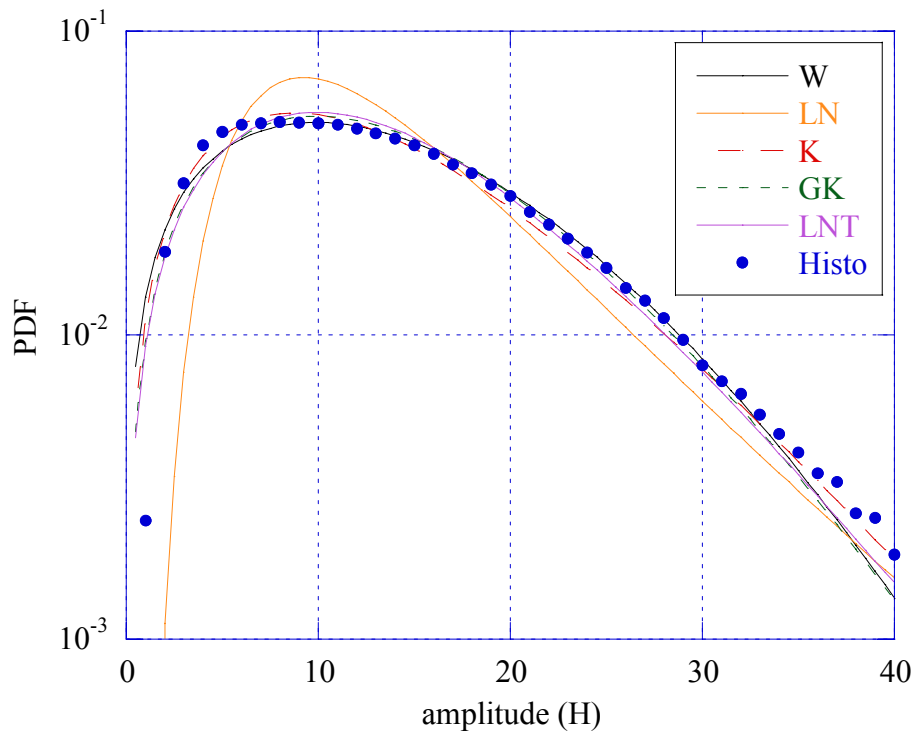


**Figure 1.36** - PDF of clutter for the patch  $(400,1784) \times (1,300)$ .

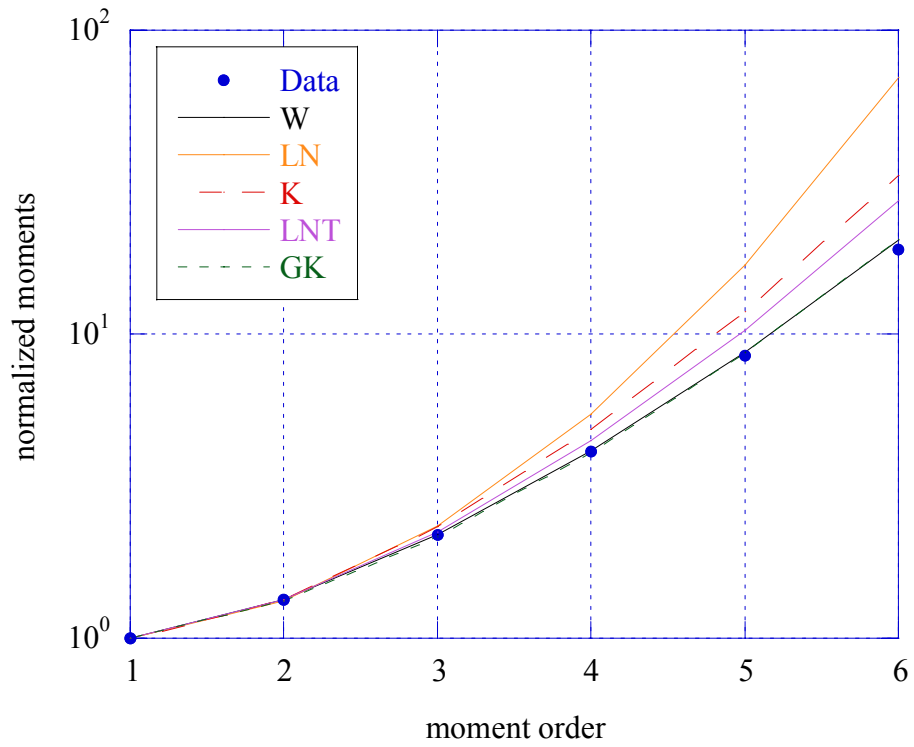


**Figure 1.37** - Normalized moments for the patch  $(400,1784) \times (1,300)$ .

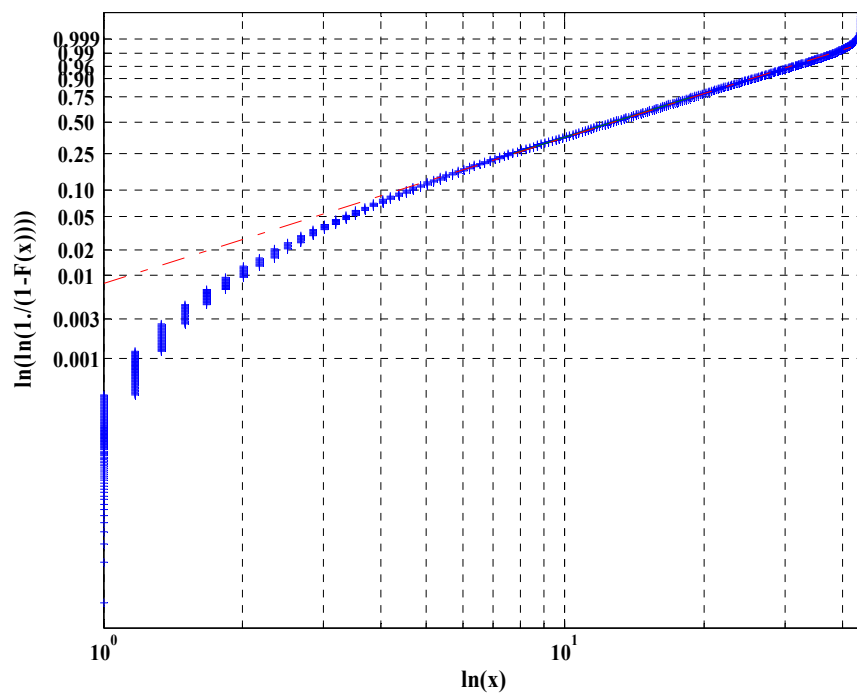


**Figure 1.38** - Weibull paper for the patch  $(400,1784) \times (1,300)$ .

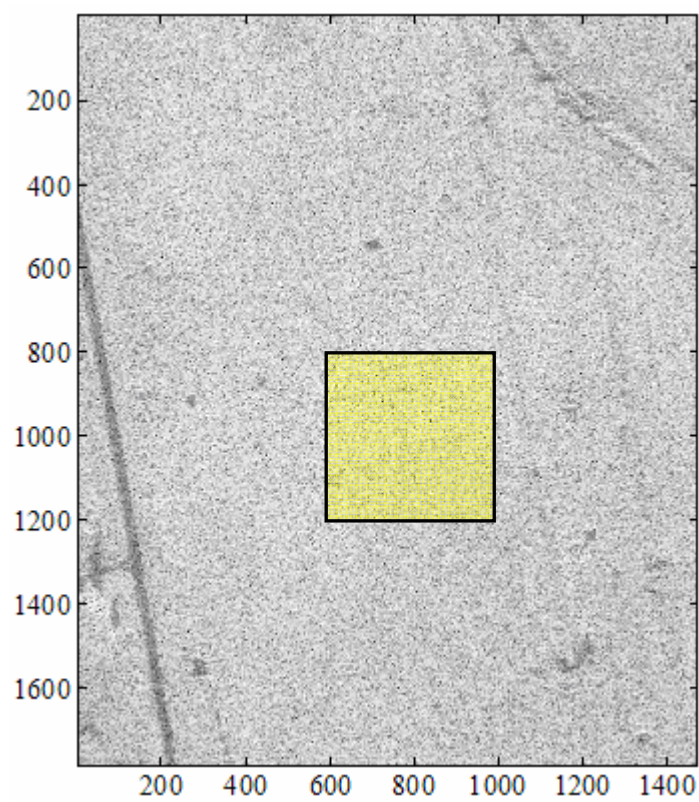


**Figure 1.39** - Grass field with the patch  $(800,1200) \times (600,1000)$ .

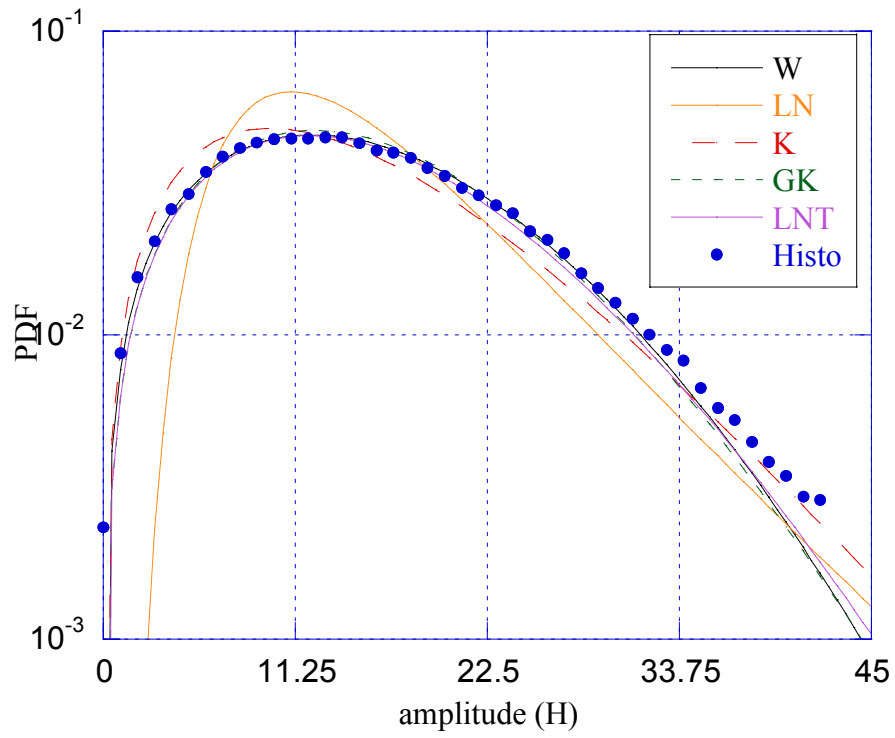


**Figure 1.40** - PDF of clutter for the patch  $(800,1200) \times (600,1000)$ .

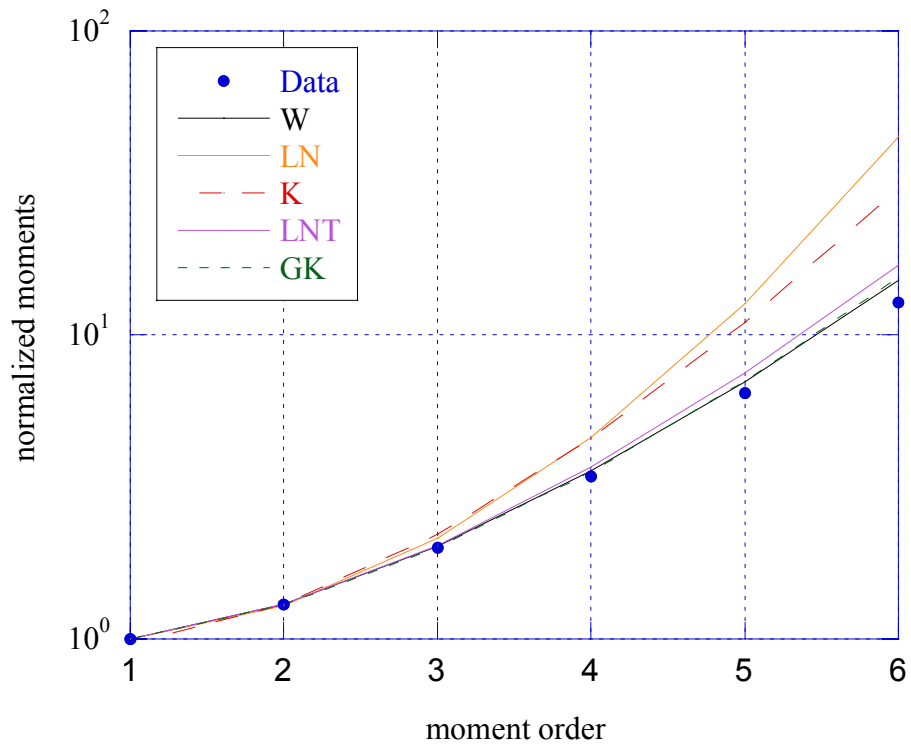


**Figure 1.41** - Normalized moments for the patch  $(800,1200) \times (600,1000)$ .

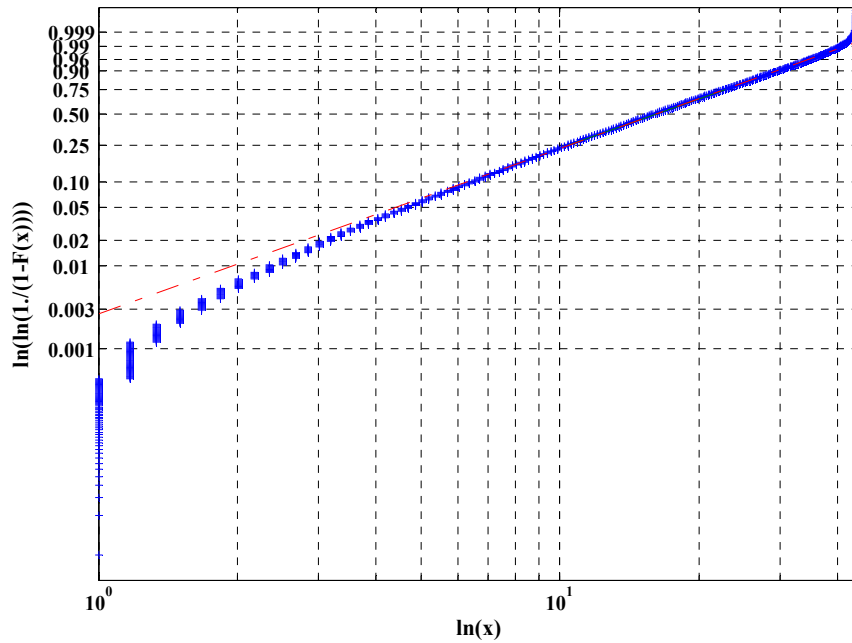


Figure 1.42 -Weibull paper for the patch (800,1200)x(600,1000).

Size of patch	Weibull		Lognormal		K		GK			LNT	
	$\hat{c}$	$\hat{b}$	$\hat{\sigma}$	$\hat{\sigma}$	$\hat{\nu}$	$\hat{\mu}$	$\hat{\nu}$	$\hat{\mu}$	$\hat{b}$	$\hat{\sigma}^2$	$\hat{m}$
(1784x1472)	1.80	16.44	12.70	0.53	2.86	142.52	0.61	222.34	4.62	0.18	130.06
(400,1784)x(1,300)	1.63	14.67	11.13	0.58	2.86	120.45	0.30	121.25	4.93	0.37	100.08
(800,1200)x(600,1000)	1.90	18.17	14.20	0.50	2.86	169.11	79.5	1.57	0.45	0.08	162.08

Table 1.8 - Parameter estimates of models tested on HB06173 file.

1784x1472	W	LN	K	GK	LNT
Prob	100 %	98 %	99 %	100 %	100 %
d	$1.06 \cdot 10^{-2}$	$6.46 \cdot 10^{-2}$	$5.30 \cdot 10^{-2}$	$0.85 \cdot 10^{-2}$	$2.68 \cdot 10^{-2}$
(400,1784)x (1,300)	100 %	91 %	100 %	100 %	100 %
	$1.47 \cdot 10^{-2}$	$7.74 \cdot 10^{-2}$	$2.37 \cdot 10^{-2}$	$1.85 \cdot 10^{-2}$	$1.92 \cdot 10^{-2}$
(800,1200)x(600,1000)	100	96 %	100 %	100 %	100 %
	$0.65 \cdot 10^{-2}$	$7.58 \cdot 10^{-2}$	$5.29 \cdot 10^{-2}$	$1.23 \cdot 10^{-2}$	$2.86 \cdot 10^{-2}$

Table 1.9 - Results of KS test.



1784x1472	W	LN	K	GK	LNT
Prob	100 %	97 %	100 %	100 %	100 %
d	$1.98*10^{-2}$	$11.12*10^{-2}$	$6.47*10^{-2}$	$1.53*10^{-2}$	$2.24*10^{-2}$
(400,1784)x (1,300)	100 %	86 %	100 %	100 %	100 %
	$1.25*10^{-2}$	$12.28*10^{-2}$	$6.87*10^{-2}$	$2.42*10^{-2}$	$2.74*10^{-2}$
(800,1200)x(600,1000)	100	96 %	100 %	100 %	100 %
	$0.65*10^{-2}$	$7.58*10^{-2}$	$5.29*10^{-2}$	$1.23*10^{-2}$	$2.86*10^{-2}$

**Table 1.10** - Results of Kuiper test.

#### 1.2.4 HB06174 File

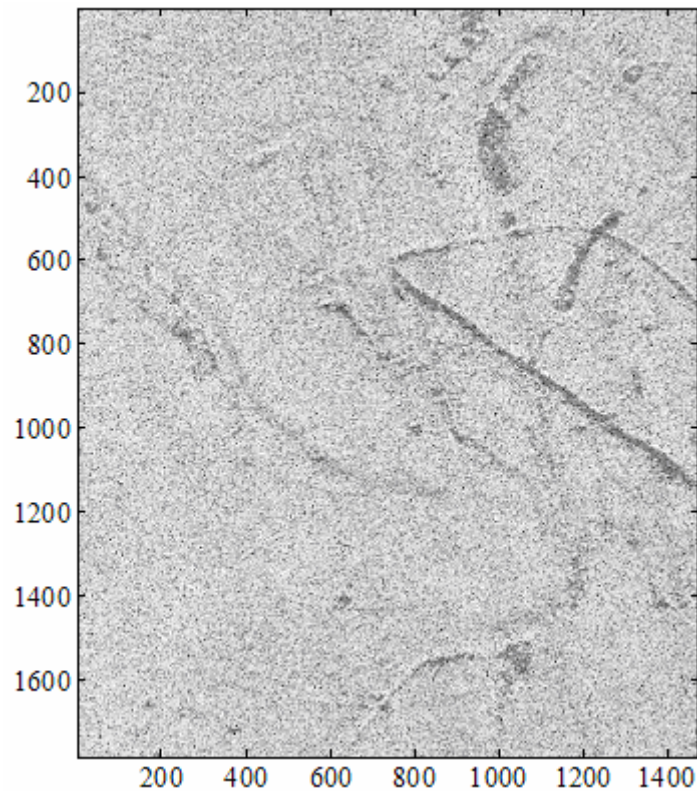


**Figure 1.43** - Grass field image of HB06174 file

The analysis has been carried out on the overall image (Fig. 1.43), on the homogeneous patch  $(1400,1784)x(1,400)$  (see Fig. 1.47), and on the patch  $(400,1000)x(800,1400)$  (Fig. 1.51). The statistical analysis is summarized in Figs. 1-43-1.54 and in Tables 1.11-1.12.



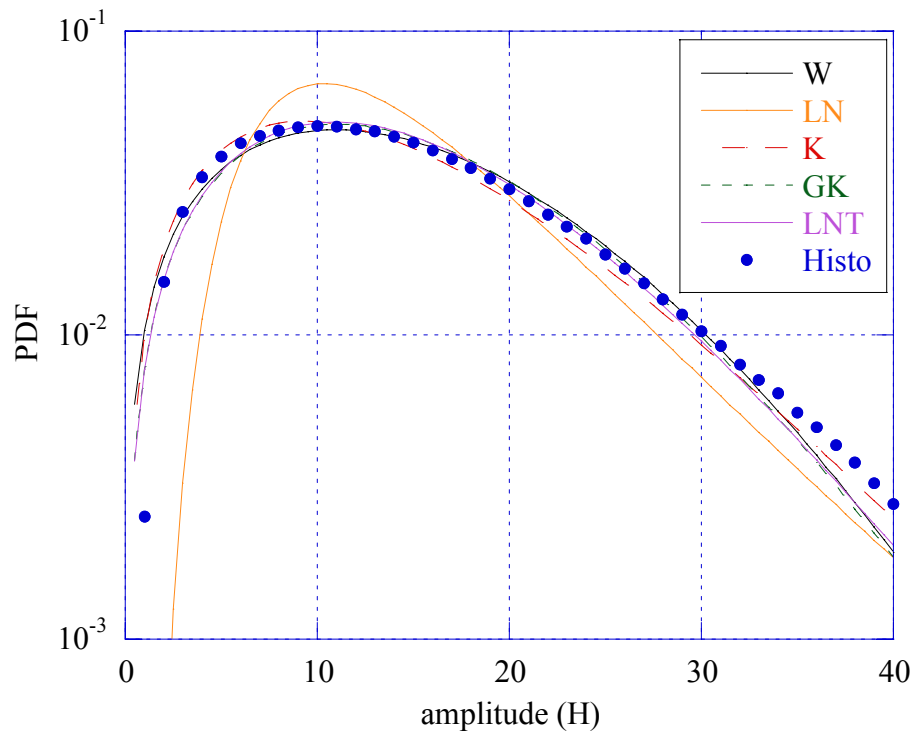


**Figure 1.44** - PDF of data clutter for the total image ( $1784 \times 1476$ ).

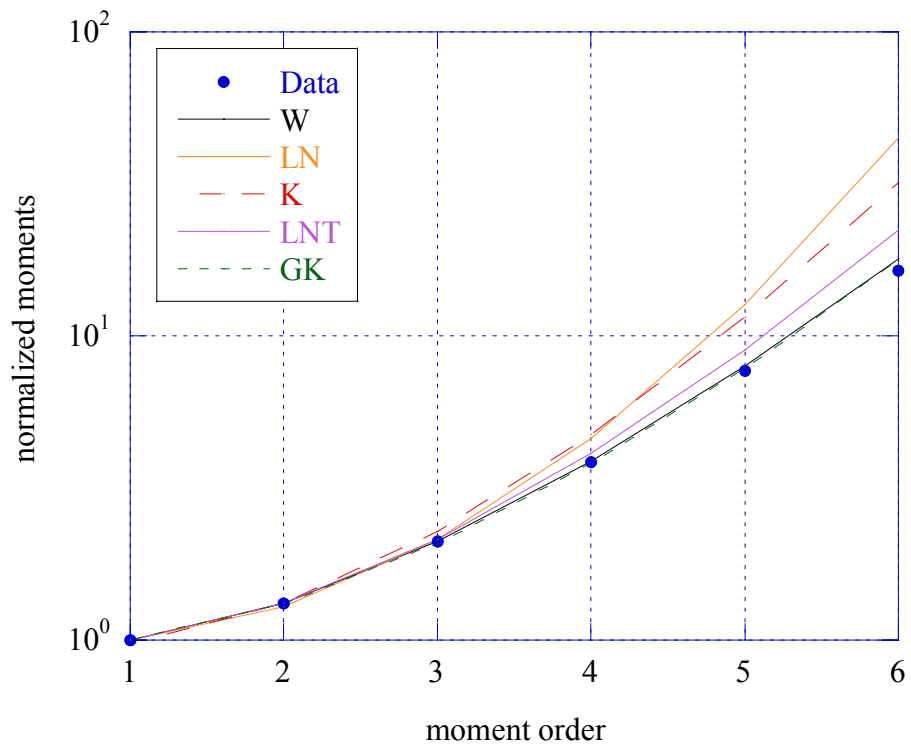


**Figure 1.45** - Normalized moments for the total image ( $1784 \times 1476$ ).

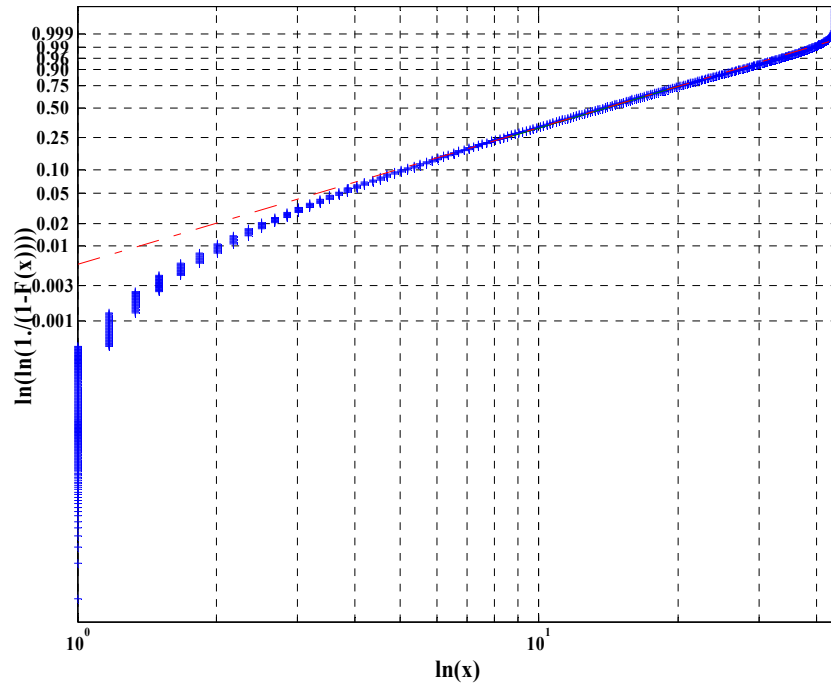


**Figure 1.46** - Weibull paper for the total image (1784x1476).

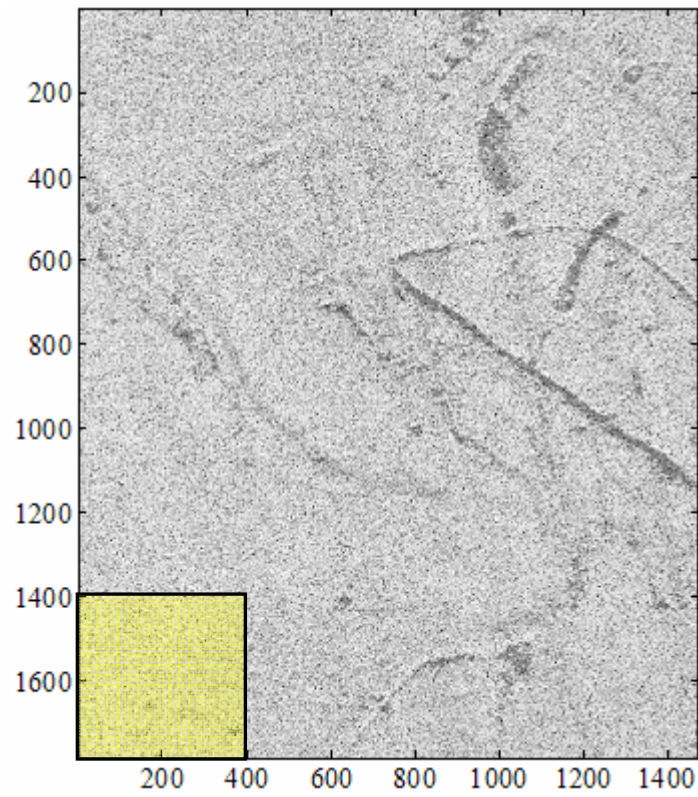


**Figure 1.47** - Image with the evidenced patch (1400,1784)x(1,400).

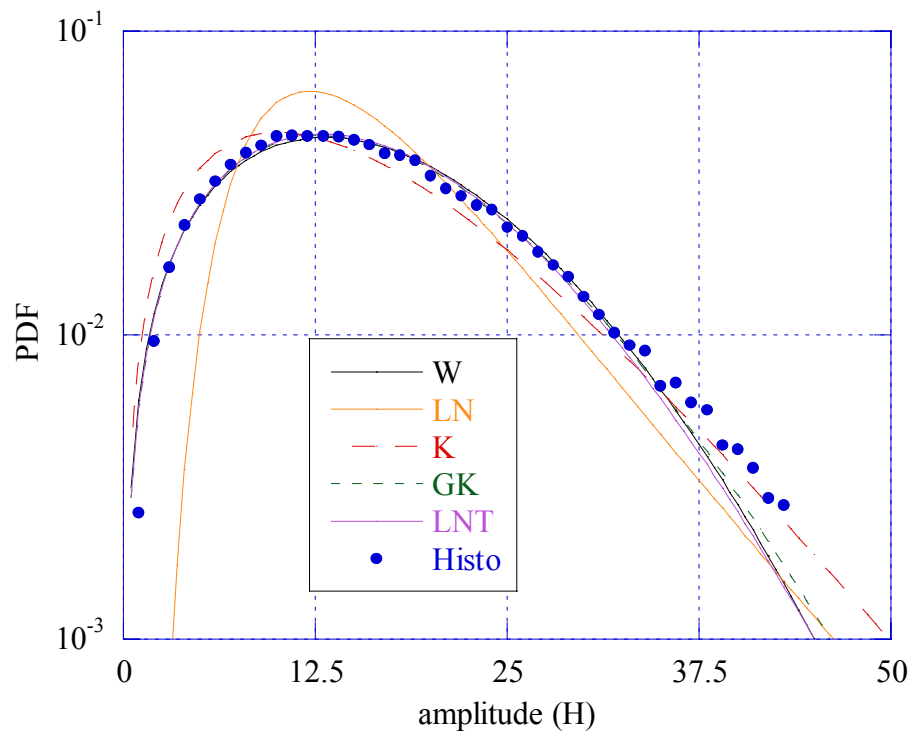


**Figure 1.48** - PDF of data clutter for the patch  $(1400,1784) \times (1,400)$ .

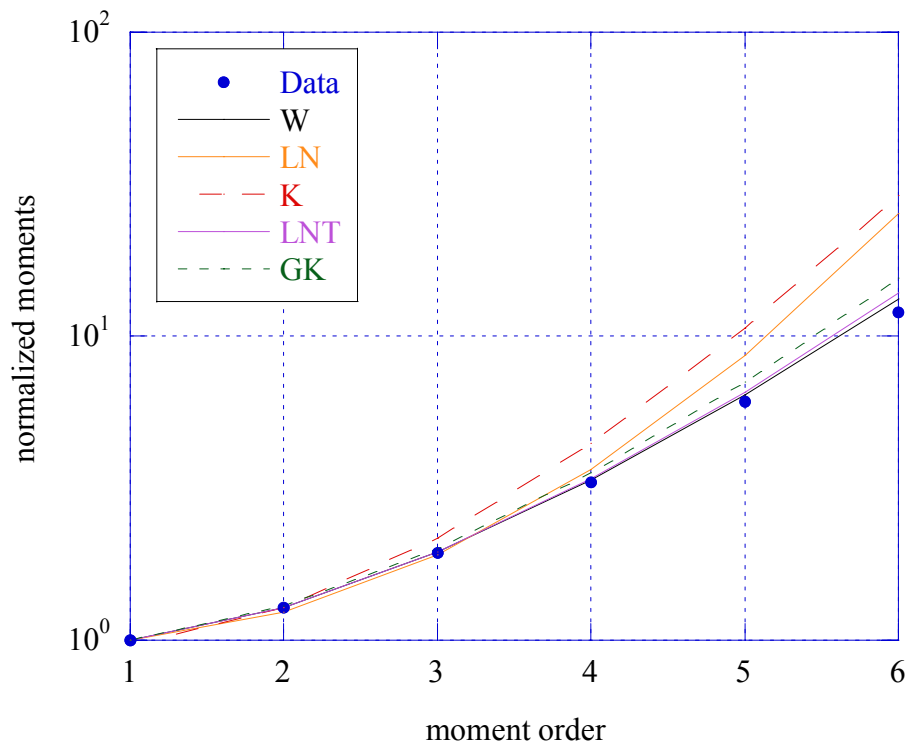


**Figure 1.49** - Normalized moments for the patch  $(1400,1784) \times (1,400)$ .

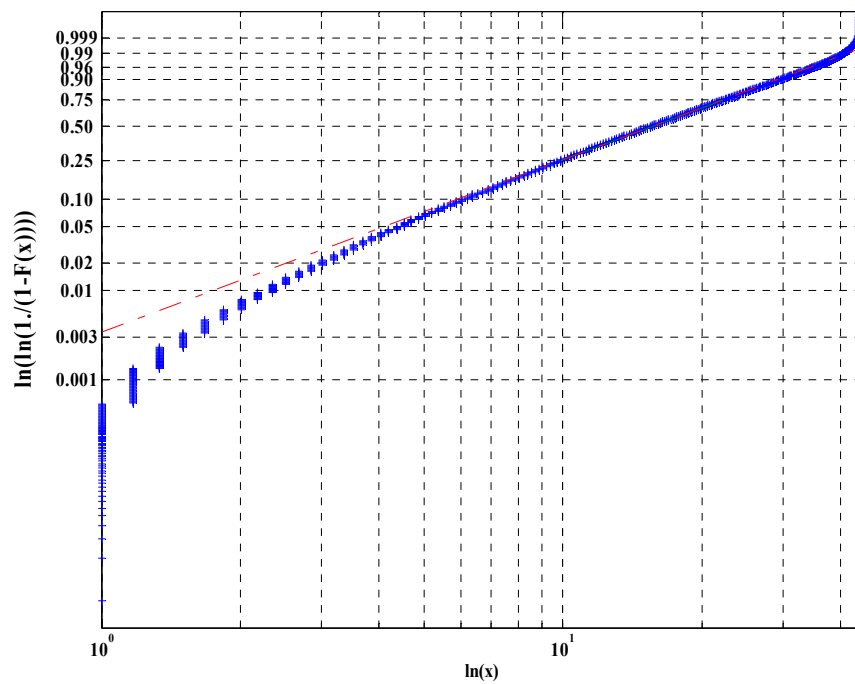


**Figure 1.50** - Weibull paper for the patch  $(1400,1784) \times (1,400)$ .

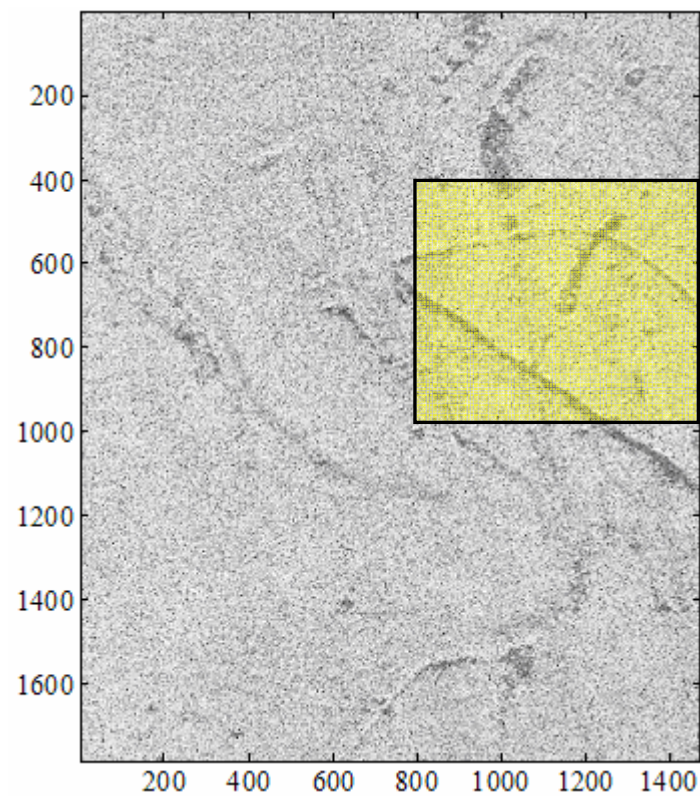


**Figure 1.51** - Image with the patch  $(400,1000) \times (800,1400)$ .

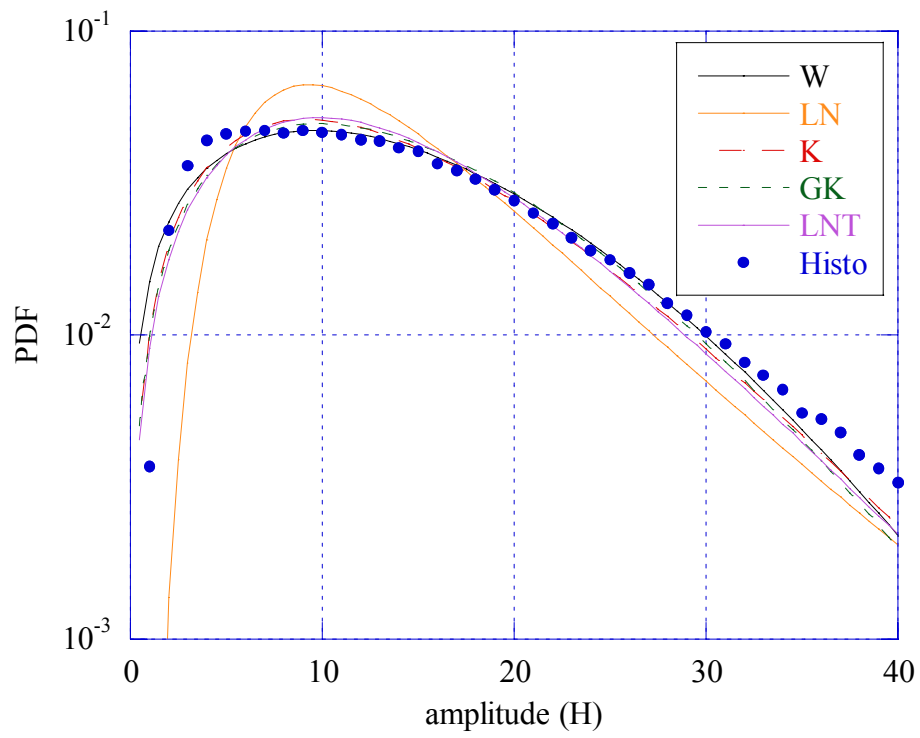


**Figure 1.52** - PDF of data clutter for the patch  $(400,1000) \times (800,1400)$ .

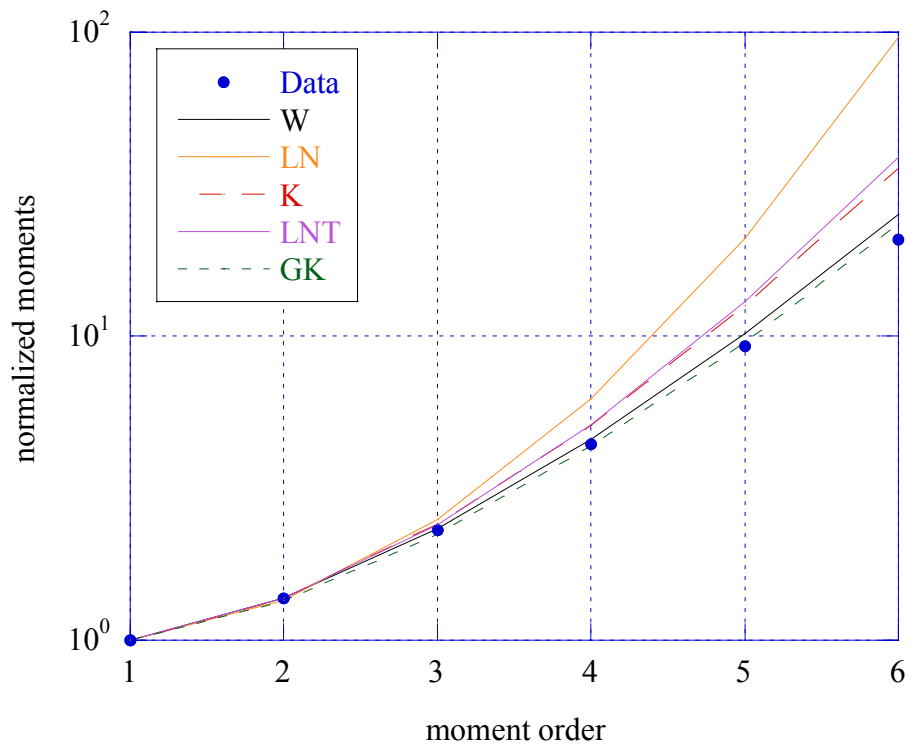


**Figure 1.53** - Normalized moments for the patch  $(400,1000) \times (800,1400)$ .

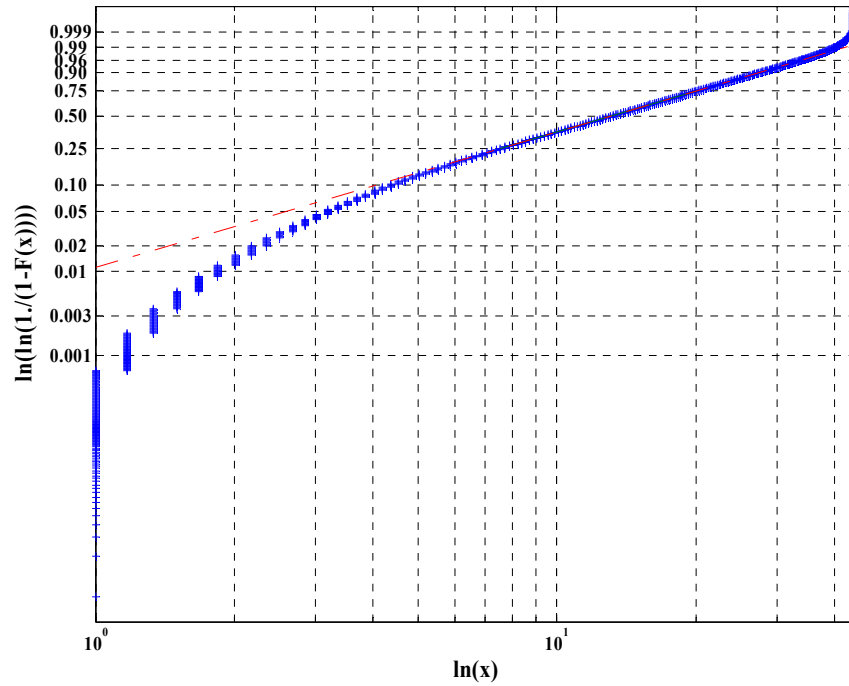


Figure 1.54 - Weibull paper for the patch (400,1000)x(800,1400).

Size of patch	Weibull		Lognormal		K		GK			LNT	
	$\hat{c}$	$\hat{b}$	$\hat{\delta}$	$\hat{\sigma}$	$\hat{\nu}$	$\hat{\mu}$	$\hat{\nu}$	$\hat{\mu}$	$\hat{b}$	$\hat{\sigma}^2$	$\hat{m}$
(1784x1472)	1.69	15.87	12.17	0.55	2.86	137.68	0.30	128.16	5.92	0.30	118.59
(1400,1784)x(1,400)	1.83	17.76	12.77	0.50	2.86	164.34	1.02	360.99	4.18	0.14	152.91
(400,1000)x(800,1400)	1.56	15.25	11.45	0.60	2.18	134.44	0.21	100.27	6.10	0.47	106.50

Table 1.11 - Parameter estimates of models tested on HB06174 file.

1784x1472	W	LN	K	GK	LNT
Prob	100 %	88 %	100 %	100 %	100 %
d	$1.15 \cdot 10^{-2}$	$8.16 \cdot 10^{-2}$	$2.03 \cdot 10^{-2}$	$1.52 \cdot 10^{-2}$	$1.20 \cdot 10^{-2}$
(1400,1784)x (1,400)	100 %	86 %	100 %	100 %	100 %
	$1.10 \cdot 10^{-2}$	$8.33 \cdot 10^{-2}$	$5.82 \cdot 10^{-2}$	$0.78 \cdot 10^{-2}$	$1.33 \cdot 10^{-2}$
(400,1000)x(800,1400)	100	96 %	100 %	100 %	100 %
	$1.41 \cdot 10^{-2}$	$8.73 \cdot 10^{-2}$	$1.72 \cdot 10^{-2}$	$2.76 \cdot 10^{-2}$	$2.93 \cdot 10^{-2}$

Table 1.12 - Results of KS test.

1784x1472	W	LN	K	GK	LNT
Prob	100 %	88 %	100 %	100 %	100 %
d	$2.28*10^{-2}$	$11.31*10^{-2}$	$4.03*10^{-2}$	$2.48*10^{-2}$	$2.21*10^{-2}$
(1400,1784)x (1,400)					
	100 %	86 %	100 %	100 %	100 %
	$1.83*10^{-2}$	$12.64*10^{-2}$	$7.50*10^{-2}$	$1.37*10^{-2}$	$1.96*10^{-2}$
(400,1000)x(800,1400)					
	100	96 %	100 %	100 %	100 %
	$2.76*10^{-2}$	$12.94*10^{-2}$	$2.37*10^{-2}$	$4.17*10^{-2}$	$4.82*10^{-2}$

**Table 1.13** - Results of Kuiper test.

### 1.2.5 HB06176 File

Figure 1.55 shows the image of this file. We can observe that this image is very homogeneous, for this reason we have considered the whole image and one patch only. The results are summarized in the following figures.

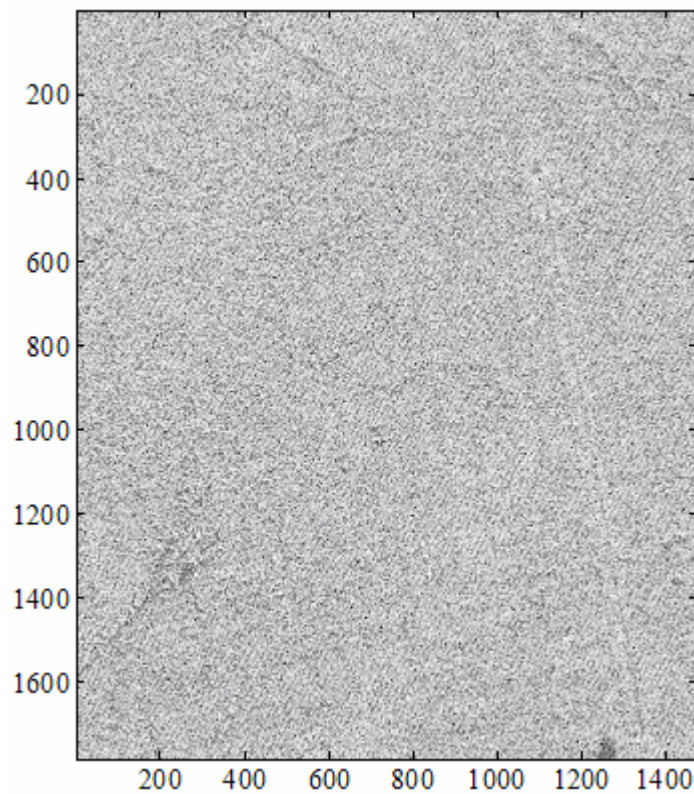


**Figure 1.55** - Grass field of HB06176 file.

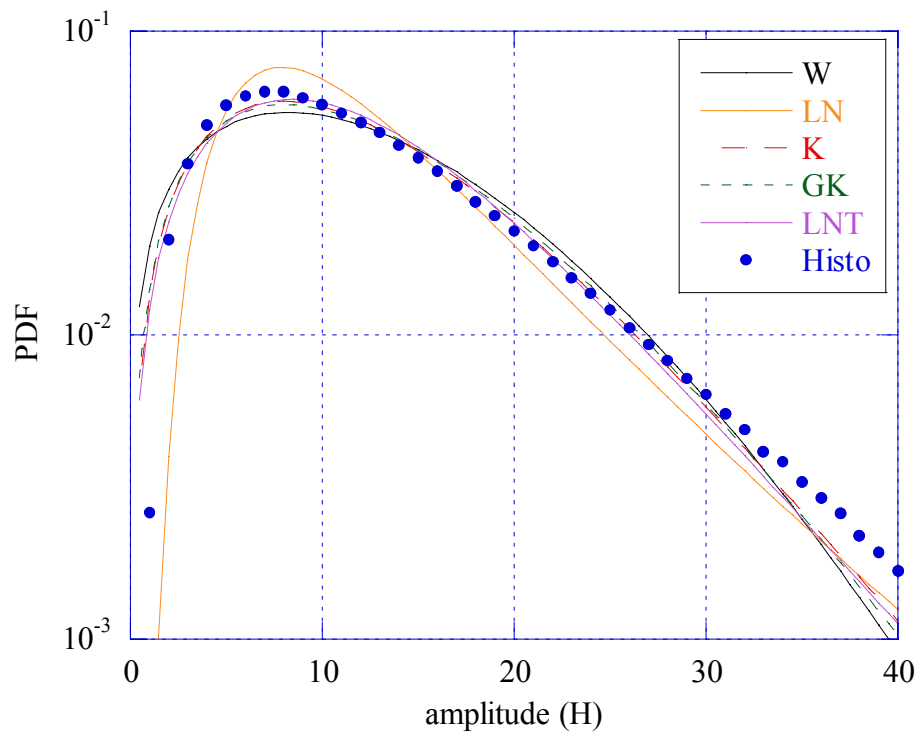


**Figure 1.56** - PDF of clutter for the whole image ( $1784 \times 1476$ ).

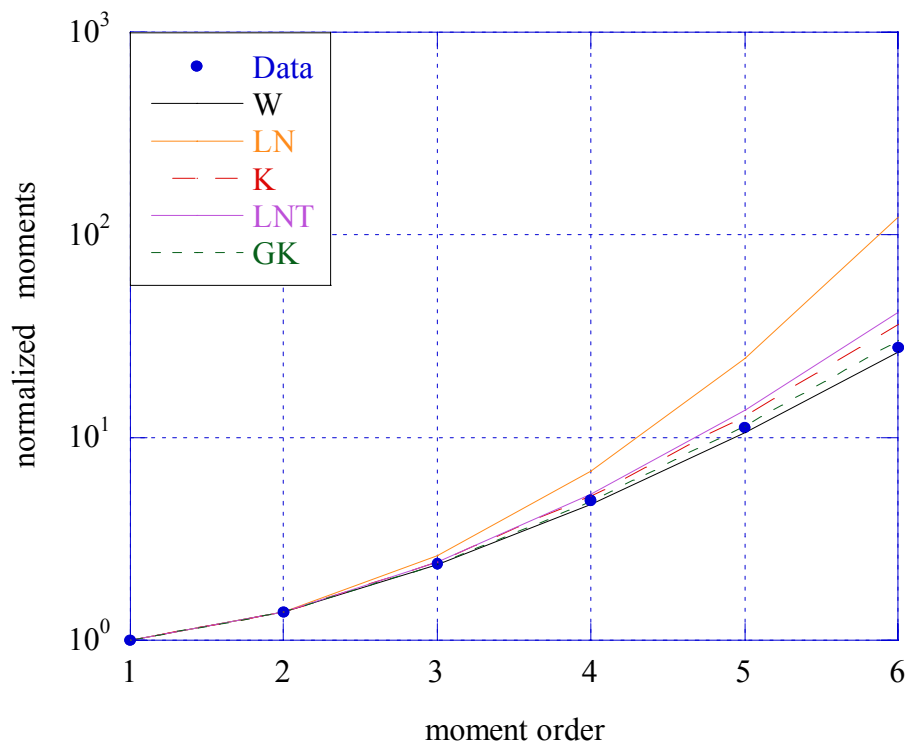


**Figure 1.57** - Normalized moments for the whole image ( $1784 \times 1476$ ).



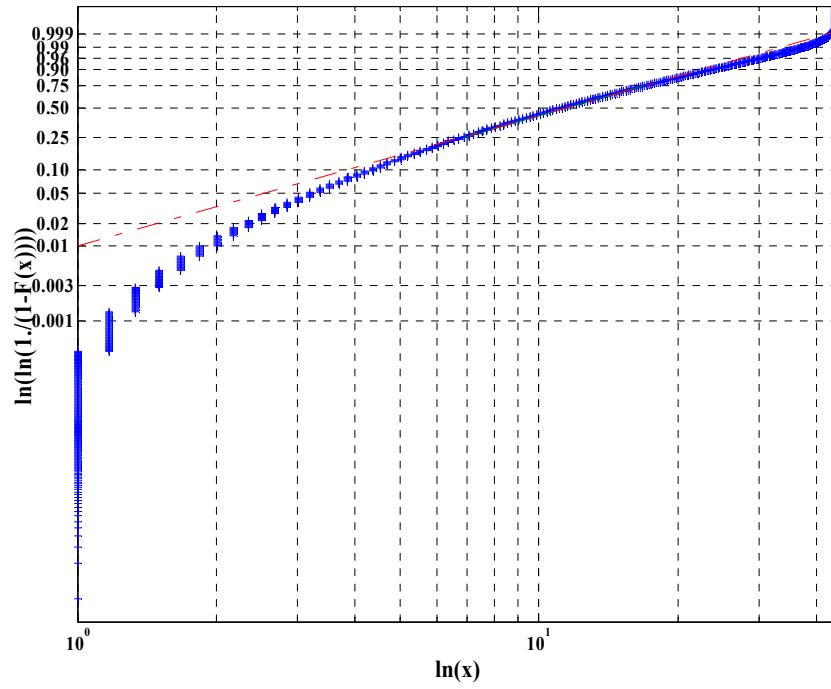


**Figure 1.58** - Weibull paper for the whole image (1784x1476).

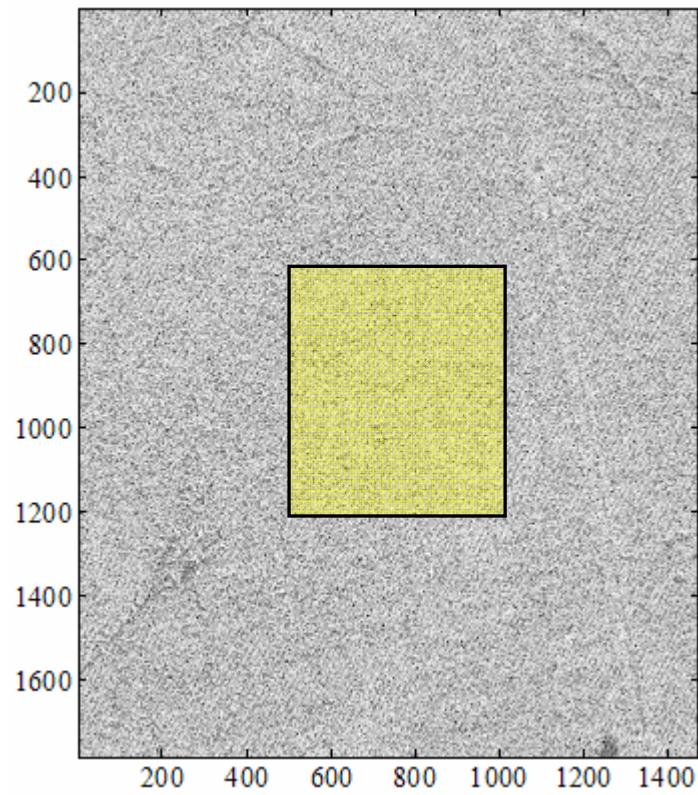


**Figure 1.59** - Image with the patch (600,1200)x(500,1000).

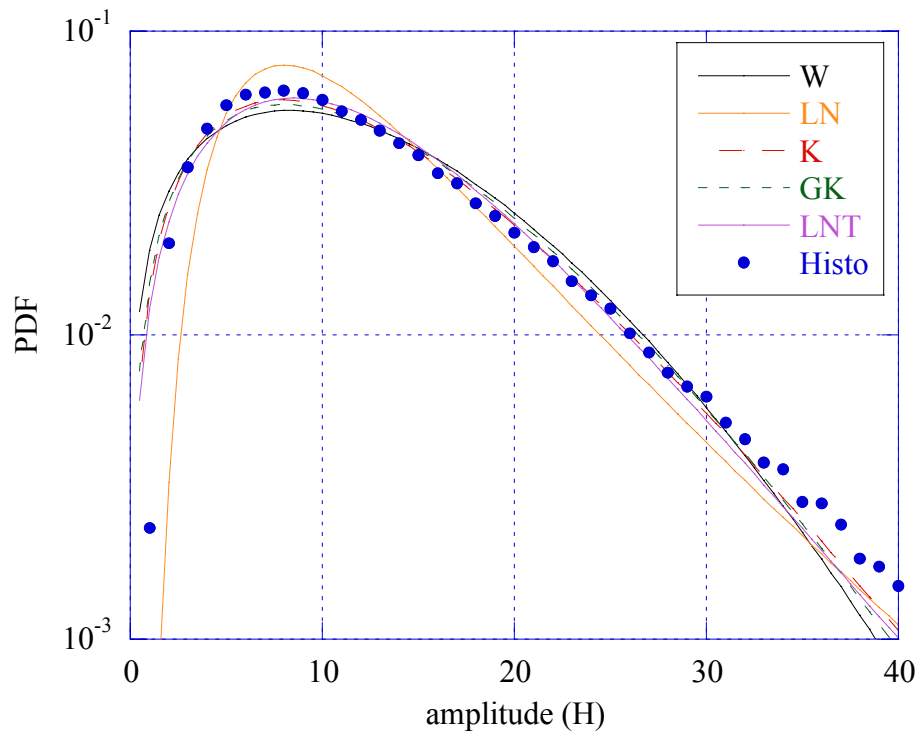


**Figure 1.60** - PDF of clutter for the patch  $(600,1200) \times (500,1000)$ .

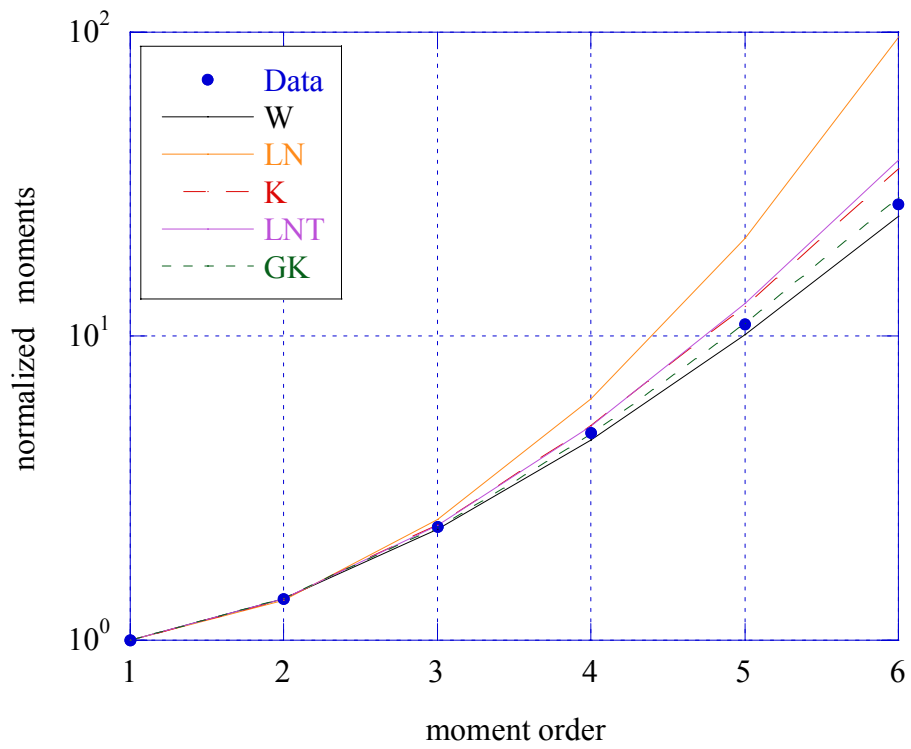


**Figure 1.61** - Normalized moments for the patch  $(600,1200) \times (500,1000)$ .

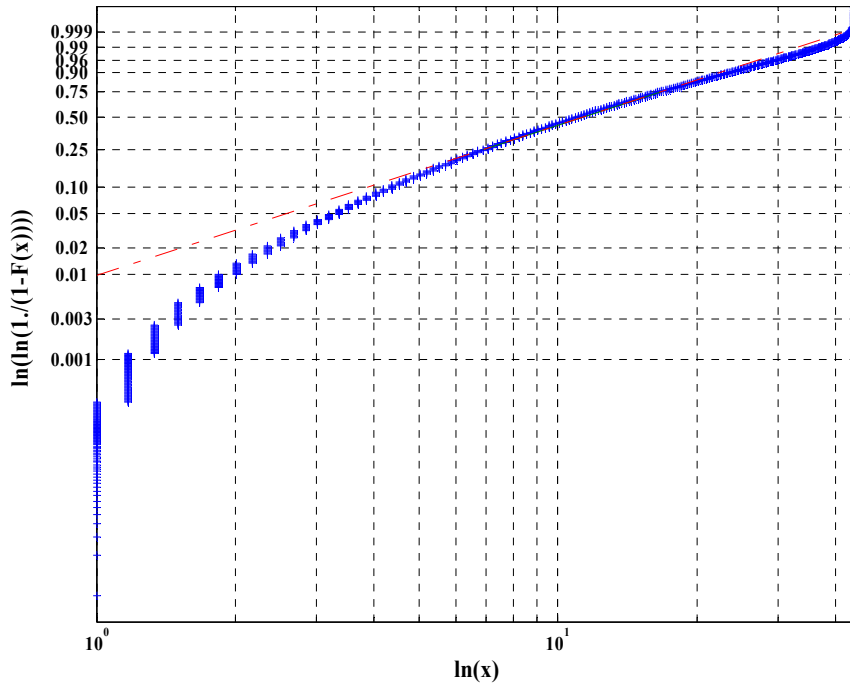


Figure 1.62 - Weibull paper for the patch (600,1200)x(500,1000).

Size of patch	Weibull		Lognormal		K		GK			LNT	
	$\hat{c}$	$\hat{b}$	$\hat{\delta}$	$\hat{\sigma}$	$\hat{\nu}$	$\hat{\mu}$	$\hat{\nu}$	$\hat{\mu}$	$\hat{b}$	$\hat{\sigma}^2$	$\hat{m}$
(1784x1472)	1.52	12.07	9.73	0.62	1.98	100.37	0.34	126.31	2.32	0.51	77.60
(600,1200)x(500,1000)	1.54	12.96	9.64	0.62	2.18	97.81	0.27	104.13	2.99	4.88	76.63

Table 1.14 - Parameter estimates of models tested on HB06176 file.

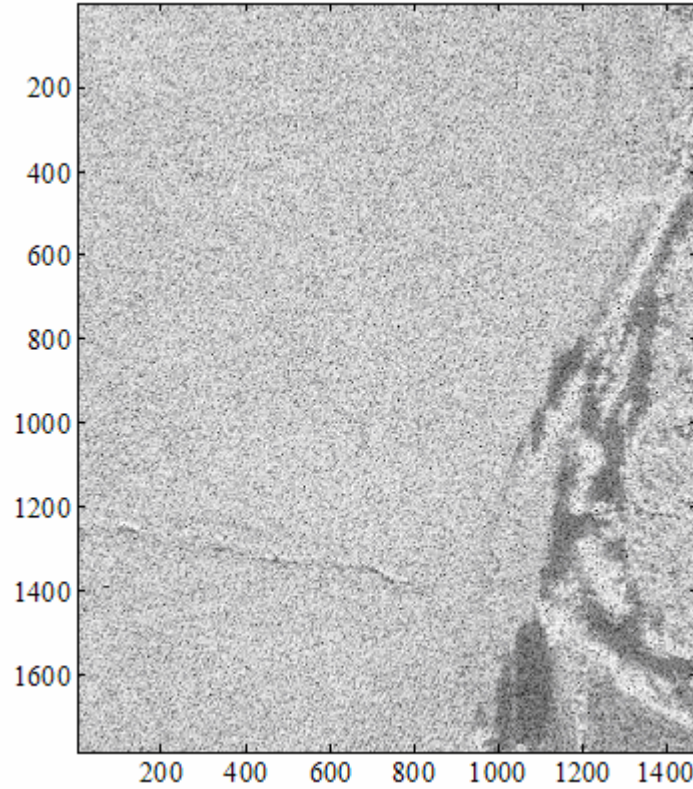
1784x1472	W	LN	K	GK	LNT
Prob	100 %	99 %	100 %	100 %	100 %
d	$2.02 \cdot 10^{-2}$	$5.29 \cdot 10^{-2}$	$1.69 \cdot 10^{-2}$	$1.85 \cdot 10^{-2}$	$1.80 \cdot 10^{-2}$
(600,1200)x (500,1000)					
	100 %	100 %	100 %	100 %	100 %
	$2.00 \cdot 10^{-2}$	$5.56 \cdot 10^{-2}$	$1.96 \cdot 10^{-2}$	$2.16 \cdot 10^{-2}$	$1.80 \cdot 10^{-2}$

Table 1.15 - Results of KS test.

1784x1472	W	LN	K	GK	LNT
Prob	100 %	100 %	100 %	100 %	100 %
d	$5.66 \cdot 10^{-2}$	$8.45 \cdot 10^{-2}$	$2.85 \cdot 10^{-2}$	$2.67 \cdot 10^{-2}$	$2.08 \cdot 10^{-2}$
(600,1200)x (500,1000)					
	100 %	100 %	100 %	100 %	100 %
	$5.77 \cdot 10^{-2}$	$8.71 \cdot 10^{-2}$	$2.76 \cdot 10^{-2}$	$4.07 \cdot 10^{-2}$	$2.14 \cdot 10^{-2}$

Table 1.16 - Results of Kuiper test.

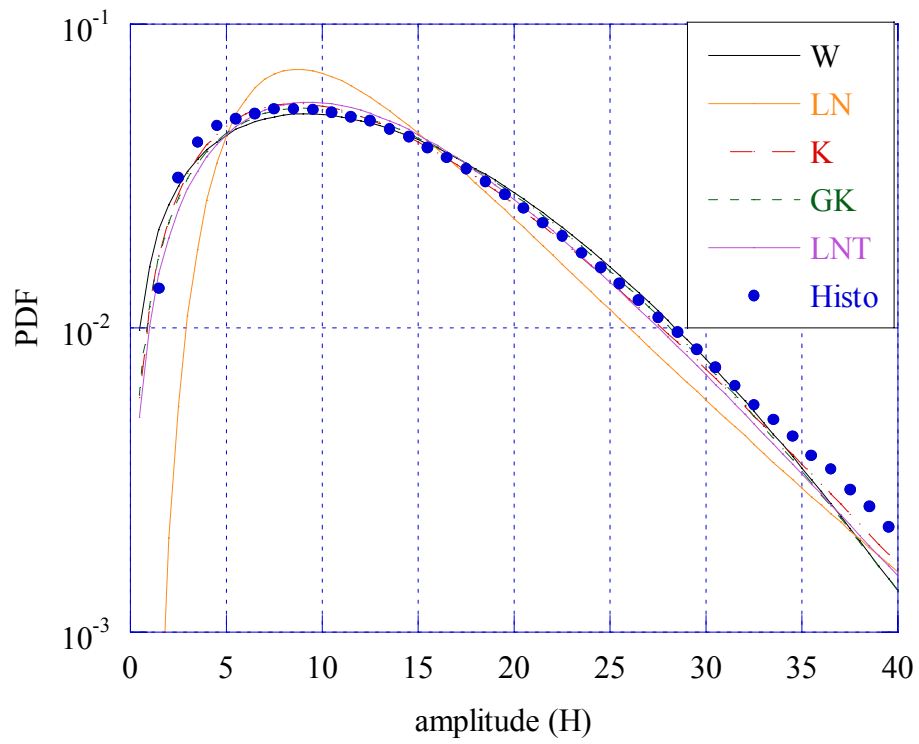
### 1.2.6 HB06177 File



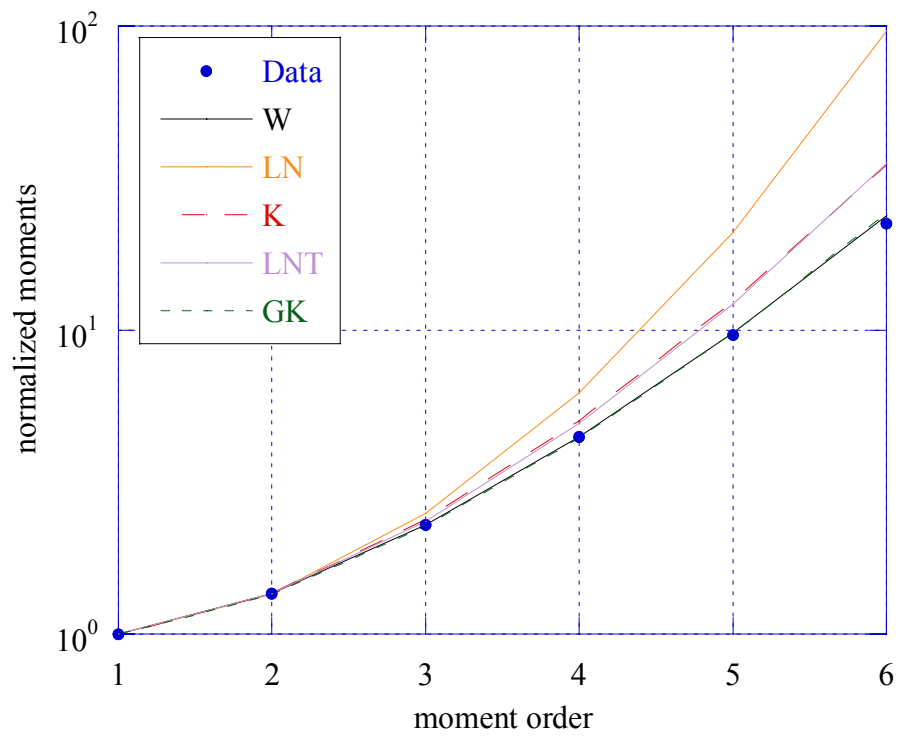
**Figure 1.63** - Grass field for HB06177 file.

Figure 1.63 shows the considered image, which represents a region of terrain mainly homogeneous and a small area (on the right of figure) characterized by dense vegetation and shadows. The analyzed patches of this image are  $((1,800) \times (1,800))$ ,  $((600,1200) \times (800,1476))$  and  $((1400,1784) \times (1100,1476))$ . The results of the statistical analysis are shown in Fig. 1.64-1.78 and Tables 1.17-1.19.

The results of the patches  $(1,800) \times (1,800)$  and  $(600,1200) \times (800,1476)$  are similar to those of the previous files and of the overall image. Almost all the models, but the log-normal, we tested show a good fitting. Non-negligible differences are apparent in the results relating to the smallest patch  $(1400,1784) \times (1100,1476)$ . The clutter is spikier ( $c \cong 1$ ), the histogram presents longer tails and the log-normal model as well shows a good fitting. These differences are due to the presence of dense vegetation and shadows, then, the area is not more homogeneous.



**Figure 1.64** - PDF of data clutter for the whole image (*1784x1476*).



**Figure 1.65** - Normalized moments for the whole image (*1784x1476*).

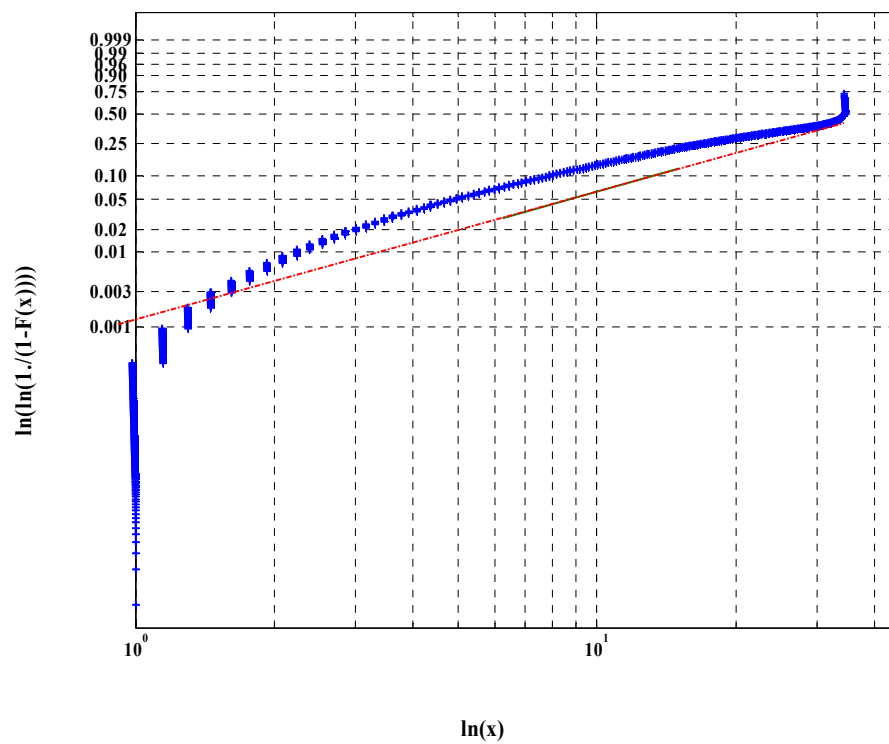


**Figure 1.66** - Weibull paper for the whole image (1784x1476).

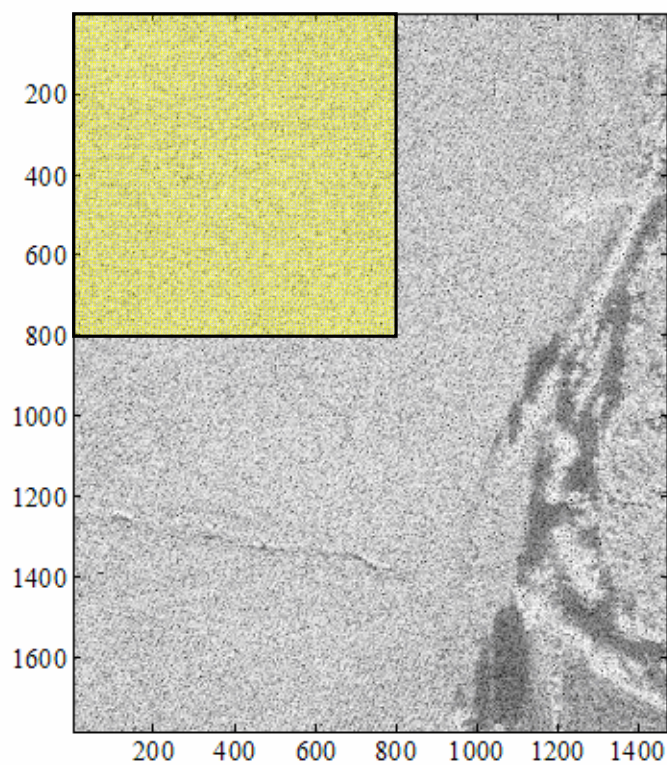


**Figure 1.67** - Grass field in the patch (1,800)x(1,800).

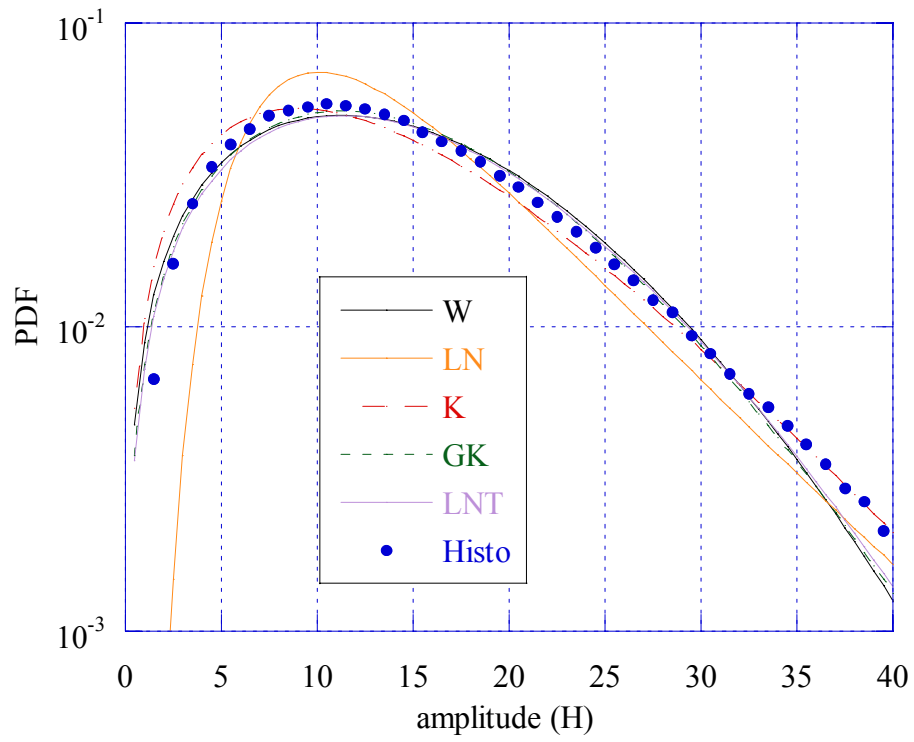


**Figure 1.68** - PDFs of clutter amplitude for the patch  $(1,800) \times (1,800)$ .

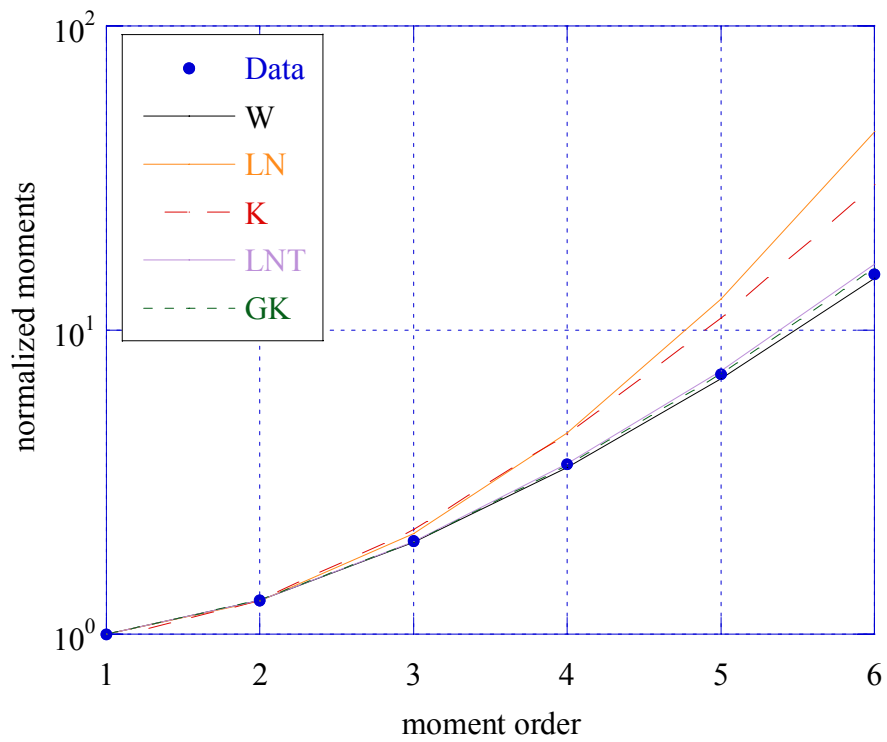


**Figure 1.69** - Normalized moments for the patch  $(1,800) \times (1,800)$ .



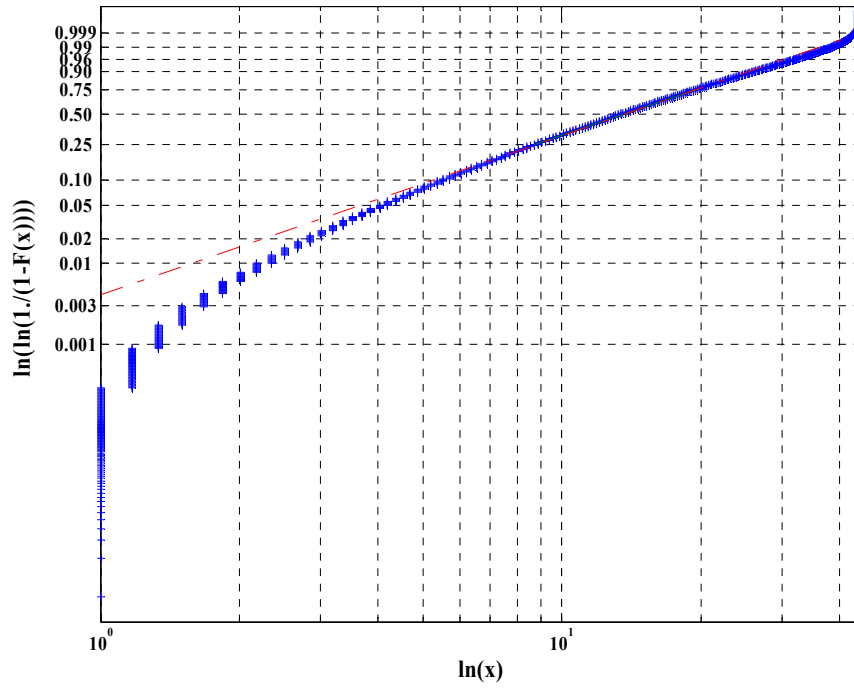


**Figure 1.70** - Weibull paper for the patch (1,800)x(1,800).

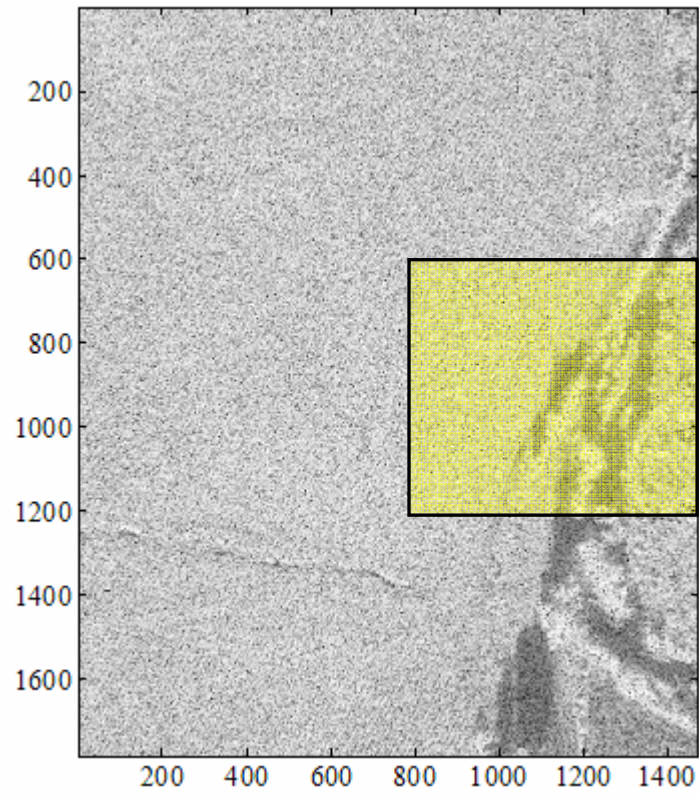


**Figure 1.71** - Image of the patch (600,1200)x(800,1476).



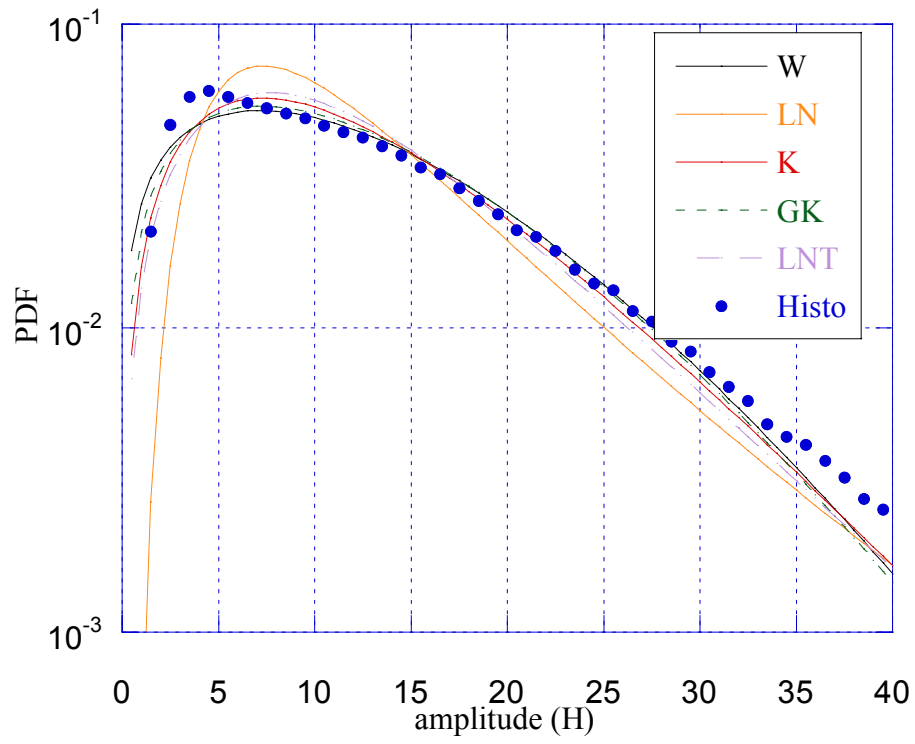


**Figure 1.72** - PDFs of data clutter for the patch  $(600,1200) \times (800,1476)$ .

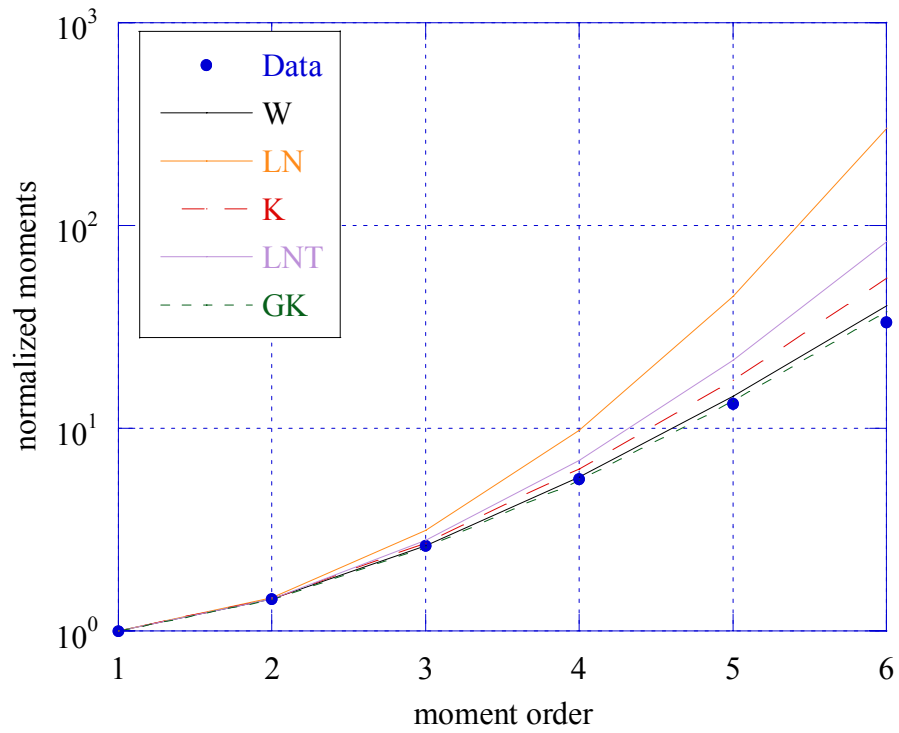


**Figure 1.73** - Normalized moments for the patch  $(600,1200) \times (800,1476)$ .

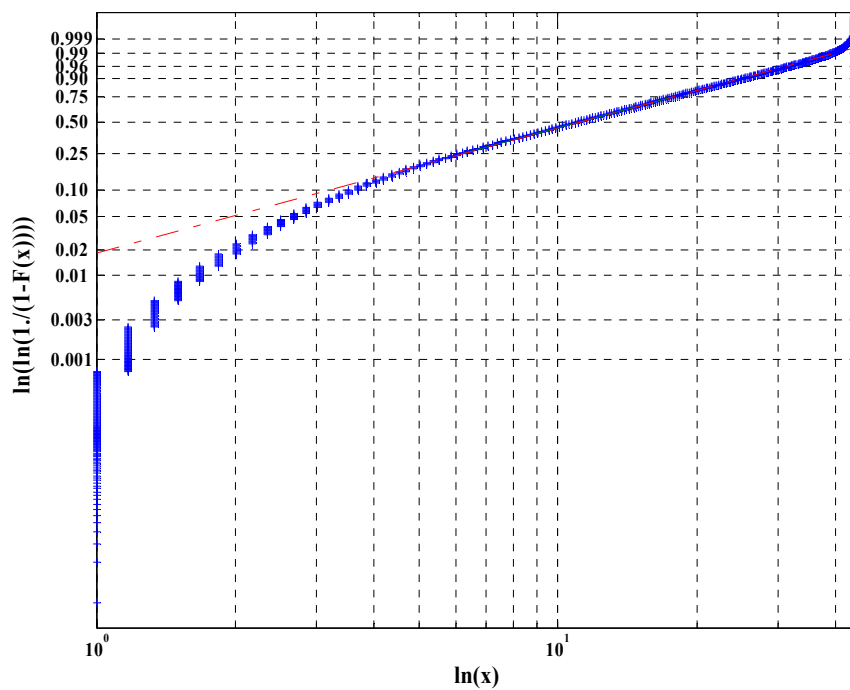


**Figure 1.74** - Weibull paper for the patch (600,1200)x(800,1476).

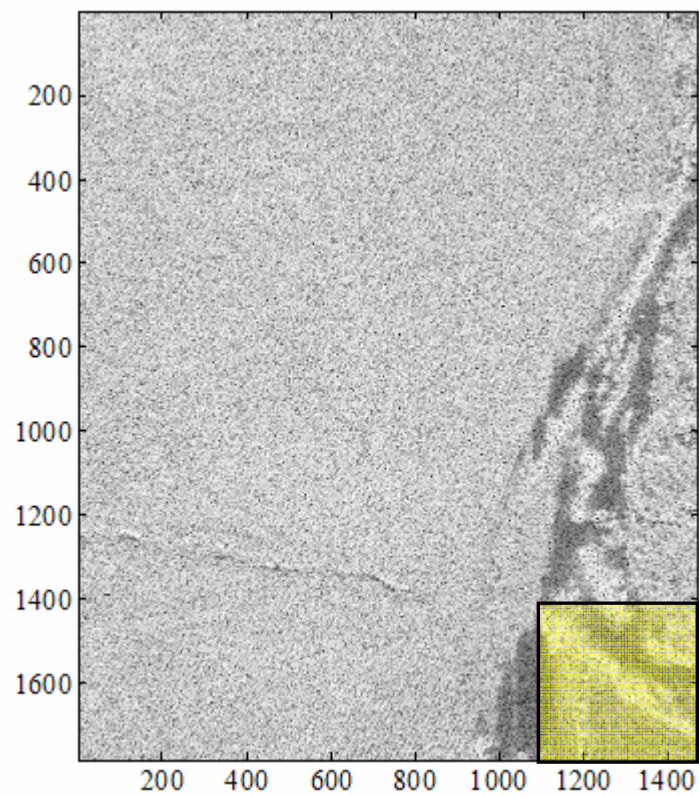


**Figure 1.75** - Patch (1400,1784)x(1100,1476).

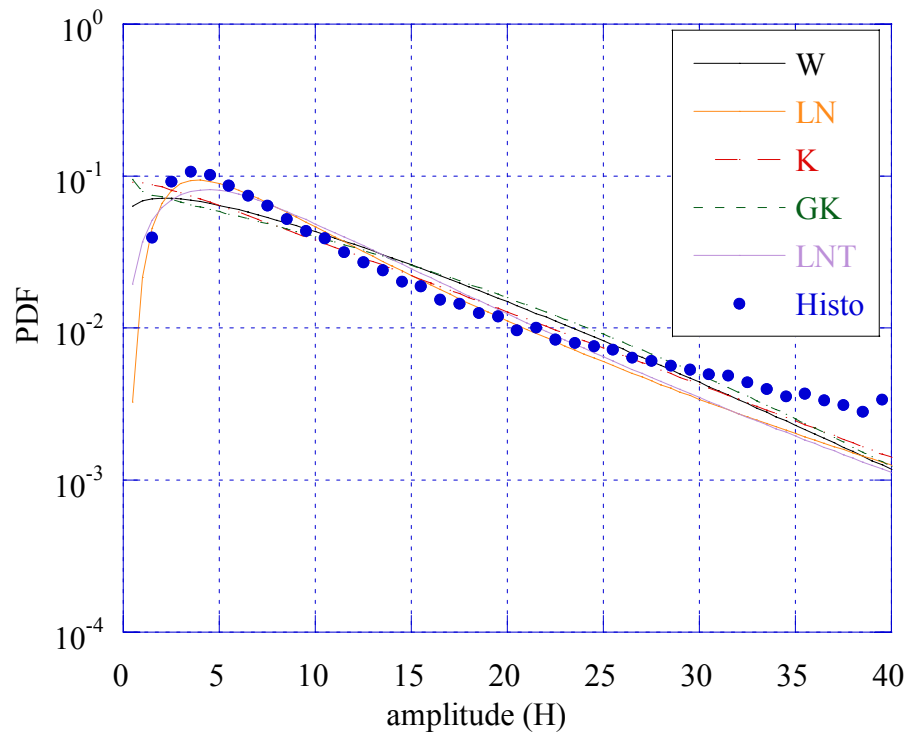


**Figure 1.76** - PDFs of data for the patch  $(1400,1784) \times (1100,1476)$ .

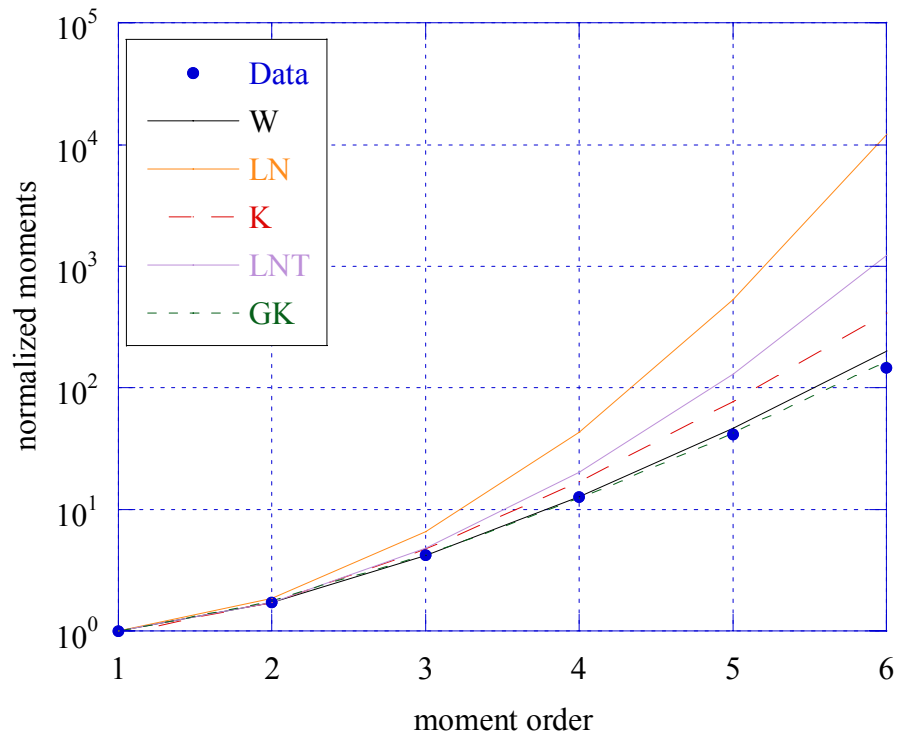


**Figure 1.77** - Normalized moments for the patch  $(1400,1784) \times (1100,1476)$ .

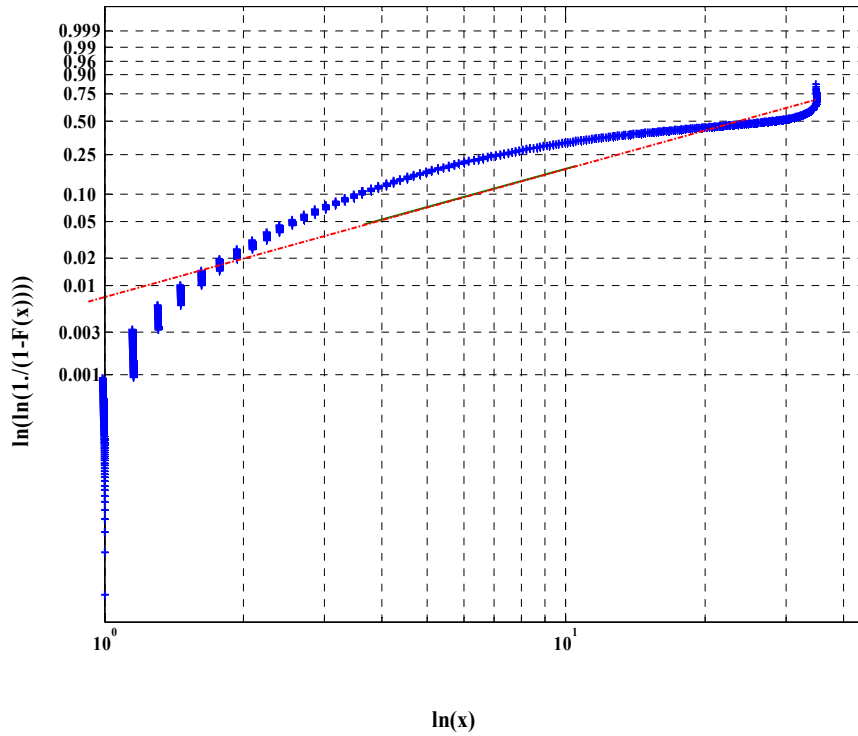


Figure 1.78 - Weibull paper for the patch (1400,1784)x(1100,1476).

Size of patch	Weibull		Lognormal		K		GK			LNT	
	$\hat{c}$	$\hat{b}$	$\hat{\delta}$	$\hat{\sigma}$	$\hat{\nu}$	$\hat{\mu}$	$\hat{\nu}$	$\hat{\mu}$	$\hat{b}$	$\hat{\sigma}^2$	$\hat{m}$
(1784x1472)	1.57	14.21	10.66	0.60	2.46	116.04	0.25	104.88	4.99	0.45	92.66
(1,800)x(1,800)	1.76	15.50	11.97	0.53	2.86	127.72	0.61	204.05	2.85	0.21	114.85
(600,1200)x(800,1476)	1.40	12.13	9.57	0.67	1.33	109.12	0.18	86.62	4.76	0.72	76.16
(1400,1784)x(1100,1476)	1.05	9.18	6.15	0.87	0.54	76.82	0.06	39.44	5.74	1.60	34.50

Table 1.17 - Parameter estimates of models tested on HB06177 file.

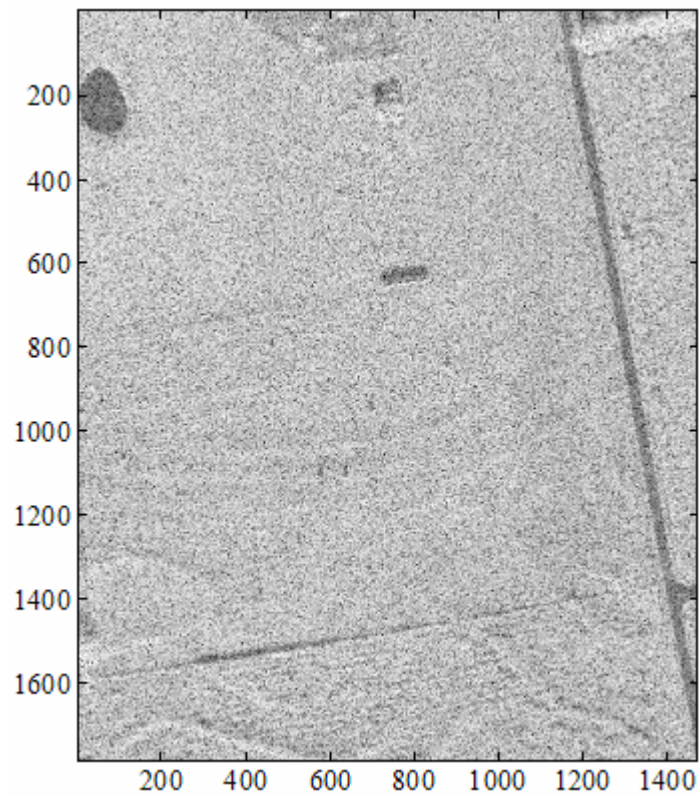
1784x1472	W	LN	K	GK	LNT
Prob	100 %	94 %	100 %	100 %	100 %
d	$1.61 \cdot 10^{-2}$	$7.28 \cdot 10^{-2}$	$0.99 \cdot 10^{-2}$	$1.08 \cdot 10^{-2}$	$1.73 \cdot 10^{-2}$
(1,800)x (1,800)	100 %	99 %	100 %	100 %	100 %
	$1.87 \cdot 10^{-2}$	$5.96 \cdot 10^{-2}$	$5.10 \cdot 10^{-2}$	$1.50 \cdot 10^{-2}$	$1.43 \cdot 10^{-2}$
(600,1200)x (800,1476)	100 %	91 %	100 %	100 %	100 %
	$2.46 \cdot 10^{-2}$	$7.71 \cdot 10^{-2}$	$2.81 \cdot 10^{-2}$	$2.30 \cdot 10^{-2}$	$2.87 \cdot 10^{-2}$
(1400,1784)x (1100,1476)	89 %	100 %	43 %	63 %	100 %
	$8.01 \cdot 10^{-2}$	$2.31 \cdot 10^{-2}$	$12.00 \cdot 10^{-2}$	$10.32 \cdot 10^{-2}$	$4.86 \cdot 10^{-2}$

Table 1.18 - Results of KS test.

1784x1472	W	LN	K	GK	LNT
Prob	100 %	96 %	100 %	100 %	100 %
d	$2.84 \cdot 10^{-2}$	$11.64 \cdot 10^{-2}$	$1.57 \cdot 10^{-2}$	$1.99 \cdot 10^{-2}$	$2.76 \cdot 10^{-2}$
(1,800)x (1,800)					
	100 %	99 %	100 %	100 %	100 %
	$2.40 \cdot 10^{-2}$	$9.93 \cdot 10^{-2}$	$5.94 \cdot 10^{-2}$	$2.53 \cdot 10^{-2}$	$2.47 \cdot 10^{-2}$
(600,1200)x (800,1476)					
	100 %	92 %	100 %	100 %	100 %
	$4.27 \cdot 10^{-2}$	$11.24 \cdot 10^{-2}$	$4.02 \cdot 10^{-2}$	$4.02 \cdot 10^{-2}$	$5.94 \cdot 10^{-2}$
(1400,1784)x (1100,1476)					
	73 %	100 %	65 %	36 %	100 %
	$10.46 \cdot 10^{-2}$	$4.47 \cdot 10^{-2}$	$15.33 \cdot 10^{-2}$	$18.11 \cdot 10^{-2}$	$7.84 \cdot 10^{-2}$

**Table 1.19** - Results of Kuiper test.

### 1.2.7 HB06188 File



**Figure 1.79** - Grass field of file *HB06188* file.

Of this file we tested the whole image, a homogeneous patch  $((800,1400) \times (1000,1474))$  and the patch  $((1,600) \times (1000,1474))$ , containing a man-made object (a street). Results are summarized in the following figures and tables.

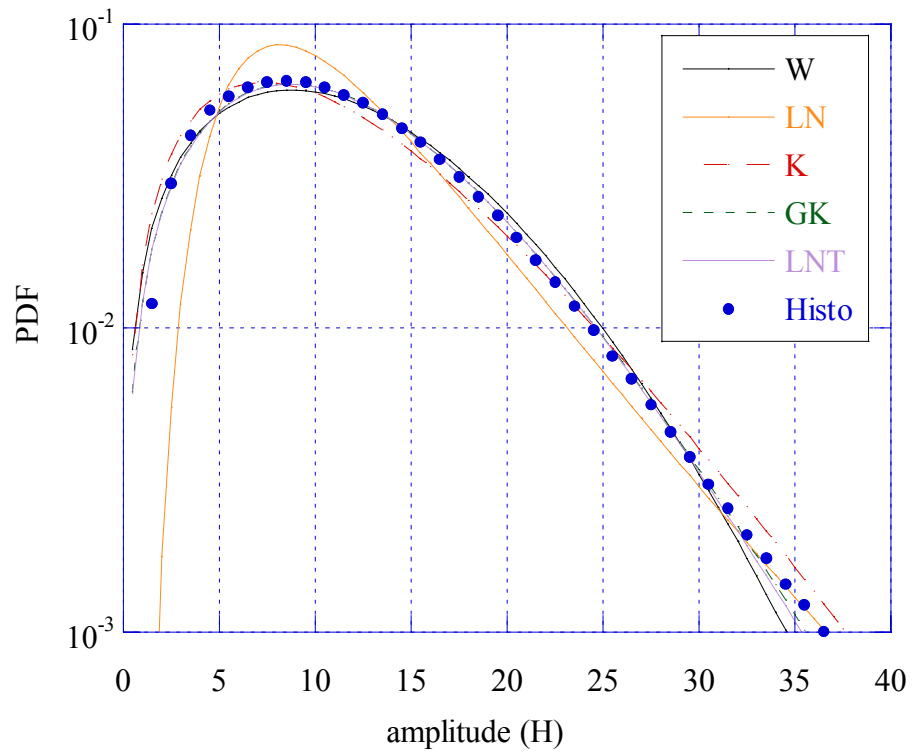


**Figure 1.80** - PDF of clutter for the whole image (1784x1474).

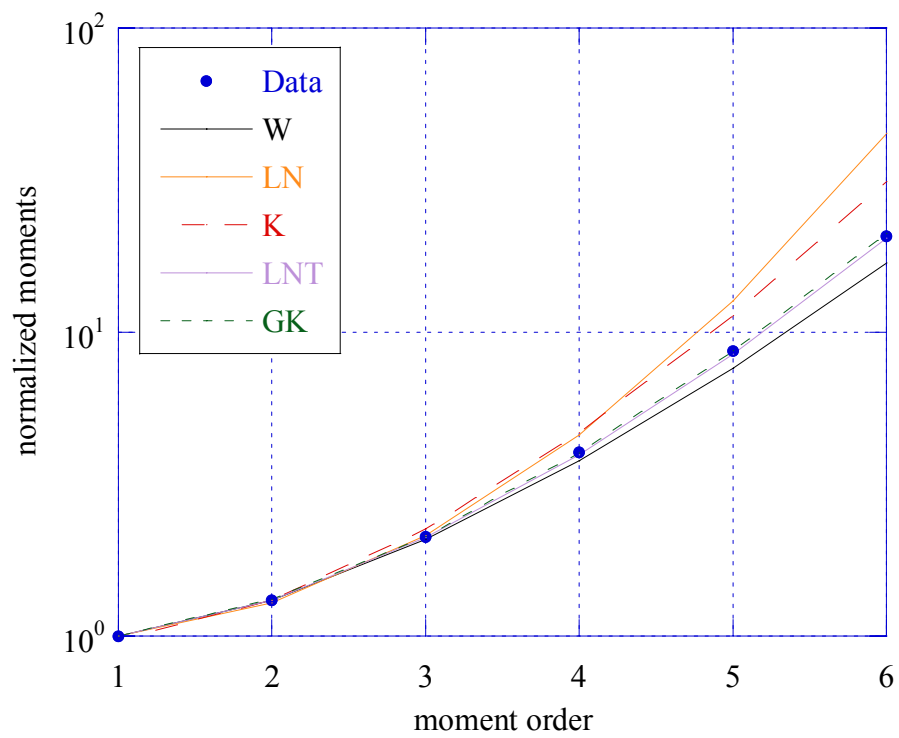


**Figure 1.81** - Normalized moments for the whole image (1784x1474).

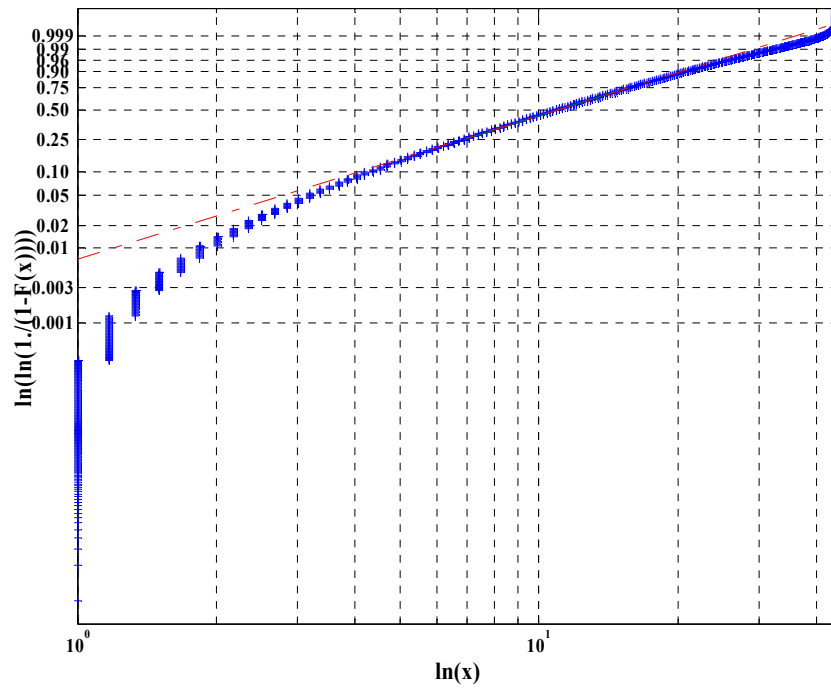


**Figure 1.82** - Weibull paper for the whole image.

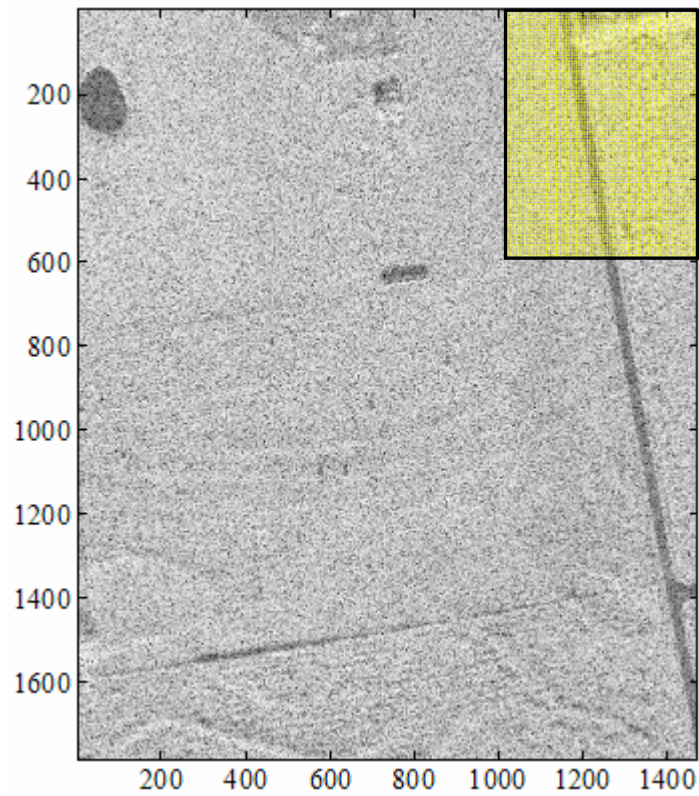


**Figure 1.83** - Grass field in the patch  $(1,600) \times (1000, 1474)$ .

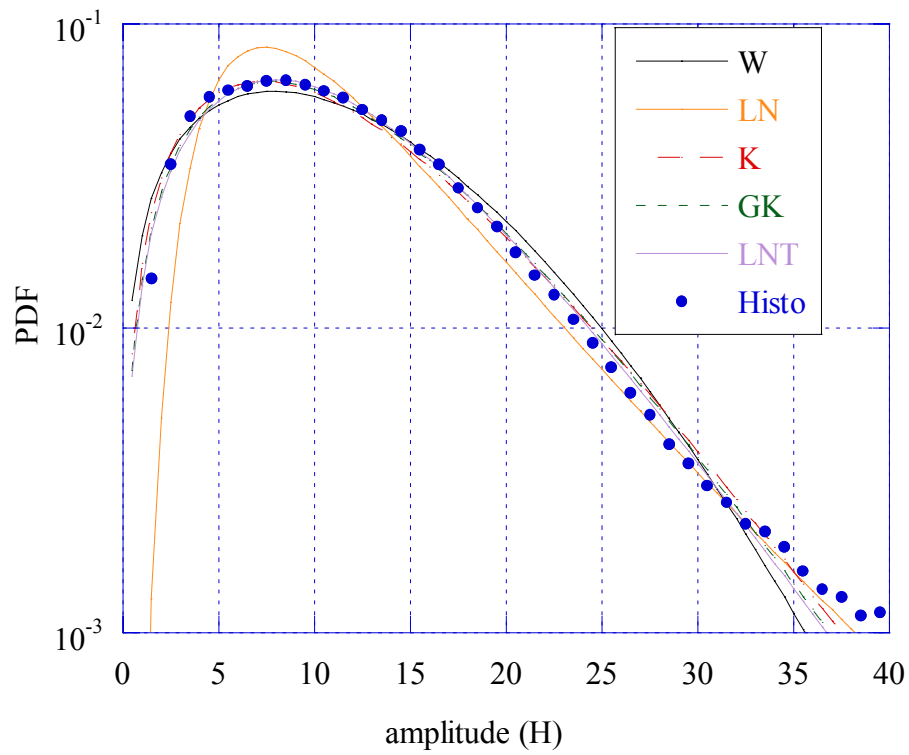


**Figure 1.84** - PDF of clutter amplitude for the patch  $(1,600) \times (1000,1474)$ .

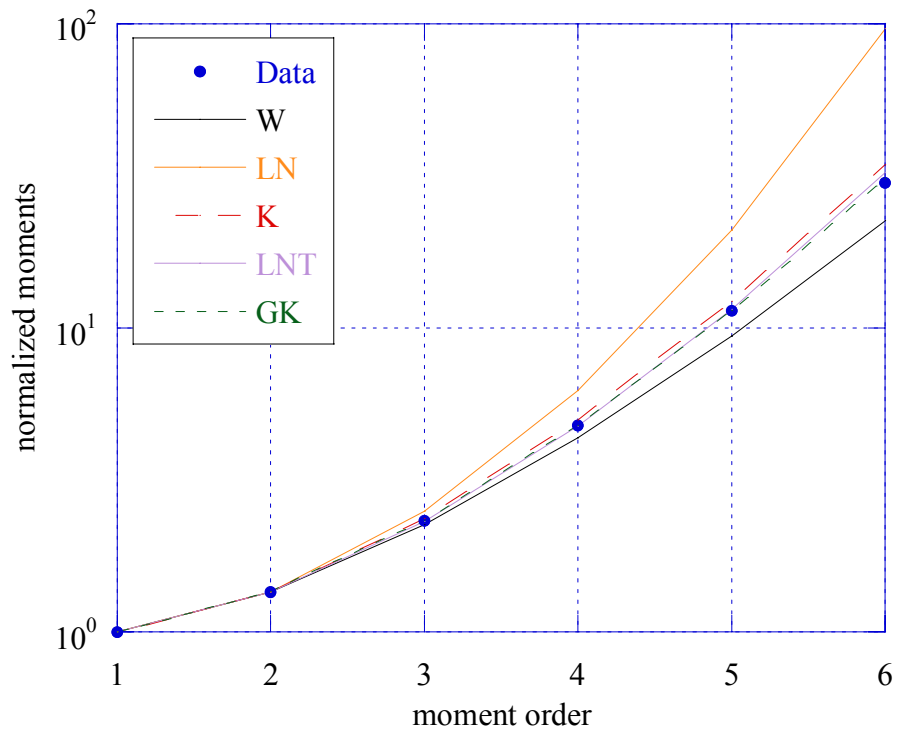


**Figure 1.85** - Normalized moments for the patch  $(1,600) \times (1000,1474)$ .



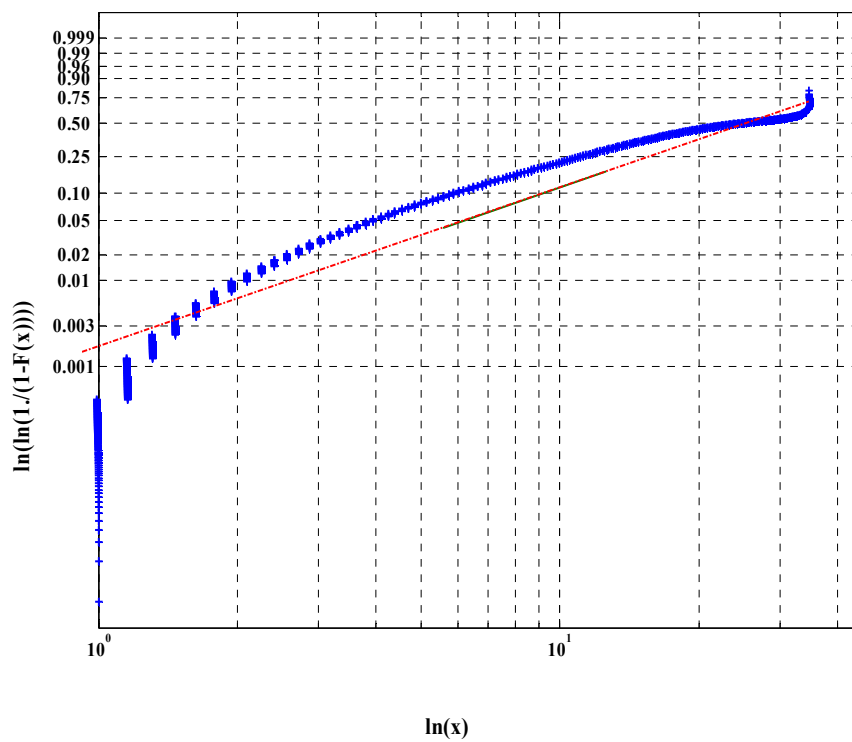


**Figure 1.86** - Weibull paper for the patch  $(1,600) \times (1000,1474)$ .

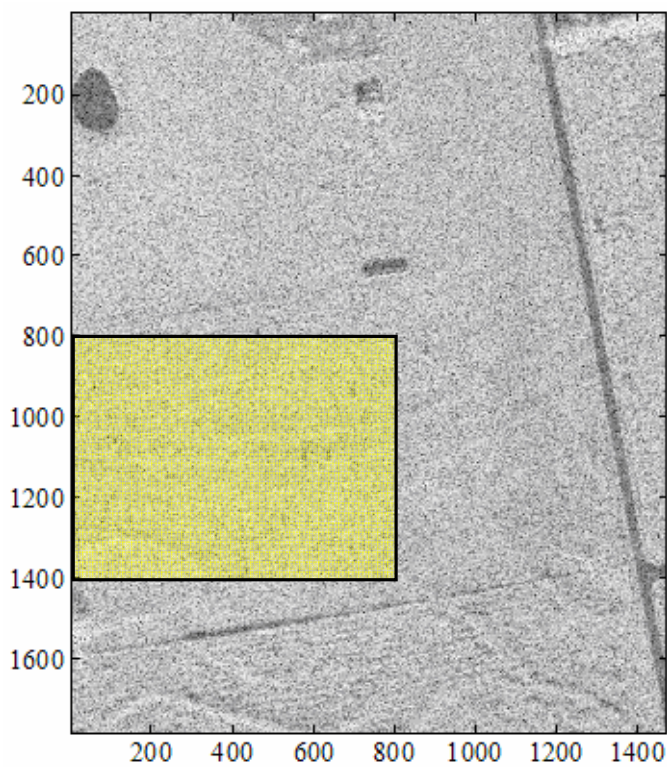


**Figure 1.87** - Grass field in the patch  $(800,1400) \times (1,800)$ .

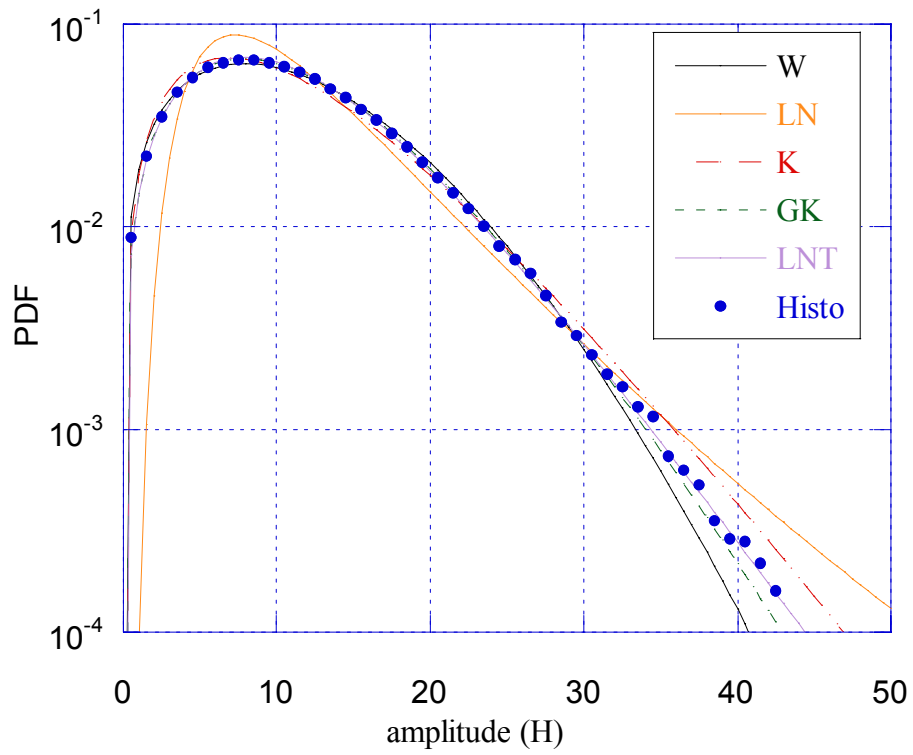


**Figure 1.88** - PDF of clutter amplitude for the patch  $(800, 1400) \times (1, 800)$ .

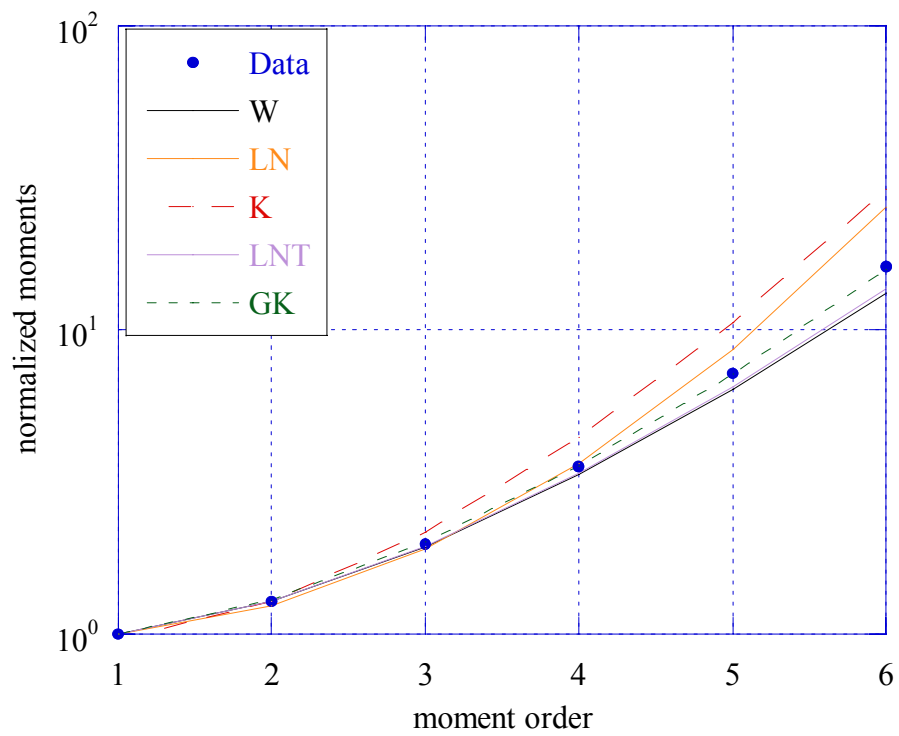


**Figure 1.89** - Normalized moments for the patch  $(800, 1400) \times (1, 800)$ .

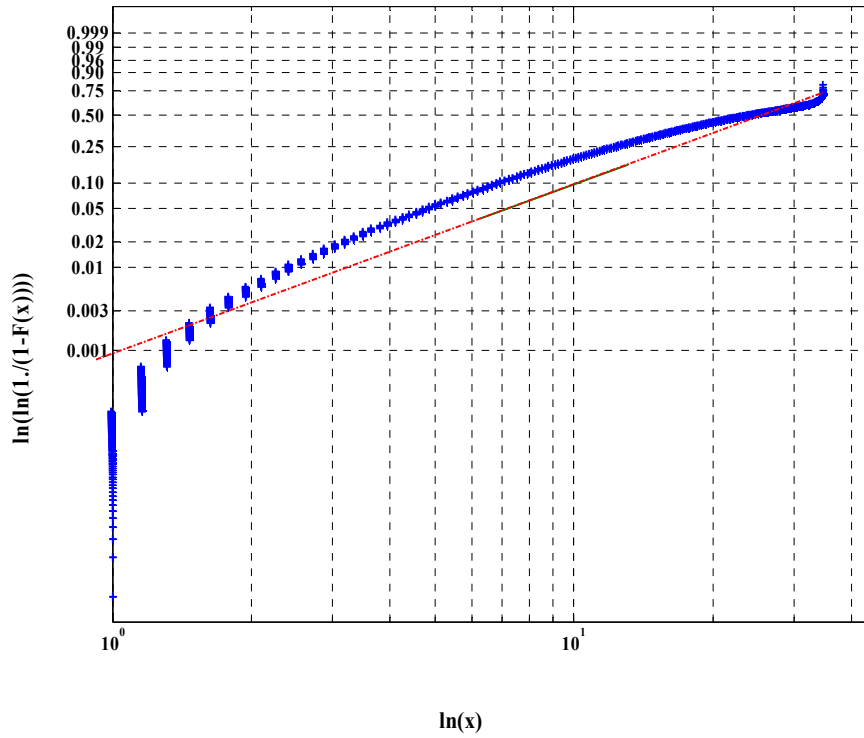


**Figure 1.90** - Weibull paper for the patch  $(800,1400) \times (1,800)$ .

Size of patch	Weibull		Lognormal		K		GK			LNT	
	$\hat{c}$	$\hat{b}$	$\hat{\delta}$	$\hat{\sigma}$	$\hat{\nu}$	$\hat{\mu}$	$\hat{\nu}$	$\hat{\mu}$	$\hat{b}$	$\hat{\sigma}^2$	$\hat{m}$
(1784x1472)	1.67	12.22	9.38	0.55	2.86	82.09	0.82	169.63	2.29	0.31	70.20
(1,600)x(1000,1476)	1.56	11.88	8.91	0.60	2.18	81.33	0.76	167.45	1.86	0.46	64.66
(800,1400)x(1,800)	1.79	12.57	9.71	0.53	2.86	82.49	2.75	238.34	1.46	0.19	75.98

**Table 1.20** - Parameter estimates of models tested on HB06188 file.

1784x1472	W	LN	K	GK	LNT
Prob	100 %	98 %	100 %	100 %	100 %
d	$1.87 \cdot 10^{-2}$	$6.63 \cdot 10^{-2}$	$4.13 \cdot 10^{-2}$	$1.23 \cdot 10^{-2}$	$1.19 \cdot 10^{-2}$
(1,600)x (1000,1476)	100 %	99 %	100 %	100 %	100 %
	$2.53 \cdot 10^{-2}$	$5.55 \cdot 10^{-2}$	$1.93 \cdot 10^{-2}$	$1.35 \cdot 10^{-2}$	$1.20 \cdot 10^{-2}$
(800,1400)x (1,800)	100 %	96 %	97 %	100 %	100 %
	$1.79 \cdot 10^{-2}$	$6.94 \cdot 10^{-2}$	$6.68 \cdot 10^{-2}$	$1.84 \cdot 10^{-2}$	$1.76 \cdot 10^{-2}$

**Table 1.21** - Results of KS test.

1784x1472	W	LN	K	GK	LNT
Prob	100 %	99 %	100 %	100 %	100 %
d	$2.50 \cdot 10^{-2}$	$10.97 \cdot 10^{-2}$	$5.00 \cdot 10^{-2}$	$1.84 \cdot 10^{-2}$	$1.95 \cdot 10^{-2}$
(1,600)x (1000,1476)					
	100 %	99 %	100 %	100 %	100 %
	$4.60 \cdot 10^{-2}$	$9.17 \cdot 10^{-2}$	$2.80 \cdot 10^{-2}$	$2.21 \cdot 10^{-2}$	$1.75 \cdot 10^{-2}$
(800,1400)x (1,800)					
	100 %	96 %	97 %	100 %	100 %
	$2.58 \cdot 10^{-2}$	$10.97 \cdot 10^{-2}$	$8.01 \cdot 10^{-2}$	$2.12 \cdot 10^{-2}$	$2.90 \cdot 10^{-2}$

**Table 1.22** - Results of Kuiper test.

### 1.2.8 Conclusions

From our analysis we can conclude that, in general, the clutter scattered by a grass field is not very spiky and can be well modeled by Weibull, GK and K models. We used the estimated shape parameter of the Weibull PDF as a measure of the spikiness of the clutter. In our data, this parameter is, in average, close to 1.7 (for  $c=2$  we have a Rayleigh distribution) then the clutter is homogeneous. We obtained a much lower value only for the patch  $(1400,1784) \times (1100,1476)$  of the HB06177 file reported in Figure 1.75. For this patch  $c=1.054$  and this difference is mainly due to the presence of dense vegetation and shadows.

To complete our statistical analysis we applied KS and Kuiper goodness-of-fit tests. Both tests provided very similar results, but they do not allow us to distinguish clearly between the different models we used.

## 1.3 Terrain with dense vegetation and trees

### 1.2.1 HB06202 file

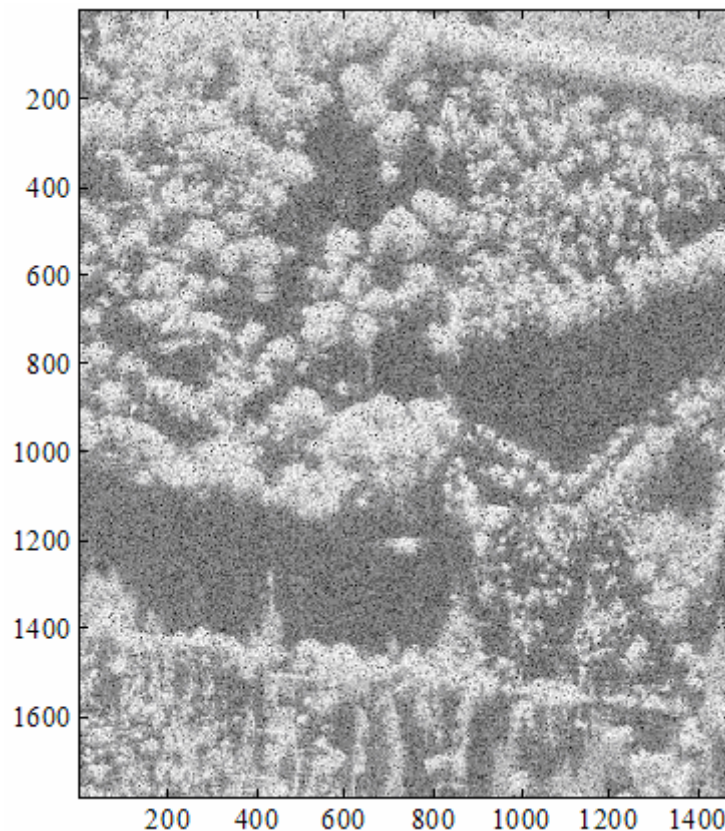


**Figure 1.91** - Image of HB06202 file. Terrain with dense vegetation and trees.

We now consider the image of file HB06202 which represents, as shown in Figure 1.91, a region with dense vegetation and trees. We performed same statistical analysis as for the images with grass field on the whole image. The histogram and the moments are plotted in Fig. 1.92 and 1.93 respectively.

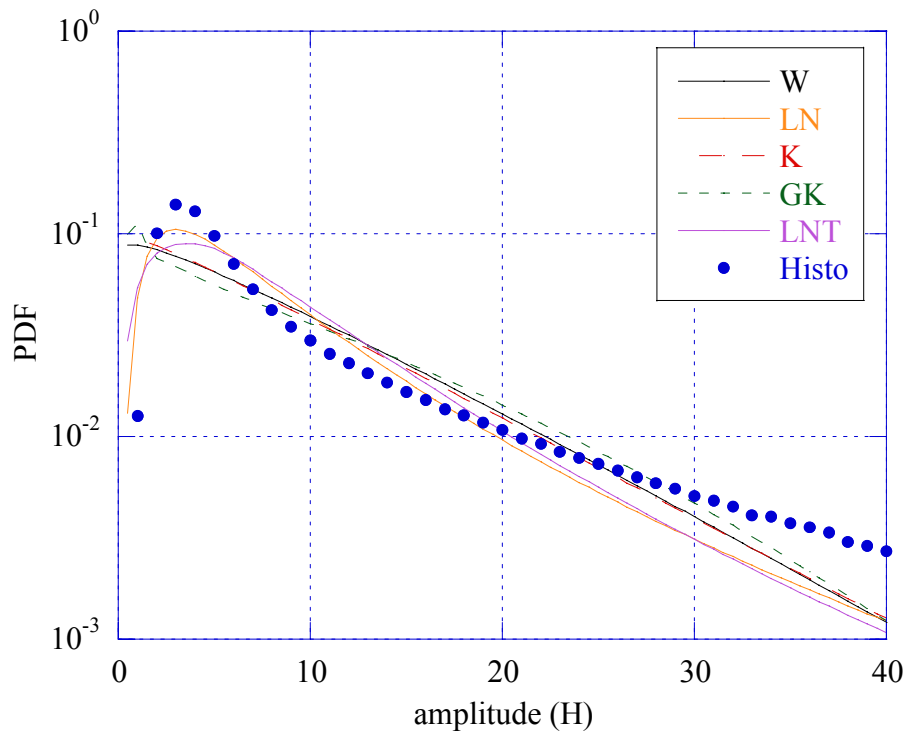


**Figure 1.92** - PDF of data clutter for the whole image (1784x1478).

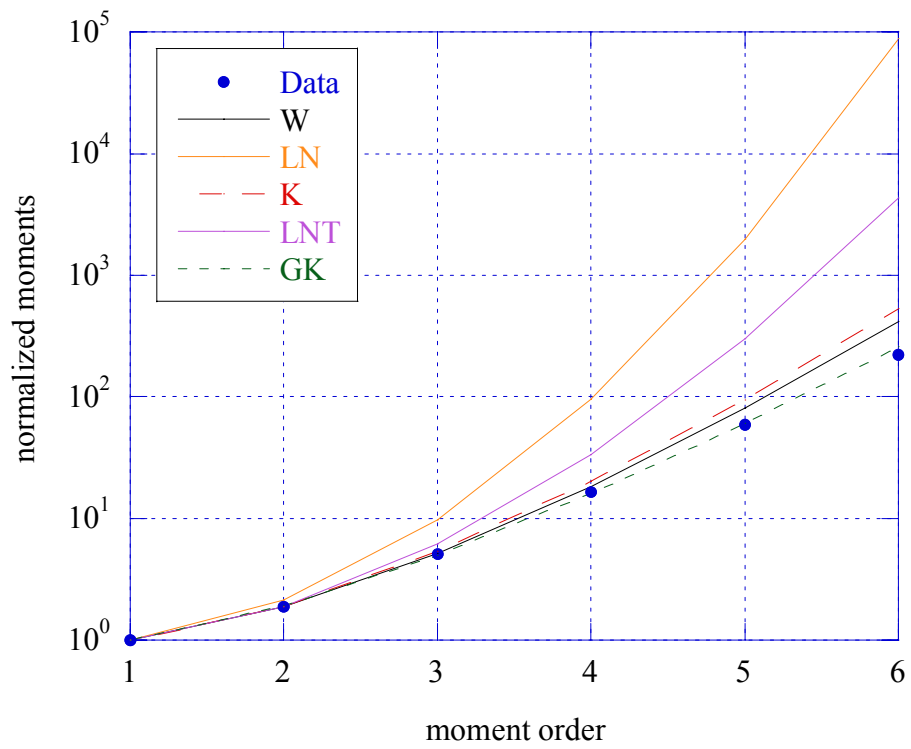


**Figure 1.93** - Normalized moments for the whole image (1784x1478)

By observing Figure 1.92 we can conclude that none of tested models exhibits a good fitting with the data. Based on this result, we introduced another model which takes into account the presence of thermal noise that, maybe, is not negligible in the shadowed areas. This new model is the “K+ thermal noise”. It is characterized by the following first order PDF and moments [Far97]:

### K+ thermal noise model

$$\text{PDF} \quad p_r(r) = \frac{(\nu/\mu)^\nu}{\Gamma(\nu)} \int_0^\infty \frac{r \cdot \tau^{\nu-1}}{\tau + \sigma_G^2} \exp\left(-\frac{r^2}{2(\tau + \sigma_G^2)}\right) \times \exp\left(-\frac{\nu}{\mu} \tau\right) d\tau \quad (1.26)$$

$$\text{Moments} \quad E\{R^k\} = \frac{(\nu/\mu)^\nu}{\Gamma(\nu)} \int_0^\infty r^{k+1} \int_0^\infty \frac{\tau^{\nu-1}}{\tau + \sigma_G^2} \exp\left(-\frac{r^2}{2(\tau + \sigma_G^2)}\right) \times \exp\left(-\frac{\nu}{\mu} \tau\right) d\tau \quad (1.27)$$

To estimate the characteristic parameters  $\nu$ ,  $\mu$  and  $\sigma_G^2$  we applied again the method of moments. In this case we considered the moments of second, fourth and sixth order and we rewrite their expressions as a function of the clutter-to-noise ratio  $CNR = \mu/\sigma_G^2$  obtaining the following analytical expressions:

$$E\{R^2\} = 2\sigma_G^2(1 + CNR) \quad (1.28)$$

$$E\{R^4\} = 8\sigma_G^4 \left(1 + 2CNR + \frac{(\nu+1)}{\nu} CNR^2\right) \quad (1.29)$$

$$E\{R^6\} = 4\sigma_G^6 \left(12 + 36 \cdot CNR + 37 \cdot CNR^2 \cdot \frac{\nu+1}{\nu} + 12 \cdot CNR^3 \cdot \frac{(\nu+1)(\nu+2)}{\nu^2}\right) \quad (1.30)$$

We resolve the system of eqs. (1.28)-(1.30) as a function of  $CNR$ ,  $\nu$  and  $\sigma_G^2$ . Then we obtained  $\mu$  from the  $CNR$  value.

The result of this model is plotted in Fig. 1.94 and the estimated parameters are reported in Table 1.22.

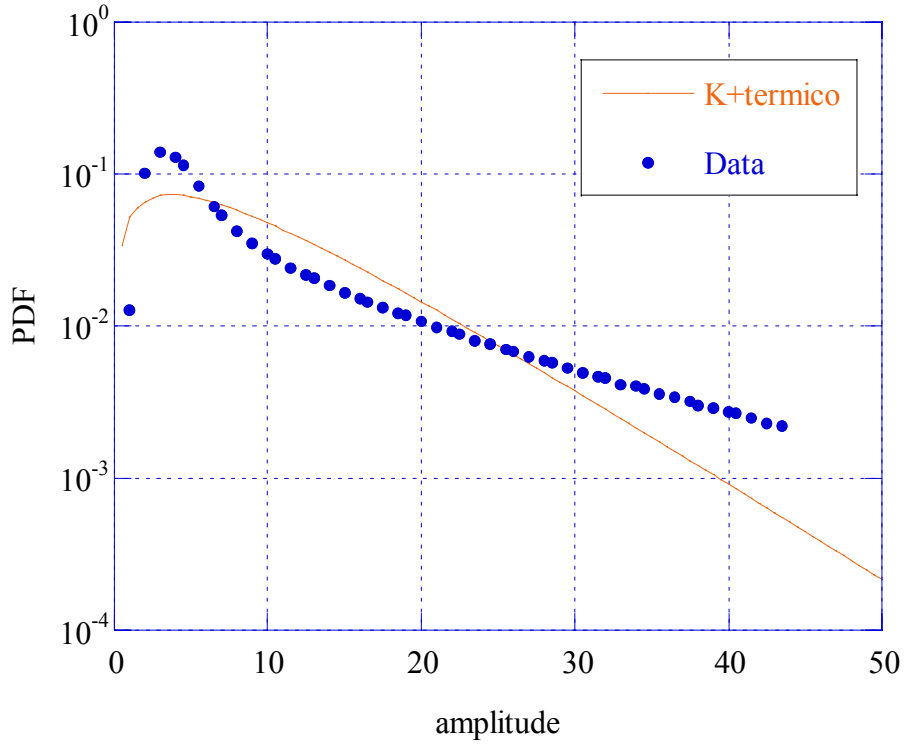


**Figure 1.94** - PDF of clutter amplitude: K+ thermal noise model.

$\hat{\mu}$	$\hat{\nu}$	$\hat{\sigma}_G^2$
80.996	0.98159	$5.3834 \cdot 10^{-13}$

**Table 1.23** - Parameters estimate of K+ thermal noise model.

Unfortunately the fitting is not good, and then we decided to change the parameter estimation method. Instead of using the method of moments, we minimized the square difference between histogram  $f(r)$  and K+ thermal noise curve  $p_r(r)$ , that is

$$\boldsymbol{\theta} = \underset{\boldsymbol{\theta}}{\operatorname{argmin}} \sum_i \left( f(r_i) - p_r(r_i) \right)^2 \quad (1.31)$$

where  $\boldsymbol{\theta}$  is the vector of parameters to estimate  $(\mu, \nu, \sigma_G^2)$  and  $r_i$  ( $i=1,2,3,..$ ) the vector of data amplitude. Even with this new estimation method, the K+thermal noise model fails.

On these data we tested also the Generalized Compound (GC) model. The GC model has been recently proposed for very high resolution data in [Ana99] as an alternative to the



compound-Gaussian model. In the Generalized compound model the Gaussianity hypothesis on the speckle is relaxed and the Generalized Gamma (G $\Gamma$ ) distribution is proposed for both speckle and texture. The expression of the G $\Gamma$  is:

$$p(r; a, b, \nu) = \frac{b}{a\Gamma(\nu)} \left(\frac{r}{a}\right)^{b\nu-1} \exp\left(-\left(\frac{r}{a}\right)^b\right) \quad r \geq 0 \quad (1.32)$$

where  $a$  is scale parameter,  $\nu$  is the shape parameter and  $b$  is the “power” parameter. This PDF is more general than Rayleigh and Gamma PDFs. The G $\Gamma$  PDF can be used to describe distributions with long tails. The standard models for the clutter as Rayleigh ( $b=2, \nu=1$ ), lognormal ( $b, \nu \rightarrow 0, \infty$ ), Weibull ( $\nu=1$ ), and the Gamma ( $b=1$ ) are special case of G $\Gamma$  PDF.

In this case the distribution of amplitude, conditioned to the texture, is given by:

$$f_{G\Gamma}(r|s) = \frac{b_1}{s\Gamma(\nu_1)} \left(\frac{r}{s}\right)^{b_1\nu_1-1} \exp\left(-\left(\frac{r}{s}\right)^{b_1}\right) \quad x \geq 0 \quad (1.33)$$

$s$  is the component of modulation ( $\sqrt{\tau}$ ) which is G $\Gamma$  distributed:

$$f_{G\Gamma}(s) = \frac{b_2}{a\Gamma(\nu_2)} \left(\frac{s}{a}\right)^{b_2\nu_2-1} \exp\left(-\left(\frac{s}{a}\right)^{b_2}\right) \quad s \geq 0 \quad (1.34)$$

The PDF of clutter  $r$  is GC distributed:

$$f_{GC}(r) = \int_0^\infty f_{G\Gamma}(r|s) f_{G\Gamma}(s) ds \quad (1.35)$$

If we replace (1.33) and (1.34) in (1.35) we obtain the integral representation of GC PDF:

$$f_{GC}(r; a, b_1, b_2, \nu_1, \nu_2) = \frac{b_1 b_2}{\Gamma(\nu_1) \Gamma(\nu_2)} \cdot \frac{r^{b_1\nu_1-1}}{a^{b_2\nu_2}} \int_0^\infty s^{b_2\nu_2-b_1\nu_1-1} \cdot \exp\left[-\left(\frac{s}{a}\right)^{b_2} - \left(\frac{r}{s}\right)^{b_1}\right] ds \quad (1.36)$$

In general, the integral that appears in the eq. (1.36) does not present a closed form. A closed form exists only if  $b_1 = b_2 = b$  and the resulting PDF is called GC-GK:

$$f_{GK}(r; a, b, \nu_1, \nu_2) = \frac{2b}{a\Gamma(\nu_1)\Gamma(\nu_2)} \left(\frac{r}{a}\right)^{b/2(\nu_1+\nu_2)-1} \cdot K_{\nu_2-\nu_1} \left[ 2\left(\frac{r}{a}\right)^{b/2} \right] \quad r \geq 0 \quad (1.37)$$

where  $K_\nu(r)$  is the modified Bessel function. The moments for the GC-GK PDF are given by the following expression:

$$E[r^k] = a^k \frac{\Gamma\left(\frac{k}{b} + \nu_1\right) \Gamma\left(\frac{k}{b} + \nu_2\right)}{\Gamma(\nu_1)\Gamma(\nu_2)} \quad (1.38)$$

To estimate the parameters characterizing the model, we used the same method applied for the Generalized K model with generalized Gamma distributed texture, that is we minimized the functional:

$$J(\nu_1, \nu_2, b) = \sum_{k=2}^5 \left| \frac{\hat{m}(k)}{m_n(k)} - 1 \right|^2 \quad (1.39)$$

where  $m_n(k)$  is the normalized theoretical moment of order  $n$

$$m_n^{-1}(k) = \frac{E\{r\}^k}{E\{r^k\}} = \frac{\Gamma^k\left(\nu_1 + \frac{1}{b}\right) \Gamma^k\left(\nu_2 + \frac{1}{b}\right)}{\Gamma\left(\frac{k}{b} + \nu_1\right) \Gamma\left(\frac{k}{b} + \nu_2\right)} \cdot \frac{1}{[\Gamma(\nu_1)\Gamma(\nu_2)]^{k-1}} \quad (1.40)$$

while  $\hat{m}(k)$  are the moments experimentally estimated.

The parameter  $a$  is then given by:

$$\hat{a} = \frac{m(1)\Gamma(\hat{\nu}_2)\Gamma(\hat{\nu}_1)}{\Gamma\left(\hat{\nu}_1 + \frac{1}{\hat{b}}\right)\Gamma\left(\frac{1}{\hat{b}} + \hat{\nu}_2\right)} \quad (1.41)$$

The results of the GC-GK model are reported in Figs. 1.95 and 1.96. It is apparent that the fitting is not good.

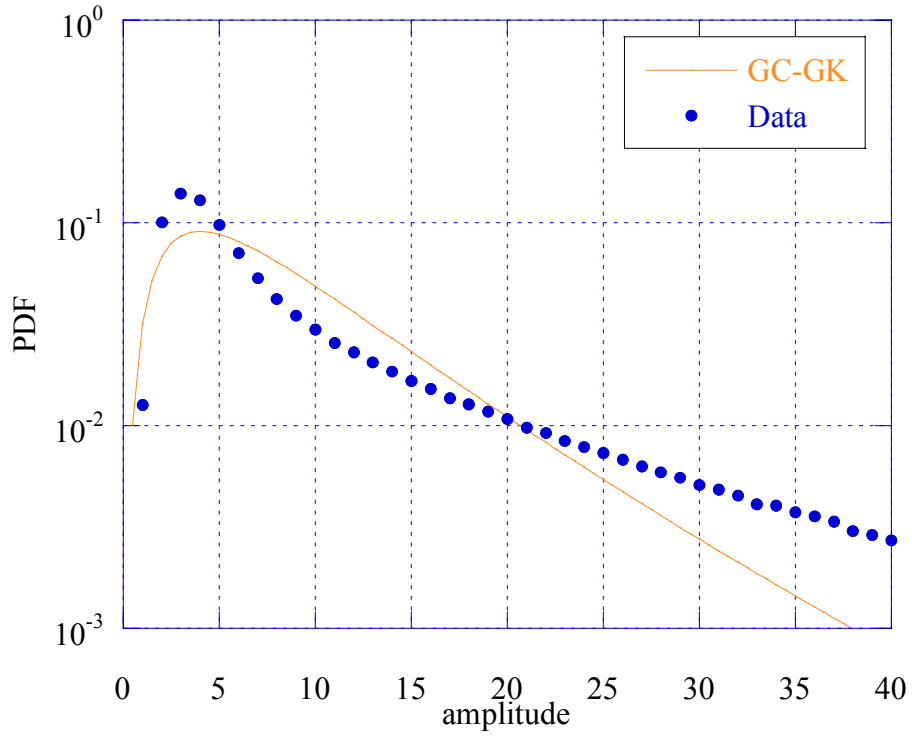


**Figure 1.95** - PDF of clutter amplitude.

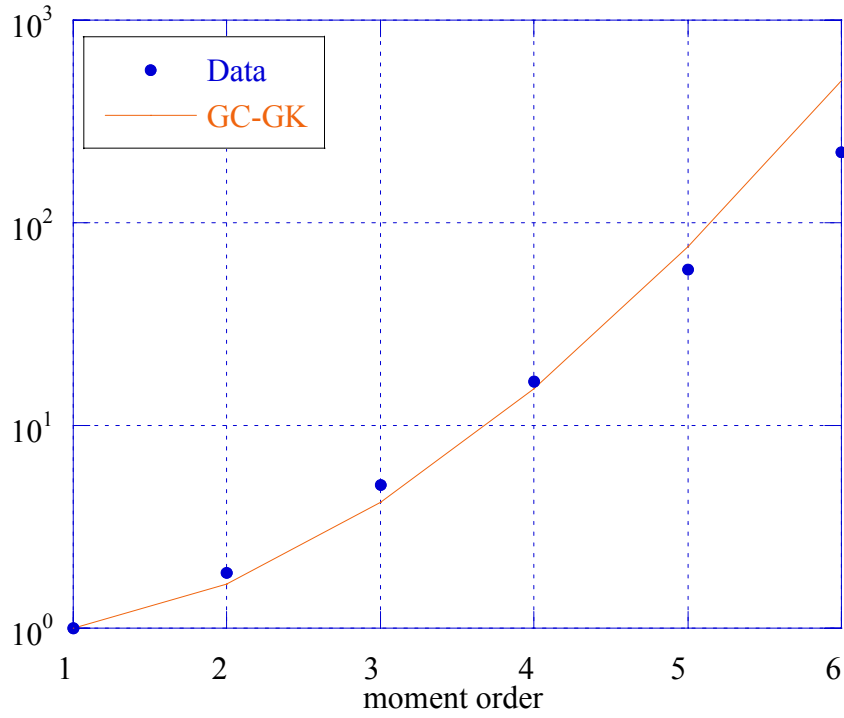


**Figure 1.96** - Normalized moments.

In the Table 1.24 we report the parameters estimated for the GC model.

$\hat{a}$	$\hat{b}$	$\hat{v}_1$	$\hat{v}_2$
0.078138	0.76288	6.127	5.9443

**Table 1.24** - Parameters values for the GC-GK model.

The last model we tested on the data is the Inverse Gamma (IG). It is a particular case of the Compound-Gaussian model, where the texture ( $\tau$ ) PDF is the Inverse Gamma (as a consequence  $1/\tau$  is Gamma distributed). The expression of the Inverse Gamma PDF is [Bal05]:

$$f_{\tau}(\tau; \alpha, \beta) = \frac{1}{\beta^{\alpha} \Gamma(\alpha)} \tau^{-(\alpha+1)} e^{-\frac{1}{\beta\tau}} \quad (1.42)$$

where  $\alpha$  is the shape parameter and  $\beta$  is the scale parameter.

If the speckle amplitude is Rayleigh distributed, the amplitude of clutter is distributed such that:

$$f_R(r) = \int_0^\infty \frac{1}{\beta^\alpha \Gamma(\alpha)} \tau^{-(\alpha+1)} e^{-\frac{1}{\beta\tau}} \frac{2r}{\tau} e^{-\frac{r^2}{\tau}} d\tau = \frac{2r}{\beta^\alpha \Gamma(\alpha)} \int_0^\infty \tau^{-(\alpha+2)} e^{-\frac{\beta r^2 + 1}{\beta\tau}} d\tau \quad (1.43)$$

If we define  $x = \frac{\beta r^2 + 1}{\beta\tau}$ , and replace it in eq. (1.43) we obtain the IGT (Inverse Gamma texture) PDF:

$$f_R(r) = \frac{2r\beta}{(\beta r^2 + 1)^{\alpha+1} \Gamma(\alpha)} \int_0^\infty x^\alpha e^{-x} dx = \frac{2r\beta \Gamma(\alpha+1)}{(\beta r^2 + 1)^{\alpha+1} \Gamma(\alpha)} \quad (1.44)$$

The expression for the moments is

$$E\{R^n\} = 2\alpha\beta \int_0^\infty \frac{r^{n+1}}{(\beta r^2 + 1)^{\alpha+1}} dr \quad (1.45)$$

By applying the substitution  $k = \beta r^2$  and the identities:

$$B(z, w) = \int_0^\infty \frac{t^{z-1}}{(1+t)^{z+w}} dt = \frac{\Gamma(z)\Gamma(w)}{\Gamma(z+w)} \quad \Gamma(\alpha+1) = \alpha \cdot \Gamma(\alpha) \quad (1.46)$$

we obtain the following closed form expression:

$$E\{R^n\} = \left(\frac{1}{\beta}\right)^{\frac{n}{2}} \alpha \int_0^\infty \frac{k^{\frac{n}{2}}}{(k+1)^{\alpha+1}} dk = \left(\frac{1}{\beta}\right)^{\frac{n}{2}} \frac{\Gamma\left(\frac{n}{2}+1\right)\Gamma\left(\alpha-\frac{n}{2}\right)}{\Gamma(\alpha)} \quad (1.47)$$

Eq. (1.47) converges if and only if  $\alpha \geq n/2$ .

The results relating to this model are shown in Fig. 1.97 where the data histogram is compared to the IGT PDF. To estimate  $\alpha$  and  $\beta$  we used the MoM. The parameter estimates are  $\alpha=1.2498$  and  $\beta=0.016672$ . The fitting is not good.

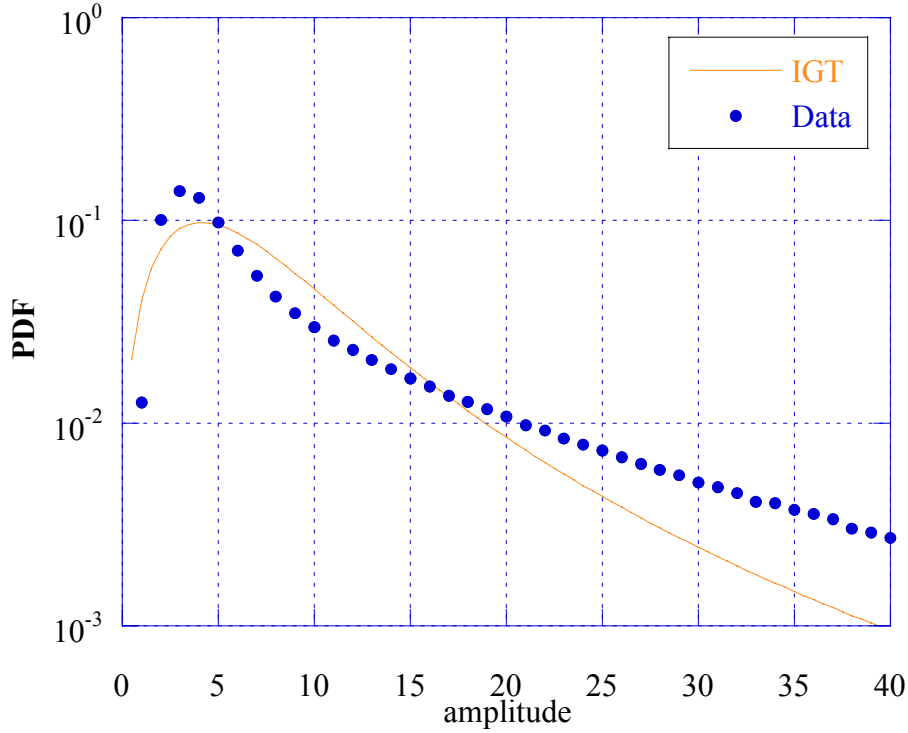


**Figure 1.97** - PDF of clutter amplitude.

### 1.2.2 Texture and speckle estimation and statistical analysis

After testing some statistical model on the overall amplitude of the clutter from dense vegetated areas, we performed a statistical analysis on speckle and texture separately. First we considered the data of file HB06202 where each tested model failed in modeling the amplitude histogram. Supposing that the clutter process is a compound process  $r(n) = \sqrt{\tau(n)}x(n)$ , texture and speckle have very different correlation times and the speckle is a unitary power process, we estimated them from the amplitude data. Due to the physical nature of the texture that takes into account the space variations of the local power of the image, it can be considered as a long time (or space) correlated process. Then the texture can be supposed constant (or very slowly varying) on small patches of the image and it can be estimated from the amplitude data as [Gin00]

$$\hat{\tau}(i, j) = \frac{1}{N_r N_{cr}} \sum_{k=iN_r}^{(i+1)N_r-1} \sum_{m=jN_{cr}}^{(j+1)N_{cr}-1} r(k, m)^2 \quad (1.48)$$

where  $N_r$  and  $N_{cr}$  are the number of samples in range and cross-range respectively used for the estimation, then the dimensions (in pixels) of each patch. In performing this estimation we fixed  $N_r=N_{cr}=10$ , without overlap. It is apparent from eq. (1.48) that every 100 samples of clutter amplitude we obtained only 1 texture sample. The dimension of the square window has been chosen as a compromise between accuracy of the texture estimate and variation time of the texture itself. A larger window could improve the texture estimate only if the texture would be constant in a larger space interval, otherwise the estimation calculates only an average texture.

The speckle can be estimated by normalizing the data amplitude with respect to the estimated texture, thus

$$\hat{x}(k, m) = \frac{r(k, m)}{\sqrt{\hat{\tau}(i, j)}} \quad k \in [iN_r, (i+1)N_r], \quad m \in [jN_{cr}, (j+1)N_{cr}] \quad (1.49)$$

The speckle of file HB06202 is plotted in Fig. 1.98. It is a noise-like process even if, somewhere, it is possible to see some residue of the texture structure.

On the speckle we performed a statistical analysis very similar to that carried out on the amplitude. We used same models, Weibull, Rayleigh, K, GK, LN and LNT with same notation even if LNT, as instance, refers to Gaussian compound model with Log-normal texture and here we are analyzing the speckle. In this context we are interested in the statistical model, not in its physical nature. The results are shown in Figs. 1.99 and 1.100. The best fitting has been obtained with K and LNT PDFs, as verified in the Tables 1.25 and 1.26 where we report the results of KS and Kuiper tests.

The plot of the GK PDF shows a strange behavior that is due to a numerical problem in the integration of eq. (1.14).

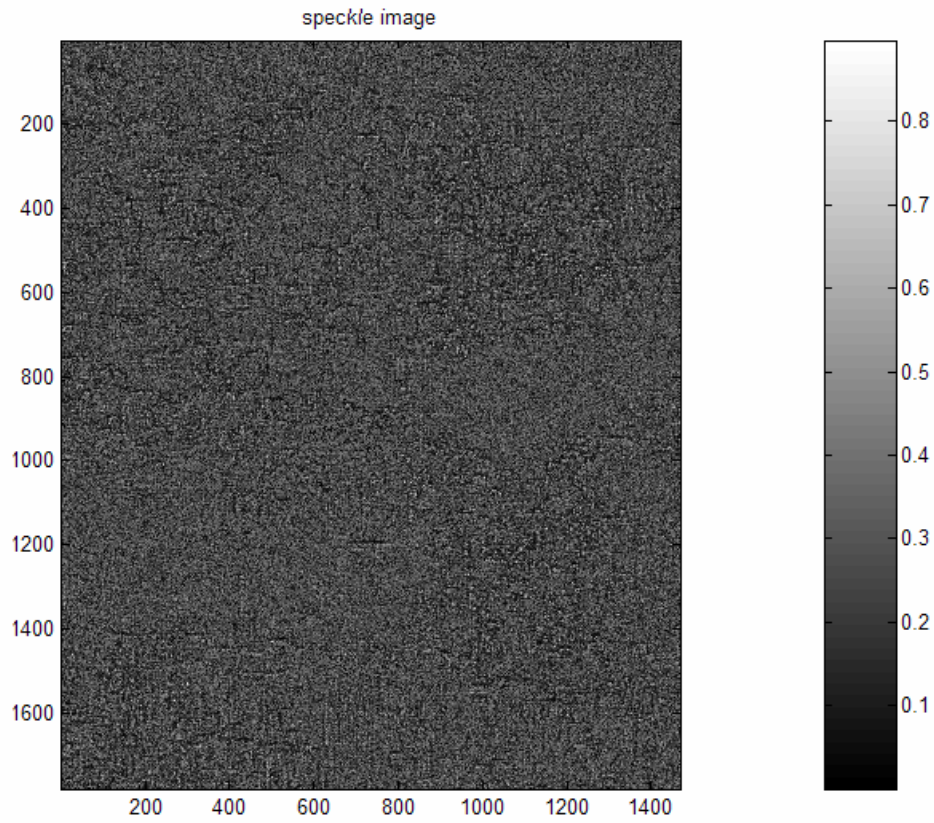


**Figure 1.98** - Image of speckle estimated by using matrixes  $10 \times 10$  without overlap.

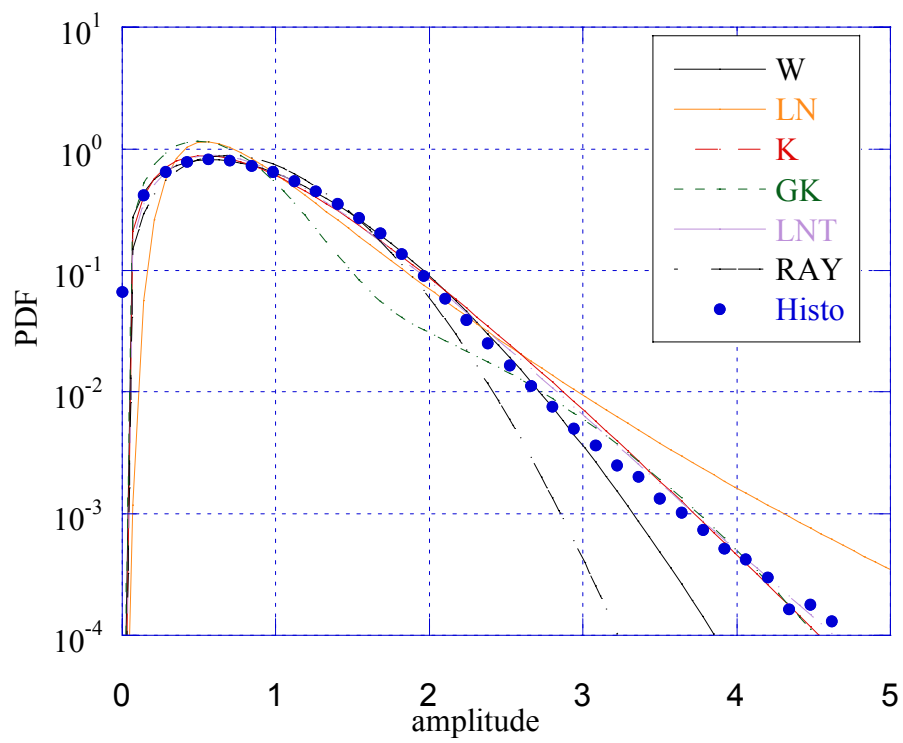


**Figure 1.99** - PDF of speckle estimated with matrix  $10 \times 10$ .



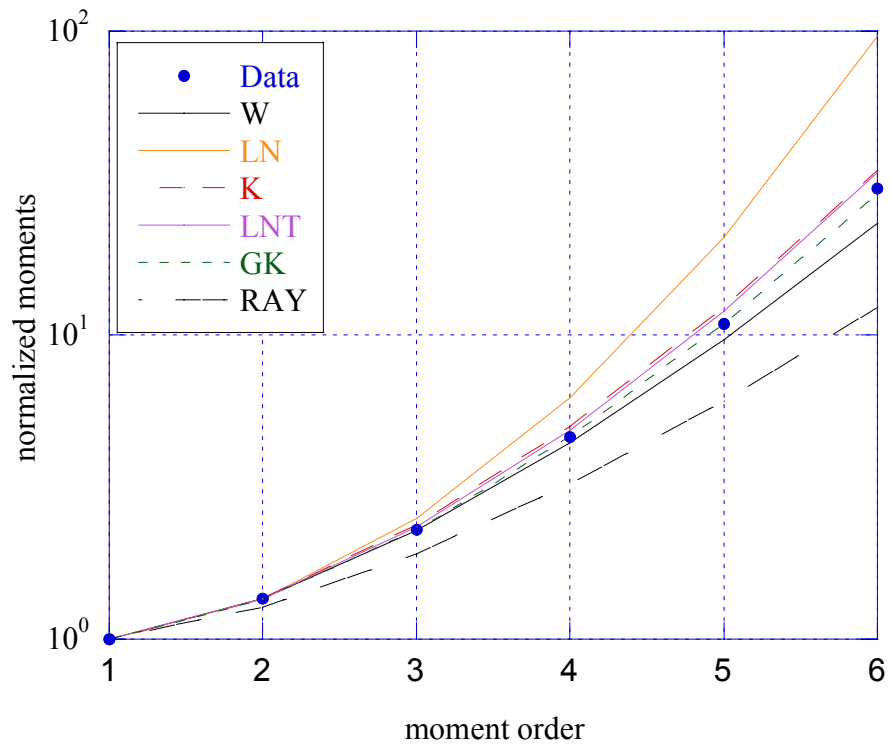


Figure 1.100 - Normalized moments of speckle estimated with matrix  $10 \times 10$ .

1784x1472	W	LN	K	GK	R	LNT
Prob	100 %	94 %	100 %	8 %	100 %	100 %
d	$2.71 \cdot 10^{-2}$	$7.40 \cdot 10^{-2}$	$2.25 \cdot 10^{-2}$	$17.70 \cdot 10^{-2}$	$4.30 \cdot 10^{-2}$	$1.76 \cdot 10^{-2}$

Table 1.25 - Results of KS test on the speckle (matrix  $10 \times 10$ ).

1784x1472	W	LN	K	GK	R	LNT
Prob	100 %	90 %	100 %	36 %	100 %	100 %
d	$2.92 \cdot 10^{-2}$	$12.82 \cdot 10^{-2}$	$2.22 \cdot 10^{-2}$	$18.14 \cdot 10^{-2}$	$6.73 \cdot 10^{-2}$	$2.27 \cdot 10^{-2}$

Table 1.26 - Results of Kuiper test on the speckle (matrix  $10 \times 10$ ).

Size of patch	Weibull		Lognormal		K		GK			R	LNT	
	$\hat{c}$	$\hat{b}$	$\hat{\delta}$	$\hat{\sigma}$	$\hat{\nu}$	$\hat{\mu}$	$\hat{\nu}$	$\hat{\mu}$	$\hat{b}$	$\hat{\sigma}^2$	$\hat{\sigma}^2$	$\hat{m}$
(1784x1472)	1.71	0.96	0.74	0.55	2.86	0.50	10.98	0.18	0.59	0.97	0.27	0.44

Table 1.27 Parameters estimate for the speckle (matrix  $10 \times 10$ ).

In the Table 1.27 we report the characteristic parameters values. Clearly the speckle is not Gaussian distributed.

In Figure 1.11 we report the image of despeckled texture (window  $10 \times 10$  without overlap). The structure of the wood is evident.

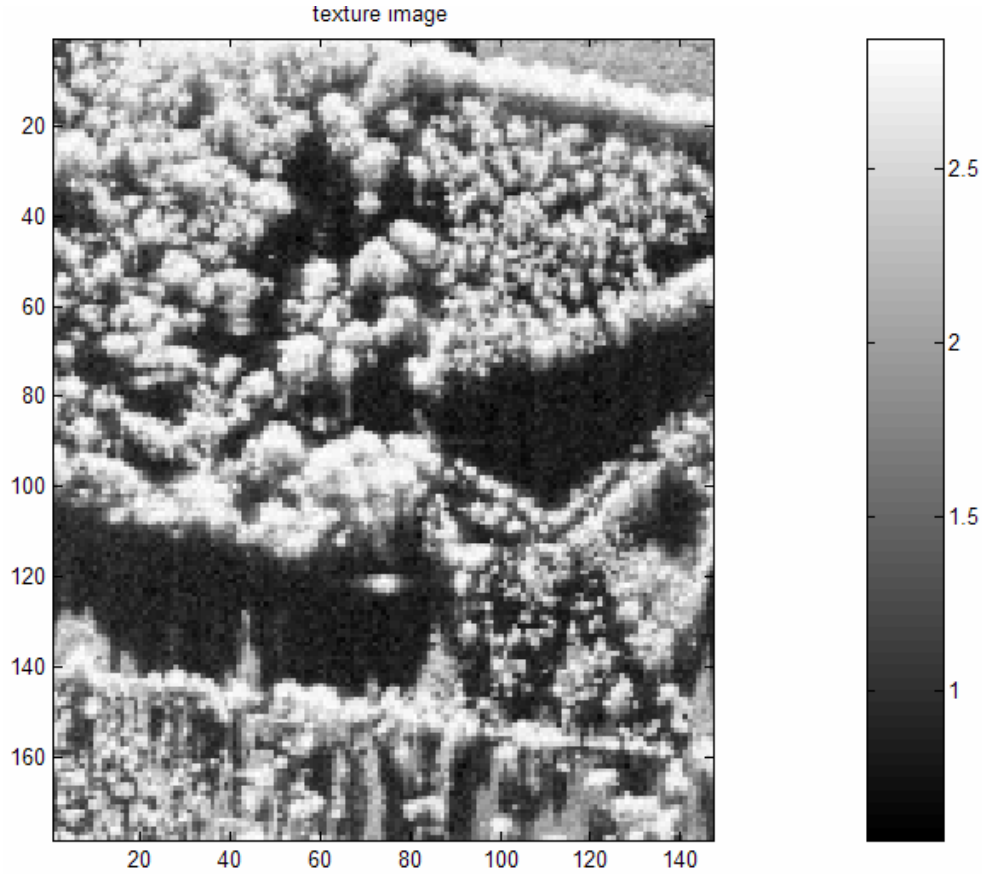


**Figure 1.101** - Image of texture estimated with a  $10 \times 10$  window without overlap.

We performed same estimation using also a 20-dimensional square window (instead of a 10-dimensional window), without overlap. The following figures report the obtained results.

From Figure 1.102, representing the estimated speckle, we can observe that there is again some residue of the texture, more evident than in Fig. 1.98.

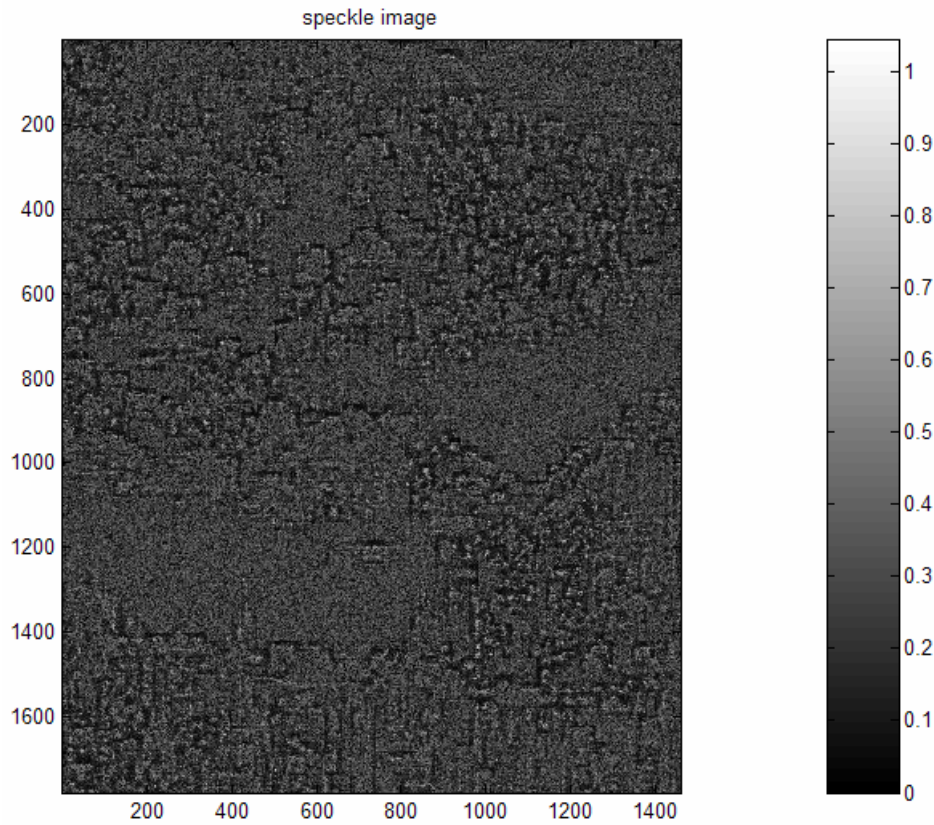


**Figure 1.102** - Image of speckle estimated by using matrices of  $20 \times 20$  elements without overlap.

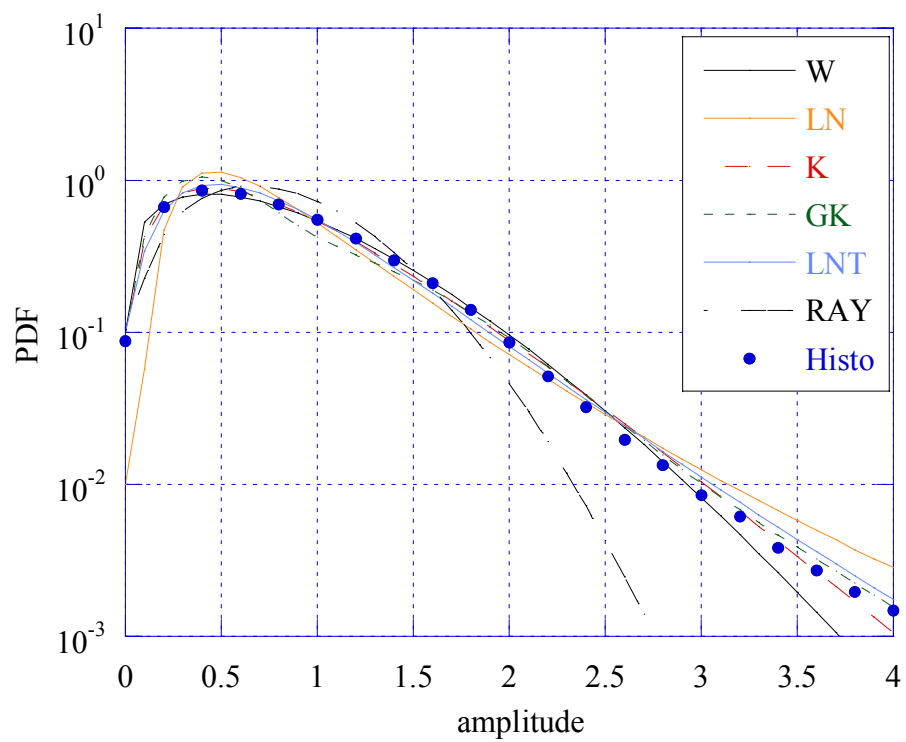


**Figure 1.103** - PDF of speckle estimated with matrix  $20 \times 20$  without overlap.

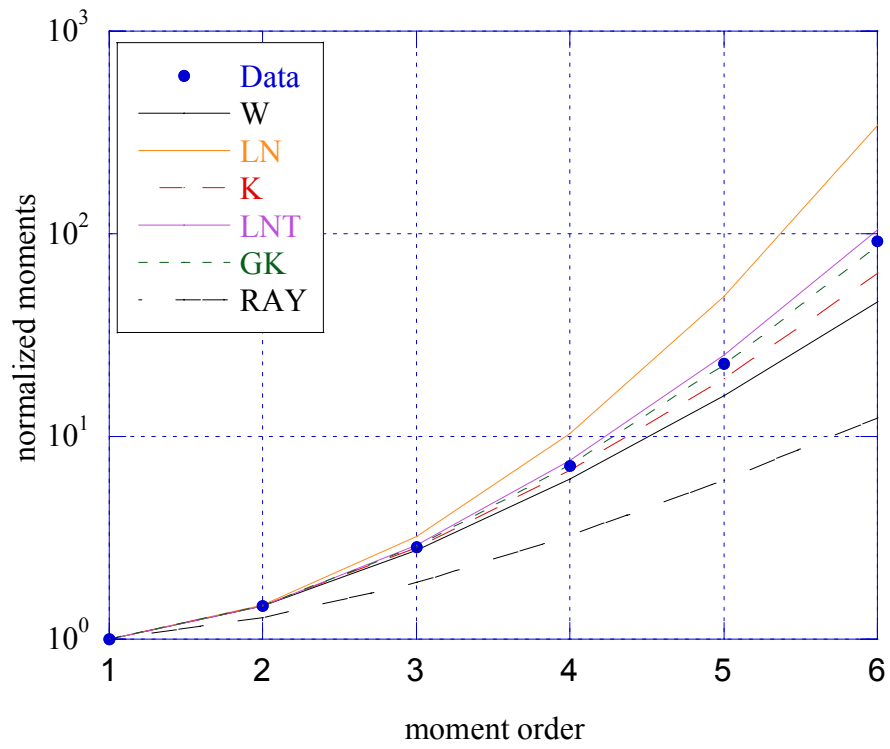


**Figure 1.104** - Normalized moments of speckle estimated with matrix  $20 \times 20$  without overlap

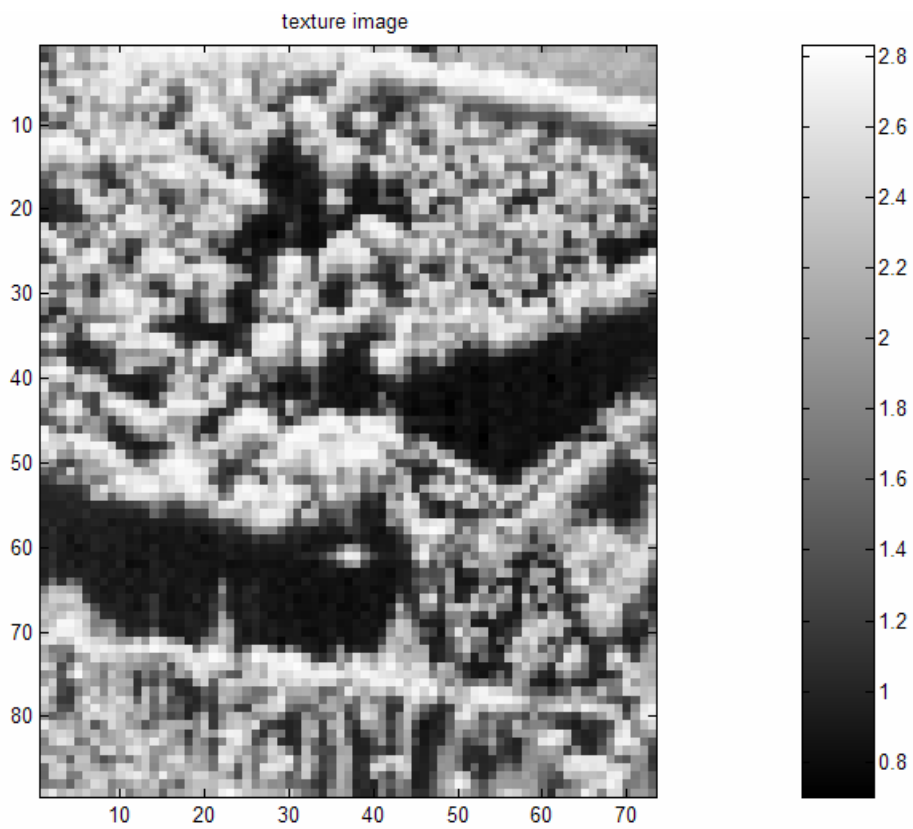


**Figure 1.105** - Image of texture estimated with matrix  $20 \times 20$  without overlap.

Size of patch	Weibull		Lognormal		K		GK			R	LNT	
	$\hat{c}$	$\hat{b}$	$\hat{\delta}$	$\hat{\sigma}$	$\hat{\nu}$	$\hat{\mu}$	$\hat{\nu}$	$\hat{\mu}$	$\hat{b}$	$\hat{\sigma}^2$	$\hat{\sigma}^2$	$\hat{m}$
(1784x1472)	1.49	0.91	0.68	0.62	1.74	0.50	69.25	$1.48 \times 10^{-10}$	0.16	0.93	0.57	0.38

**Table 1.28** - Parameters estimates for the speckle (matrices 20x20 without overlap).

1784x1472	W	LN	K	GK	R	LNT
Prob	100 %	98 %	100 %	99 %	89 %	100 %
d	$1.96 \cdot 10^{-2}$	$6.64 \cdot 10^{-2}$	$1.10 \cdot 10^{-2}$	$6.10 \cdot 10^{-2}$	$8.03 \cdot 10^{-2}$	$2.15 \cdot 10^{-2}$

**Table 1.29** - Results of KS test on the speckle (matrices 20x20 without overlap).

1784x1472	W	LN	K	GK	R	LNT
Prob	100 %	98 %	100 %	100 %	94 %	100 %
d	$2.39 \cdot 10^{-2}$	$11.03 \cdot 10^{-2}$	$1.46 \cdot 10^{-2}$	$7.31 \cdot 10^{-2}$	$12.20 \cdot 10^{-2}$	$2.66 \cdot 10^{-2}$

**Table 1.30** - Results of Kuiper test on the speckle (matrices 20x20 without overlap).

From Figure 1.103 we can observe that Weibull, K and LNT models are close to the histogram. The best fitting is given by K and LNT models. The results in Tables 1.29 and 1.30 of KS and Kuiper tests are in good agreement with the figure of PDFs.

We completed the statistical analysis for this file by estimating the histogram of the texture. To dispose of much more data, we decided to estimate again the texture using a 20-dimensional matrix but with an overlap of 95% in range and 95% in cross range. The new texture image is reported in Fig. 1.106. Fig. 1.107 and Fig. 1.108 show respectively the histogram and the estimated cumulative distribution function (CDF) of the texture of Fig. 1.106. It is evident that, after a peak for low values, the histogram drops almost linearly in the range [50, 560] then abruptly decreases for higher texture values.

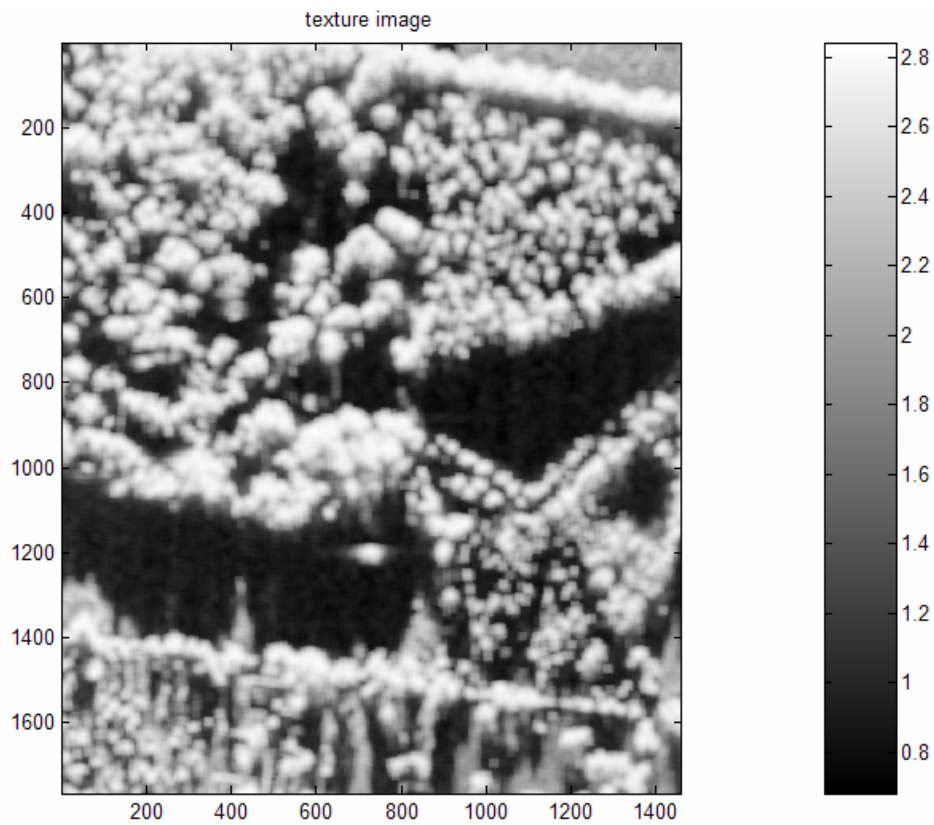


**Figure 1.106** - Texture image of HB06202 file (matrices  $20 \times 20$ , overlap 95%)

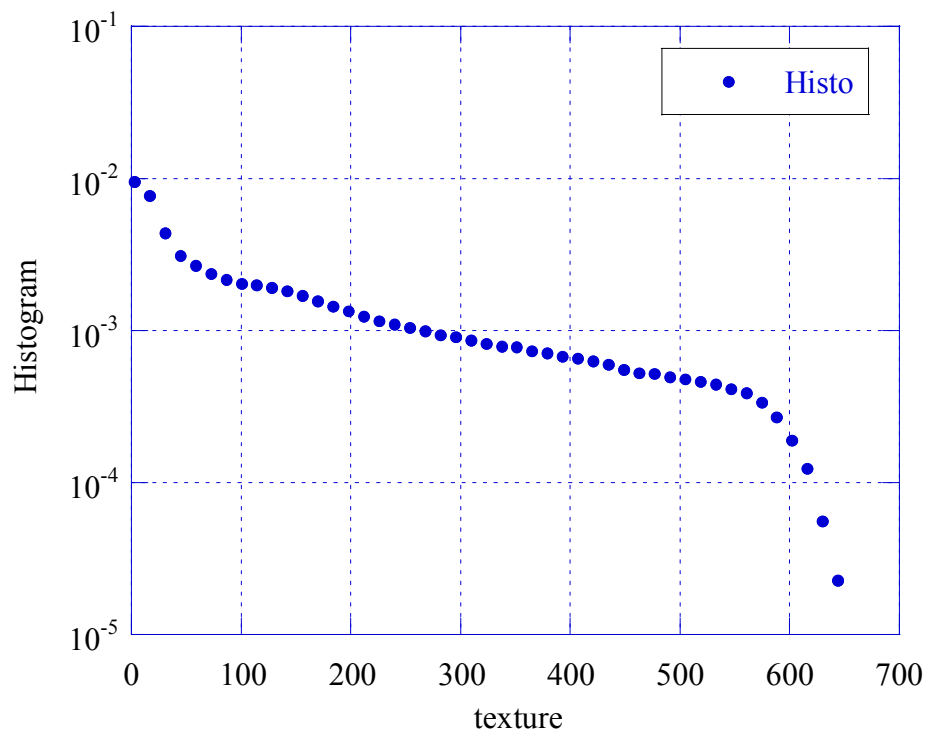


**Figure 1.107** - Texture histogram of HB06202 file ( $20 \times 20$ , overlap 95%).

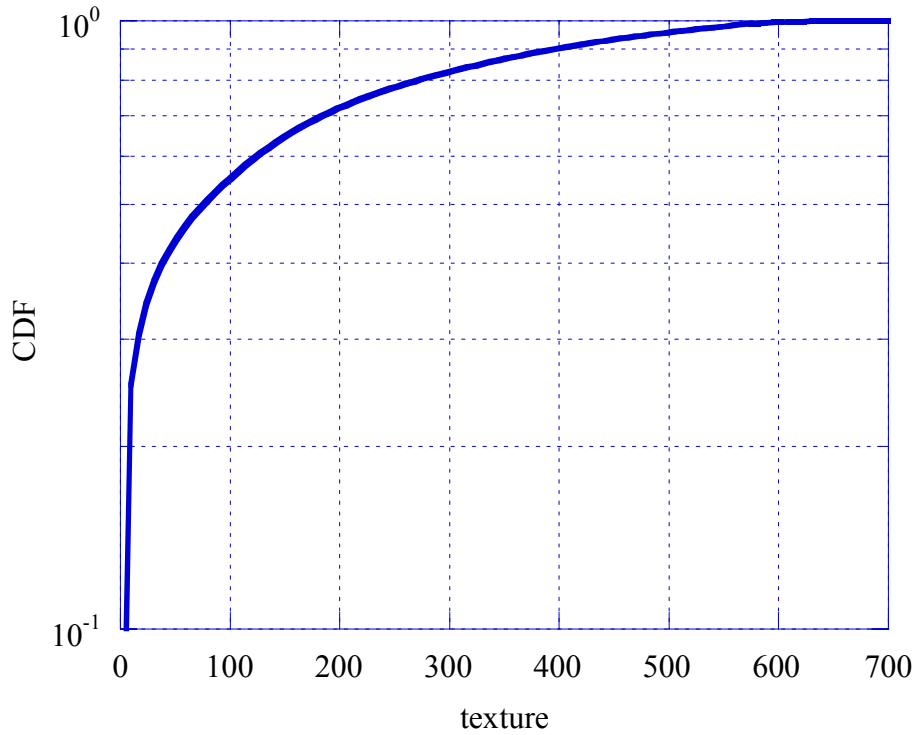


**Figure 1.108** Texture CDF of HB06202 file (matrixes  $20 \times 20$ , overlap 95%).

### 1.2.3 Statistic analysis of the patches of HB06202 file

We repeated similar analysis on three patches of the figures, for speckle and texture. For estimating the speckle we applied a  $20 \times 20$  matrix without overlap and for estimating the texture the same window but with and overlap of 95%.

The two patches in Figs. 1.109 and 1.115 depict shadowed areas, the patch in Fig. 1.121 and almost homogeneous wood.

The results of the statistical analysis are in the following figures. The texture histograms of the shadowed areas show a high peak for very low values of the texture and then an almost linearly decreasing tail for higher values. The behavior of the CDFs in Fig. 1.114 and 1.120 shows that 80 % of the texture values are lower than 20 (steep slope in the range  $[0, 20]$  followed by smooth rise in the range  $[20, 700]$ ). This trend is due to the low RCS of the shadowed areas.

On the contrary, Figs. 1.123 and 1.124, relating to the wood area, are similar to those of the overall image.



The speckle of the shadowed areas exhibits a good fitting with K, LNT and GK models but it is not spiky. As a matter of fact, the shape parameter of the K distribution, that is a measure of the non-Gaussianity, is greater than 2 (for spiky speckle  $\hat{\nu} < 2$ ).

Actually, we expected to find only thermal noise in the shadowed areas, that is, almost delta distributed texture and Rayleigh distributed speckle. The deviations from this model are maybe due to the presence of double-bounce scattering from the trees and also some white pixels in the patches originated by tree scattering.

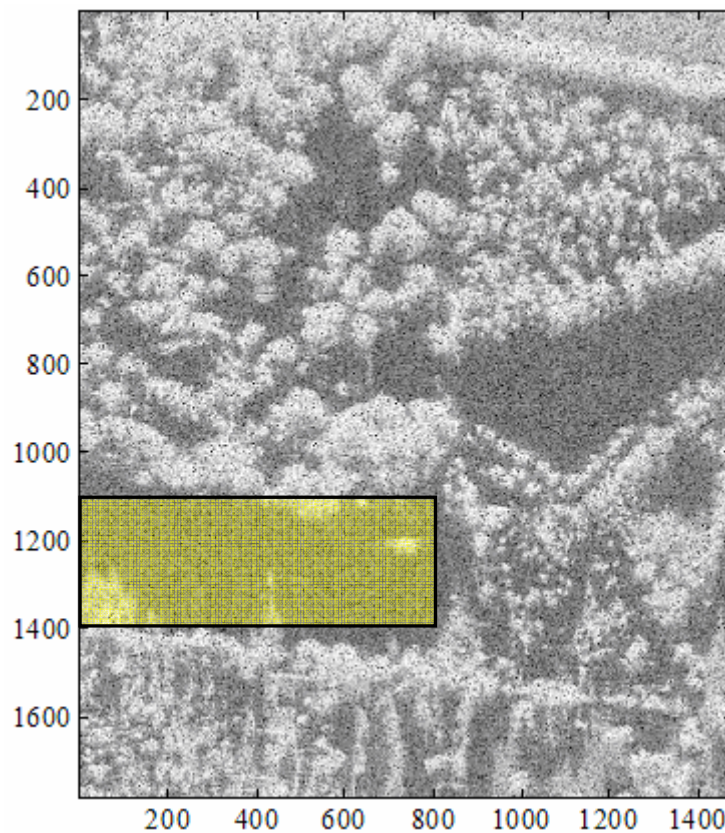


**Figure 1.109** - Image of the patch  $(1100,1400) \times (1,800)$ .



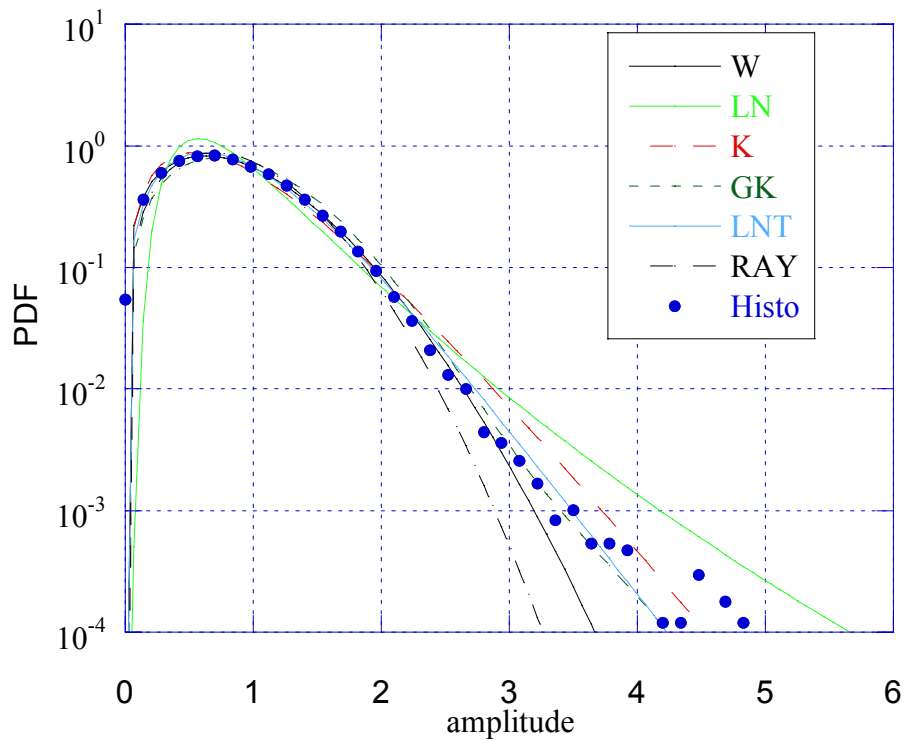


**Figure 1.110** - PDF of the speckle for the patch  $(1100,1400) \times (1,800)$ .

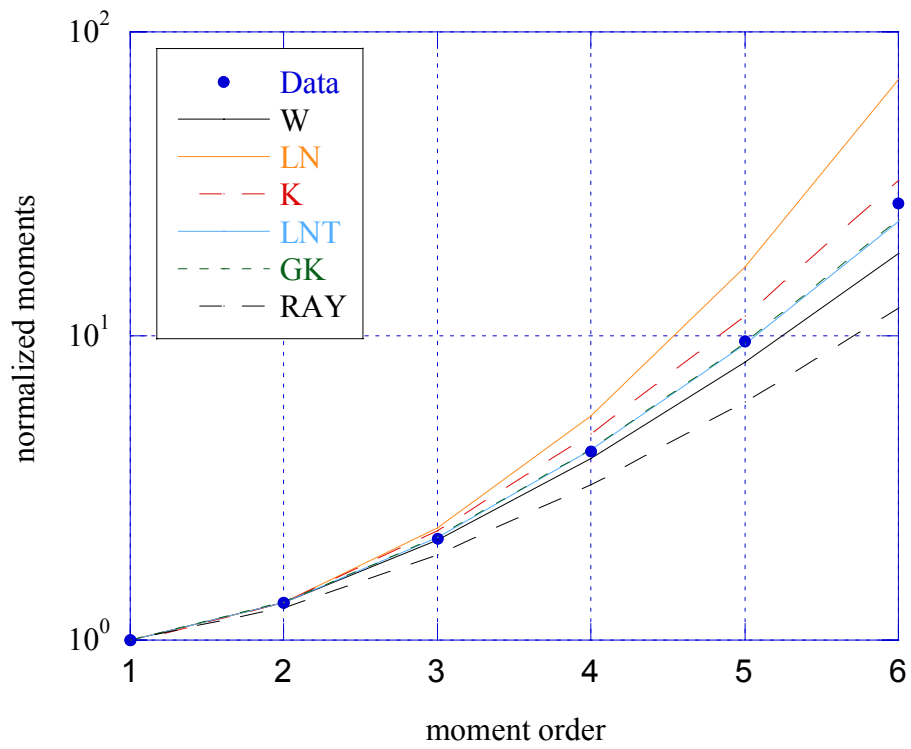


**Figure 1.111** - Normalized moments for the speckle of the patch  $(1100,1400) \times (1,800)$ .

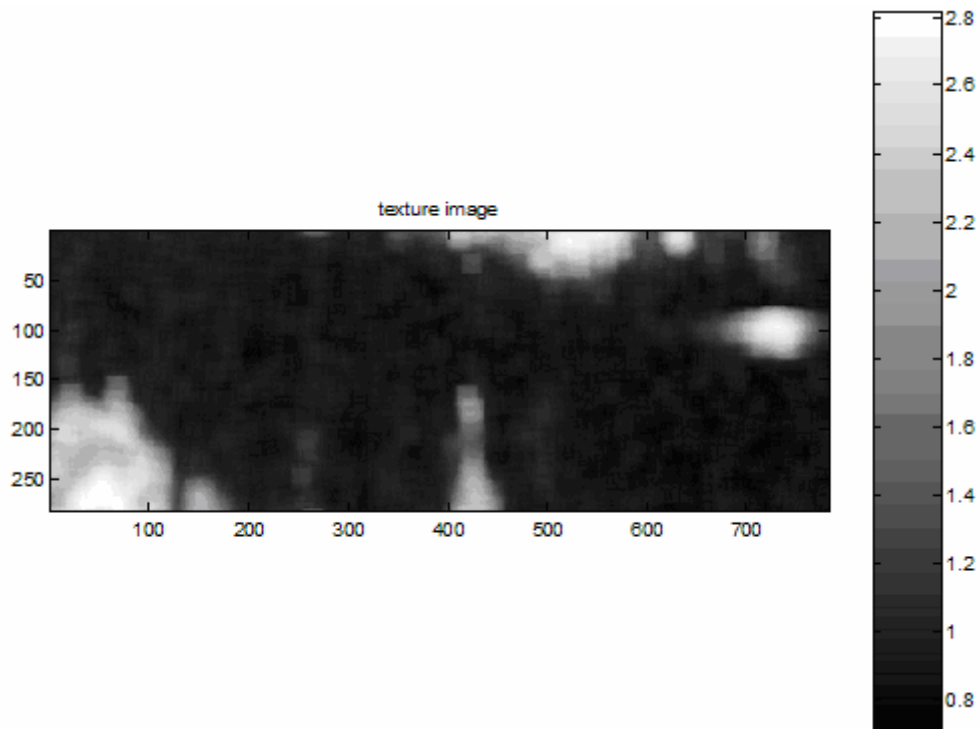


**Figure 1.112** - Texture of the patch  $(1100,1400) \times (1,800)$ .

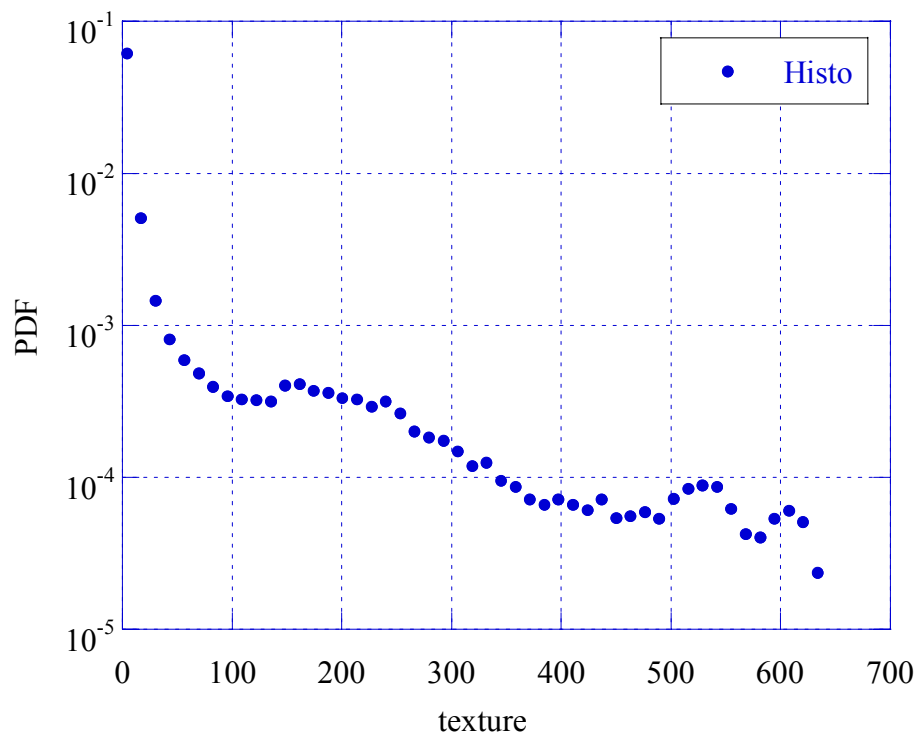


**Figure 1.113** - Texture PDF for the patch  $(1100,1400) \times (1,800)$

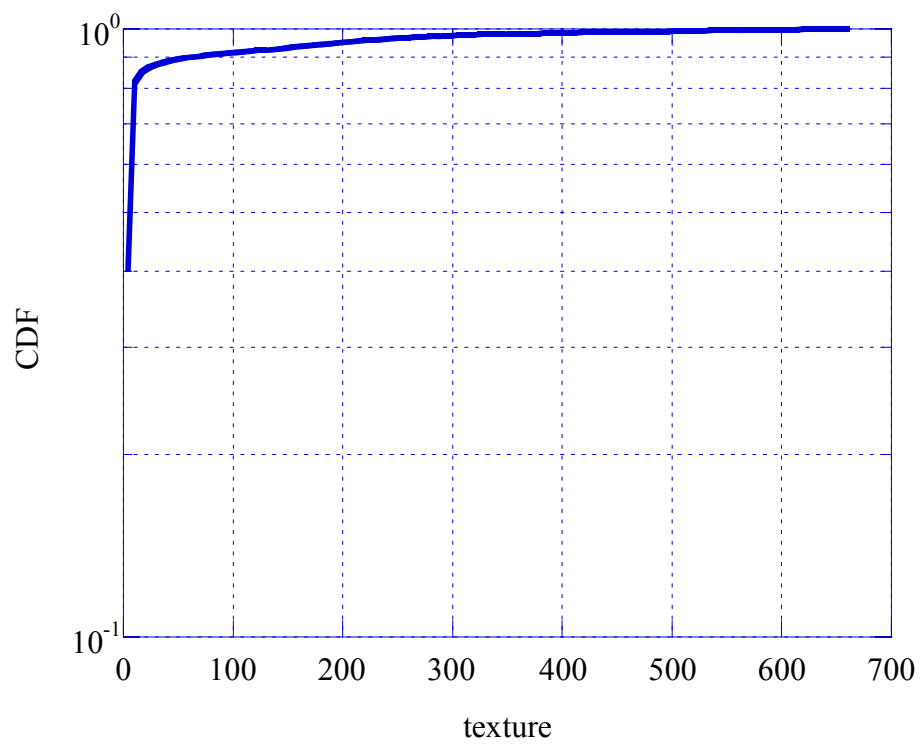


**Figure 1.114** - Texture CDF for the patch  $(1100,1400) \times (1,800)$

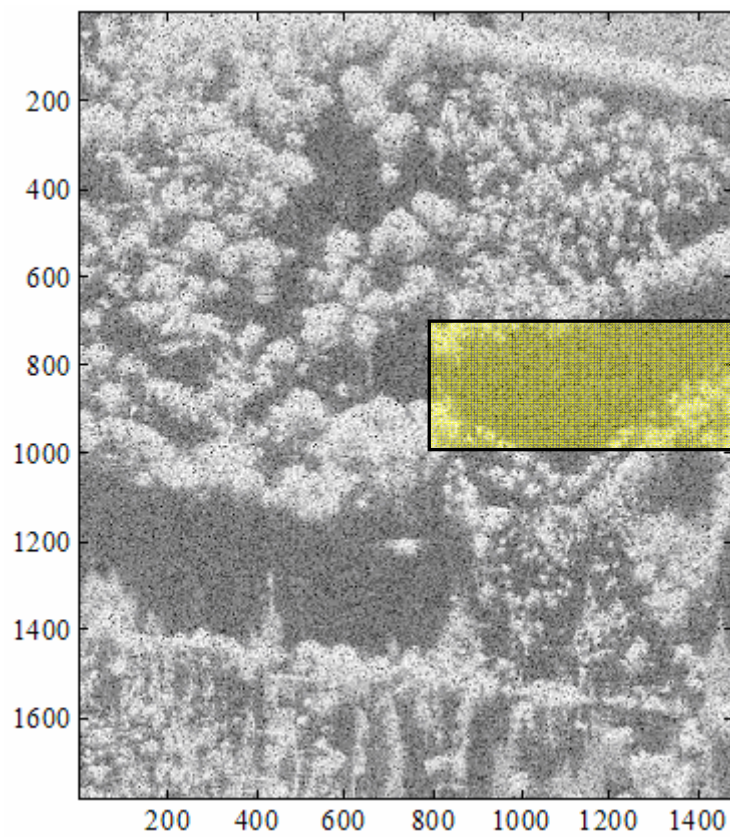


**Figure 1.115** - Image of the patch  $(700,1000) \times (800,1400)$ .

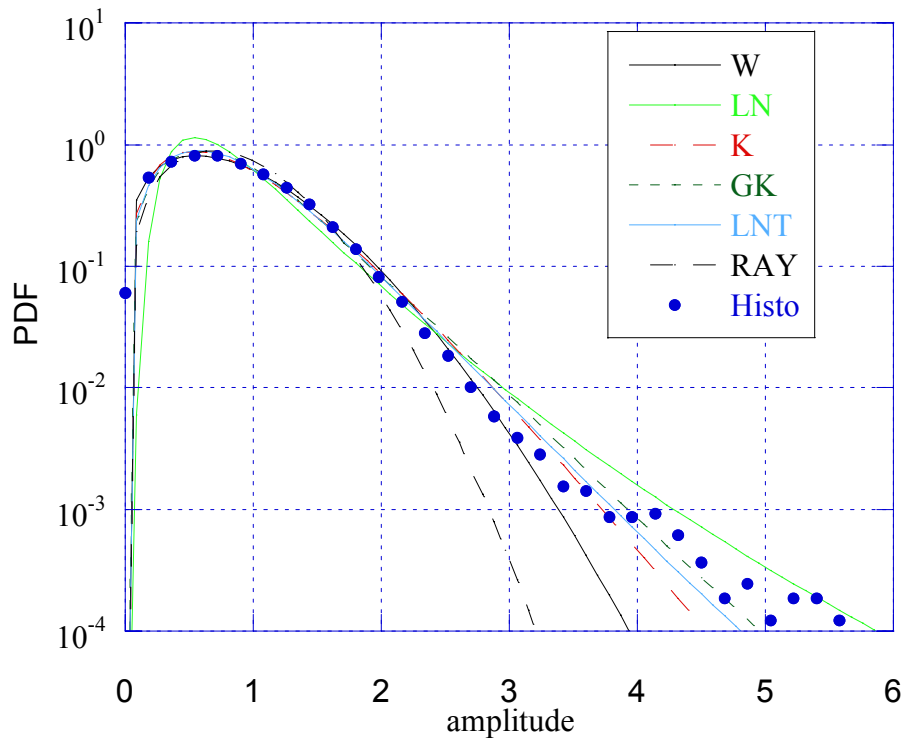


**Figure 1.116** - PDF of the speckle for the patch  $(700,1000) \times (800,1400)$ .

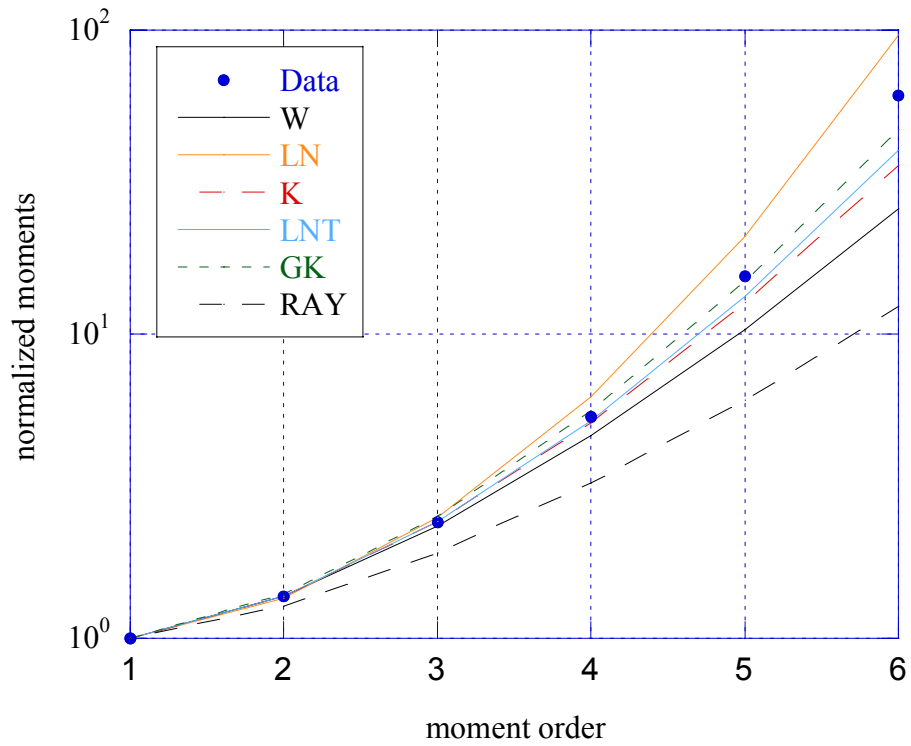


**Figure 1.117** - Normalized moments of the speckle of the patch  $(700,1000) \times (800,1400)$ .

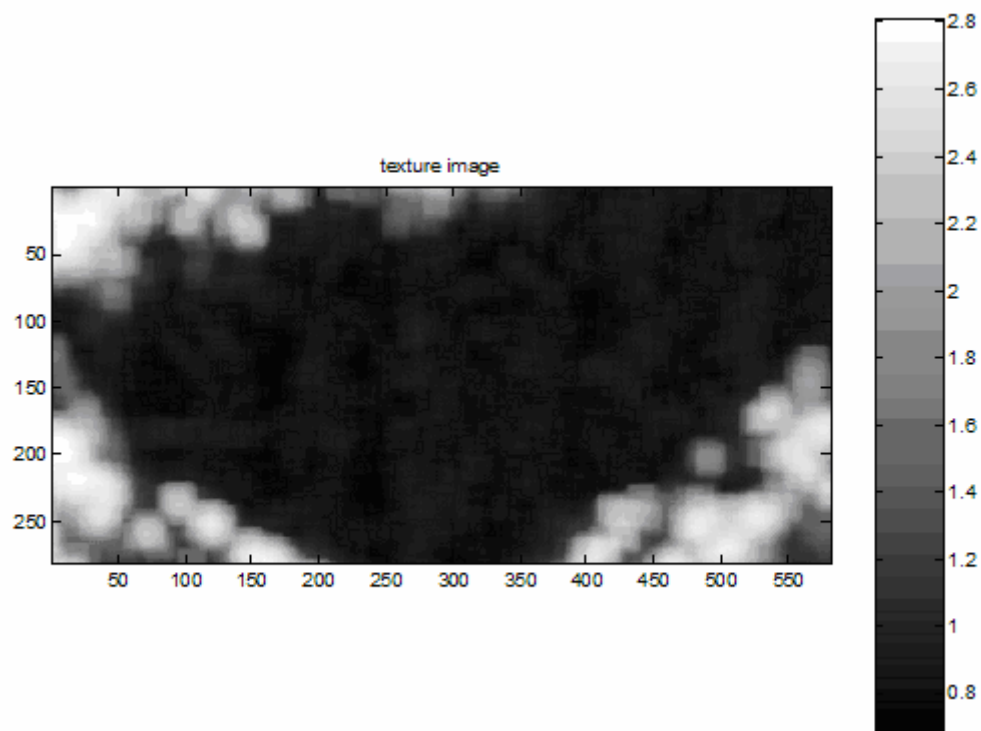


**Figure 1.118** - Texture image of the patch  $(700,1000) \times (800,1400)$ .

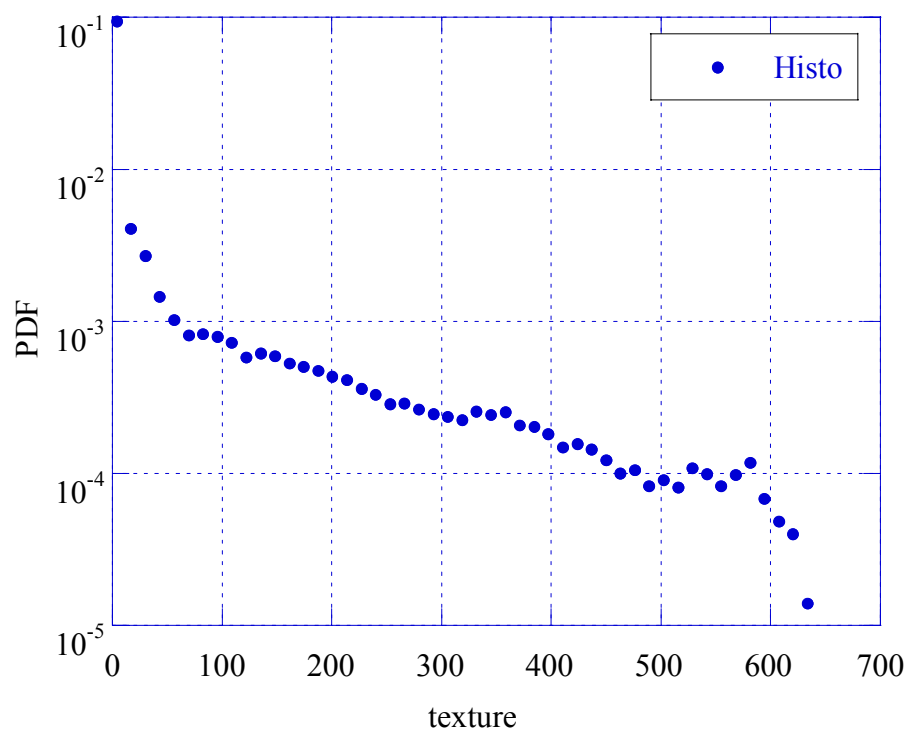


**Figure 1.119** - Texture PDF of the patch  $(700,1000) \times (800,1400)$

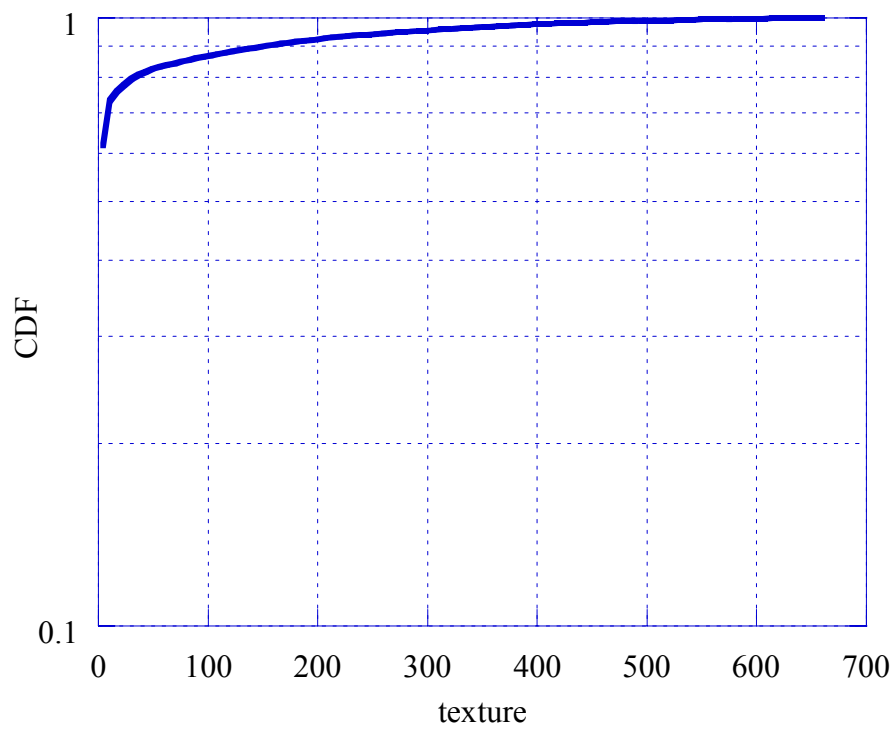


**Figure 1.120** - Texture CDF of the patch  $(700,1000) \times (800,1400)$

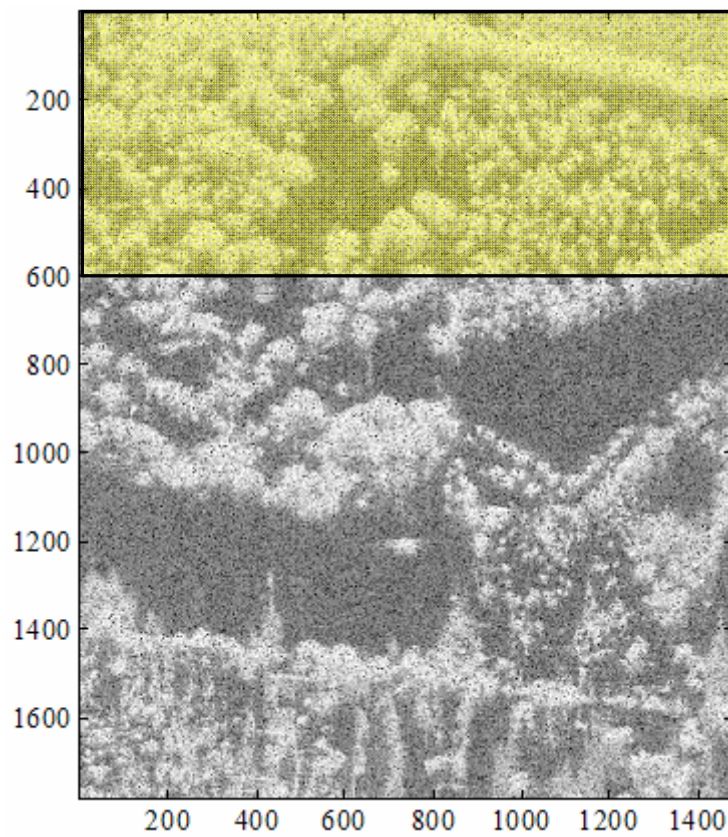


**Figure 1.121** - Image of the patch  $(1,600) \times (1,1478)$ .

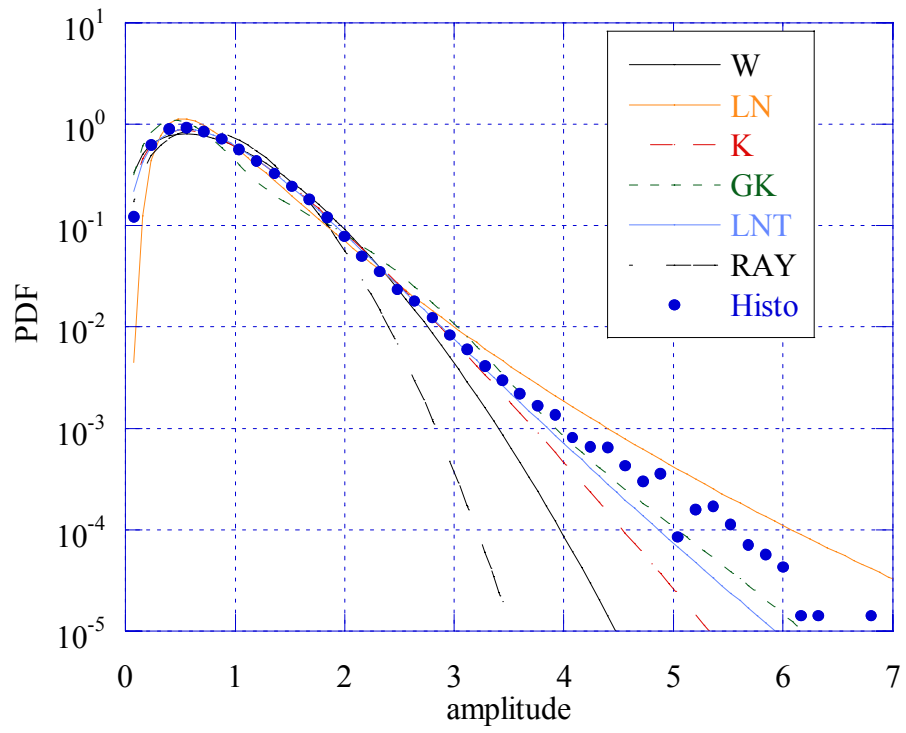


**Figure 1.122** - PDF of the speckle of the patch  $(1,600) \times (1,1478)$

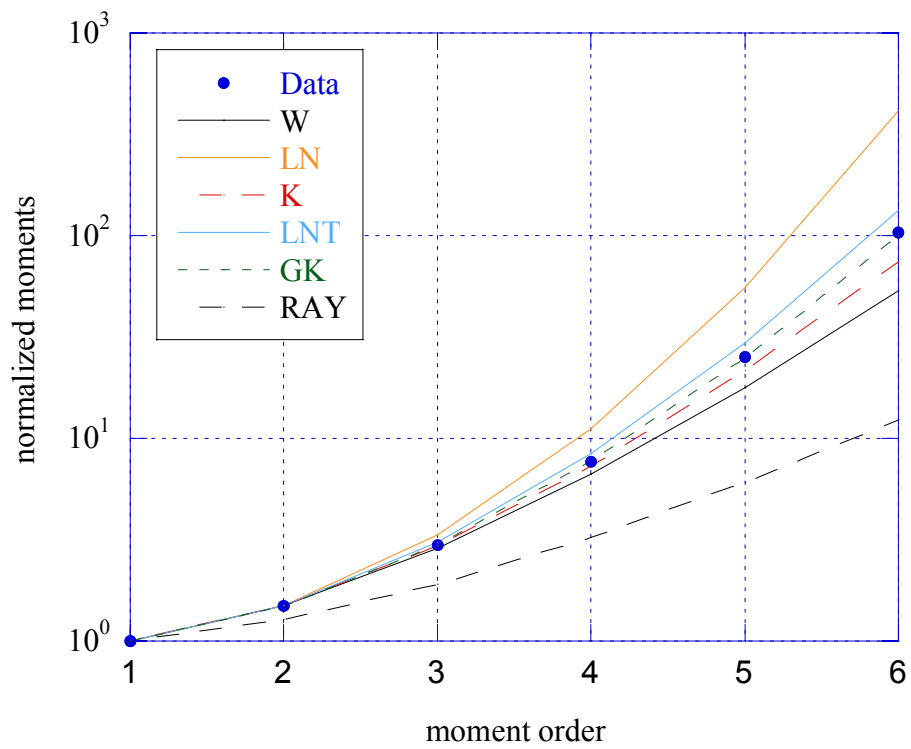


**Figure 1.123** - Normalized moments for the speckle of the patch  $(1,600) \times (1,1478)$

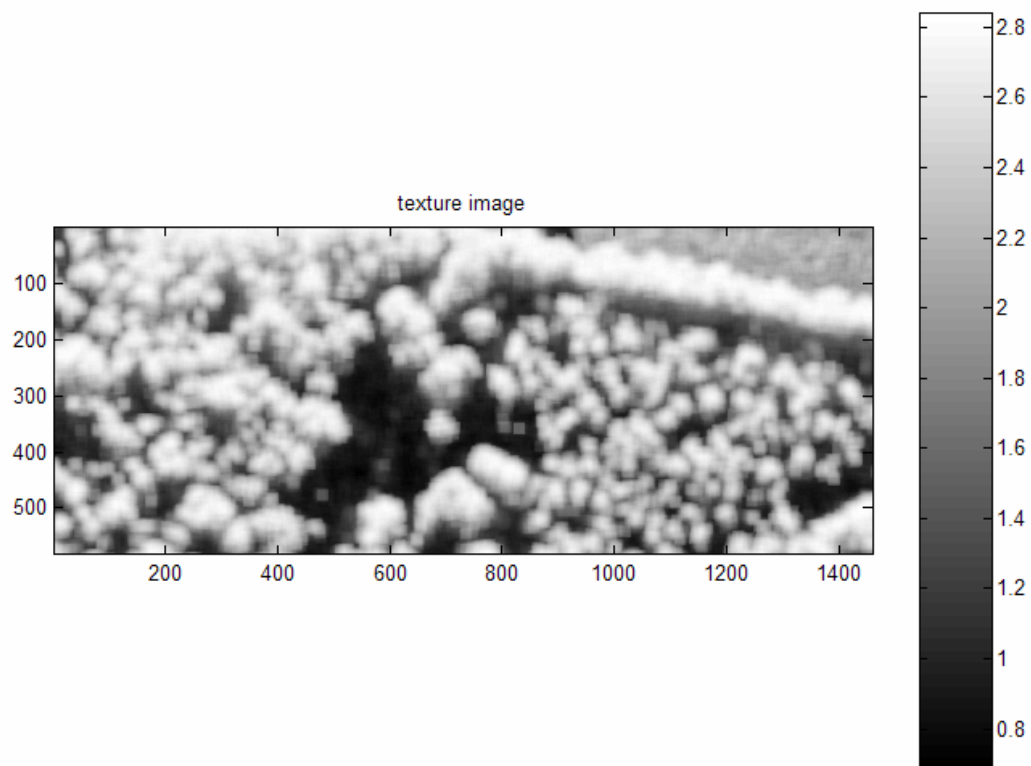


**Figure 1.124** - Texture image of the patch  $(1,600) \times (1,1478)$ .

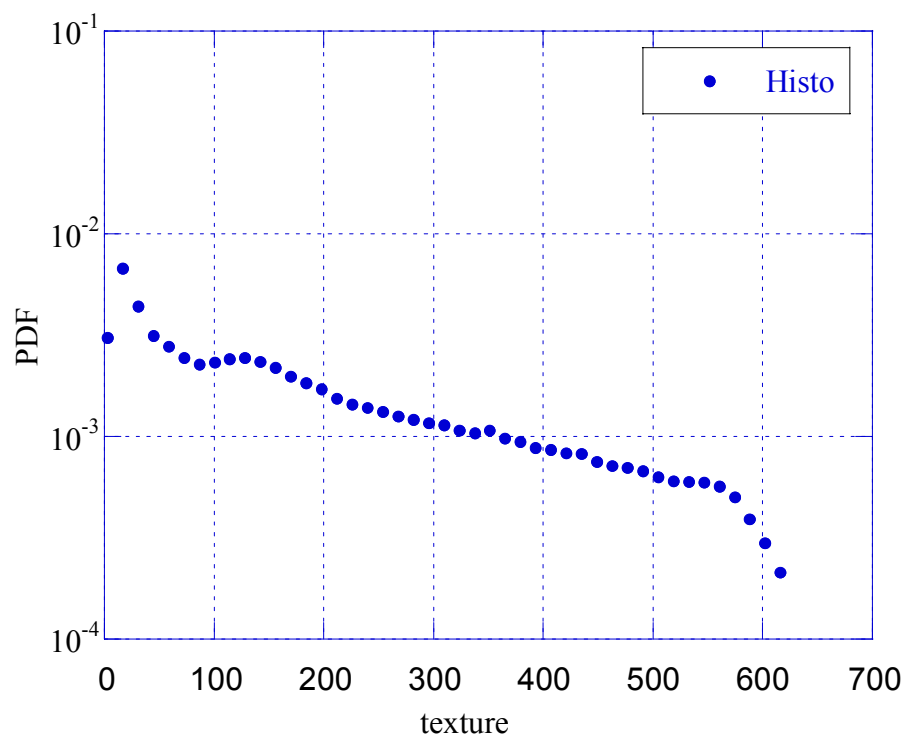


**Figure 1.125** - Texture PDF of the patch  $(1,600) \times (1,1478)$



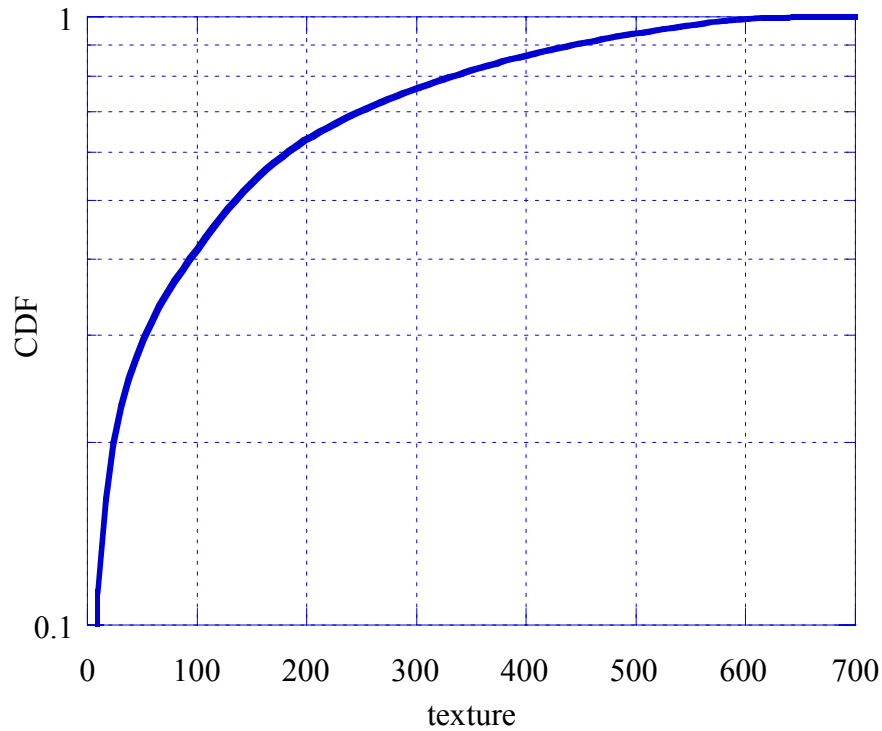


**Figure 1.126** - Texture CDF of the patch  $(1,600) \times (1,1478)$

Patch size	W		LN		K		GK			R	LNT	
	$\hat{c}$	$\hat{b}$	$\hat{\delta}$	$\hat{\sigma}$	$\hat{\nu}$	$\hat{\mu}$	$\hat{\nu}$	$\hat{\mu}$	$\hat{b}$	$\hat{\sigma}^2$	$\hat{\sigma}^2$	$\hat{m}$
(1100,1400)x (800,1400)	1.80	0.97	0.75	0.53	2.86	0.50	79.25	$2.65 \cdot 10^{-6}$	0.26	0.98	0.18	0.46
(700,1000)x(1,1478)	1.67	0.95	0.73	0.55	2.86	0.50	69.81	$1.74 \cdot 10^{-8}$	0.19	0.96	0.31	0.43
(1,600)x(1,1478)	1.45	0.90	0.67	0.63	1.56	0.50	32.36	$2.60 \cdot 10^{-6}$	0.22	0.93	0.63	0.36

**Table 1.31** Parameters of models utilized for the speckle analysis of HB06202 file.

Following the method previously described for the dense vegetation file, we analyzed also speckle and texture of the grass field file HB06171, looking for another confirm of the Gaussian-compound model.

In the following figures we report the speckle image, PDF and moments for estimated speckle and texture, relating to the whole image of the HB06171 file. The speckle histogram show a good fitting with the Weibull model whose estimated shape parameter is  $c=1.7$  (almost Rayleigh distributed) and the texture histogram with generalized Gamma PDF. These

results are in good agreement with those obtained for the clutter amplitude model. The compound-Gaussian model is a good candidate to fit the grass field clutter.

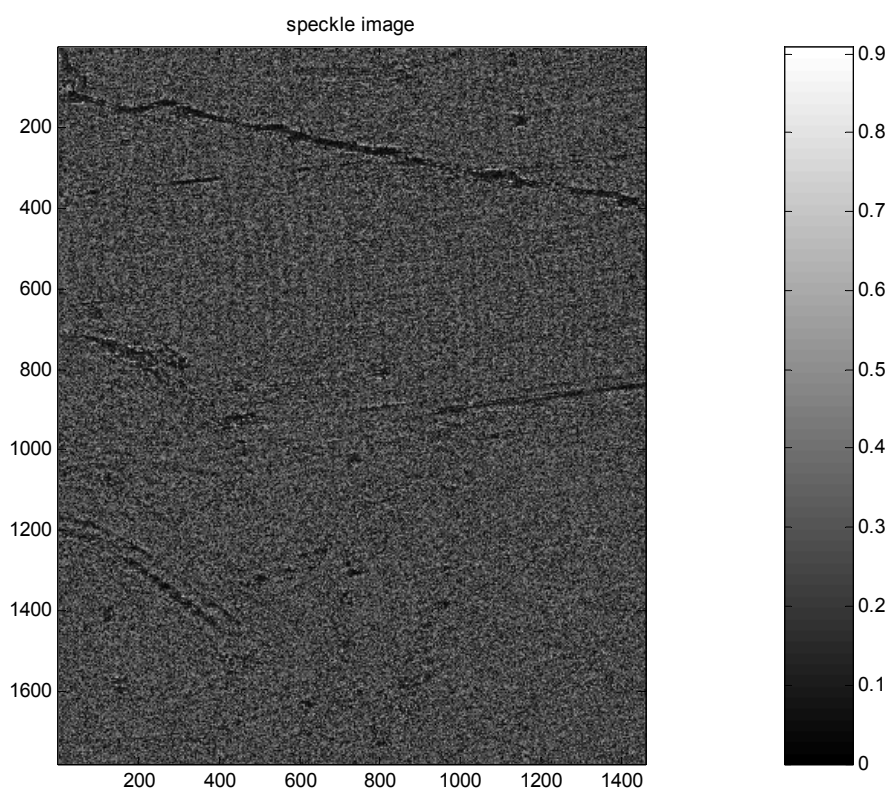


**Figure 1.127** - Image of the speckle of file HB06171.

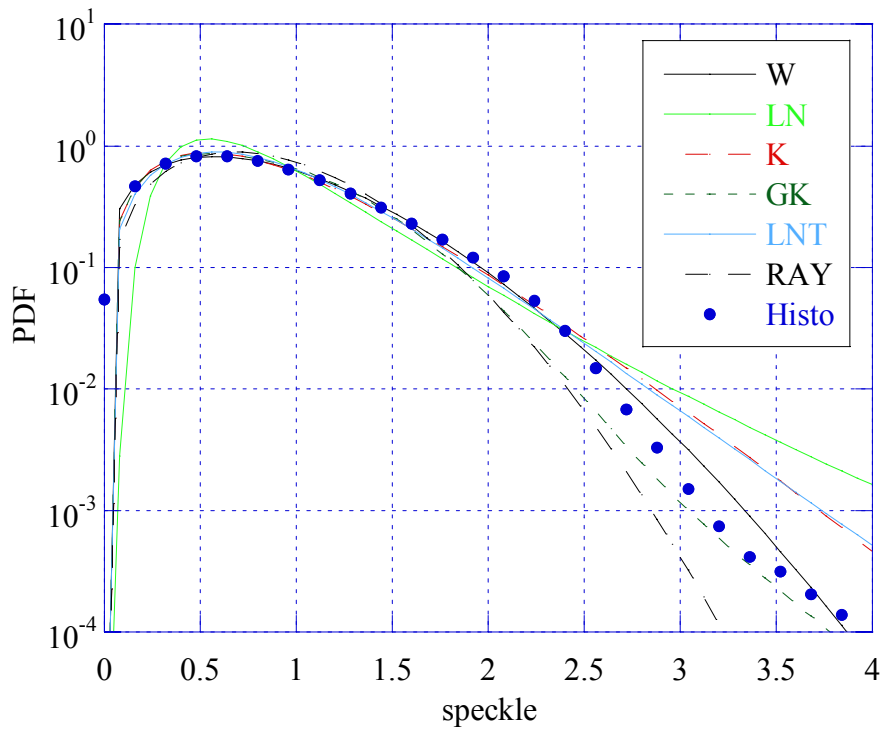


**Figure 1.128** - PDF of speckle for the file HB06171 (matrices  $20 \times 20$  without overlap)

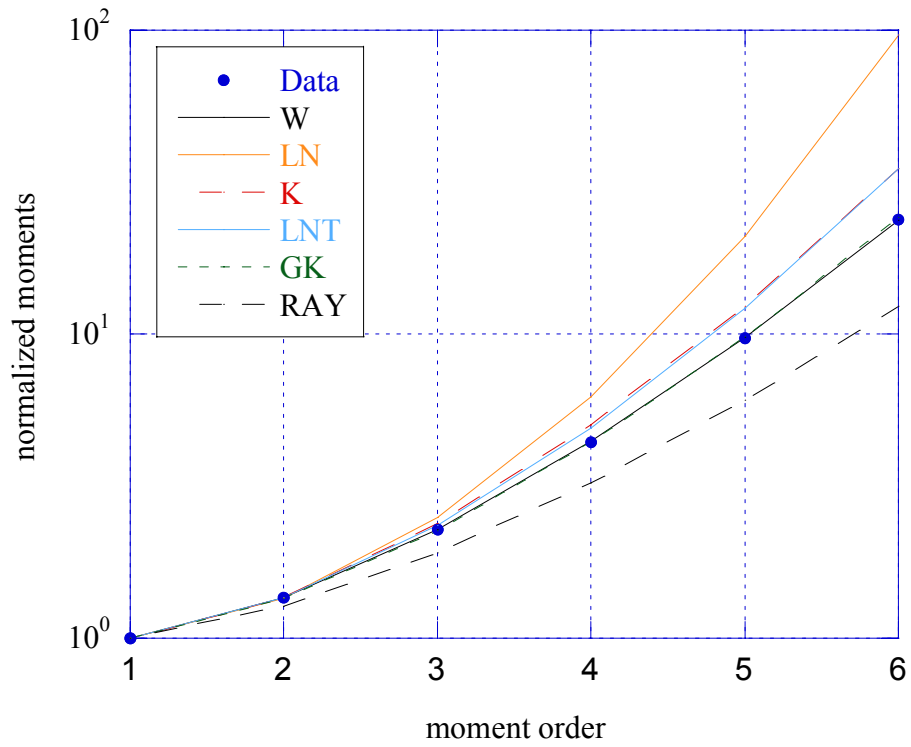


**Figure 1.129** - Normalized moments of the speckle for the file HB06171.

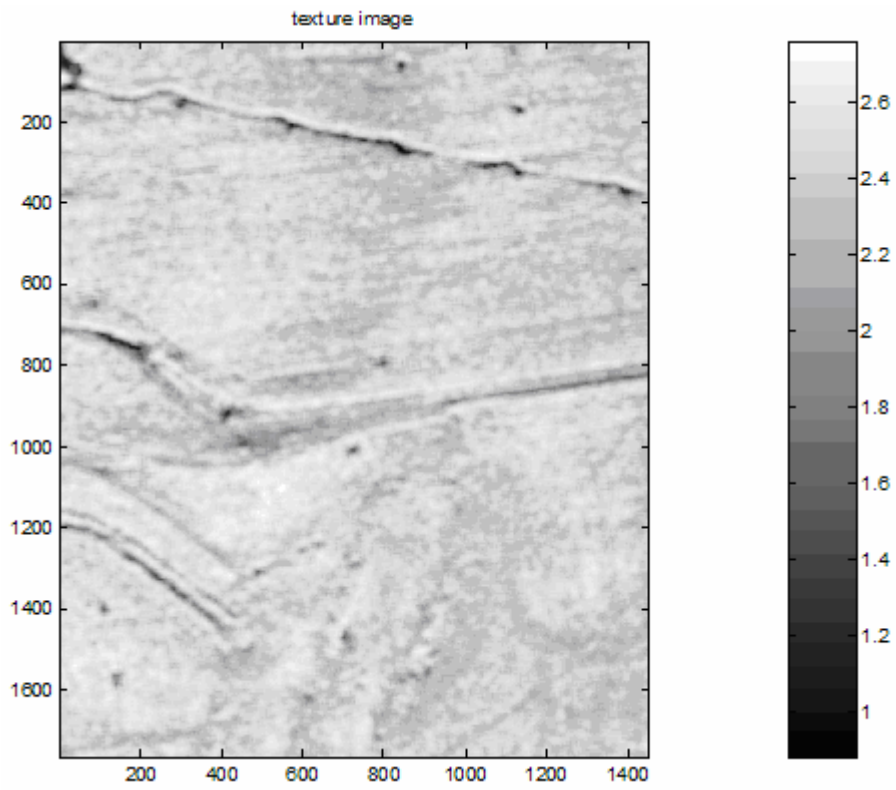


**Figure 1.130** - Image of the texture of the file HB06171.

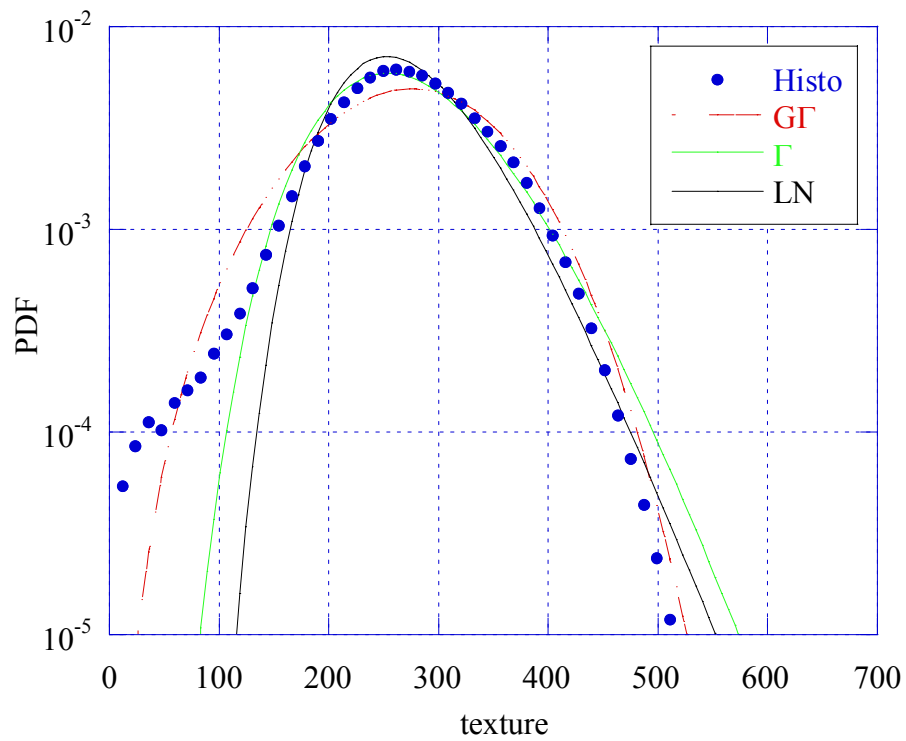


**Figure 1.131** - PDF of texture of the file HB06171

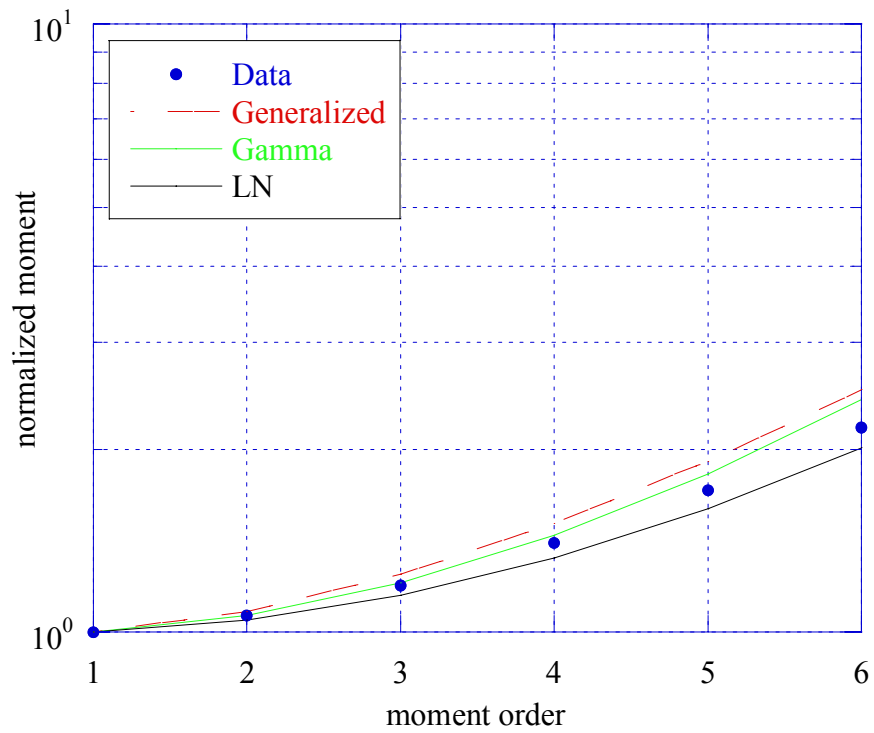


**Figure 1.132** - Normalized moments of the texture for the file HB06171.

Image size	W		LN		K		GK			R	LNT	
	$\hat{c}$	$\hat{b}$	$\hat{\delta}$	$\hat{\sigma}$	$\hat{\nu}$	$\hat{\mu}$	$\hat{\nu}$	$\hat{\mu}$	$\hat{b}$	$\hat{\sigma}^2$	$\hat{\sigma}^2$	$\hat{m}$
(1784x1472)	1.70	0.96	0.74	0.55	2.86	0.50	0.51	0.75	2.64	0.97	0.28	0.44

**Table 1.32** - Parameter values for the speckle of the file HB06171.

Image size	$\hat{\mu}$ $\Gamma$		G $\Gamma$			LN	
	$\hat{\mu}$	$\hat{\nu}$	$\hat{\nu}$	$\hat{\mu}$	$\hat{b}$	$\hat{\delta}$	$\hat{\sigma}$
(1784x1472)	17.74	15.28	1.05	294.88	2.77	264.85	0.22

**Table 1.33** Parameters of the texture for the file HB06171.

## 1.2.4 Conclusions

We performed a statistical analysis on clutter amplitude, texture and speckle scattered by grass fields and woods. Based on our results we can conclude that the compound-Gaussian model presents a good fitting with the data relating to the grass. These results are confirmed

by amplitude and both texture and speckle histograms. The speckle is Rayleigh distributed and, the texture Gamma,  $G\Gamma$  or LN distributed.

On the contrary the compound-Gaussian model fails in fitting the wood clutter. None of the tested model shows a good agreement with the amplitude and texture histograms, and the speckle is clearly heavy tailed (non-Rayleigh distributed).

## CHAPTER 2

# FREQUENCY ANALYSIS

In this chapter we show the results of the frequency analysis carried out on the MSTAR data. The power spectral density (PSD) of the data has been estimated by means of the weighted periodogram, defined as:

$$S(e^{j\omega}) = \frac{\frac{1}{N} \left| \sum_{n=0}^{N-1} w(n)x(n)e^{-j\omega n} \right|^2}{\frac{1}{N} \sum_{n=0}^{N-1} |w(n)|^2} \quad (2.1)$$

where  $x(n)$  is the  $n$ th element of the data vector  $\mathbf{x}$  and  $\mathbf{w}$  is the weighting window. In our case  $N=2048$  and  $\mathbf{w}$  is a rectangular window with unitary amplitude.

The autocorrelation function can be estimated indirectly, as the inverse Fourier transform of the PSD, or directly from the data, as:

$$\hat{R}_x(m) = \frac{1}{N - |m|} \sum_{n=0}^{N-1-|m|} x(n)x^*(n+m) \quad (2.2)$$

where  $m$  is the time or space lag and the symbol  $*$  stands for the complex conjugate.

Similarly, we can estimate the autocovariance function as:

$$\hat{C}_x(m) = \frac{1}{N - |m|} \sum_{n=0}^{N-1-|m|} (x(n) - \hat{\eta}_x)(x(n+m) - \hat{\eta}_x)^* \quad (2.3)$$

where  $\hat{\eta}_x = N^{-1} \sum_{n=0}^{N-1} x(n)$  is the estimated mean value of data vector  $\mathbf{x}$ .

## 2.1 Frequency analysis of grass field clutter

### 2.1.1 HB06171 File

We consider first the image of Figure 1.1, showing a homogeneous grass field, where there is not shadowing effect. We estimated on the amplitude, texture and speckle of the overall image both autocovariance and autocorrelation functions, then we repeated same analysis on the patch (893,1784)x(1,1472) of Figure 1.9.

To estimate the correlations and the covariances we applied eqs. (2.2) and (2.3) respectively first on each row (cross-range) and then on each column (range) of the image. To obtain the final correlation and autocovariance function in range and cross-range we averaged all the estimated functions in range (rows) and in cross-range (columns), that is

$$\tilde{R}_x(m) = \frac{1}{K} \sum_{k=1}^K \hat{R}_{xk}(m) \text{ and } \tilde{C}_x(m) = \frac{1}{K} \sum_{k=1}^K \hat{C}_{xk}(m) \quad (2.3)$$

where  $K$  is the number of rows or columns of the image and  $\hat{R}_{xk}$ ,  $\hat{C}_{xk}$  are the estimated correlation and covariance relating to the  $k$ th row or column.

In the figures 2.1-2.12 we report all the results we obtained. Figures 2.1, 2.2 and 2.3 represent the autocovariance for speckle, texture and data amplitude respectively. We can observe that the speckle and data amplitude are almost white (delta-correlated), texture autocovariance presents a smoother slope than speckle and amplitude. Figures 2.4, 2.5 and 2.6 relate to the cross-range direction and they show a trend similar to that of the range direction. We notice that, generally, along the range direction, the decreasing of the covariance is faster than along the cross-range direction. This is due to the decorrelation effect introduced by the shadow that is heavier in the illumination direction than in the orthogonal direction.

In the figures the autocovariance functions have been normalized with respect to their maximum value.



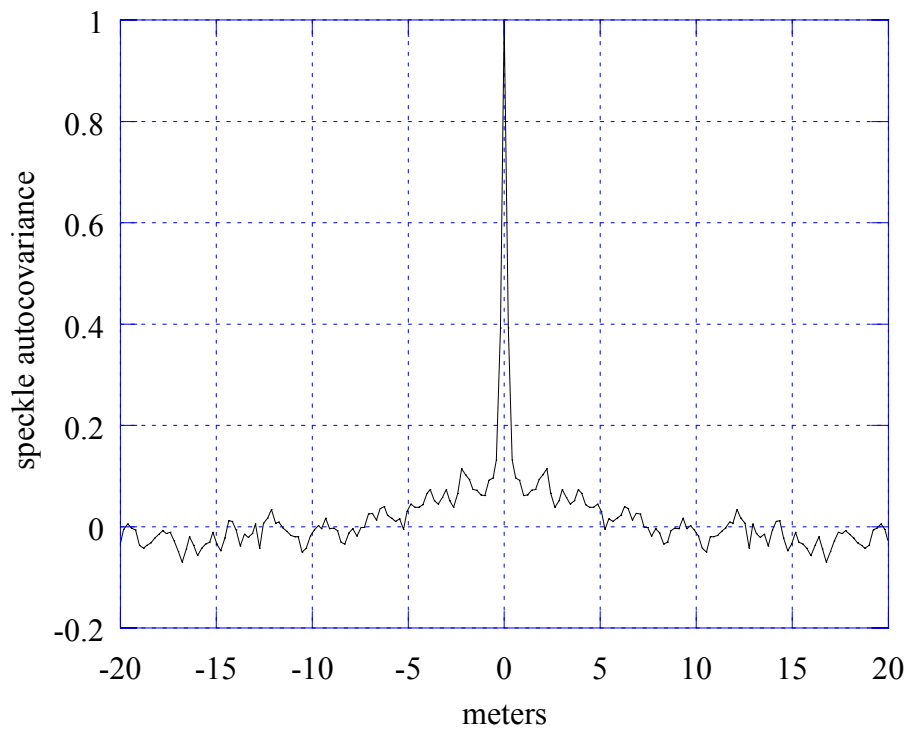


**Figure 2.1** - Range autocovariance of the speckle for the whole image (1784x1472).

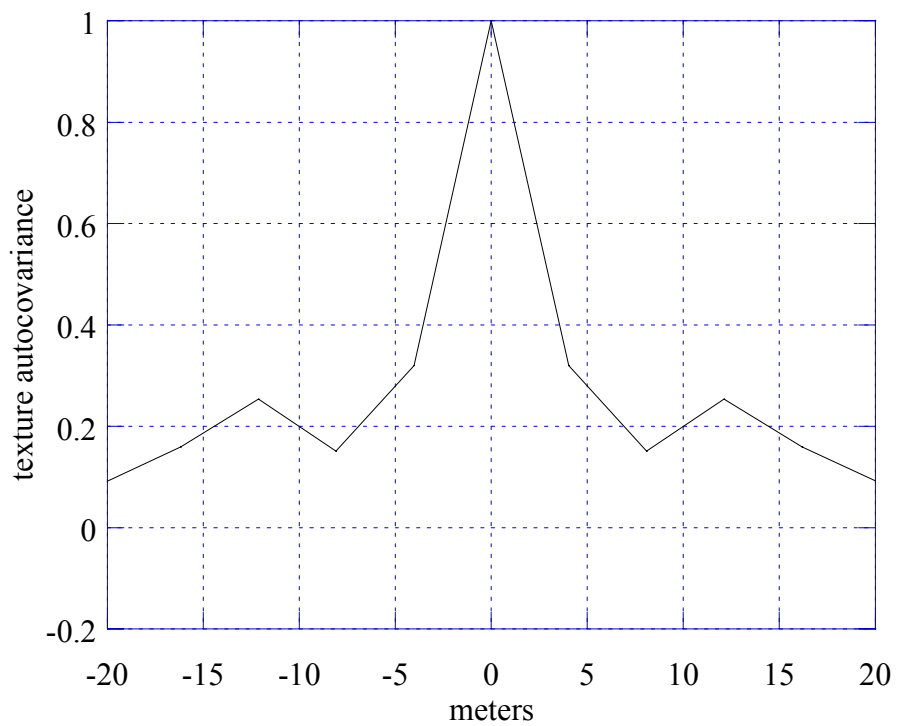


**Figure 2.2** - Range autocovariance in range of texture for the whole image (1784x1472).

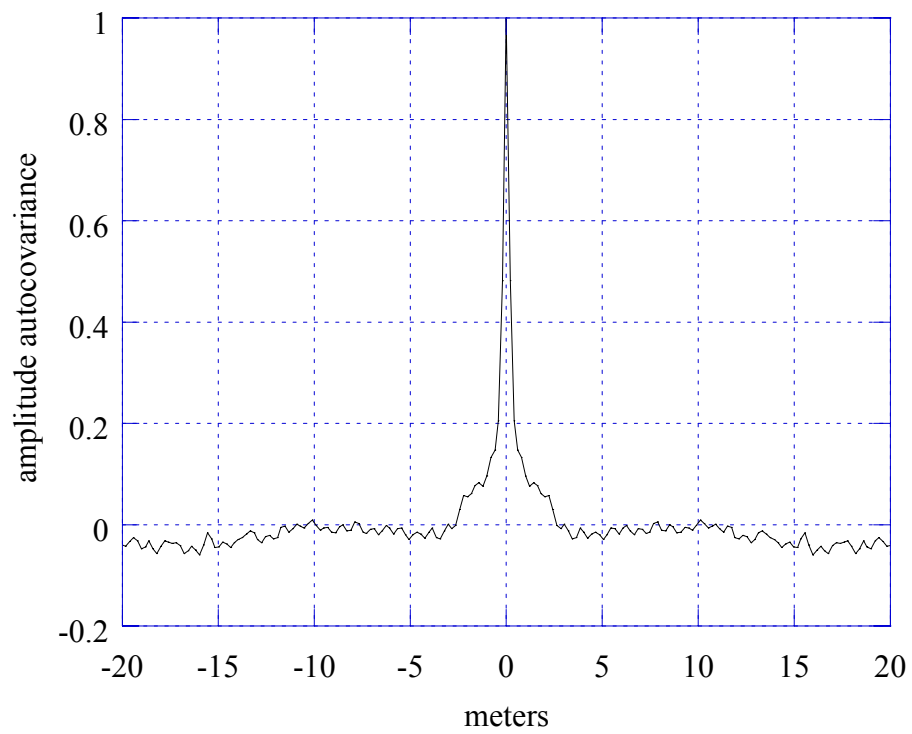


**Figure 2.3** - Range autocovariance of the amplitude for the whole image (1784x1472).

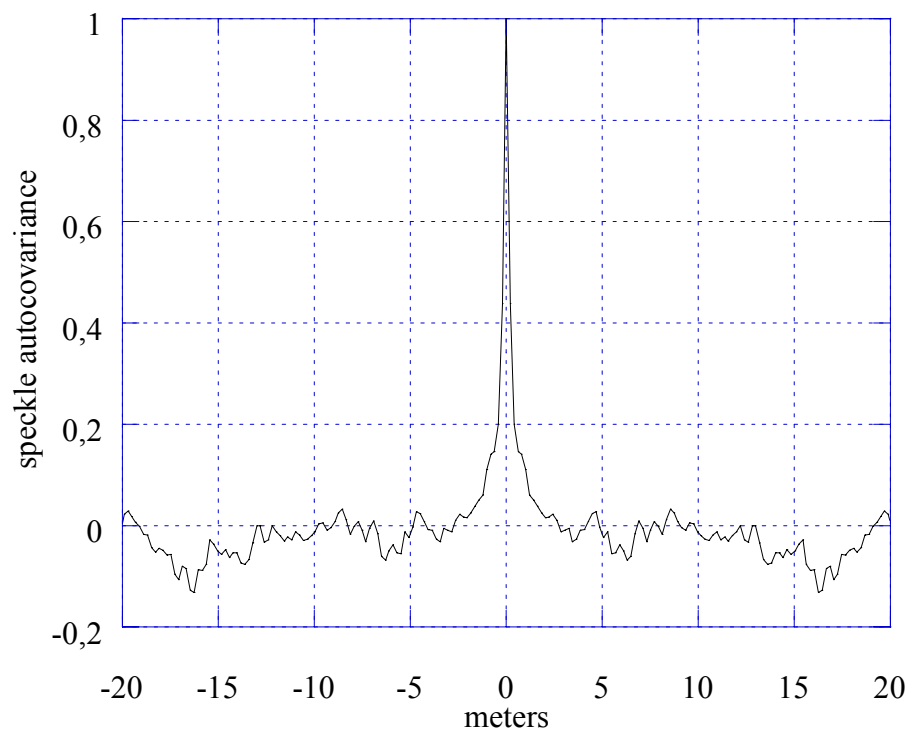


**Figure 2.4** - Cross-range autocovariance of the speckle for the whole image (1784x1472).

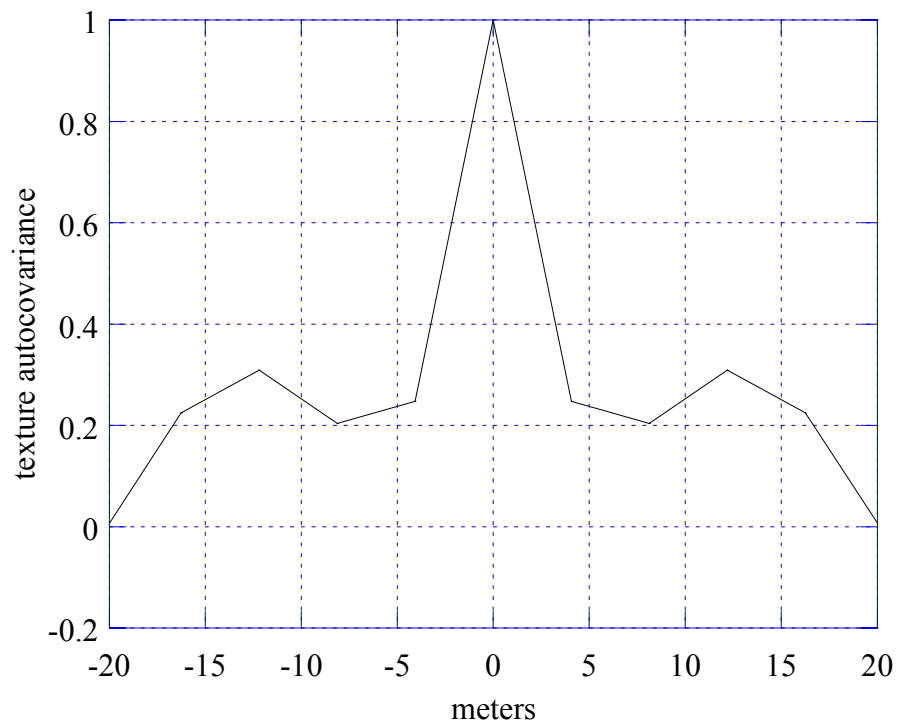


**Figure 2.5** - Cross-range autocovariance of texture for the whole image ( $1784 \times 1472$ ).

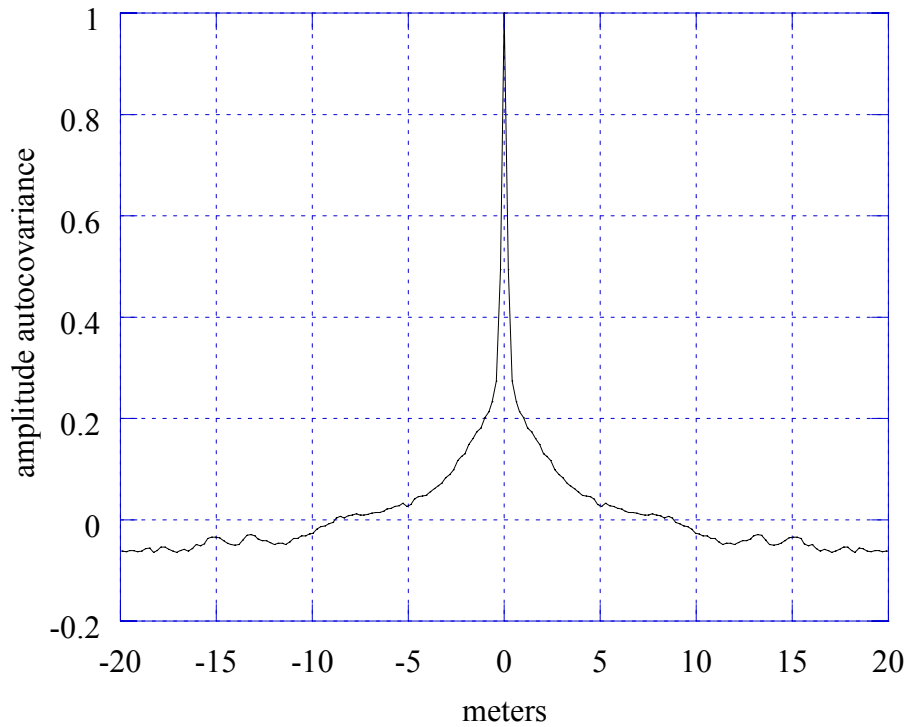


**Figure 2.6** - Cross-range autocovariance of the amplitude for the overall image ( $1784 \times 1472$ ).

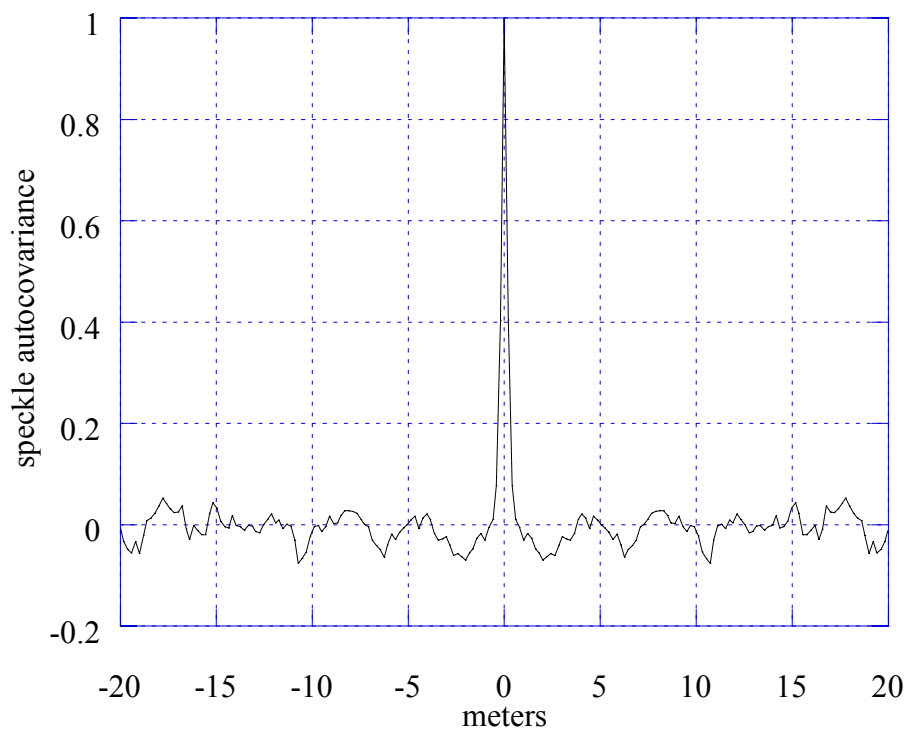


**Figure 2.7** - Range autocovariance of the speckle for the patch  $(893,1784) \times (1,1472)$ .

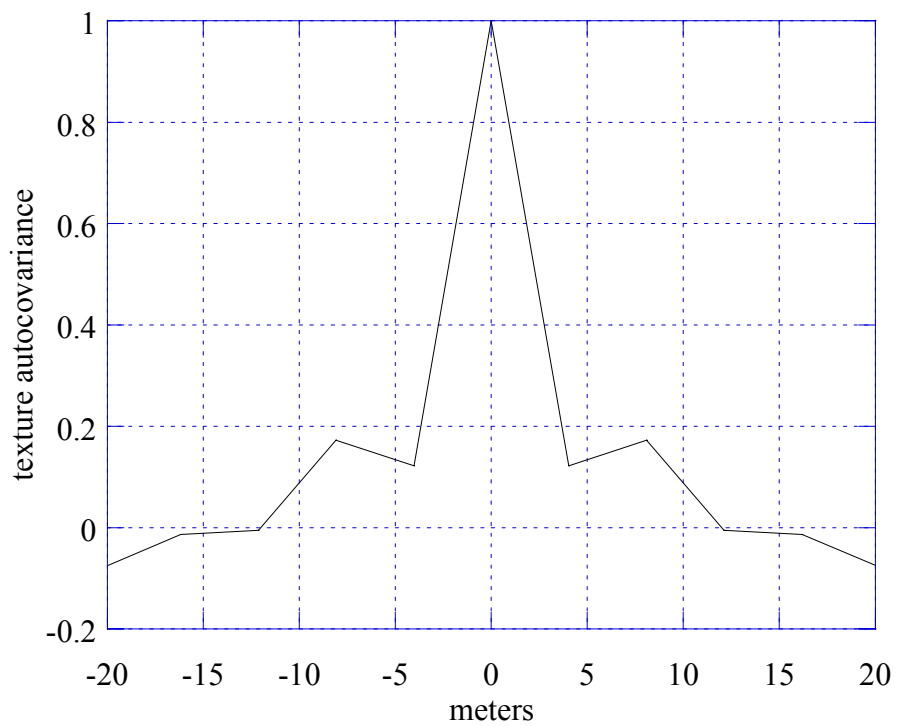


**Figure 2.8** - Range autocovariance of the texture for the patch  $(893,1784) \times (1,1472)$ .

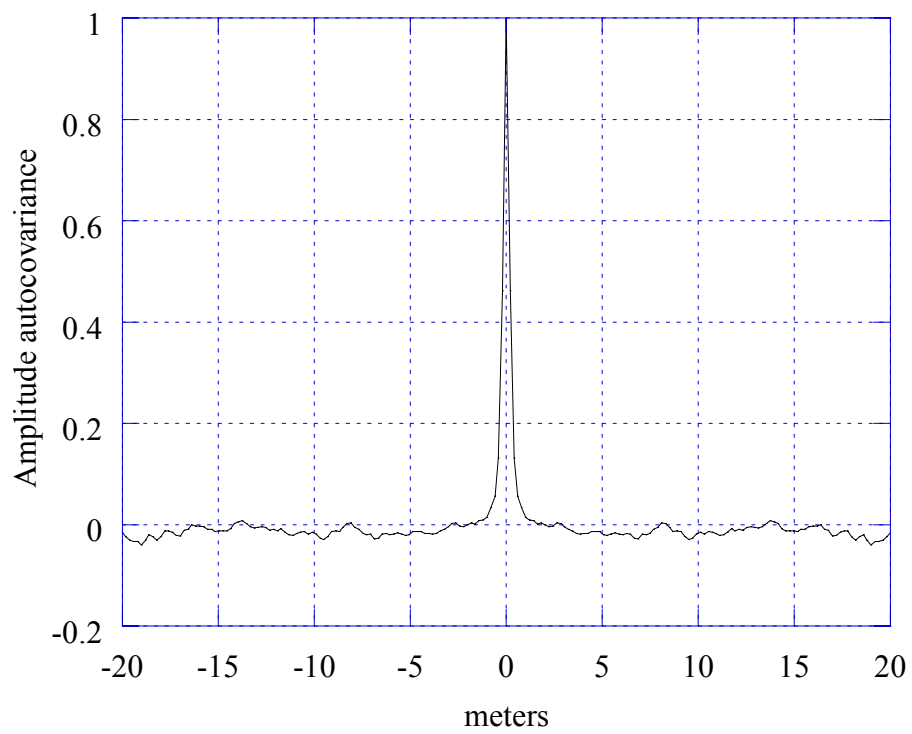


**Figure 2.9** - Range autocovariance of the amplitude for the patch  $(893,1784) \times (1,1472)$ .

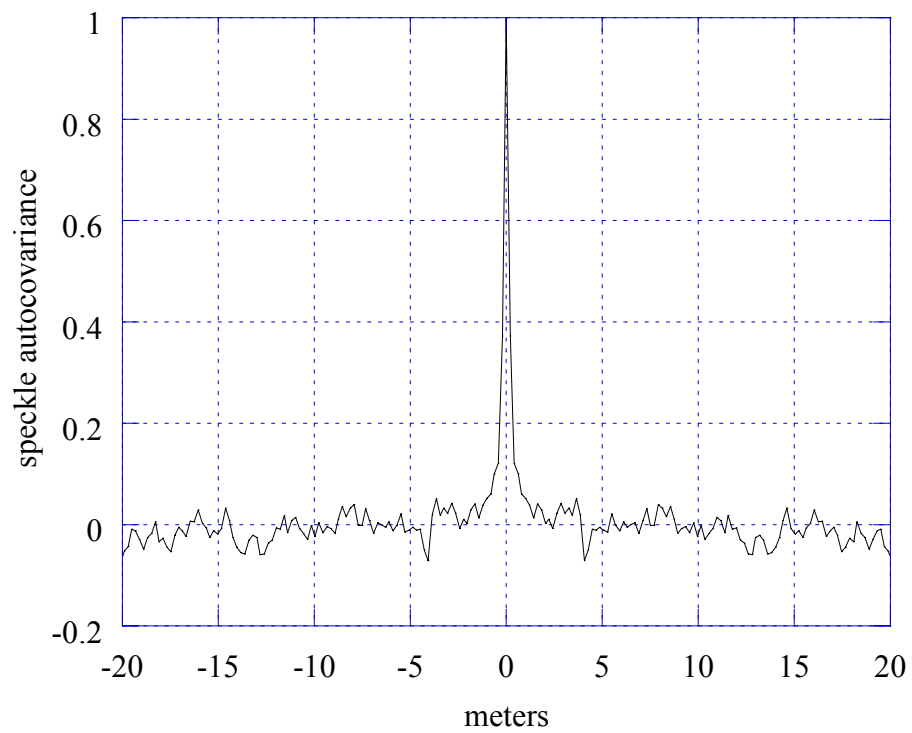


**Figure 2.10** - Cross-range autocovariance of the speckle for the patch  $(893,1784) \times (1,1472)$ .

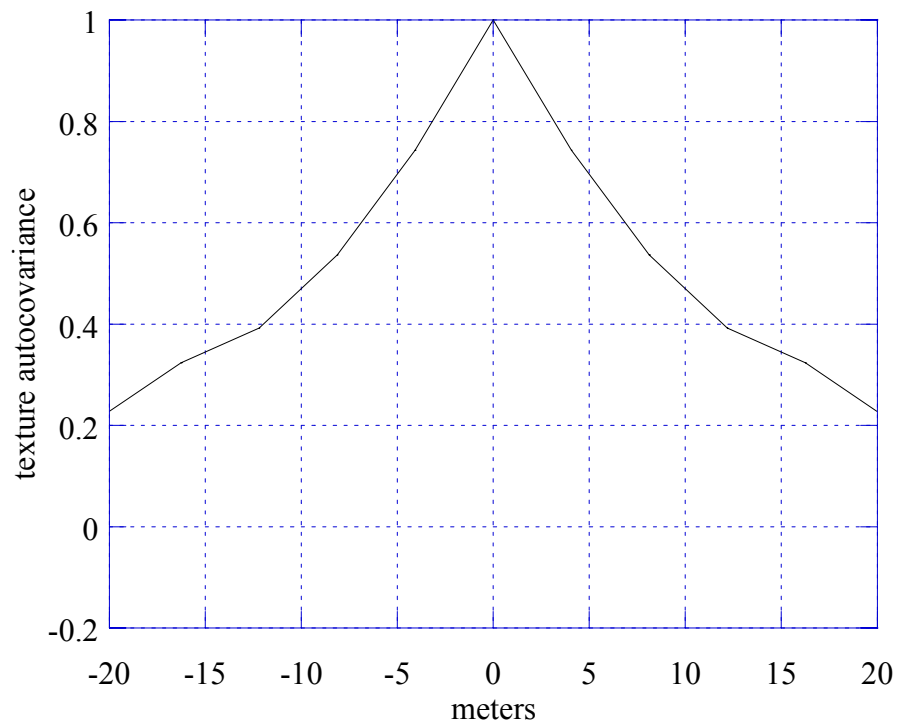


**Figure 2.11** - Cross-range autocovariance of the texture for the patch  $(893,1784) \times (1,1472)$ .

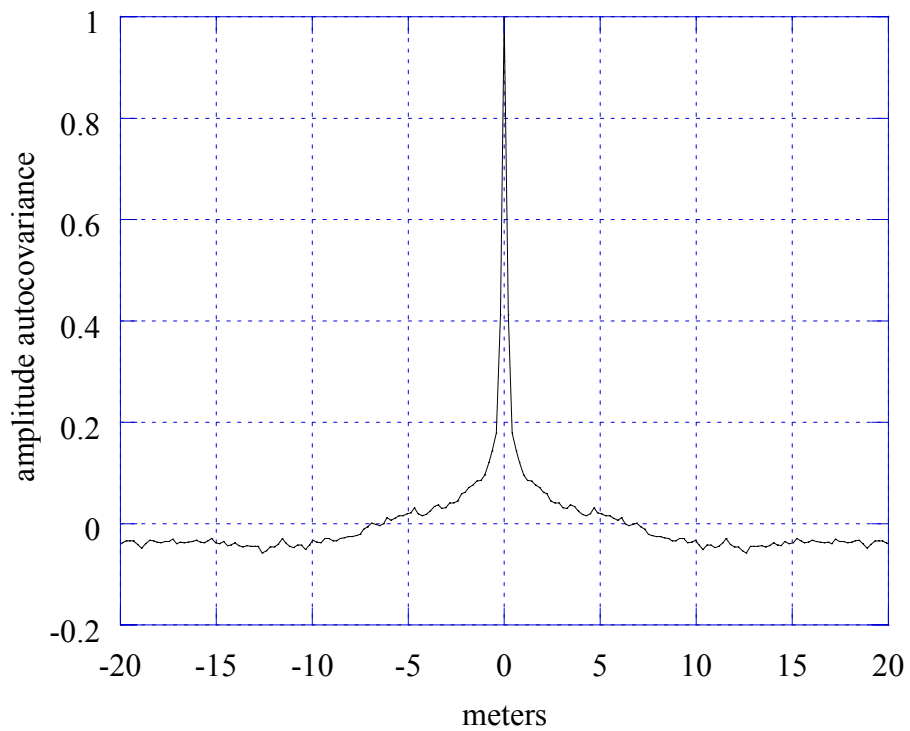


**Figure 2.12** - Cross-range autocovariance of the amplitude for the patch  $(893,1784) \times (1,1472)$ .

To complete the covariance analysis we estimated as well the 2-dimensional function of the texture as:

$$C(m, k) = \frac{1}{ML} \sum_{n=0}^{M-1-|m|} \sum_{l=0}^{L-1-|l|} [(\hat{\tau}(n, l) - \hat{\eta}_{\tau})(\hat{\tau}(n + m, l + k) - \hat{\eta}_{\tau})] \quad (2.4)$$

In Figures 2.13 and 2.14 we show the 2-dimensional covariance function of clutter amplitude as 3D-plot and as a map. The colormap is reported in the figures as a reference. Again, it is apparent that the decorrelation length is greater in cross-range than in range direction.

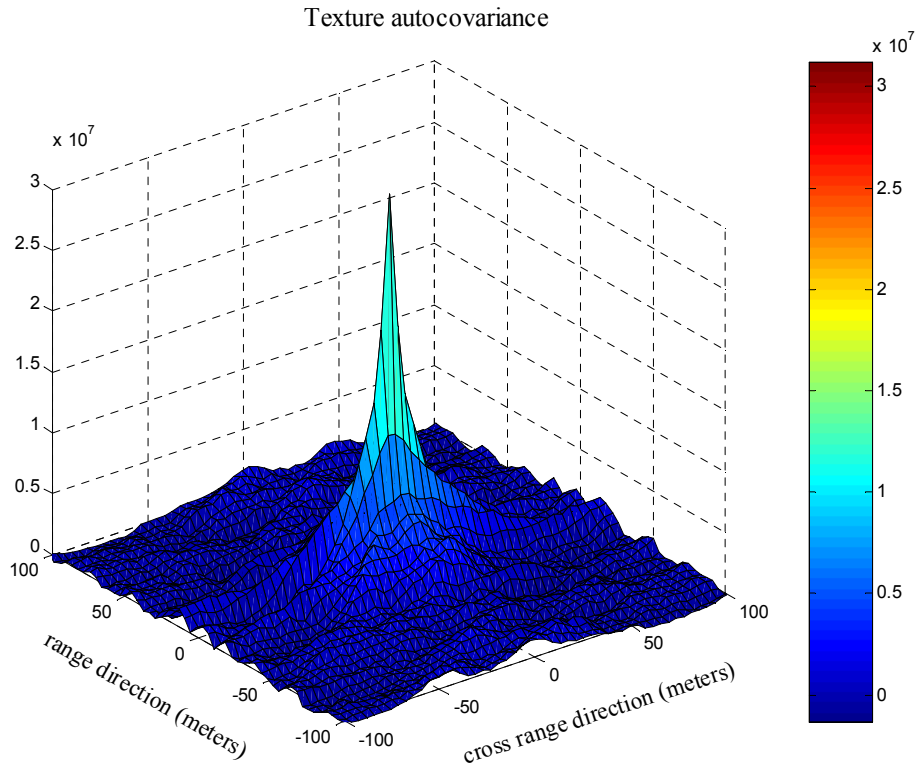


**Figure 2.13** Texture three-dimensional autocovariance function for total image of HB06171 file.

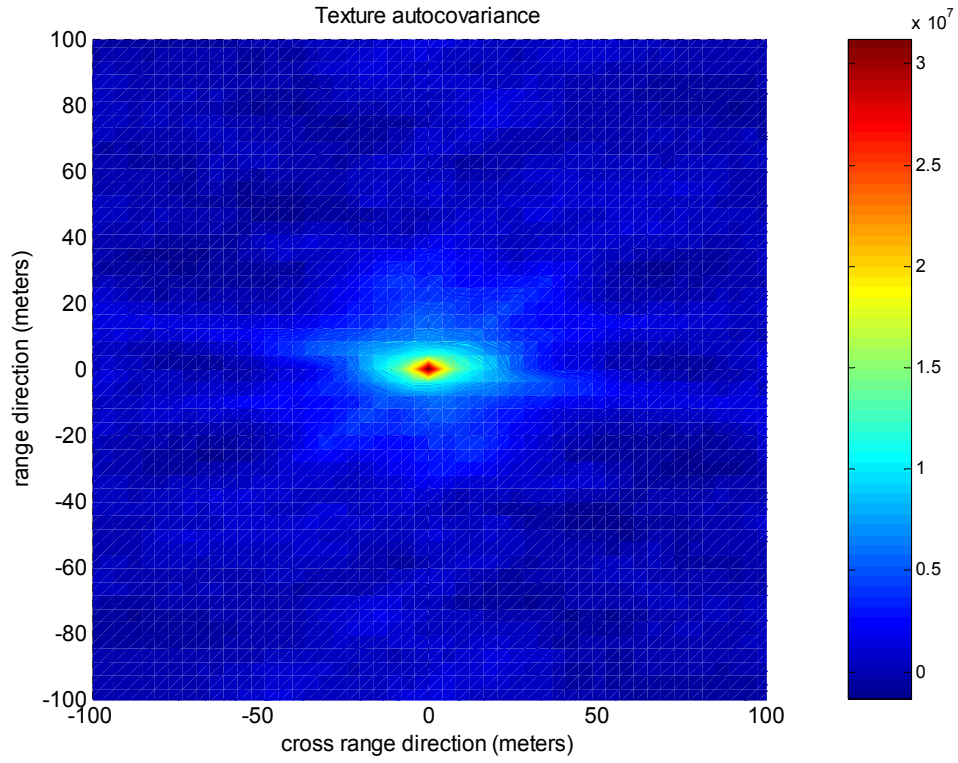


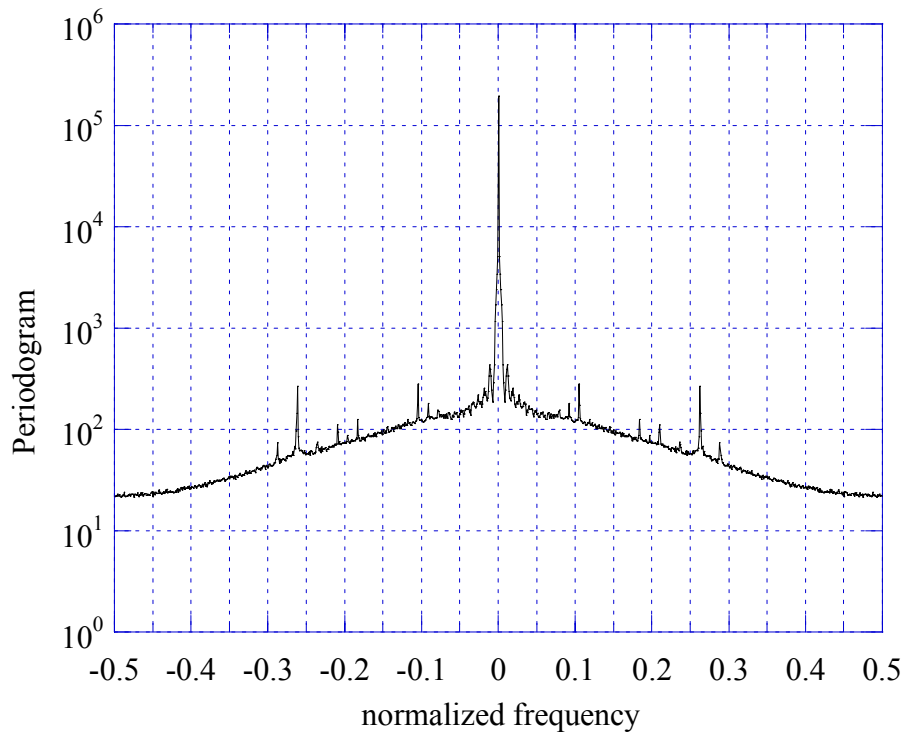
**Figure 2.14** Texture three-dimensional autocovariance function for total image of HB06171 file.

To calculate the periodogram of the data we applied eq. (2.1) to each row and column of the image, then, as for the covariance function, we averaged on all the rows and the columns and we obtained an averaged periodogram for both range and cross-range directions.

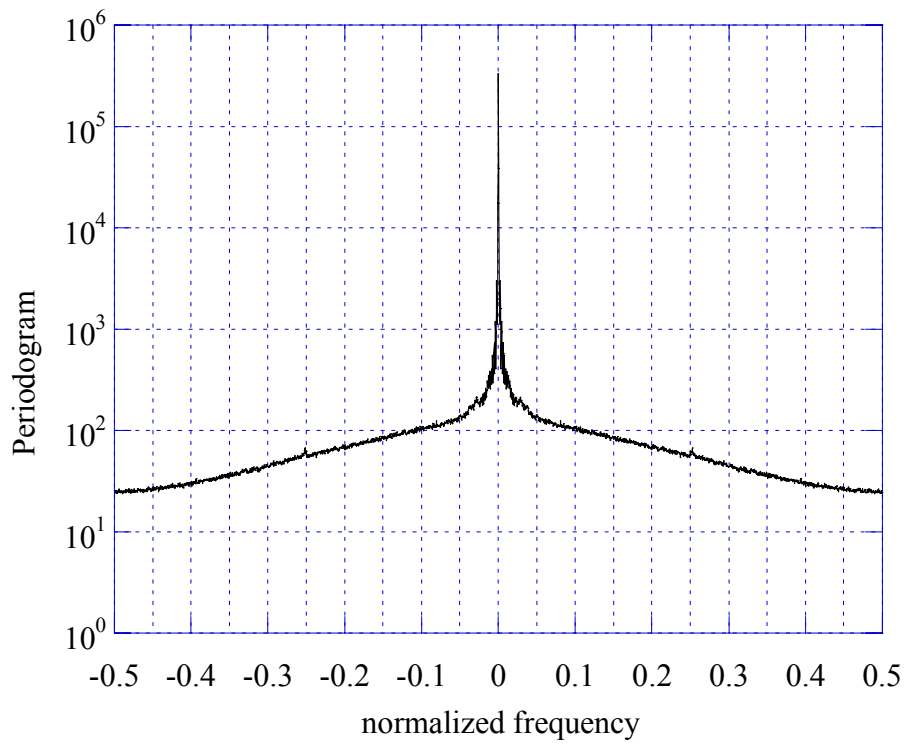
In figures 2.15 and 2.16 we report the mean periodogram in range and cross-range respectively for the whole image, in figures 2.17 and 2.18 for the patch  $(893,1784) \times (1,1472)$ . The behavior of the periodogram, in both directions and in the whole image and the patches, is very similar. It presents a peak at the null frequency due to the DC component of the data, then it decreases almost linearly in all the frequency range.

Figure 2.15 shows two spurious frequency lines at  $f=0.1$  and  $0.27$ . They are maybe due to some EM interference.





**Figure 2.15** – Mean periodogram in range for the whole image (*1784x1472*).



**Figure 2.16** – Mean periodogram in cross-range for the overall image (*1784x1472*).

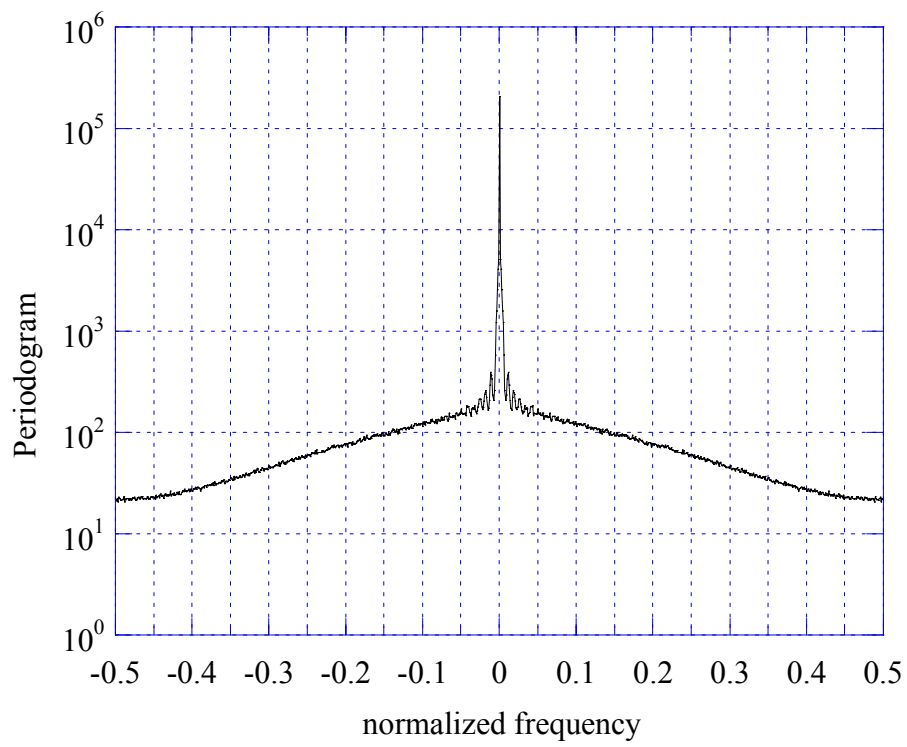


**Figure 2.17** - Mean periodogram in range for the patch  $(893,1784) \times (1,1472)$ .

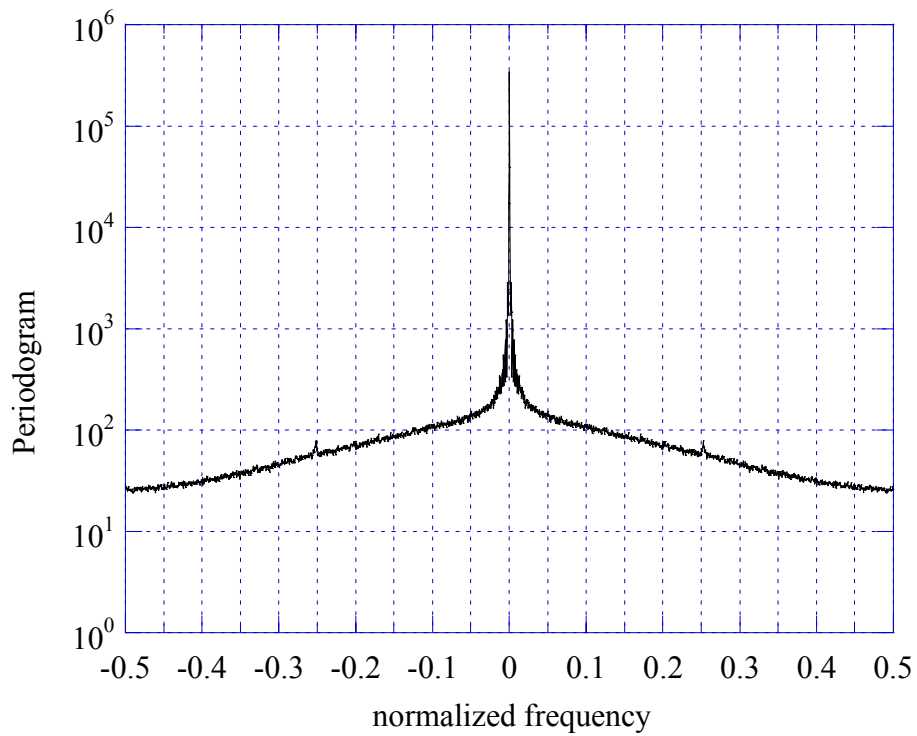


**Figure 2.18** - Mean periodogram in cross-range for the patch  $(893,1784) \times (1,1472)$ .

## 2.2 Frequency analysis of the clutter of dense vegetated areas

### 2.2.1 Periodogram of file HB06202

In this section we consider the file HB06202 (Figure 1.91). We report the results of frequency analysis, in particular the average periodogram calculated in range and cross-range direction in semilog scale. We report also the autocorrelation and autocovariance functions of data, speckle and texture. The autocovariance function has been calculated for both directions (range and cross-range) for the overall image and for three patches.

Figure 2.21 reports the average periodogram calculated in range for the whole image while Figure 2.22 reports the periodogram in cross-range direction.

The first patch that we analyzed is the  $(1100,1400) \times (1,800)$ , highlighted in Figure 1.107. The behavior of the average periodogram in range and cross-range is reported in figures 2.23 and 2.24 respectively. The second patch has dimensions  $(700,1000) \times (800,1400)$  (Figure 1.115) and, as the first, relates to a shadowed area. Conversely, last patch we considered  $(1,600) \times (1,1478)$  covers a region with dense vegetation as evident in Figure 1.121. The periodograms are plotted in Figs. 2.25-2.28.

There are not significant differences in range and cross-range directions.

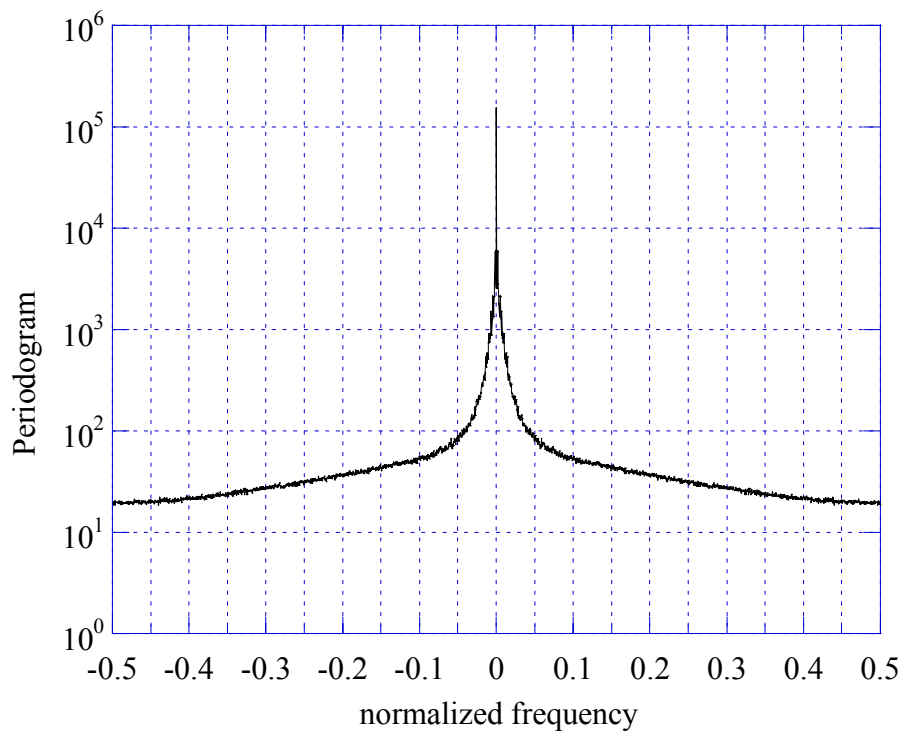


**Figure 2.21** - Average periodogram in range for the whole image (1784x1478).

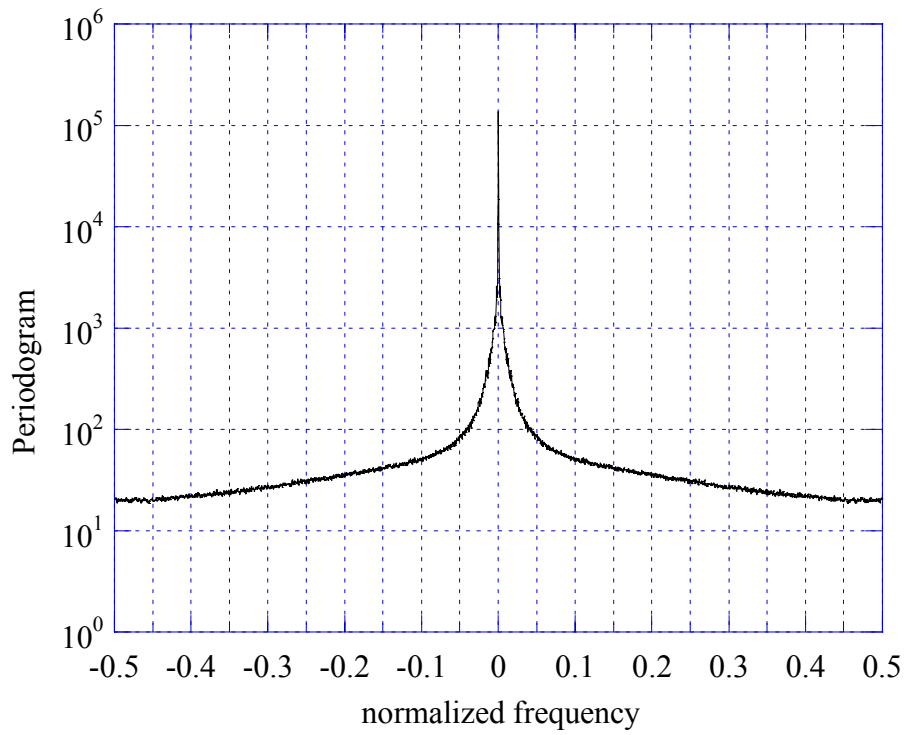


**Figure 2.22** - Average periodogram in cross-range for the whole image (1784x1478).

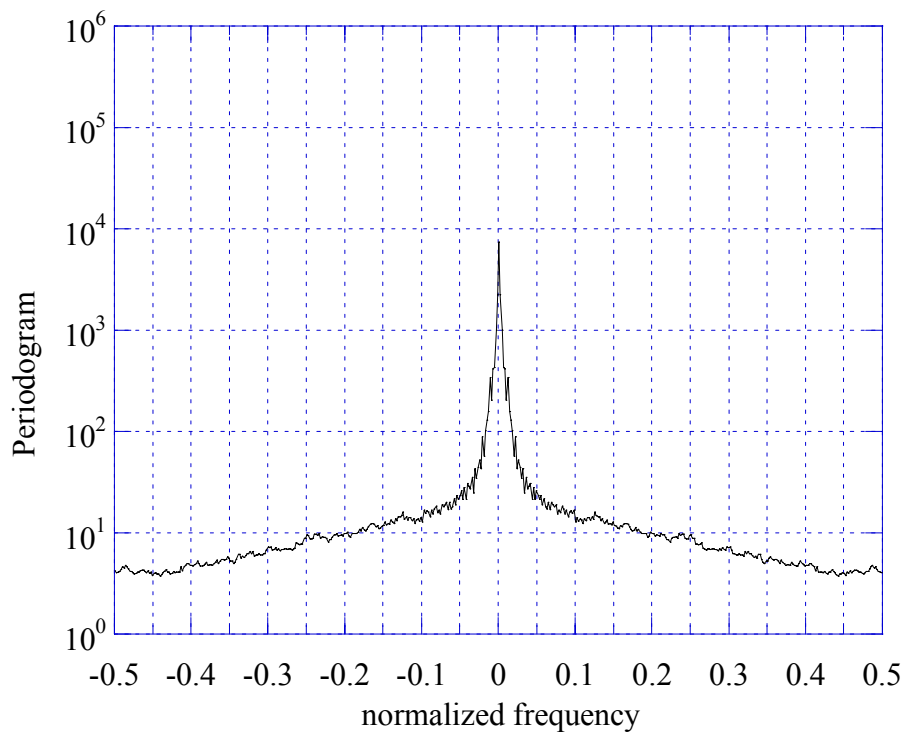


**Figure 2.23** - Average periodogram in range for the patch (1100,1400)x(1,800).

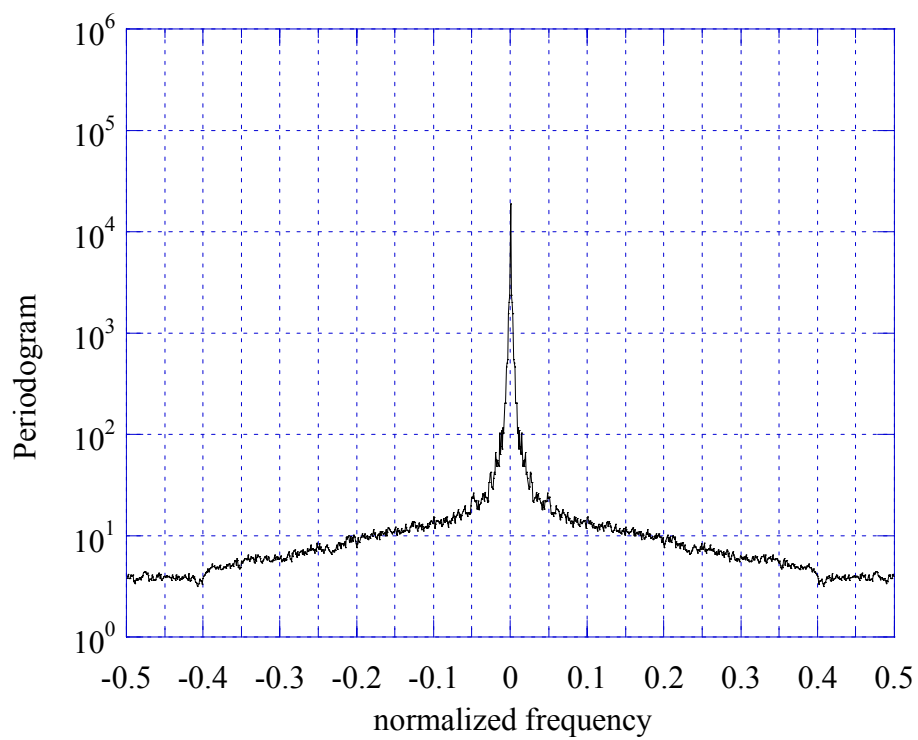


**Figure 2.24** - Average periodogram in cross-range for the patch  $(1100,1400) \times (1,800)$ .

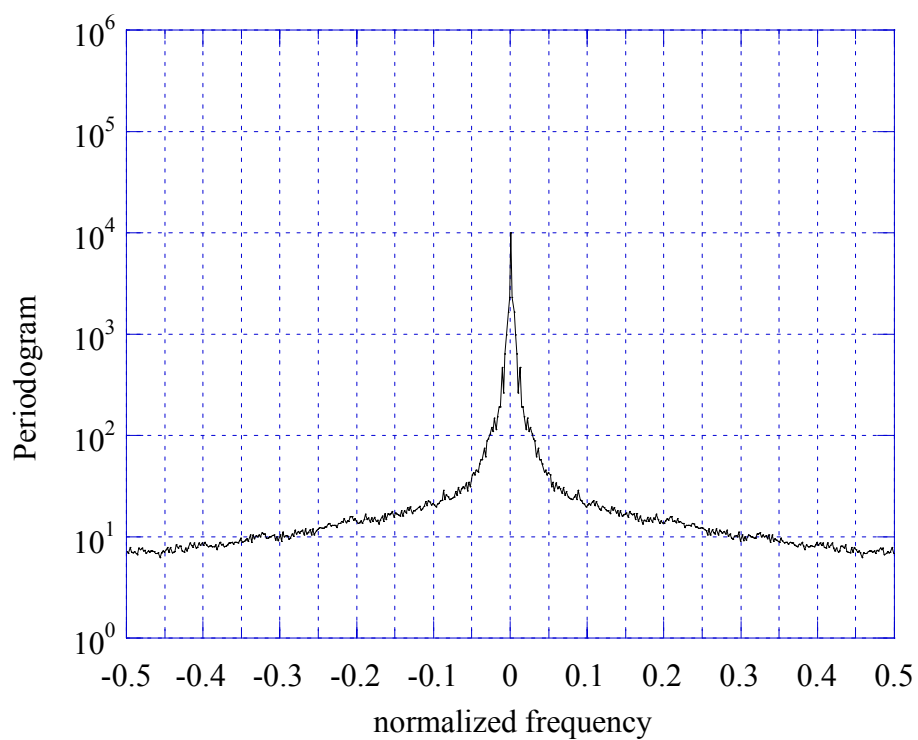


**Figure 2.25** - Average periodogram in range for the patch  $(700,1000) \times (800,1400)$ .

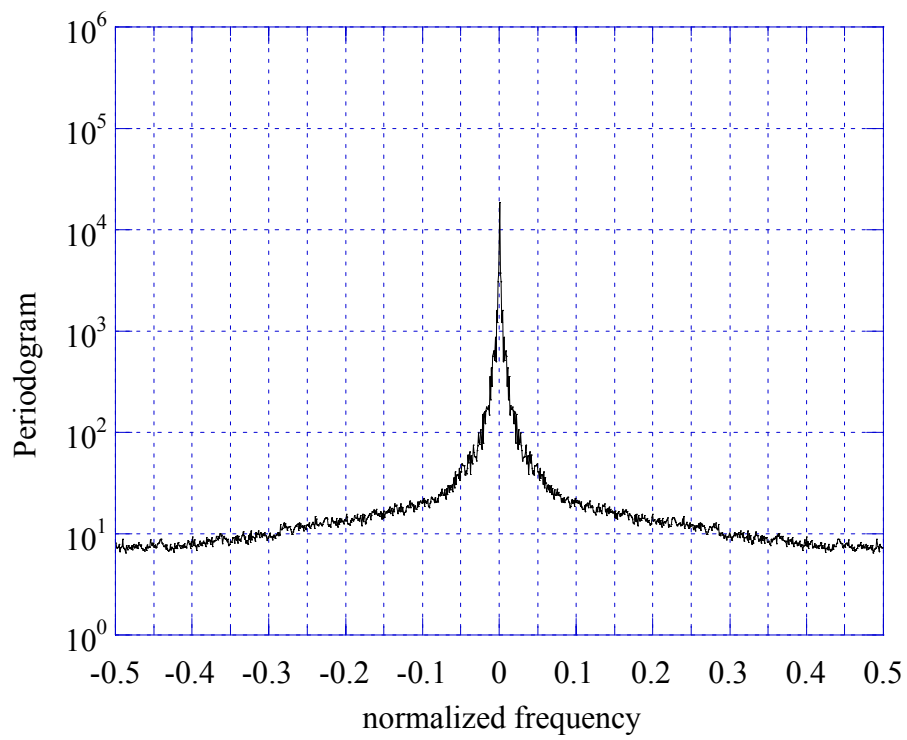


**Figure 2.26** - Average periodogram in cross-range for the patch  $(700,1000) \times (800,1400)$ .

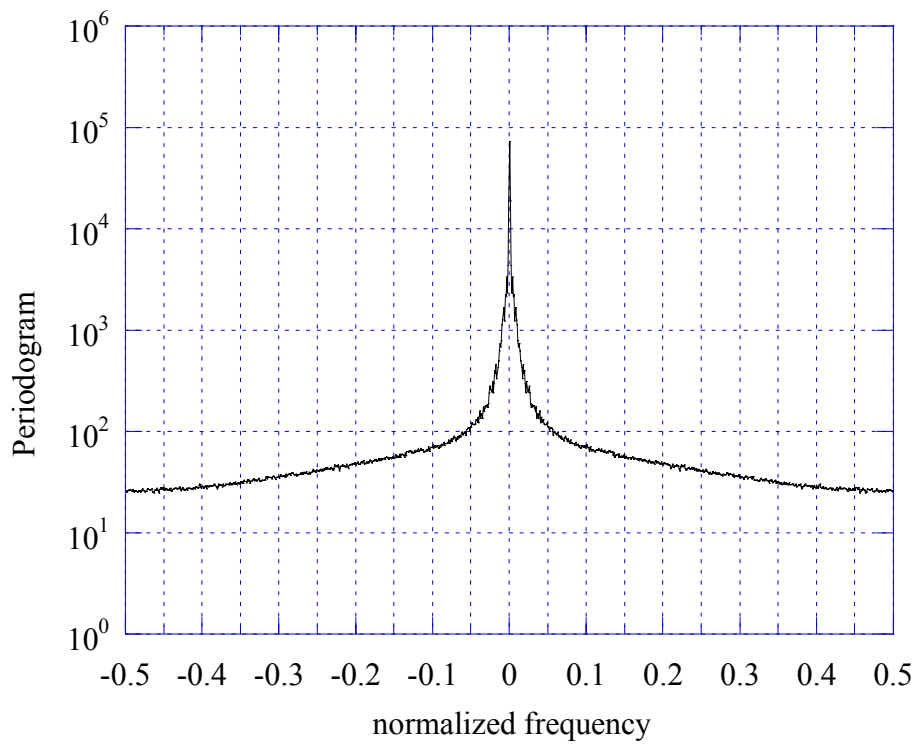


**Figure 2.27** - Average periodogram in range for the patch  $(1,600) \times (1,1478)$ .

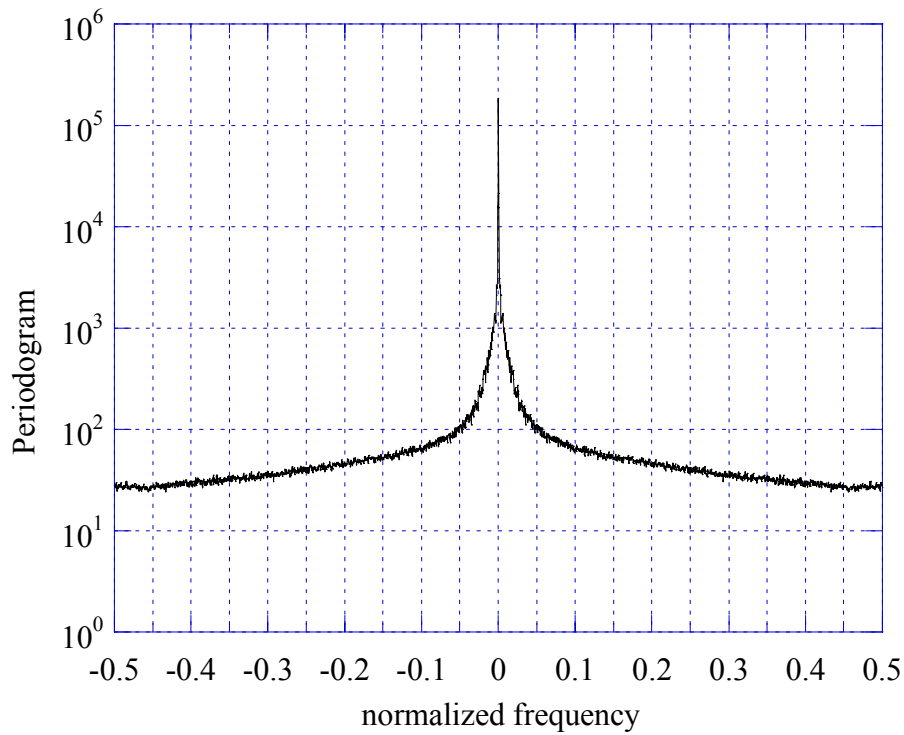


**Figure 2.28** - Average periodogram in cross- range for the patch  $(1,600) \times (1,1478)$ .

### 2.2.2 Correlations of HB06202 file: wood and trees

In the following figures we report the estimated autocovariances for the whole image and for the patch  $(893,1784) \times (1,1472)$ , in range and cross-range directions.

By observing figures 2.31 and 2.35 of speckle autocovariance we can notice that the covariance is zero already after 2.5-3 m both in range and in cross-range. Moreover, the mainlobe of the covariance function seems to be larger than in the case of grass field (see figures 2.1 and 2.4). This effect could be due to the presence of a texture residual contribution in the estimated speckle.

The amplitude covariance in Figure 2.34 and 2.37 is mainly influenced by the covariance of the speckle, and then it presents a fast drop to zero. The texture covariance, on the contrary, shows a slow decreasing, particularly in cross-range direction (see Fig. 2.36). We repeated same analysis on other files and patches; we obtained similar results even if, often, the decreasing of the texture covariance in cross-range is faster than in Fig. 2.36. The behavior of Fig. 2.36 could be due to a particular structure of the wood in the image of file HB06202.

In Figures 2.38-2.43 we report the 3D-covariance of the texture, estimated for the whole image (figs. 2.38 and 2.39), for the patch (700, 1000)x(800,1400) (figs- 2.40 and 2.41) and for the patch (1,600)x(1,1478) (Figs. 2.42 and 2.43). The long covariance length of the texture in cross-range direction is well evident in Fig. 2.38.

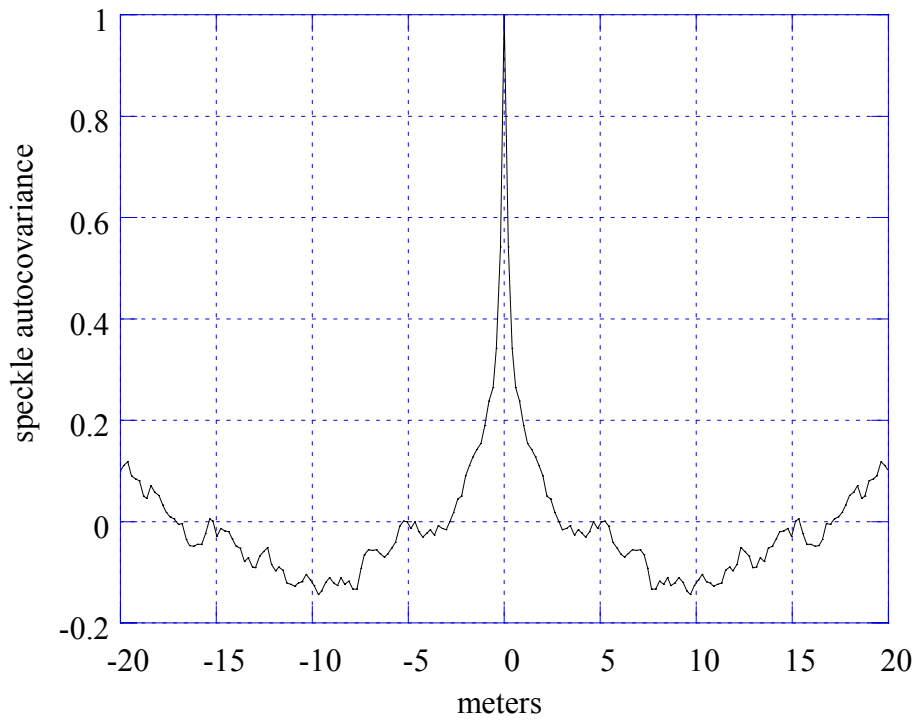


**Figure 2.31** - Autocovariance in range of the speckle for the whole image (1784x1478).



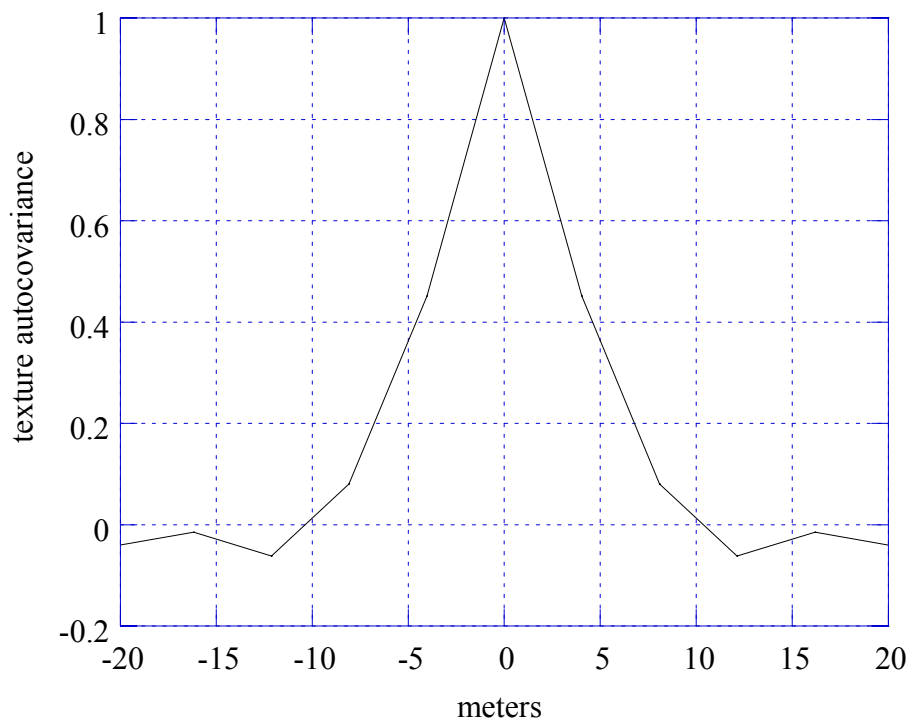


**Figure 2.32** - Autocovariance in range of the texture for the whole image (*1784x1478*).

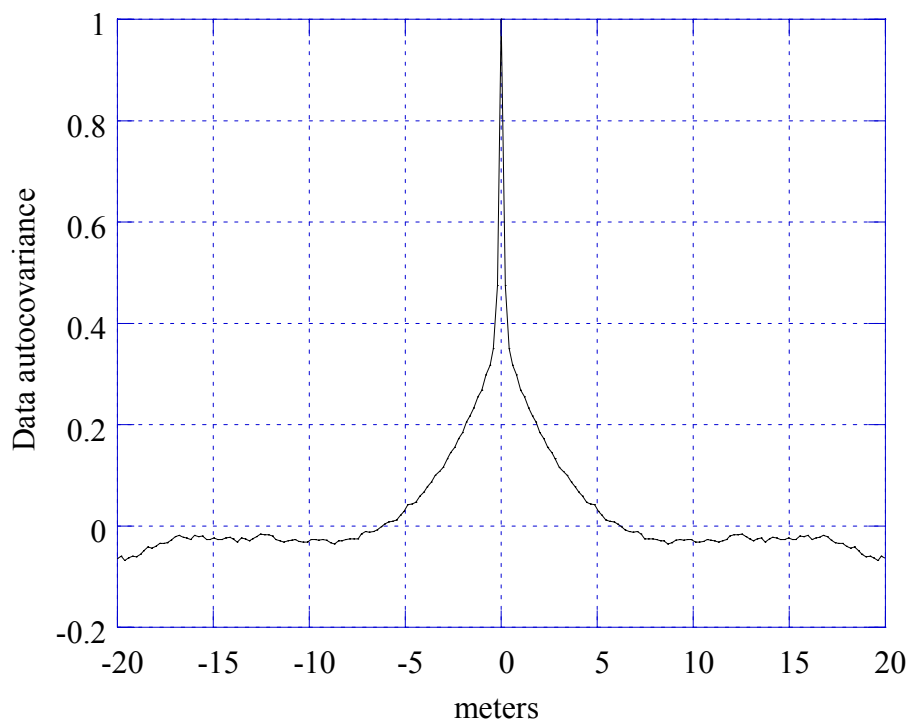


**Figure 2.34** - Autocovariance in range of the data amplitude for the whole image (*1784x1478*).

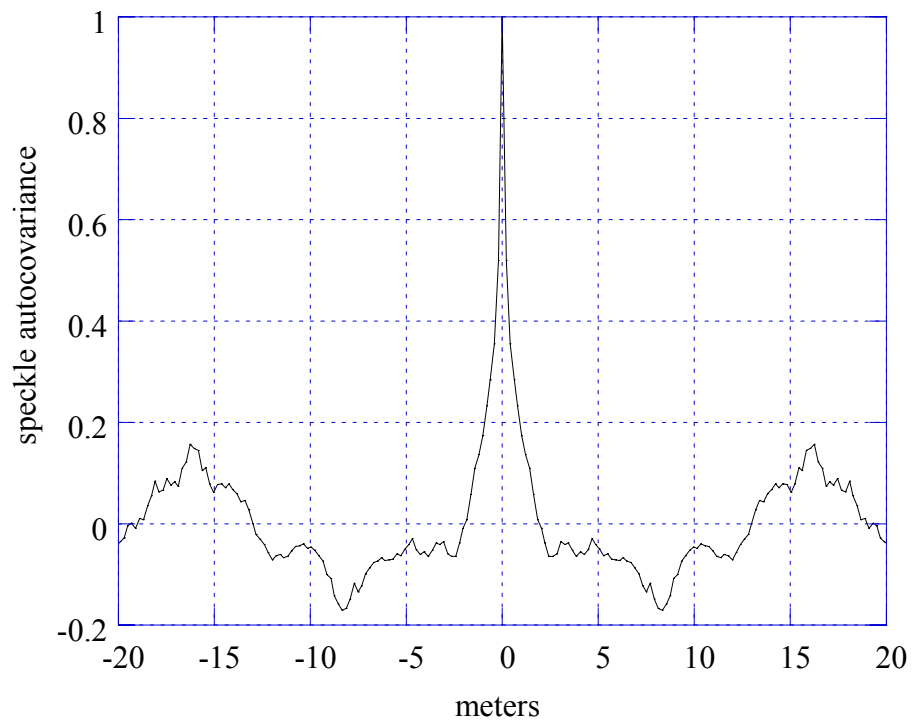


**Figure 2.35** - Autocovariance in cross-range of the speckle for the whole image ( $1784 \times 1478$ ).

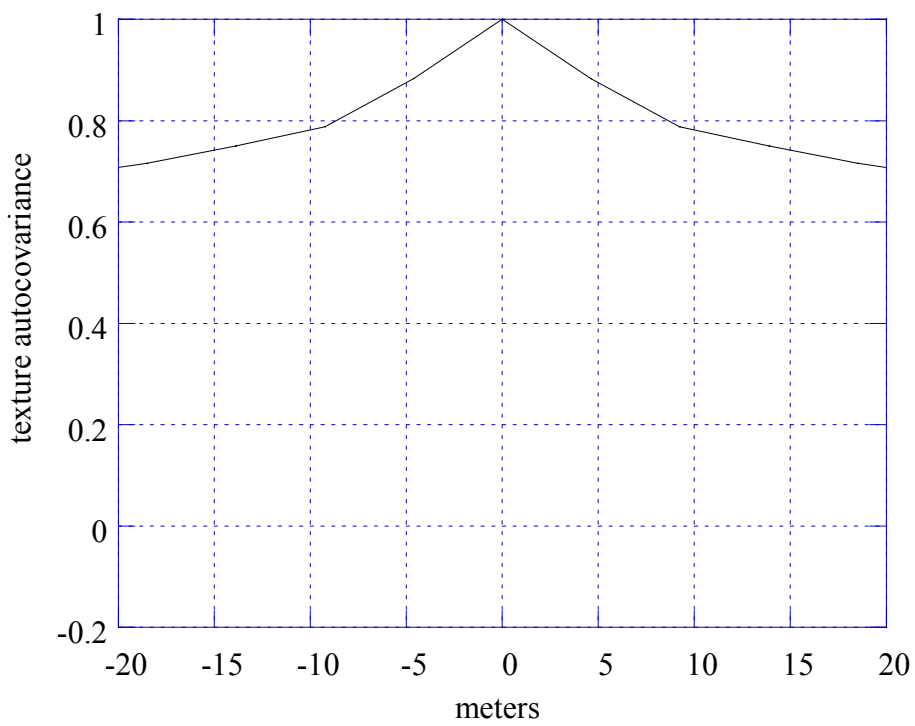


**Figure 2.36** Autocovariance in cross-range of the texture for the whole image ( $1784 \times 1478$ ).

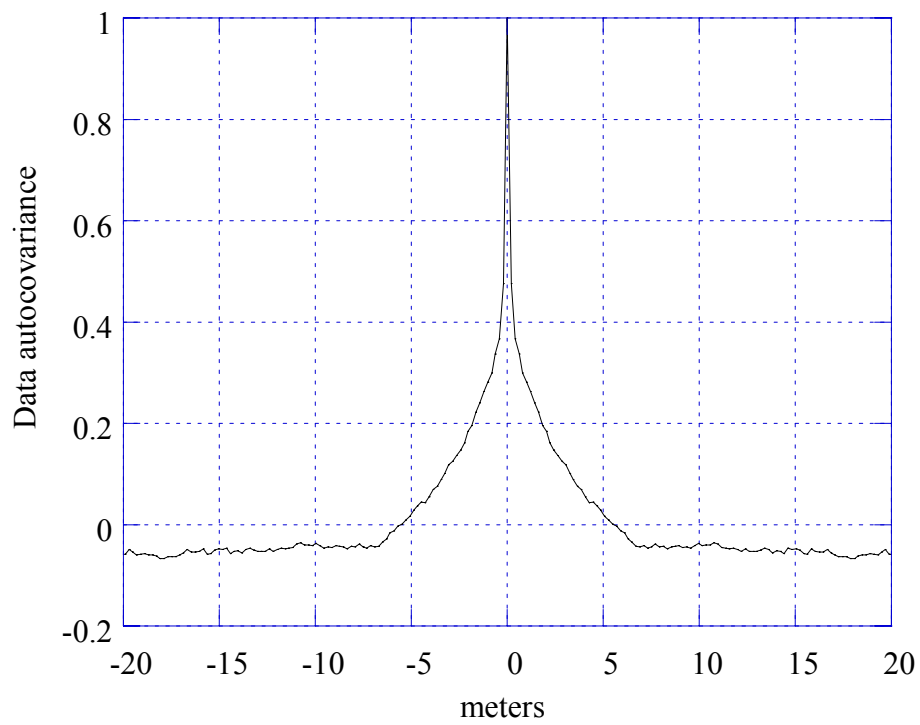


**Figure 2.37** Autocovariance in cross-range of the data amplitude for the whole image (*1784x1478*).

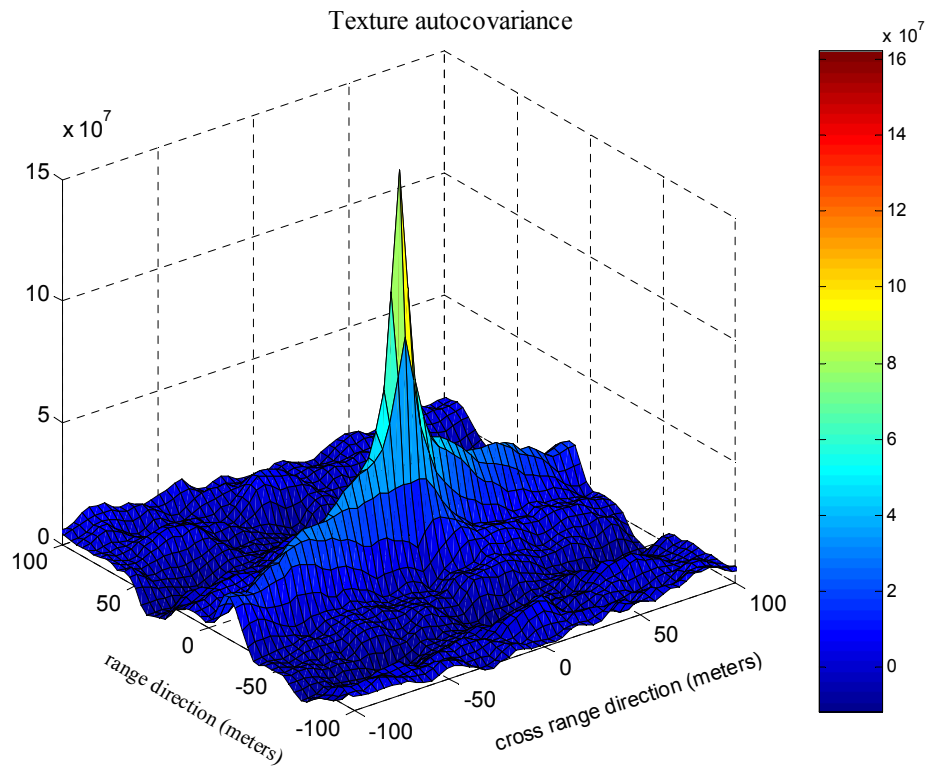


**Figure 2.38** - Texture three-dimensional autocovariance function for total image of the file HB06202.

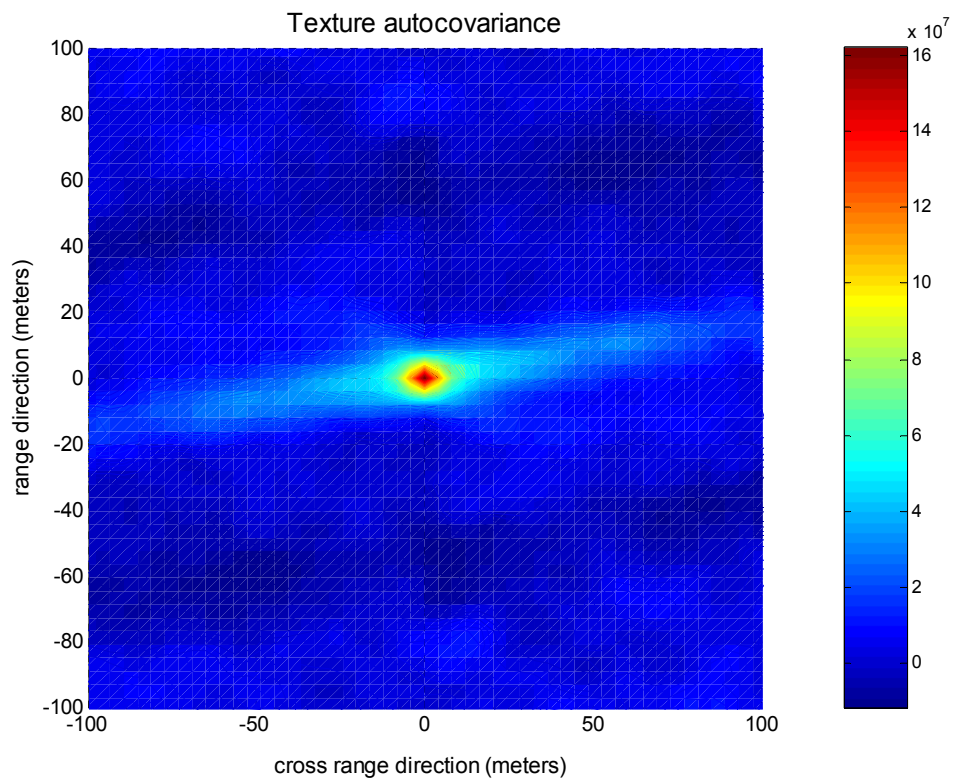


**Figure 2.39** - Texture three-dimensional autocovariance function for total image of the file HB06202.

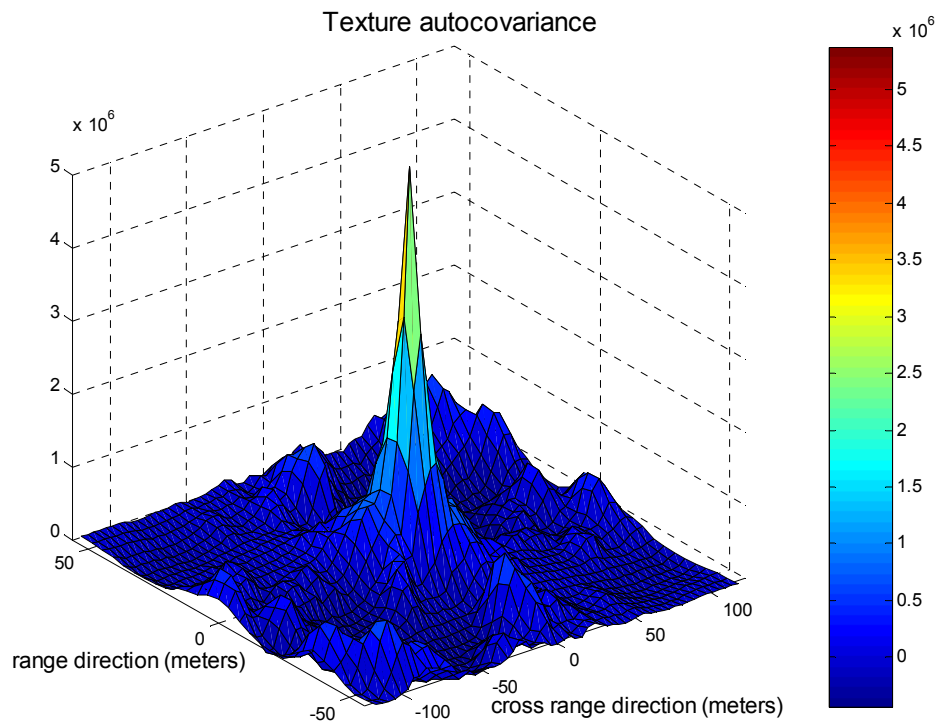


**Figure 2.40** - Texture three-dimensional autocovariance function for the patch  $(700,1000) \times (800,1400)$ .

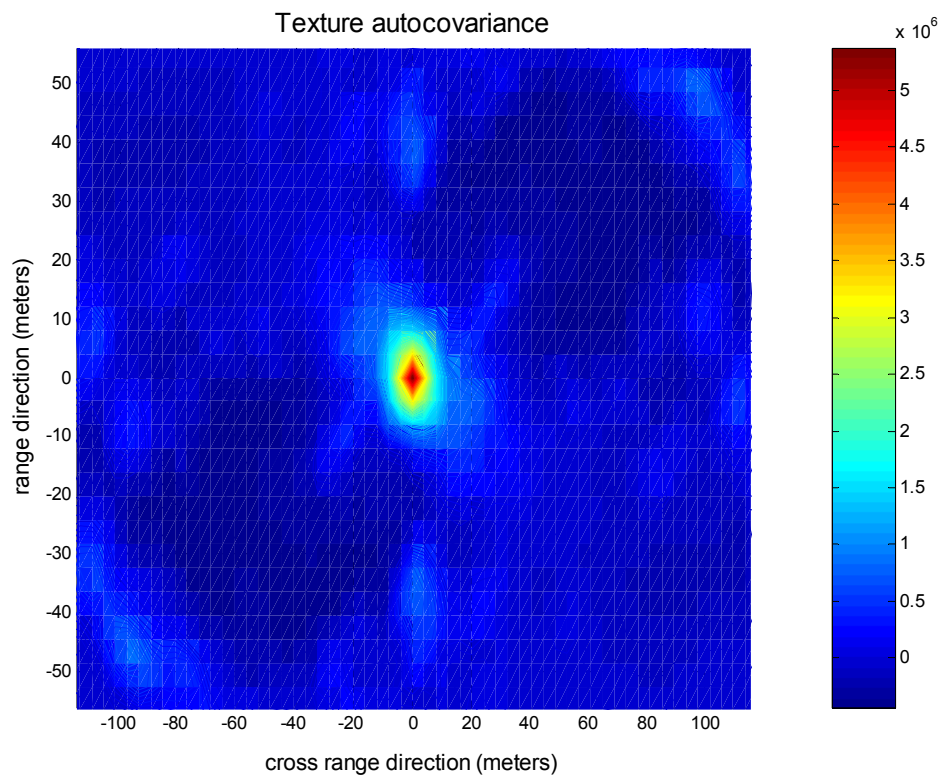


**Figure 2.41** - Texture three-dimensional autocovariance function for the patch  $(700,1000) \times (800,1400)$ .

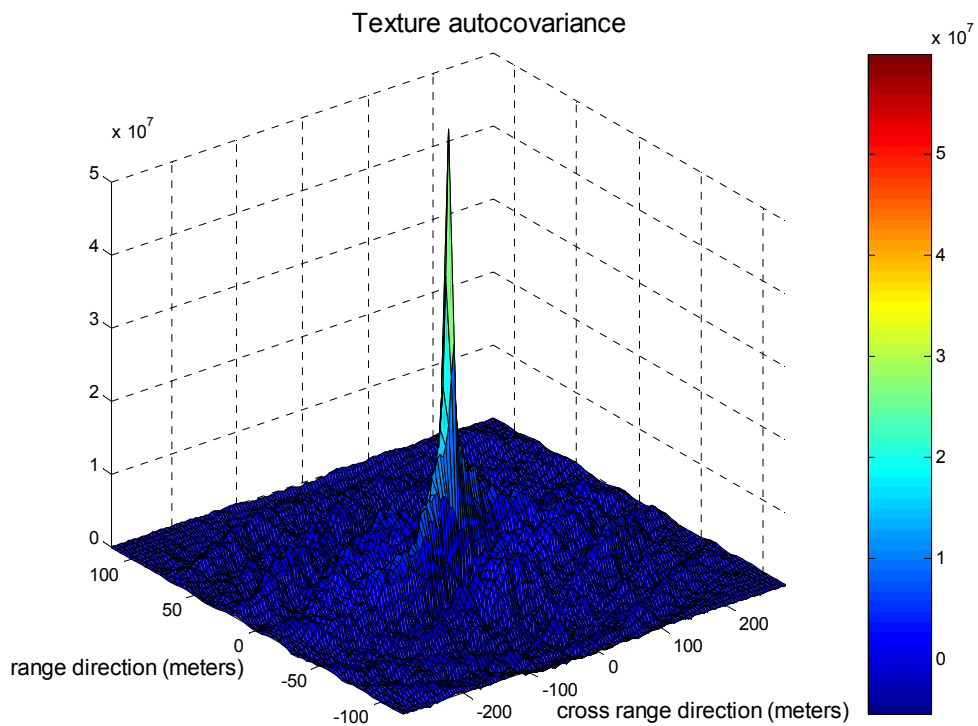


**Figure 2.42** - Texture three-dimensional autocovariance function for the patch  $(1,600) \times (1,1478)$ .

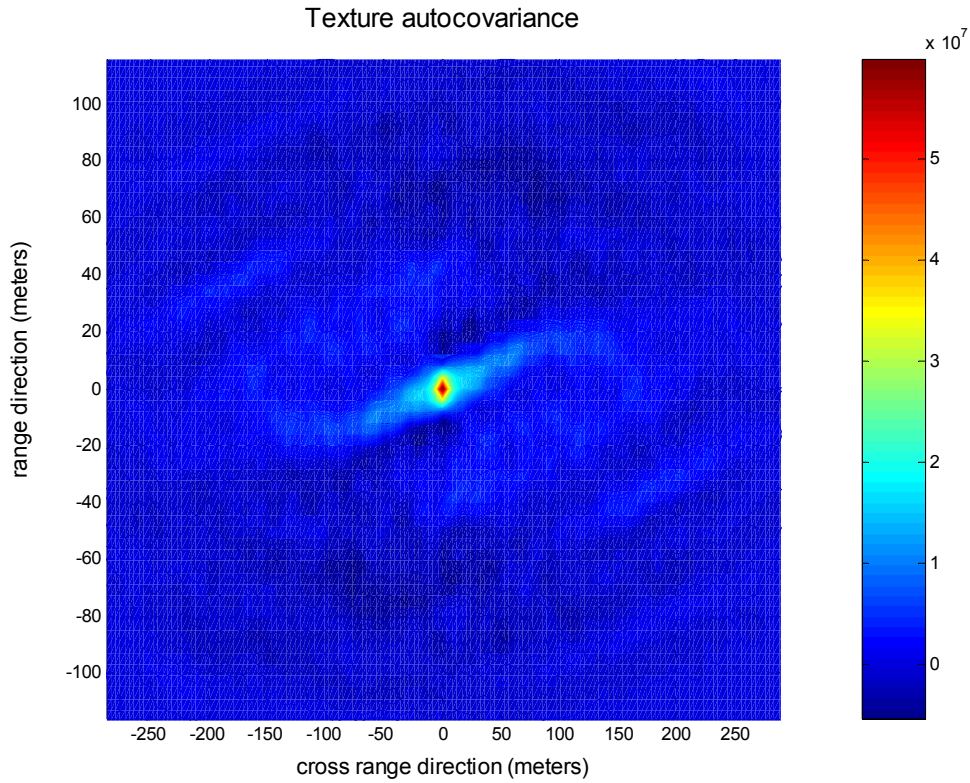


**Figure 2.43** - Texture three-dimensional autocovariance function for the patch  $(1,600) \times (1,1478)$ .

## 2.3 Theoretical texture correlation models

As shown in the previous section, the speckle is almost white in all the images. The residual correlation is mainly due to the oversampling (the pixel size is on the order of 0.2 m, the system resolution is on the order of 0.3 m). On the contrary, the texture is spatially correlated in both range and cross-range directions from the underlying nature of the terrain and vegetation illuminated by the radar.

In [Pos93] the author presents 3 different models for the autocovariance coefficient of the texture. In the first, referred to as Pure Gaussian (PG), the spatial autocovariance of the texture is assumed to have a two-dimensional Gaussian shape. Thus:

$$C_{PG}(x_1, x_2, y_1, y_2; x_0, y_0) = \exp \left[ - \left( \frac{x_1 - x_2}{x_0} \right)^2 - \left( \frac{y_1 - y_2}{y_0} \right)^2 \right] \quad (2.5)$$

where  $x_1$ ,  $x_2$ ,  $y_1$  and  $y_2$  are the spatial positions of the texture,  $x_0$  and  $y_0$  are the decorrelation lengths of the backscattered field, takes as the  $e^{-1}$  points of the assumed two-dimensional Gaussian shaped autocovariance function.

In the second texture model, the spatial autocovariance is assumed to have a two-dimensional Gaussian shape, modified by the presence of a range cosine factor, the purpose of which is to produce negative power covariances (shadows) in the range direction, a phenomenon particular evident in tree images. This model, called Shadowed Gaussian (SG) introduces another parameter, the range shadowing length  $y'_0$ . The SG model is given by:

$$C_{SG}(x_1, x_2, y_1, y_2; x_0, y_0, y'_0) = \exp \left[ - \left( \frac{x_1 - x_2}{x_0} \right)^2 - \left( \frac{y_1 - y_2}{y_0} \right)^2 \right] \cdot \cos \left[ \frac{y_0}{y'_0} \left( \frac{y_1 - y_2}{y_0} \right) \right] \quad (2.6)$$

When  $y_0/y'_0$  goes to zero, the SG model is identical to PG.

In the third model we considered, the spatial autocovariance of the texture is assumed to have a two-dimensional exponential shape modified by the presence of the same range cosine term as the SG model. The exponential form for the texture autocovariance yields a slower decay in the covariance than the Gaussian form. This model is called Shadowed Exponential (SE):

$$C_{SE}(x_1, x_2, y_1, y_2; x_0, y_0, y'_0) = \exp \left[ - \sqrt{\left( \frac{x_1 - x_2}{x_0} \right)^2 + \left( \frac{y_1 - y_2}{y_0} \right)^2} \right] \cdot \cos \left[ \frac{y_0}{y'_0} \left( \frac{y_1 - y_2}{y_0} \right) \right] \quad (2.7)$$

The texture autocovariance function for the Pure Gaussian case is separable, and can be written as the product of a Gaussian in cross-range and a Gaussian in range direction. The Shadowed Gaussian shape is separable as well. The Shadowed exponential is not separable.

## 2.4 Results

We tested all the three theoretical models of the texture covariance on our data. To estimate the parameters  $x_0$ ,  $y_0$  and  $y'_0$  we used the central row  $C(m, 0)$  and column of the covariance matrix  $C(0, k)$ , normalized with respect to the maximum value  $C(0, 0)$ , estimated

as in eq. (2.). So doing we separated the estimation along the two directions, range and cross-range. In detail, to estimate the parameter  $x_0$  of the PG and SG models, we fixed  $y_1 = y_2$  and we minimized the mean square error between the theoretical and the estimated covariance of the central row  $C(m, 0)$ , that is

$$\hat{x}_0 = \min_{x_0} \left[ \sum_{m=-Nmc/2}^{Nmc/2-1} \left( \frac{C(m, 0)}{C(0, 0)} - \exp \left[ - \left( \frac{x(m)}{x_0} \right)^2 \right] \right)^2 \right] \quad (2.8)$$

where  $N_{mc}$  is the number of column in the texture covariance matrix, and  $x(m)$  is the lag position with respect to the axis origin along the cross-range direction.

To estimate  $y_0$  for the PG model we pose

$$\hat{y}_0 = \min_{y_0} \left[ \sum_{k=-Nmr/2}^{Nmr/2-1} \left( \frac{C(0, k)}{C(0, 0)} - \exp \left[ - \left( \frac{y(k)}{y_0} \right)^2 \right] \right)^2 \right] \quad (2.9)$$

where  $N_{mr}$  is the number of column in the texture covariance matrix, and  $y(k)$  is the lag position with respect to the axis origin along the range direction.

To estimate  $y_0$  and  $y'_0$  for the SG model we pose

$$\hat{y}_0, \hat{y}'_0 = \min_{y_0, y'_0} \left[ \sum_{k=-Nmr/2}^{Nmr/2-1} \left( \frac{C(0, k)}{C(0, 0)} - \exp \left[ - \left( \frac{y(k)}{y_0} \right)^2 \right] \cos \left[ \frac{y_0}{y'_0} \left( \frac{y(k)}{y_0} \right) \right] \right)^2 \right] \quad (2.10)$$

To estimate the parameter  $x_0$  for the SE model we have:

$$\hat{x}_0 = \min_{x_0} \left[ \sum_{m=-Nmc/2}^{Nmc/2-1} \left( \frac{C(m, 0)}{C(0, 0)} - \exp \left[ - \left( \frac{x(m)}{x_0} \right)^2 \right] \right)^2 \right] \quad (2.11)$$

and for  $y_0$  and  $y'_0$



$$\hat{y}_0, \hat{y}'_0 = \min_{y_0, y'_0} \left[ \sum_{k=-Nmr/2}^{Nmr/2-1} \left( \frac{C(0, k)}{C(0, 0)} - \exp \left[ - \left( \frac{y(k)}{y_0} \right) \right] \cos \left[ \frac{y_0}{y'_0} \left( \frac{y(k)}{y_0} \right) \right] \right)^2 \right] \quad (2.12)$$

We report here the results of our analysis performed on three patches of the file HB06195 representing a wood, a grass field and shadow respectively. In Figure 2.43-2.60 we plot the theoretical models compared to the estimated texture covariance and in Tables 2.1-2.3 we report the values of the estimated parameters and the minimum mean square error (MMSE) for each model. In all the analyzed cases the best fitting is provided by the shadowed exponential model.

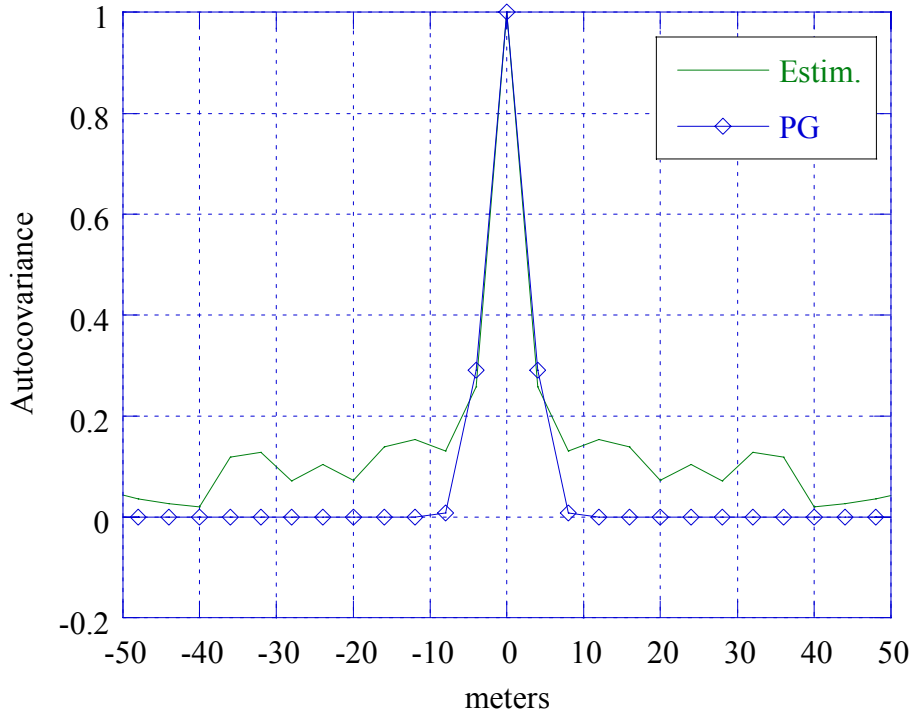


**Figure 2.43** – Texture covariance, grass field, range direction.

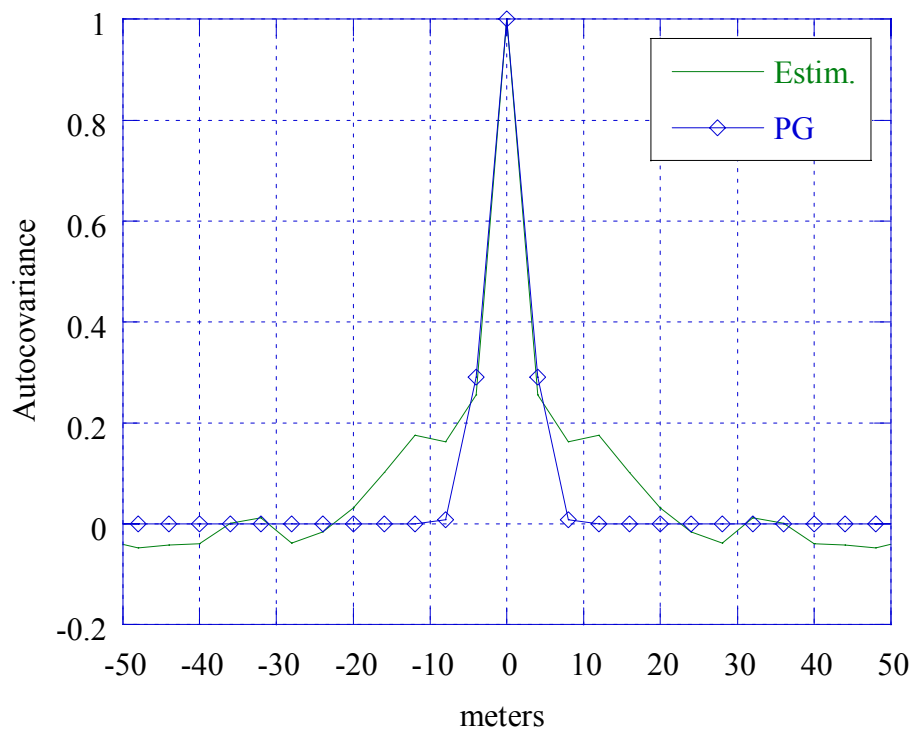


**Figure 2.44** – Texture covariance, grass field, cross-range direction.

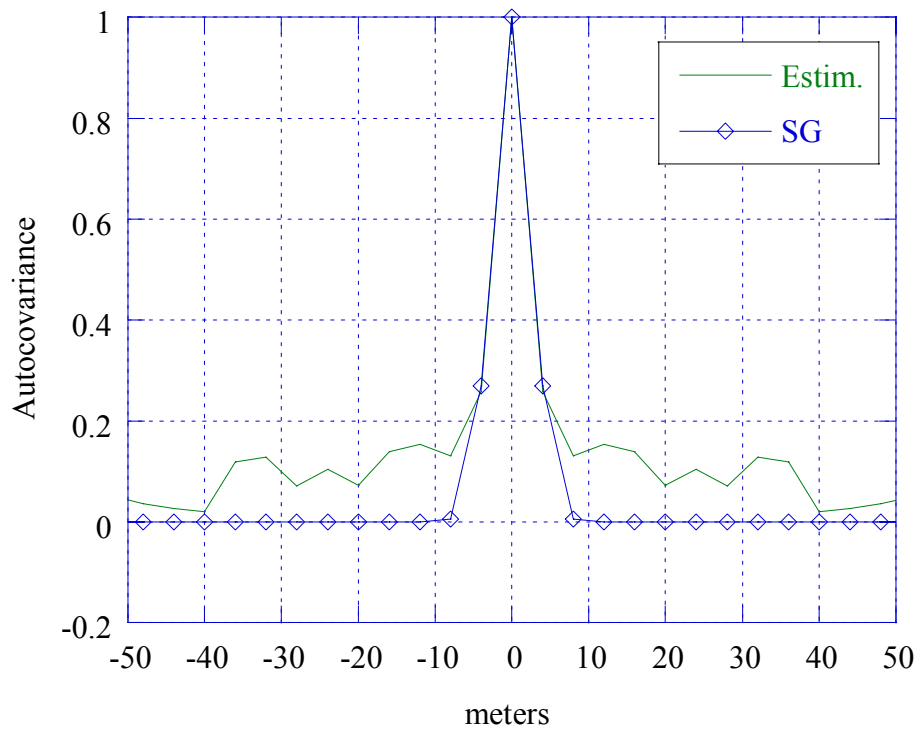


**Figure 2.45** – Texture covariance, grass field, range direction.

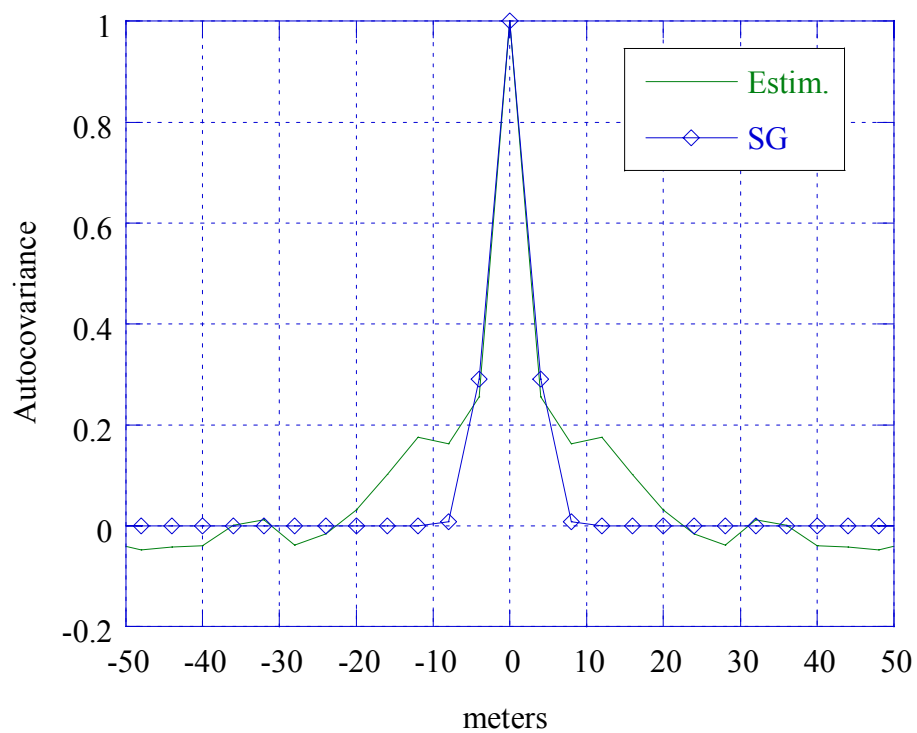


**Figure 2.46** – Texture covariance, grass field, cross-range direction.

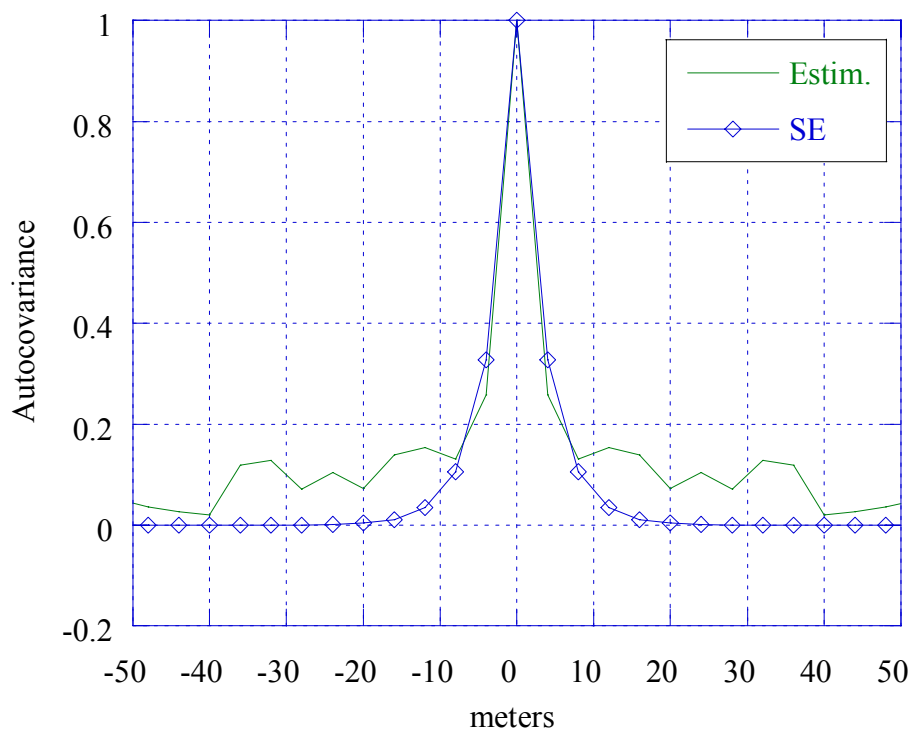


**Figure 2.47** – Texture covariance, grass field, range direction.

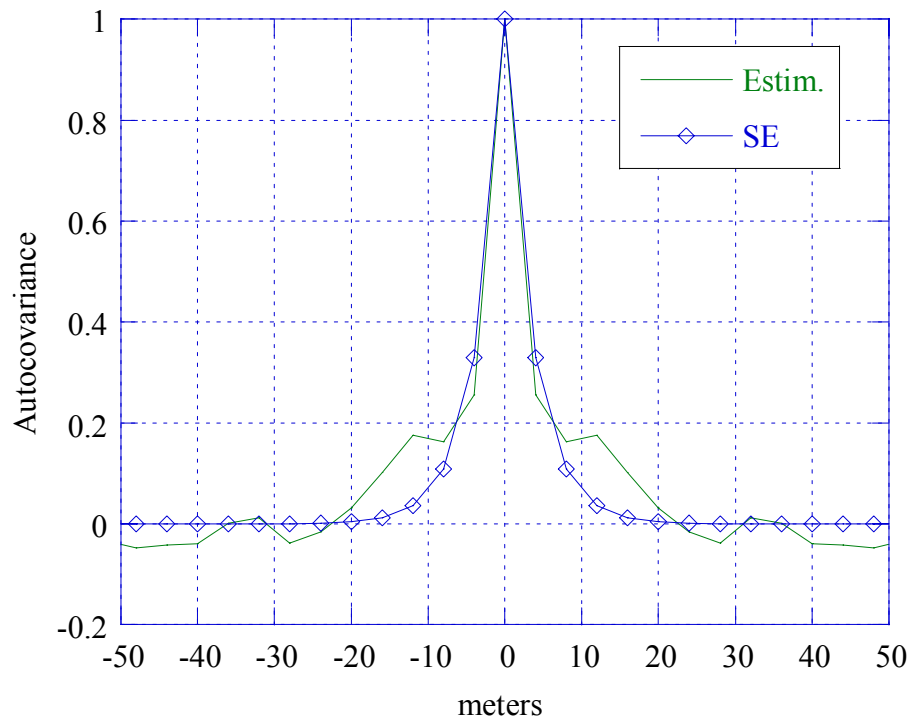


**Figure 2.48** – Texture covariance, grass field, cross-range direction.

Model	$\hat{x}_0$	$\hat{y}_0$	$\hat{y}'_0$	MMSE (cross-range)	MMSE (range)
PG	2.6 m	2.6 m	-	$5.5 \cdot 10^{-3}$	$8.3 \cdot 10^{-3}$
SG	2.6 m	2.6 m	10.4 m	$5.5 \cdot 10^{-3}$	$8.3 \cdot 10^{-3}$
SE	2.6 m	2.6 m	40 m	$2.4 \cdot 10^{-3}$	$6.6 \cdot 10^{-3}$

**Table 2.1** – Estimated parameters and MMSE, grass field.

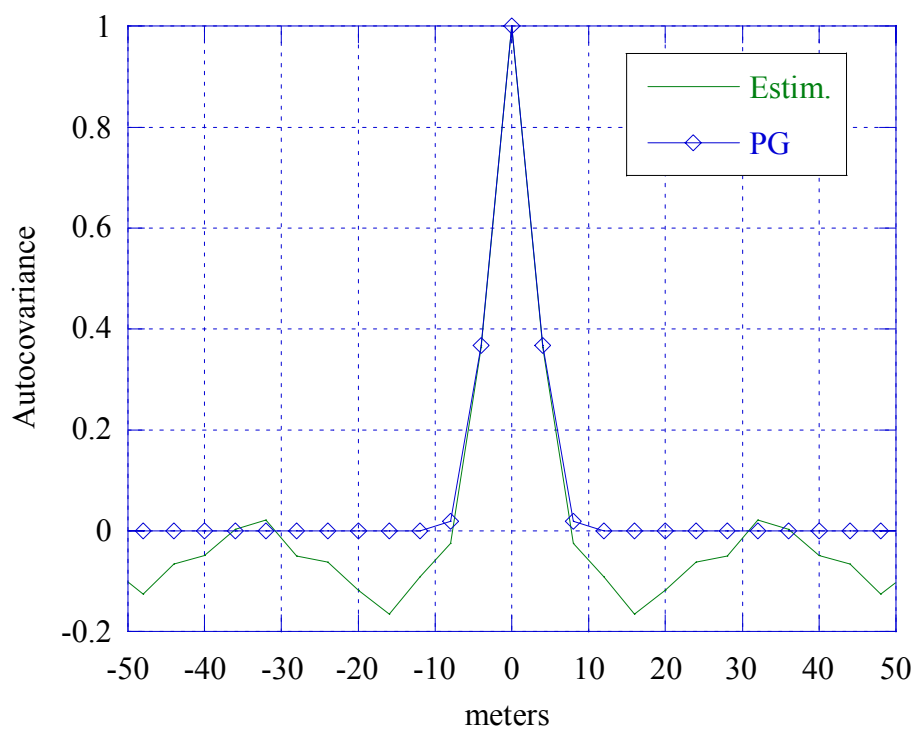


**Figure 2.49** – Texture covariance, wood and trees, range direction.

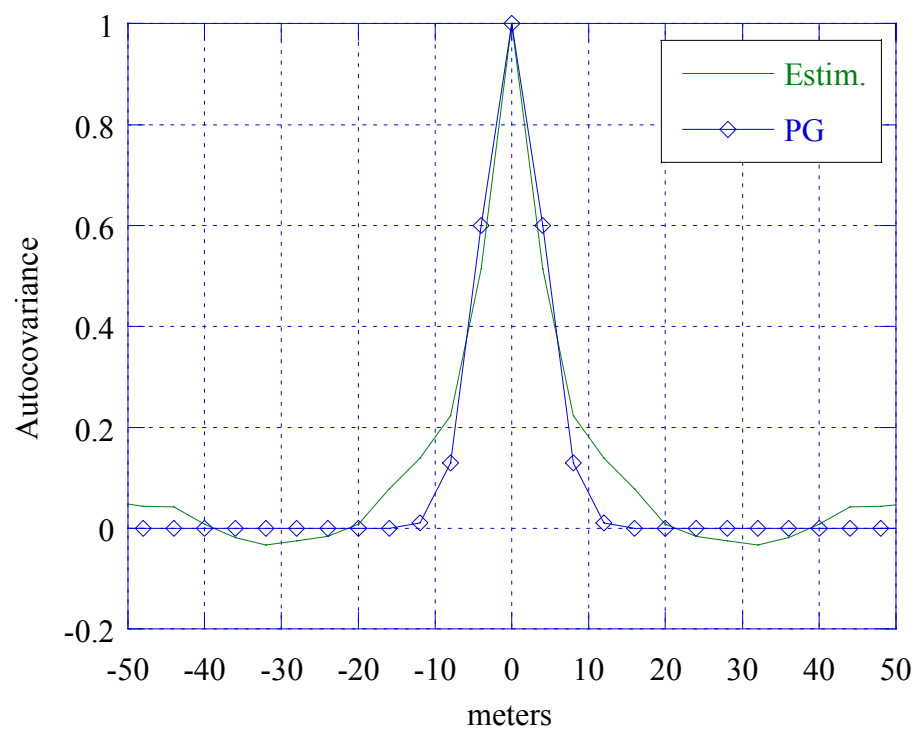


**Figure 2.50** – Texture covariance, wood and trees, cross-range direction.

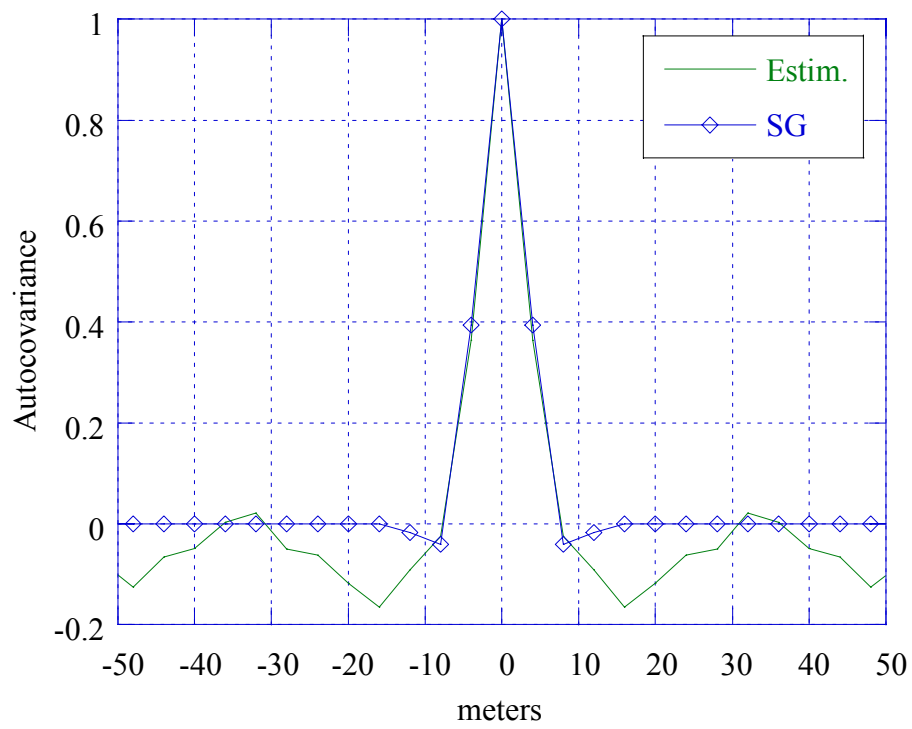


**Figure 2.51** – Texture covariance, wood and trees, range direction.

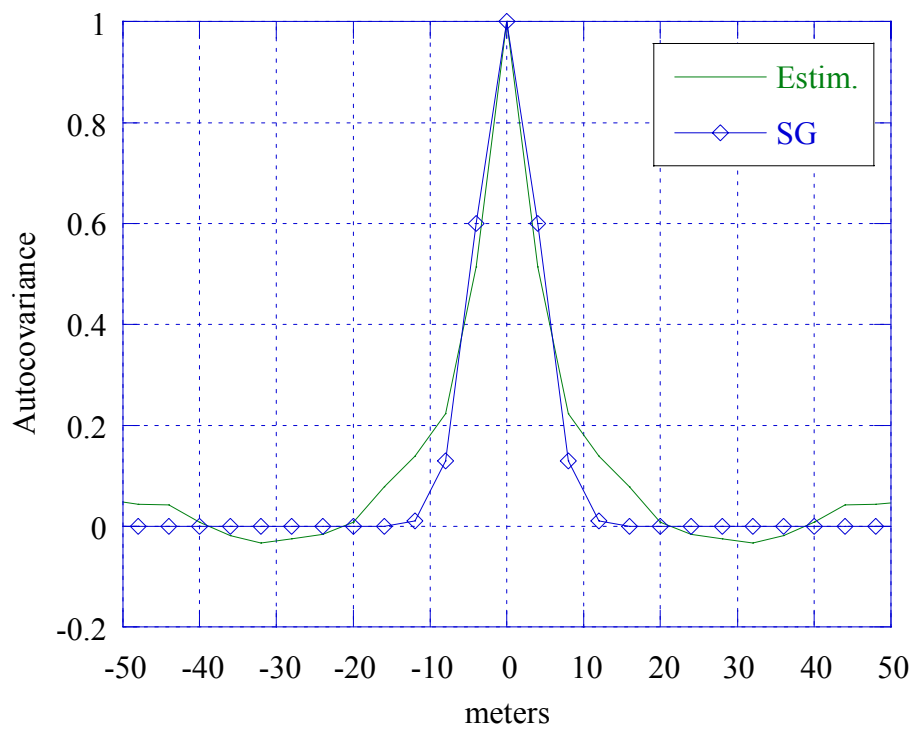


**Figure 2.52** – Texture covariance, wood and trees, cross-range direction.

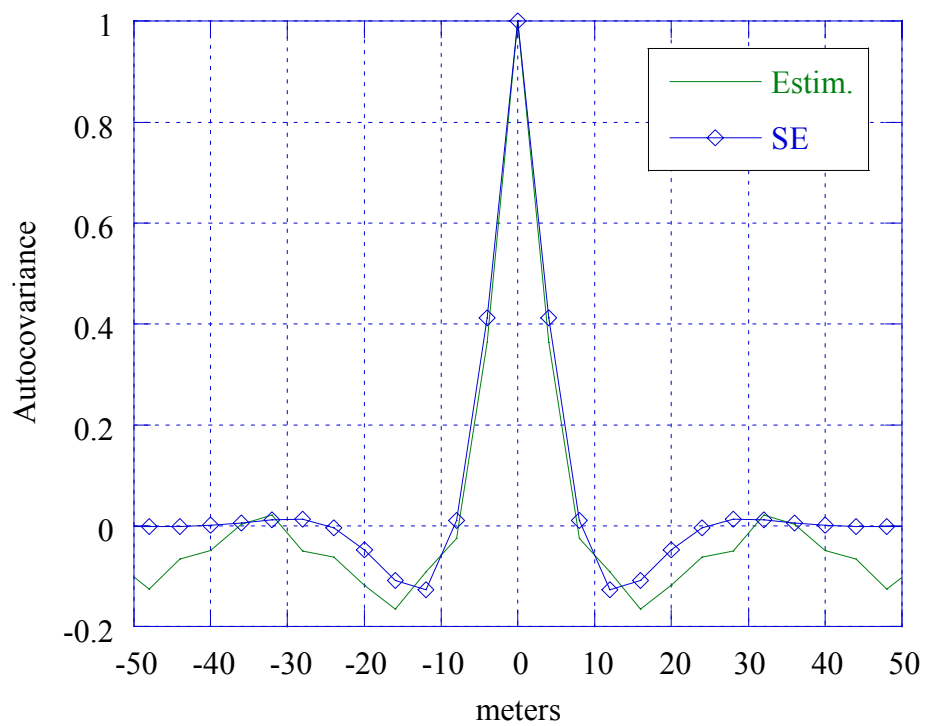


**Figure 2.53** – Texture covariance, wood and trees, range direction.

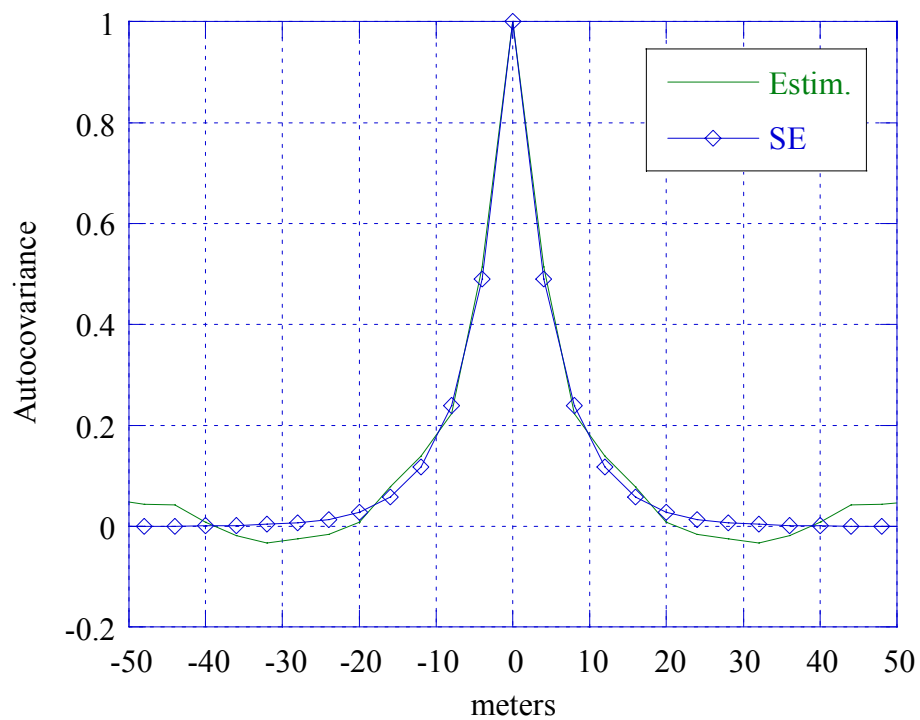


**Figure 2.54** – Texture covariance, wood and trees, cross-range direction.

Model	$\hat{x}_0$	$\hat{y}_0$	$\hat{y}'_0$	MMSE cross-range	MMSE range
PG	5.6 m	4.0 m	-	$2.9 \cdot 10^{-3}$	$7.0 \cdot 10^{-3}$
SG	5.6 m	6.0 m	4.4 m	$2.9 \cdot 10^{-3}$	$6.7 \cdot 10^{-3}$
SE	5.6 m	7.2 m	5.2 m	$9.0 \cdot 10^{-4}$	$4.8 \cdot 10^{-3}$

**Table 2.2** – Estimated parameters and MMSE, wood and trees.

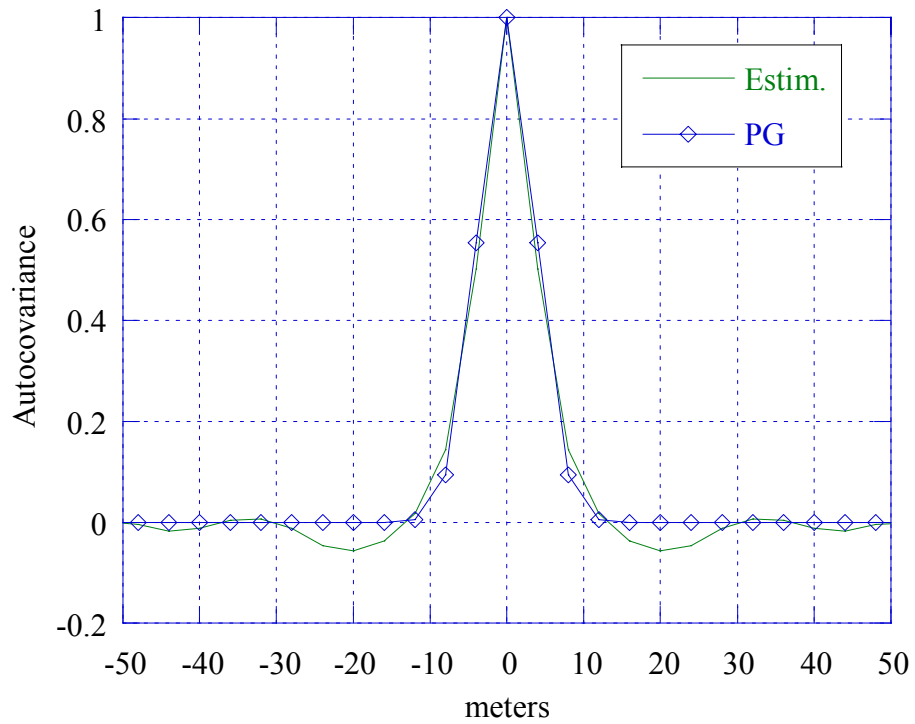


**Figure 2.55** – Texture covariance, wood and trees, range direction, file HB06192



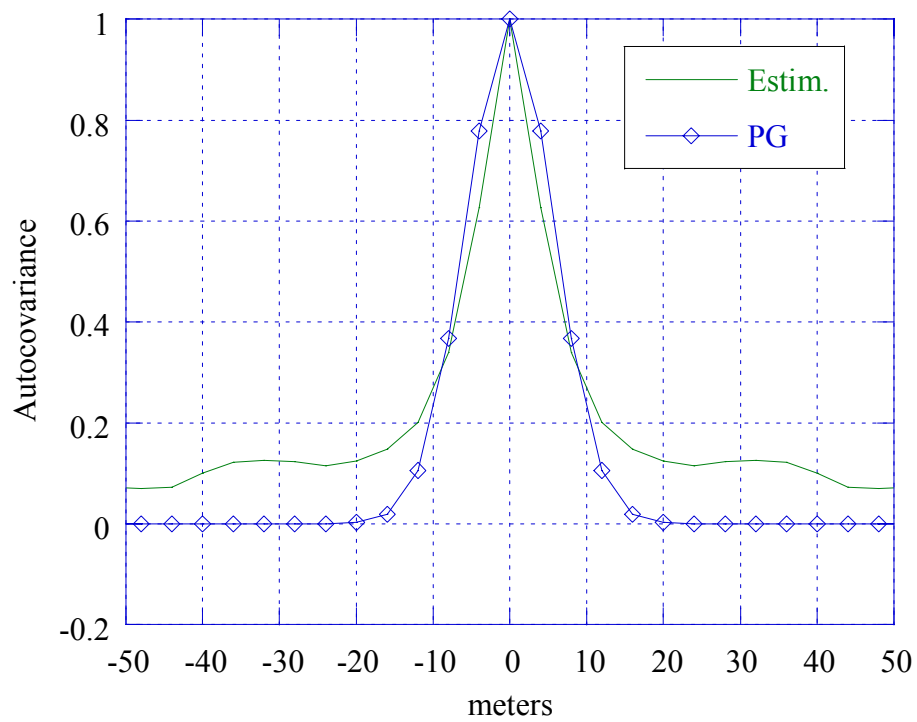


**Figure 2.56** – Texture covariance, wood and trees, cross-range direction, file HB06192.

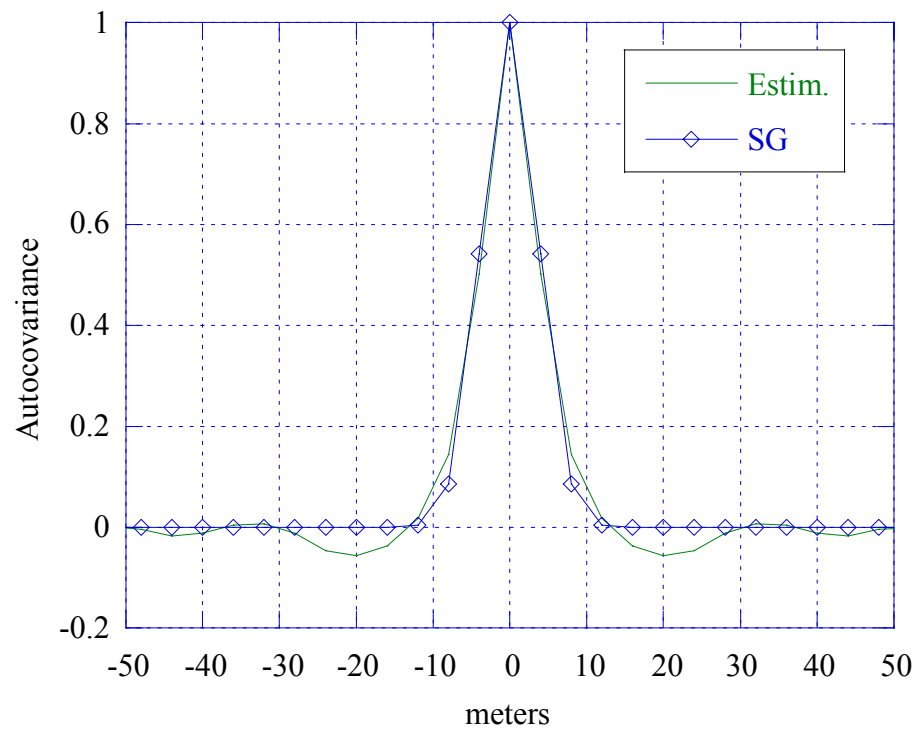


**Figure 2.57** – Texture covariance, wood and trees, range direction, file HB06192.

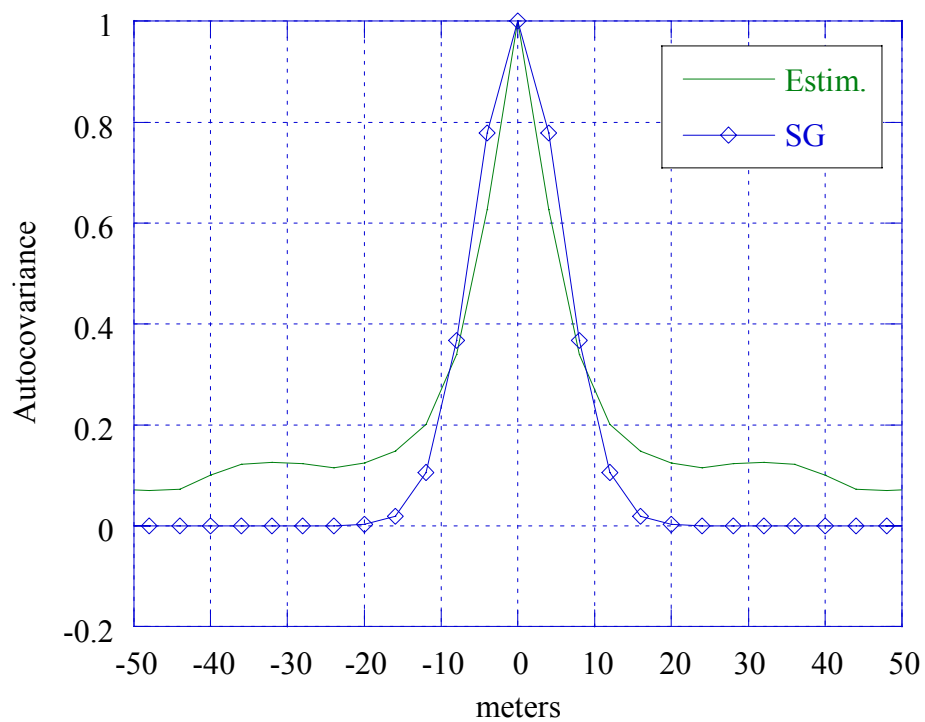


**Figure 2.58** – Texture covariance, wood and trees, cross-range direction, file HB06192.

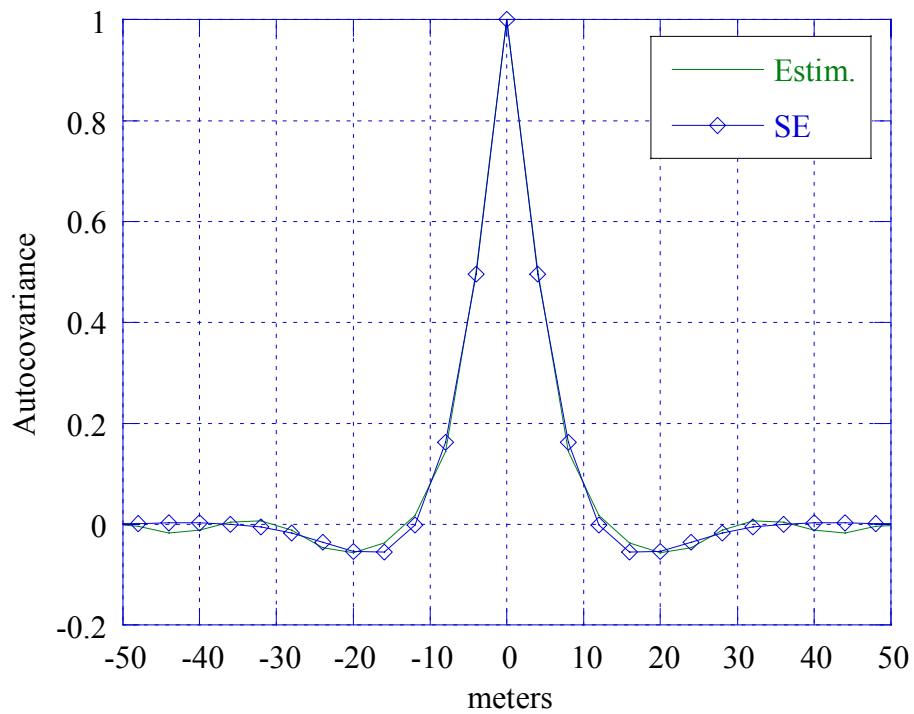


**Figure 2.59** – Texture covariance, wood and trees, range direction, file HB06192.

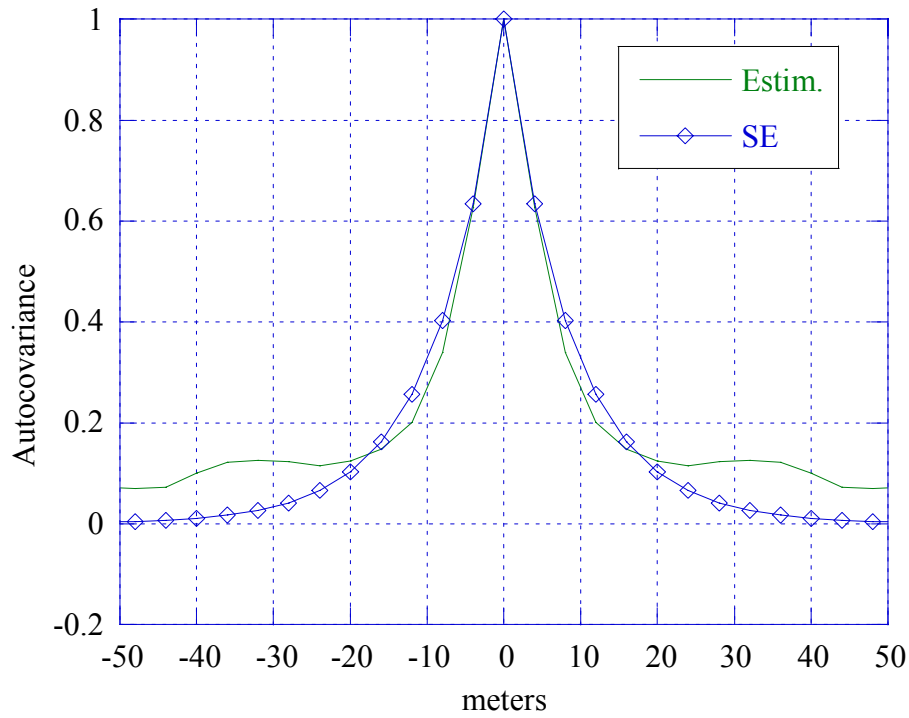


**Figure 2.60** – Texture covariance, wood and trees, cross-range direction, file HB06192.

Model	$\hat{x}_0$	$\hat{y}_0$	$\hat{y}'_0$	MMSE cross-range	MMSE range
PG	8.0 m	5.2 m	-	$2.5 \cdot 10^{-3}$	$4.0 \cdot 10^{-3}$
SG	8.0 m	5.2 m	19.2 m	$2.5 \cdot 10^{-3}$	$4.0 \cdot 10^{-3}$
SE	8.8 m	7.2 m	7.6 m	$1.2 \cdot 10^{-3}$	$2.5 \cdot 10^{-3}$

**Table 2.3** – Estimated parameters and MMSE, wood and trees, file HB06192.

## 2.5 Conclusions

Based on our results, we can conclude that, both for trees and grass field, the speckle is an almost-white process. The residual correlation is mainly due to the system oversampling. The covariance of the amplitude is mostly influenced by the covariance of the speckle, then the amplitude as well is an almost-white process. Conversely, the texture, that takes into account the structure of the vegetated areas, presents a slowing decreasing covariance, especially in cross-range direction and in dense vegetated areas. To deepen our analysis, we

tested three theoretical models for the texture covariance, the Pure Gaussian, the Shadowed Gaussian and the Shadowed Exponential. The best results have been provided by the shadowed exponential model both on trees and grass and in both range and cross-range directions. For the grass field the correlation length, as defined for the SE model, is on the order of 3 m in range and cross-range, for the wood on the order of 7 m.

## CHAPTER 3

# EXTENDED SPECKLE ANALYSIS

### 3.1 Introduction

In this chapter the statistical analysis of the non Gaussian speckle regime is extended, to get a flavor of the extent to and of the grade with which long tailed deviations from the classical Gaussian regime are found in high resolution SAR images of natural landscape areas. This analysis has been supported by four real data sets; each one has different characteristics like the presence or the absence of fields, forests, urban agglomerates and artificial elements (roads, guard rails, pylons). Moreover, the SAR sensors that acquired the images have different operating conditions: resolution, band, polarization, and illumination angle.

The approach used for the analysis is the same for each set: the first step consists in a visual inspection of the scene to understand which are the areas including nuisance elements like guard rails or pylons, and which are the areas containing interesting areas of terrain clutter (fields or forests). In a second time we applied the estimation algorithms of the speckle model parameters, and tests of the goodness of fit.

There are two classes of estimators and tests: the first class is used to investigate the speckle fluctuations to find the presence of long tailed speckle, the second class, which includes SNR estimation and a phase uniformity test, is used to confirm the results of the first class. In fact, some results could be degraded by a low SNR, or in a second way, the speckle phase could be not uniform. The statistical model that we use for fitting neglects thermal noise, thus, when SNR is not high enough, we choose to drop the model estimates. Also, for the non Gaussian speckle regime on natural areas, in which we are interested, it is expected that a random walk with a low number of effective scatterers should produce uniform phase like in the classical Gaussian case [Oli98], i.e. a circular distribution of the complex data. If this does not happen, which may be due e.g. to a predominant scatterer, we drop the model estimates. Summarizing, the first class of results provide the information for the long tailed speckle research; however, if these results are not confirmed by positive results in the second class of tests, they lose significance and are dropped.

## 3.2 Statistical models

For the speckle envelope model to be fit to the pixel amplitudes, the long-tailed Weibull distribution is assumed in this chapter. It accounts for deviations of the complex speckle pdf from the in phase and quadrature Gaussian components, i.e. Rayleigh envelope, shape parameter  $c$  less than 2 meaning long-tailed pdf (we recall that the Weibull pdf coincides with the Rayleigh pdf when  $c=2$ ). The Weibull model is intended here to model the speckle fluctuations only; for non-uniform texture scenes, the texture variations could be wrongly attributed to the speckle. Because of this problem, investigating non-Gaussian speckle statistics in real data is a difficult task, since speckle fluctuations and texture variations mix together to give the overall data pdf. To examine the speckle pdf, decoupling from texture effects is necessary. To this aim, different procedures have been applied and tested.

First, direct fitting of the Weibull speckle model over small possibly visually homogeneous [Oli98] image areas (patches) is considered. Unfortunately, arbitrarily small patches cannot be adopted to guarantee highly constant texture, since the too low number of pixels would result in inflated estimation variance. This method is expected to be intrinsically the less accurate, being sensible to possible texture variations inside the patch. Estimation of the scale and the shape parameters of the Weibull speckle pdf is carried out by classical statistical moments matching. Here, an overdetermined system of equations is used to fit the first 3 moments.

Second, for a better texture decoupling fitting to the data is carried out of a generalized compound model of the overall pdf, accounting for both speckle and texture fluctuations. In particular, the classical Gamma model for the texture is assumed, while speckle envelope is assumed again to be long-tailed Weibull distributed. The overall pdf is a Gamma-Weibull model [Ana99], which is characterized by three parameters: a scale parameter, a Gamma shape parameter  $\nu$  coding the variability of texture (when  $\nu \rightarrow \infty$  the texture is constant), and the Weibull shape parameter  $c$ . Their joint estimation is carried out by overdetermined moment matching (first 5 moments) on large image data blocks, to accurately estimate the high-order moments [Ana99]. A possible expected problem from this procedure is sensitivity to deviations of the texture from the classical Gamma model.

Finally, an approach that is expected to be more robust is to estimate the texture and then to compensate for it, by scaling the real data to bring the speckle to constant (unitary) power. After that, it is possible to proceed with speckle fitting.

### 3.3 Phase uniformity test and SNR estimation

To confirm the estimation results it is important to check our working hypotheses. The random walk model in which we are interested presumes an uniform distributed phase; also, neither the Weibull nor the Gamma-Weibull models account for thermal noise, thus we assume a high SNR. Thus, for each patch or block where we get parameter estimation we have to carry out a phase uniformity test and an SNR estimation.

The first is carried out by a Kolmogorov-Smirnov test for the hypothesis of uniform phase. It processes the pixels phase and then provides a binary response: uniform distributed phase or not. To check the SNR, we have to estimate noise power first. This is done by assuming that where the speckle is very weak, only thermal noise is present in practice. Accordingly, with a mobile window filtering of the patch size on the intensity image we reduce the speckle variations. The minimum value found is assumed as the noise mean power ( $N_0$ ). Then, by using the intensity values  $P$  of the patches, or by calculating the mean intensity  $P$  on blocks, we obtain SNR as follows:  $P / N_0 = (P_s + N_0) / N_0 = SNR + 1$ , where  $P_s$  is the mean power of the signal component; thus,  $SNR = P / N_0 - 1$ .

### 3.4 First data set

The data are from the Neckar river valley, Germany, with agricultural and hilly forest areas, as shown in fig. 3.1. The data have been acquired by the AER-II X-Band SAR from FGAN, 1m range resolution, incidence angle (from the horizontal direction)  $30^\circ$ , VV-polarization.

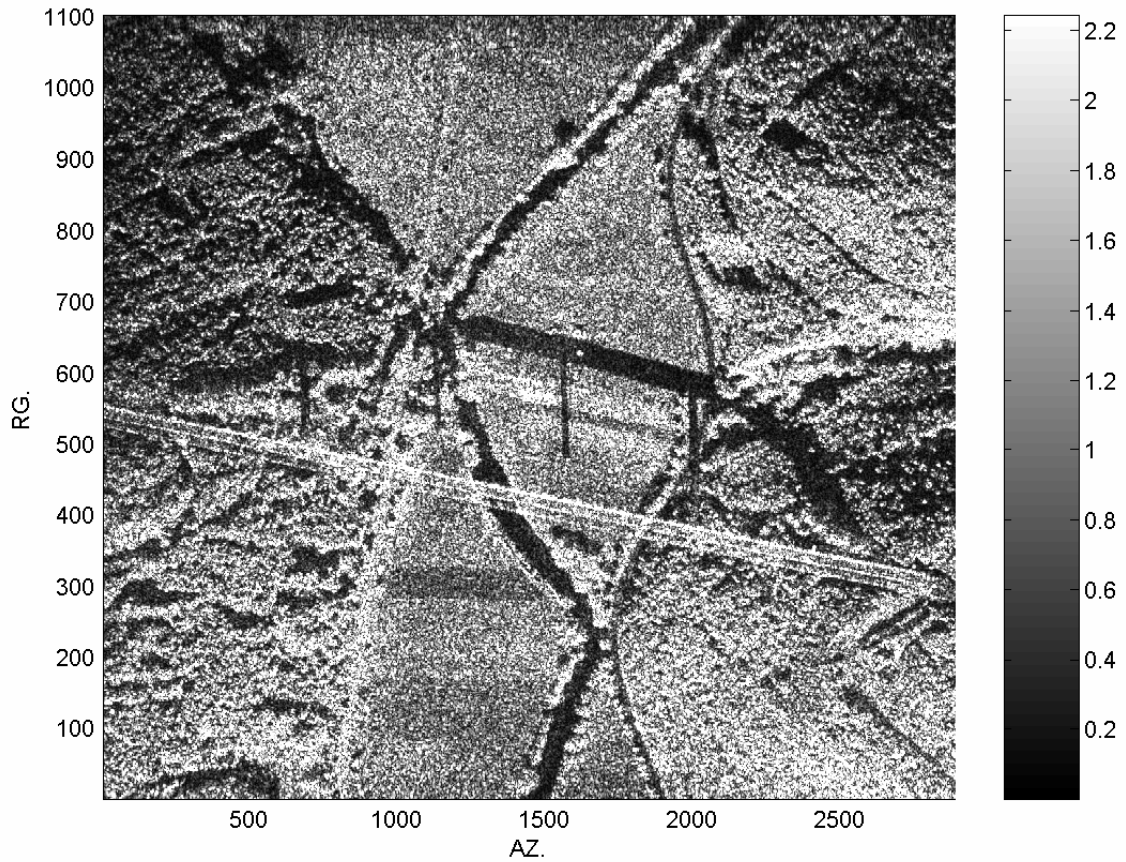


**Figure 3.1** - SAR scene.

It is possible to see a central field area, two lateral hilly forest areas and a bridge with three guard rails crossing the scene.

In a first time, we applied a direct Weibull fitting to the amplitude data from patches with dimension 20x50 (1000 pixel) in range and in azimuth, respectively, and also 11x25 (275 pixel). From a visual inspection we can infer that in some of these patches the texture is not highly constant, especially for the 20x50 case. However, further decreasing the patch dimension, and so the number of the pixels, reduces the statistical accuracy of the estimation for constant texture. So, using 20x50 and 11x25 pixels there are problems with texture, but less pixels do not return an accurate estimation (too high rmse and positively biased estimation).

The following figure shows with a color code the results of the direct Weibull shape parameter estimation for each patch: blue color codes a bad fitting (sum of the percentage differences between theoretical and estimated moments larger than 15%), or a non uniform



distributed phase in the patch, while the others colors identify the shape parameter values as from the color bar. For the 20x50 case, the minimum detected shape parameter (maximum long-tailed deviation from the classical regime) is 0.8.

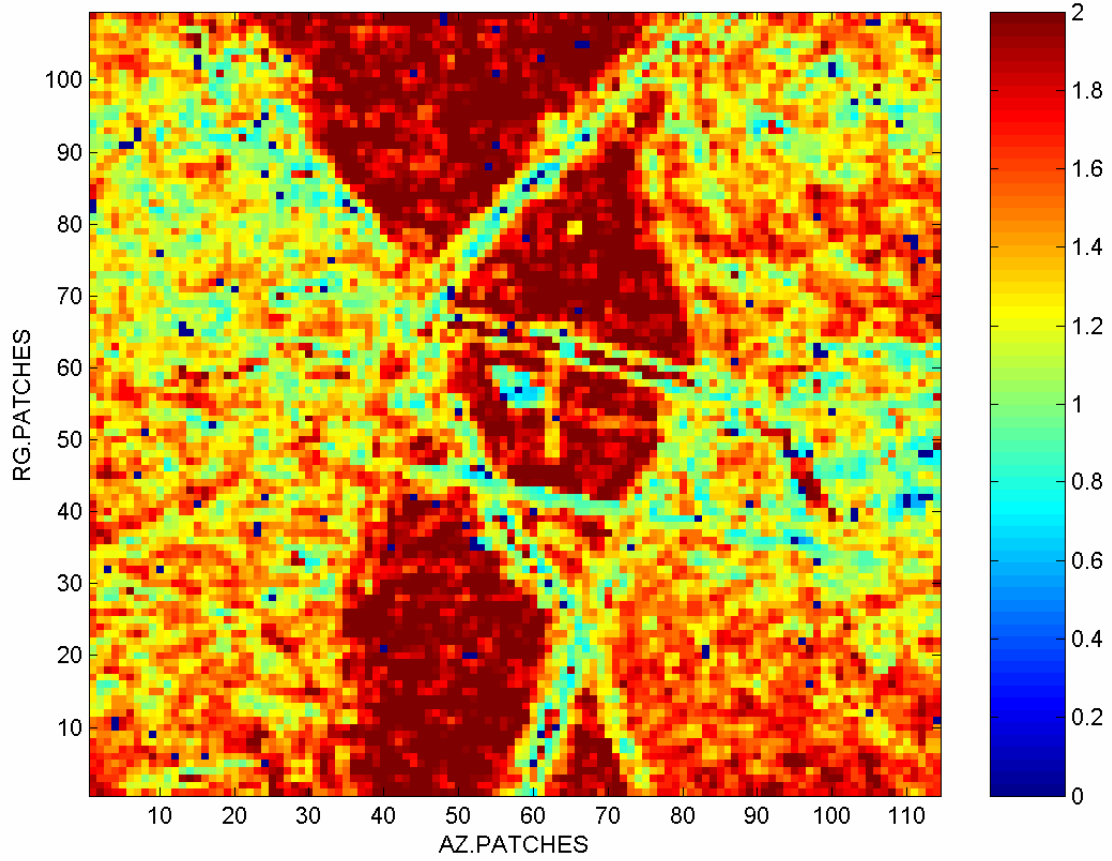


**Figure 3.2)**<sup>3</sup> - Shape parameter, patch: 20x50 (rg. x az.).

However, it is noted how a lot of Non Gaussian speckle patches are detected where there are sudden and deep texture variations, thus in these patches it is expected that direct Weibull fitting estimates larger deviations from the Gaussian speckle regime than the reality. This is also substantiated by the following analysis using 11x25 patches:

---

<sup>3</sup> Here and in the following maps, values of  $\hat{c} > 2$  are saturated to 2.

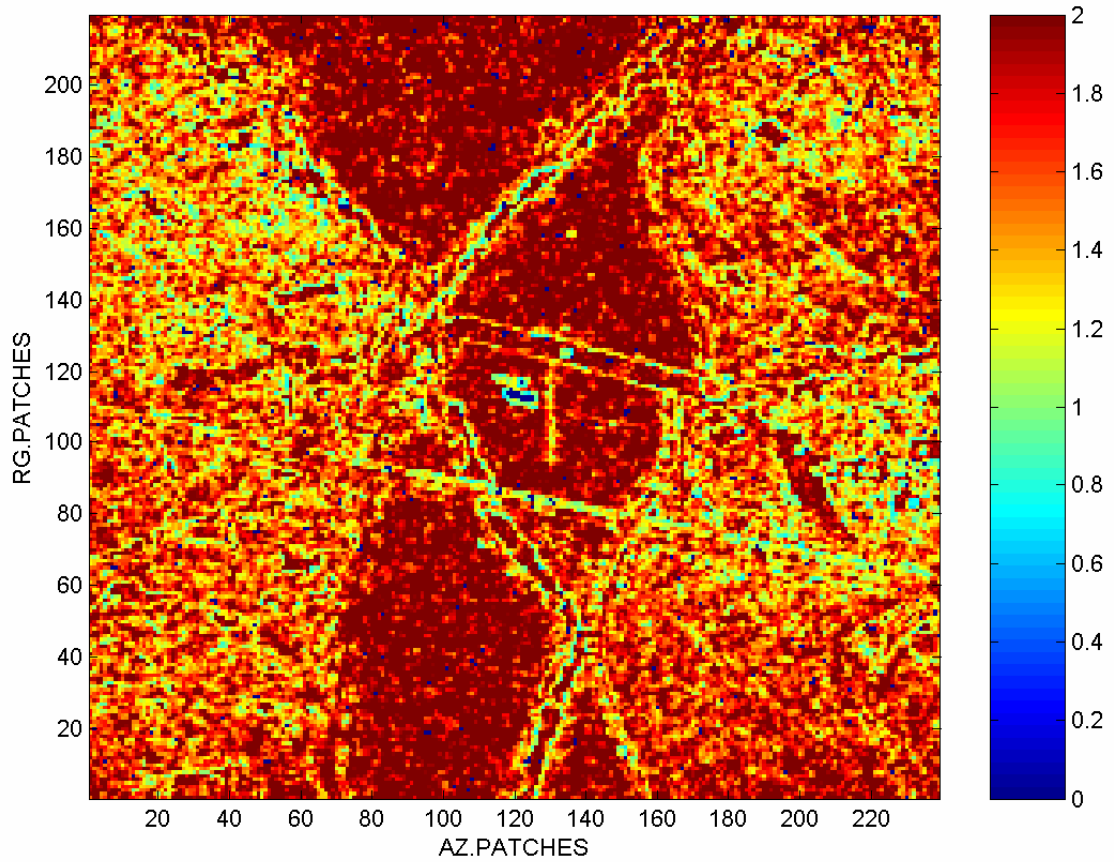


**Figure 3.3** - Shape parameter, patch: 11x25.

We can see that the deviations from Gaussianity tends to reduce. This confirms that, if we want to get a precise estimation of the shape parameter  $c$ , we have to better discern the speckle from the texture.

In this framework, we applied the Gamma-Weibull fitting on large blocks (160x400 in range and azimuth, respectively, with 50% overlap). This analysis provides the following shape parameter map. Again, the blue color codes bad fitting or non uniform phase.

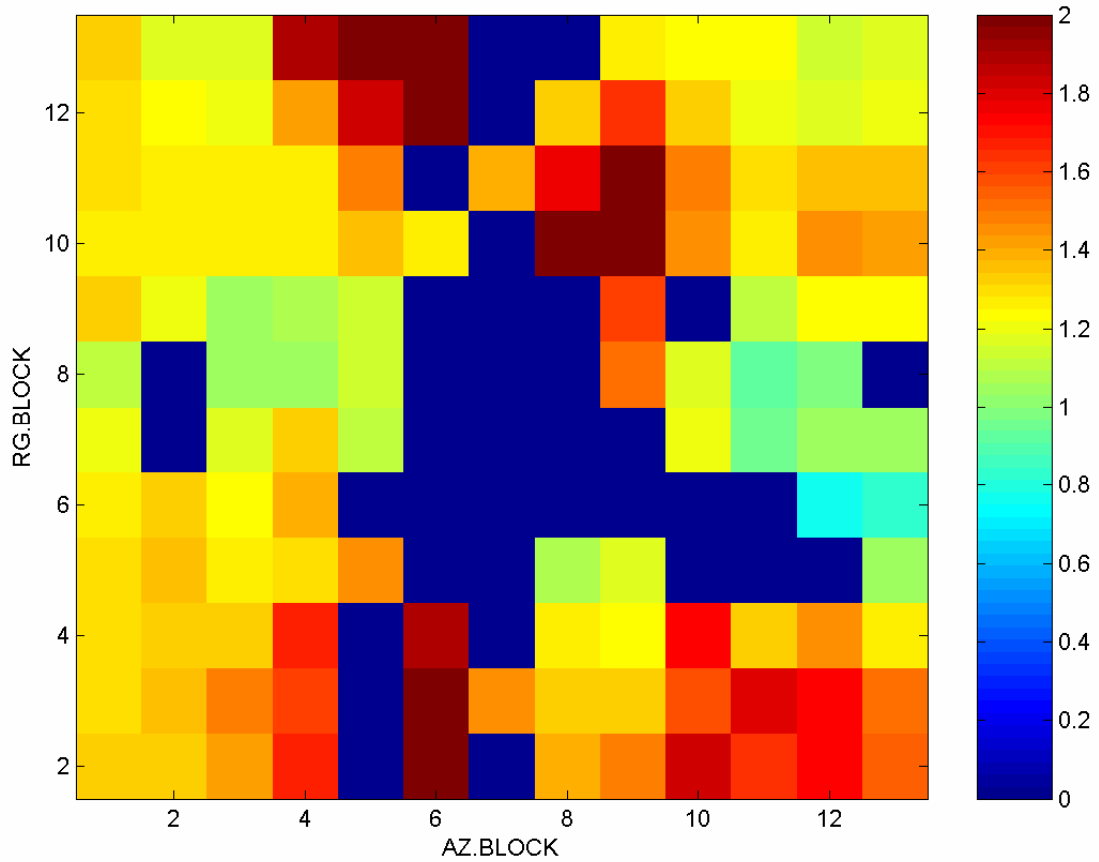


**Figure 3.4** - Shape parameter, block: 160x400.

Excluding blocks containing the bridge, the maximum detected deviation from Gaussianity is now shape parameter  $\hat{c}$  equal to 1. Thus, the values of  $\hat{c}$  are quite similar to those found with critical Weibull only fitting, so we expect that the texture is not Gamma distributed. Non accurate modelling is also indicated by the several blue blocks.

In the third analysis method, we estimate the texture in the scene by moving window filtering with a box of the patch size, and then compensate the data for it. In particular, texture is estimated on patches of size 11x25 (rg. x az.). This size was chosen since from a visual inspection the typical size of tree canopy in the forest area is of this order. However, Fig. 3.5 shows that where the texture is very variable, the compensation procedure leaves a residual texture.

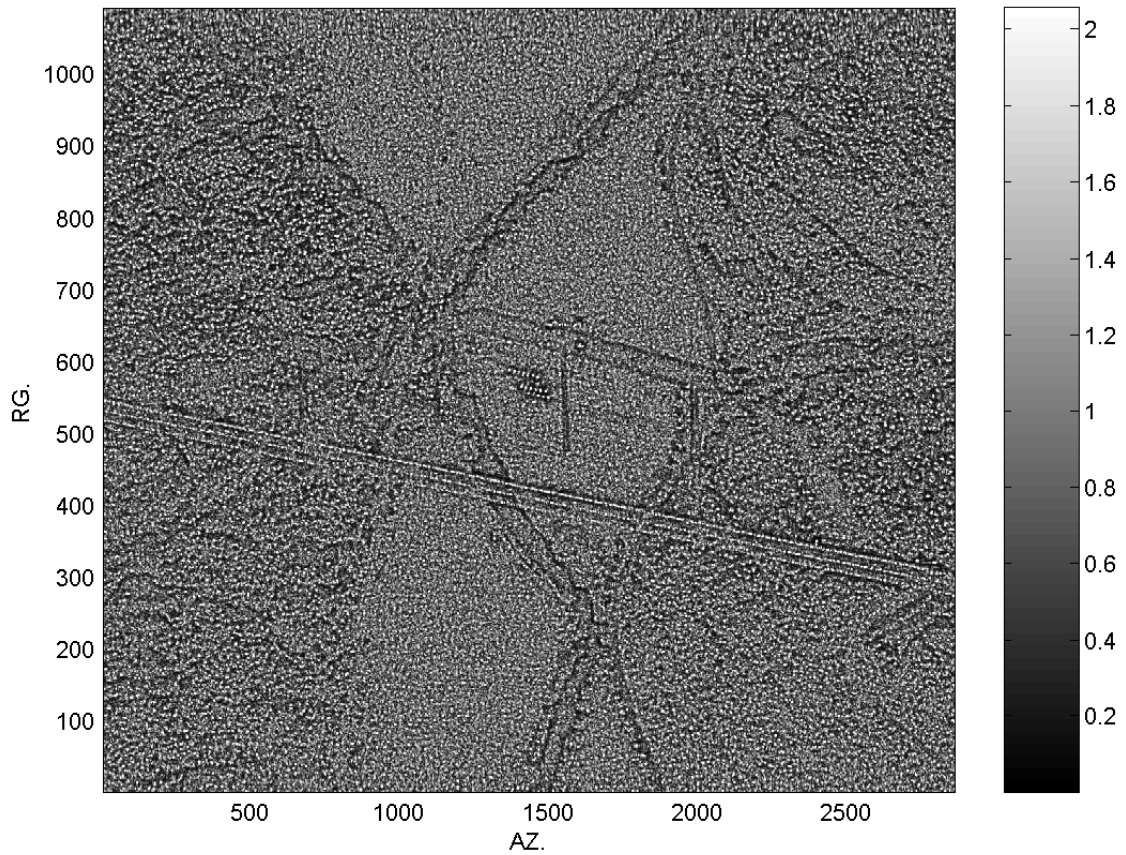


**Figure 3.5** - Scene after texture depuration.

Using a smaller patch size for texture estimation would enhance the spatial accuracy of the estimates, but at the cost of inflated variance of the estimates. Thus, we keep compensation with  $11 \times 25$  patches, and reduce the influence of possible residual texture on the subsequent Weibull parameter estimates by carrying out fitting again on large blocks. Doing this, the influence of possible local residual texture is subject to a dilution effect which makes the method robust. Using again the block size  $160 \times 400$ , the result is shown in Fig. 3.6. With this method the maximum detected long-tailed deviation from the Gaussian speckle regime is more limited than before, the minimum shape parameter being 1.44, for the block of index (10,3) in range and azimuth, respectively, which is in the forest area.

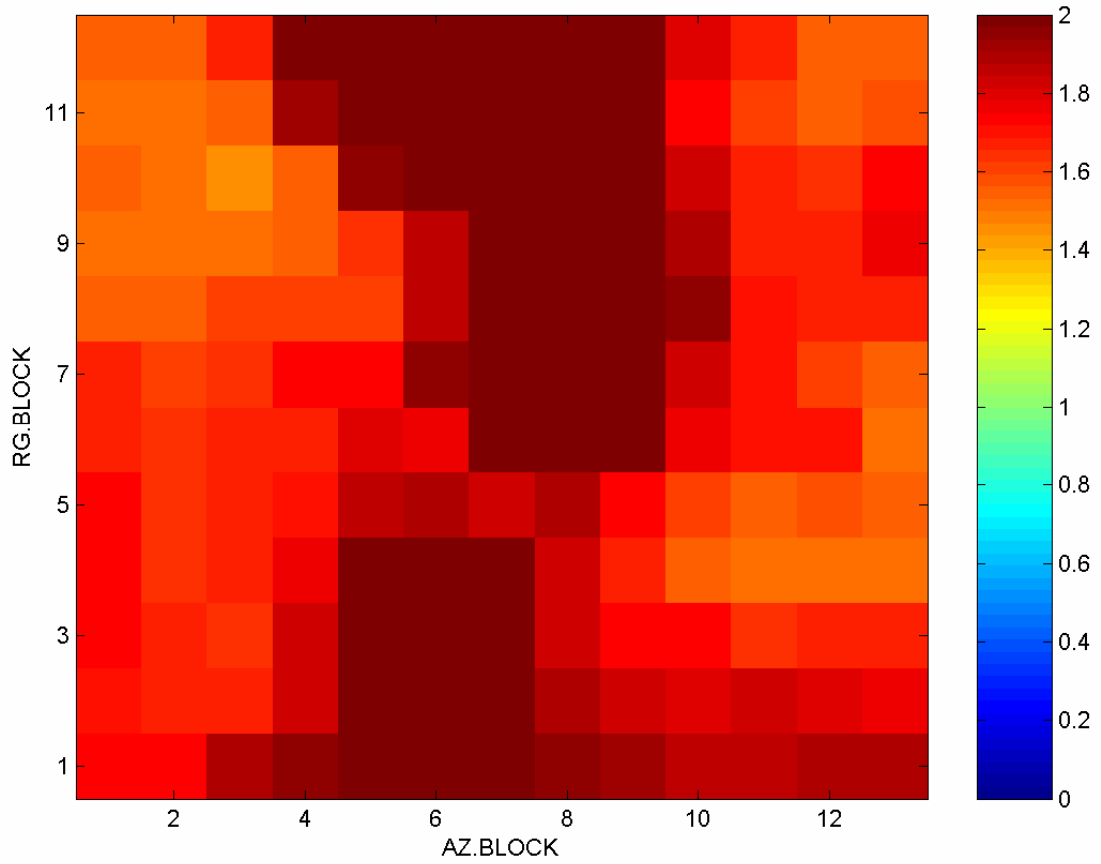


**Figure 3.6** - Shape parameter, block: 160x400.

The spatial extension of the estimated deviations from the Gaussian speckle regime has also been quantified by computing the histogram of the shape parameter values of the  $12 \times 13 = 156$  blocks, see Fig. 3.7.

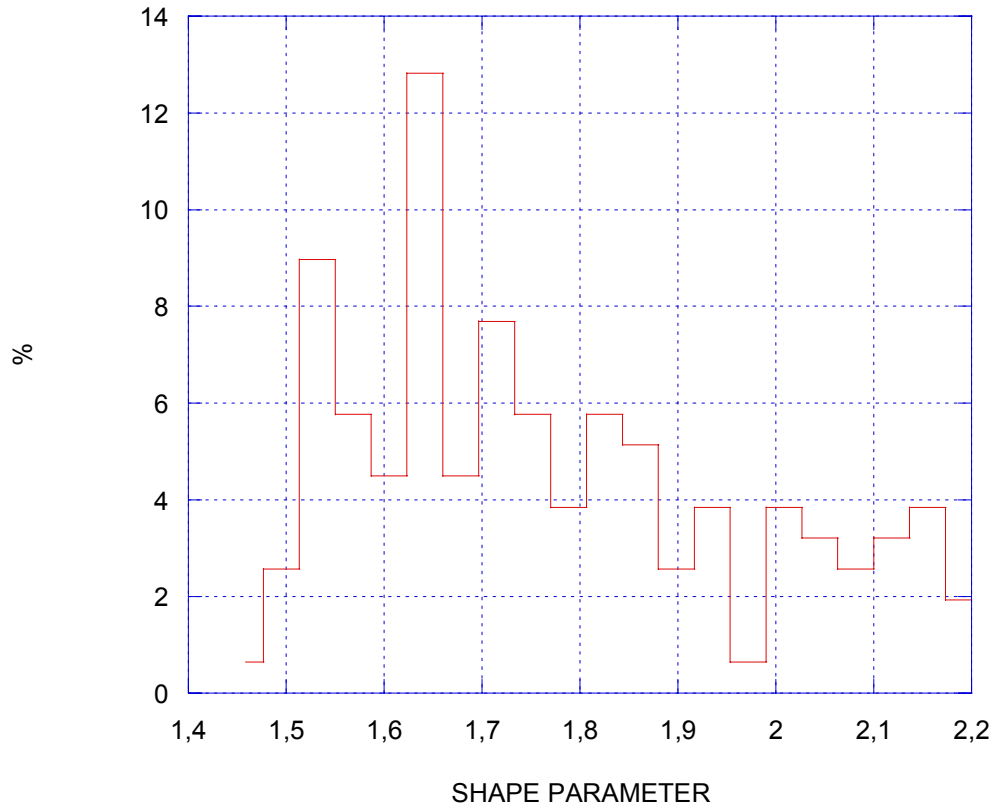


**Figure 3.7** - Histogram of  $\hat{c}$ .

Shape parameter values lower or equal to 1.5 appear in 3% of the image area, values lower or equal to 1.8 appear in 60% of the area (mostly in the forest area, see again Fig. 3.6).

To complete the analysis, we also checked if the SNR is high enough to neglect the thermal noise in the fitting model. The estimated SNR on the blocks is shown in Fig. 3.8. A high SNR is present in each block (minimum value is 22dB).

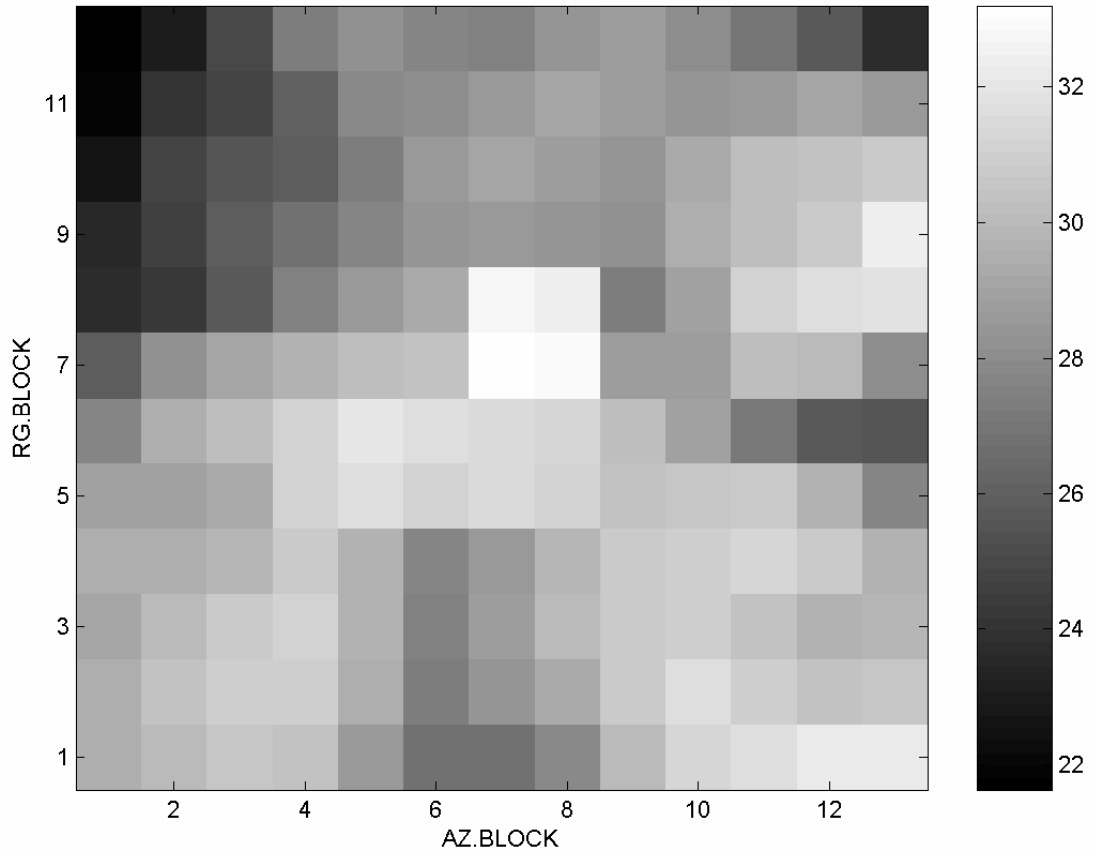


**Figure 3.8** - SNR map in dB, block: 160x400.

Also, we show the goodness of fit for the result of the most interesting block, that with rg. and az. index (10,3). To this aim, Fig. 3.9 shows a comparison between the theoretical moments of the model (for the estimated parameters) and the estimated moments from the real data. All moments are normalized to the moment of first order.

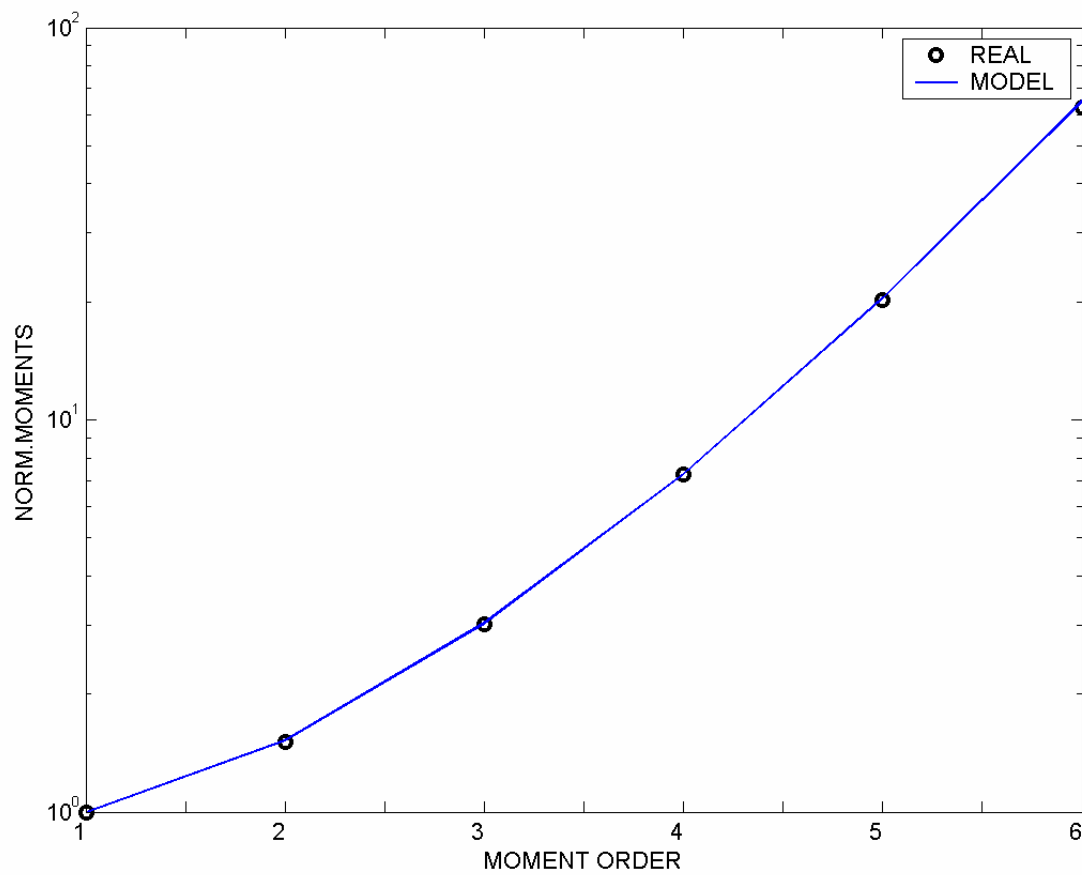


**Figure 3.9** - Moment fitting for block (10,3).

The first 5 moments of a Weibull-pdf with shape parameter 1.44 follow very well the experimental moments. Only the sixth moment is fitted with a slightly lower precision. Also, in Fig. 3.10 we compare the fitted Weibull pdf with the histogram of the compensated real data, again for block (10,3).



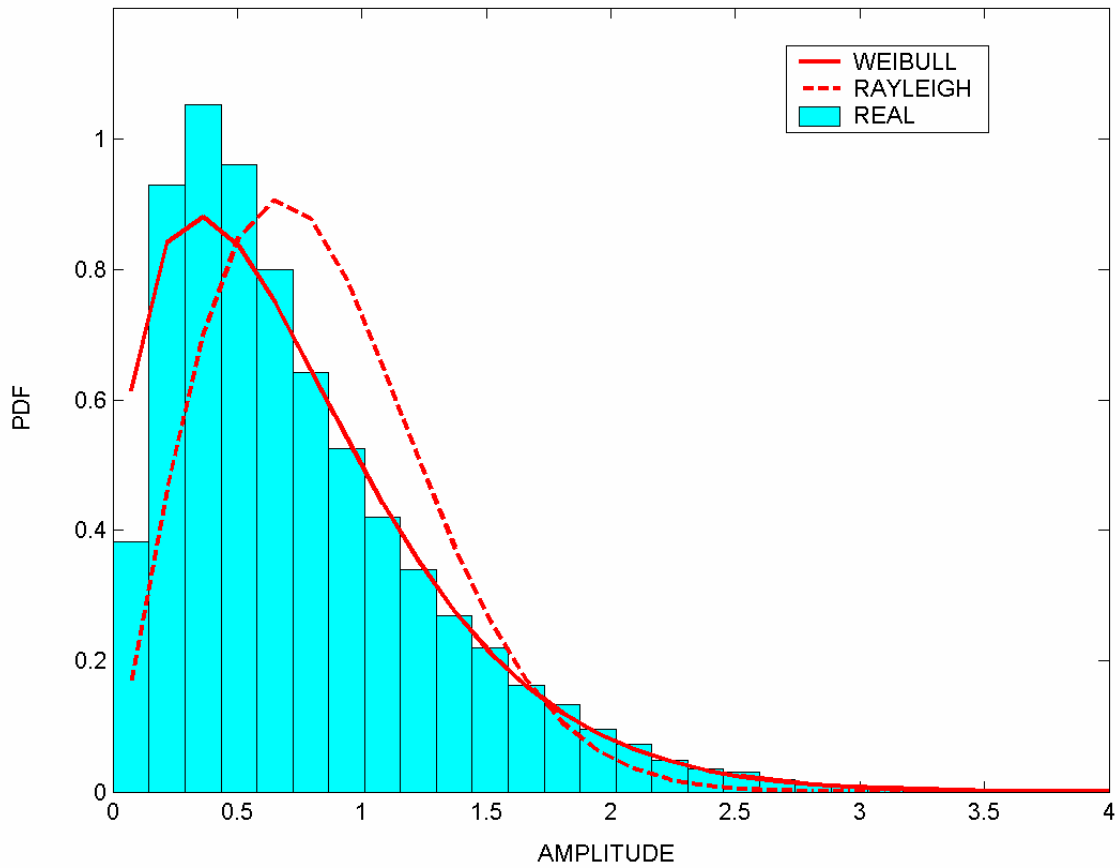


**Figure 3.10** - Pdf fitting for block (10,3).

It is apparent how the long-tailed pdf (Weibull with shape parameter 1.44) fits the data better than a Rayleigh pdf with same power.

### 3.5 Second data set

The data are from Oberpfaffenhofen, Germany, with grass, forest, and buildings areas, as shown in Fig. 3.11. The data have been acquired by the E-SAR L-Band SAR from DLR, 1.5m range resolution, HH-, VV-, and HV-polarization.

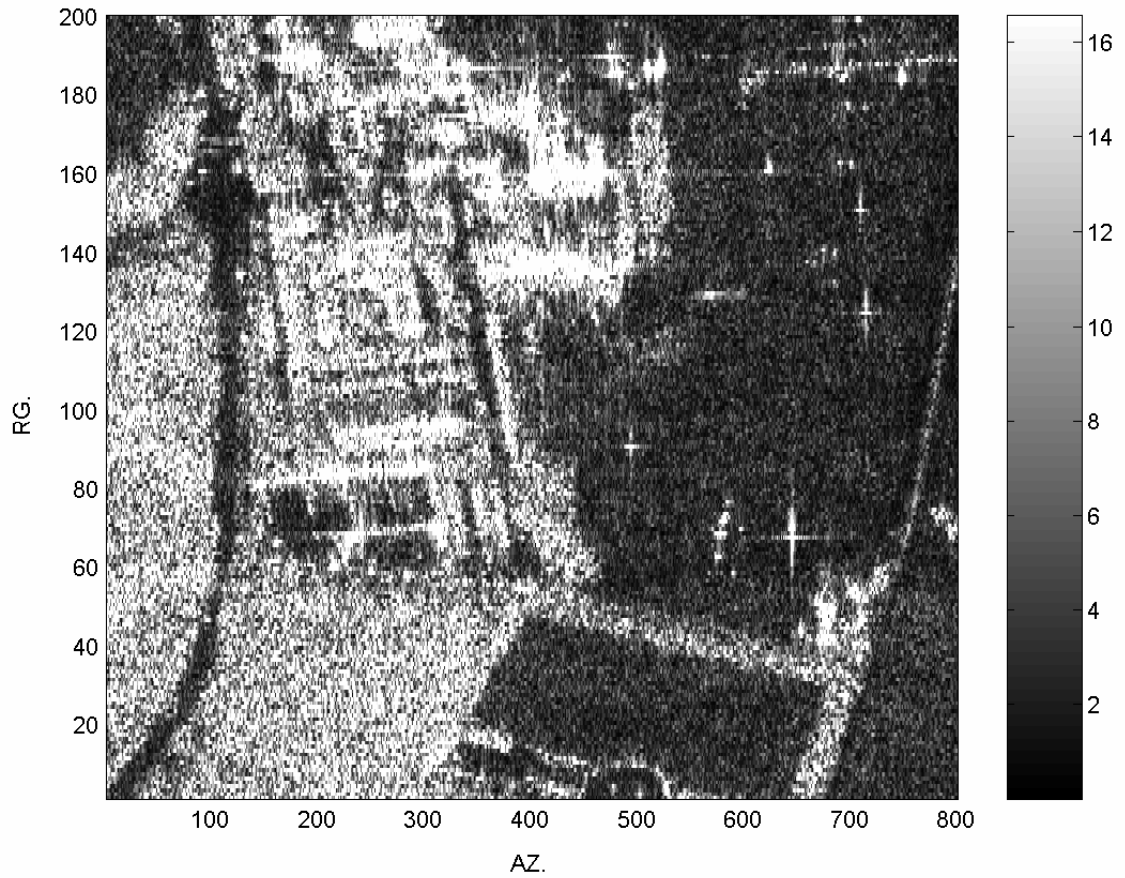


**Figure 3.11** - SAR scene (HH-pol.).

Unfortunately this SAR scene contains a number of pixels lower than the first data set. Moreover, it is not possible to estimate the speckle Weibull shape parameter on blocks with size  $160 \times 400$  as in the first data set, since these blocks would include a high number of nuisance elements like buildings or pilons. Thus, we now use blocks with size  $40 \times 100$  in range and azimuth, respectively. After checking with a visual inspection the typical size of tree canopy, we maintained the patch size for texture estimation and compensation at the same value ( $11 \times 25$ ) as before.

The following figure shows the map of the estimated shape parameters for the image with HH polarization. As usual, blue blocks are blocks where fitting is bad or phase is not uniform.

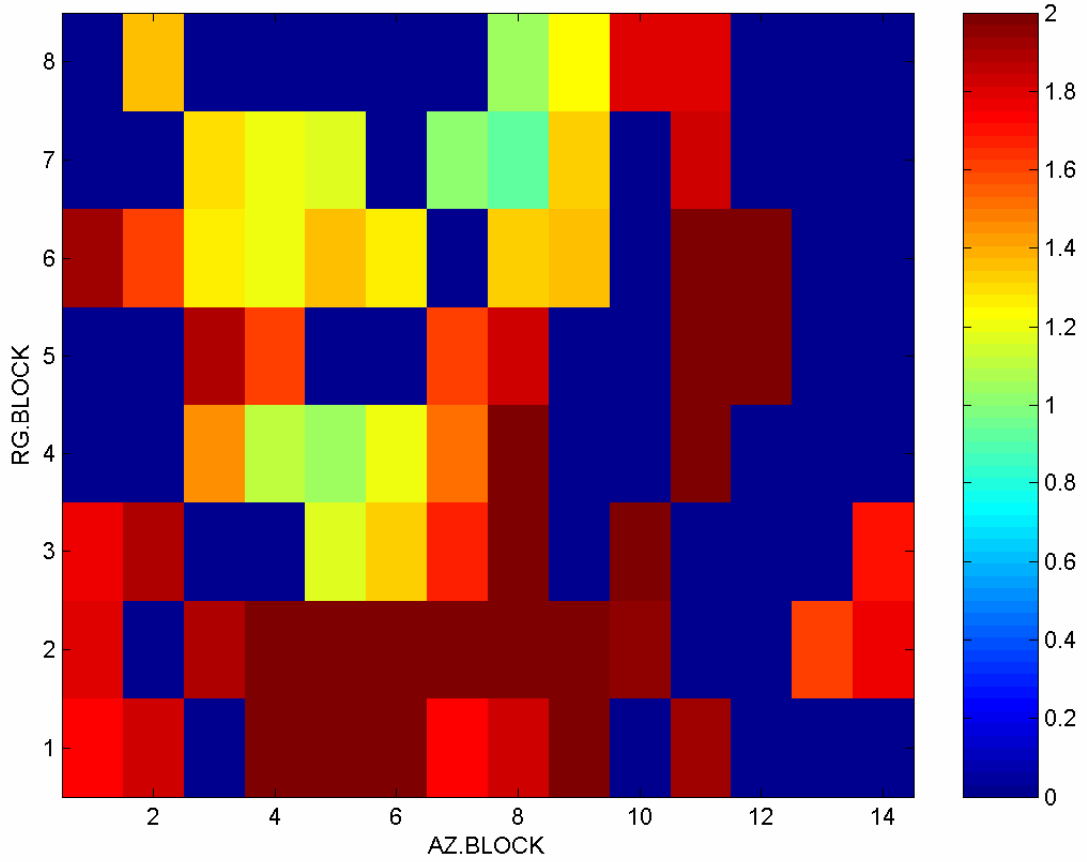


**Figure 3.12** - Shape parameter, block: 40x100.

Discarding results from blocks containing buildings, for the blocks including grass fields or forest only we find a minimum shape parameter 1.78 in block (3,1). Thus, the detected deviation from the Gaussian speckle regime on natural areas is less sensible than in the previous X-Band data set. This can be explained by the penetration of the L-band radiation in the layers of the vegetated areas. Although SAR resolution is high, the presence of distributed scatterers along the elevation direction makes the number of effective scatterers high enough to generate a more classical speckle regime.

We also notice that many blocks are blue coded in Fig. 3.12. In fact, for many of these blocks the check on model and experimental moments reveals that the model does not fit very well the amplitude of the data. The remaining blue blocks have non uniformly distributed phase according to the Kolmogorof-Smirnov test. The reason can be the presence of many pilons and other nuisance elements like buildings which produce a dominant deterministic scattering. Which blocks are declared with non uniform phase is shown in the next figure.

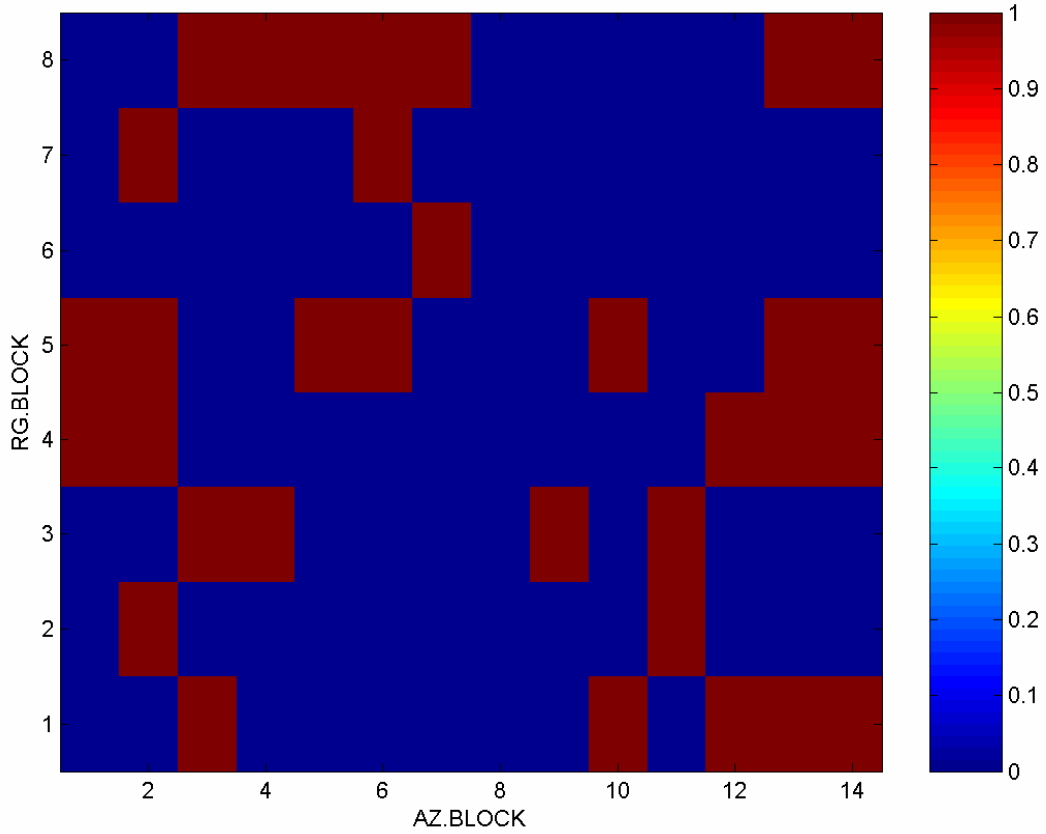


**Figure 3.13** - Non uniform phase map (brown blocks).

In this map the value 1 (brown color) codes non uniform phase. For the same blocks, in Fig. 3.12 we find blue color, the other blue blocks in Fig. 3.12 are bad fitted. In this data set we choose to investigate speckle statistics also in blocks with non uniform phase, since the Kolmogorov-Smirnov test is very selective. Phase can be declared to be non-uniformly distributed also when only a little deviation from uniformity is present. Thus, it can be important to further analyze the speckle also in these blocks.

This analysis revealed that block (1,13), containing pixels with range from 1 to 41 and azimuth from 600 to 700, that was previously dropped because of the non uniform phase declaration from the Kolmogorov-Smirnov test, exhibits a speckle shape parameter  $\hat{c} = 1.62$ . A visual inspection of the complex data scatterplot shows that distribution appears to be circular. Other blocks are not interesting, either because they contain deterministic scatterers or because the estimated shape parameter is almost Gaussian. However, observing the following figure with the scene after texture depuration, and the original scene in Fig. 3.11, it is easily seen that the interesting block (1,13) contains a few texture transitions, and also a

strong scatterer. This can sensibly affect the speckle shape parameter estimate, also accounting for the reduced dilution effect because of the small block size adopted for this data set. This has been confirmed by simulations.

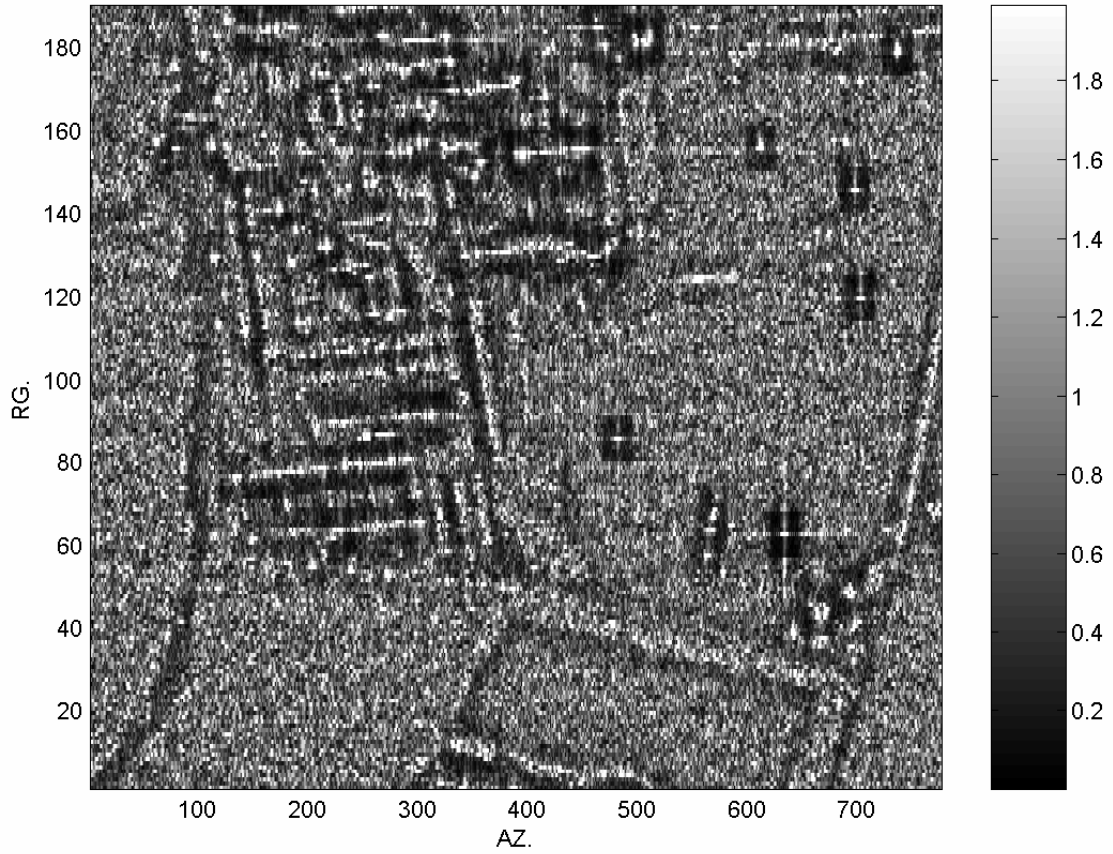


**Figure 3.14** - Scene after texture depuration.

Thus, we can infer that result  $\hat{c}=1.62$  is not reliable, and the minimum detected speckle shape parameter remains  $\hat{c}=1.78$  on block (3,1), i.e. range from 40 to 80, azimuth from 1 to 100. For this block with a non deep deviation from the Gaussian regime, we show the good fitting in terms of normalized moments:

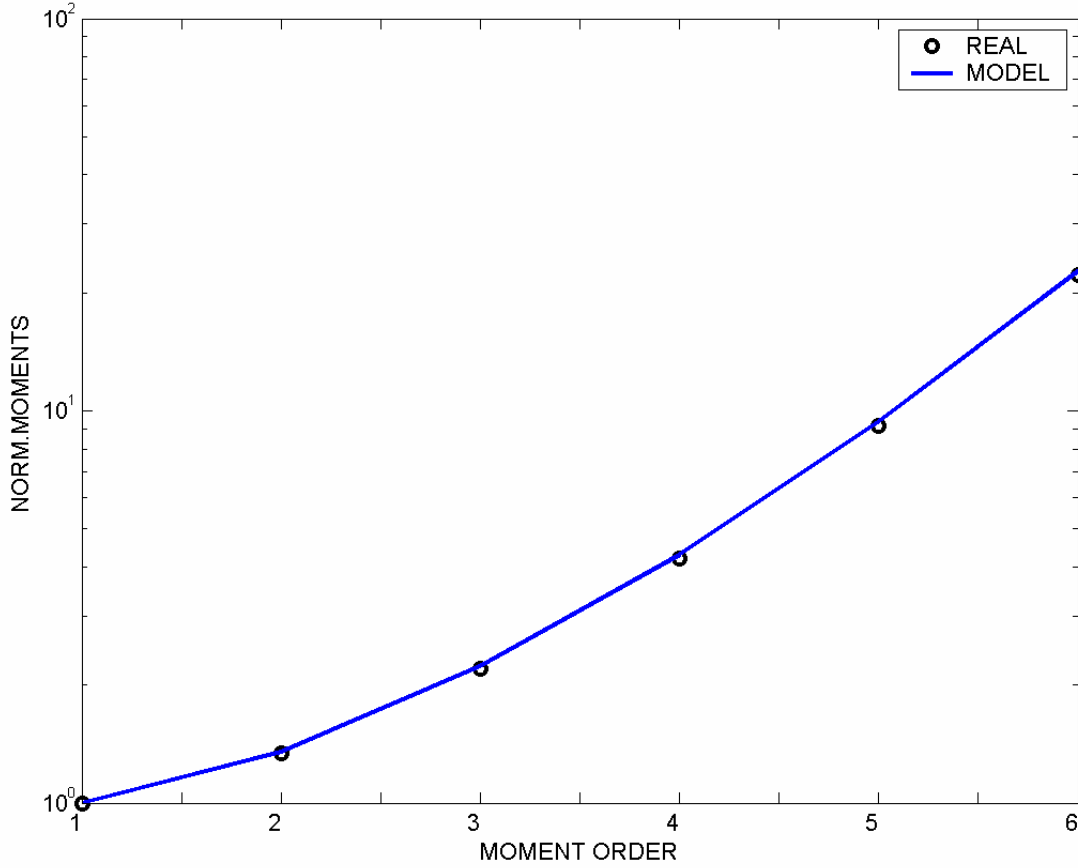


**Figure 3.15** - Moment fitting for block (3,1).

Results for the other polarizations, VV and HV, are even less interesting in terms of deviations from the classical speckle regime. The values of  $\hat{c}$  obtained over the natural areas in the image are closer to 2 than for the VV image.

### 3.6 Third data set

The data are from an agricultural zone in Recklinghausen, Germany. The data have been acquired by the AES-1 X-Band SAR from Aerosensing Radarsysteme, 0.38m range resolution, incidence angle  $45^\circ$ , HH polarization. In the SAR scene it is possible to see many agricultural fields, small zones with trees, country roads, isolated buildings, and a few strong point scatterers, probably pylons. Figure 3.16 shows a part of the scene that we examined:



**Figure 3.16** - First SAR scene portion (2000x2048 pixels, rg. x az.).

Analysis of this data set was carried out by texture estimation and compensation with moving window (patch) size  $17 \times 17$  and speckle shape parameter estimation on blocks with size  $128 \times 128$ . Patch size corresponds to that of the first and second data set, reshaped to square to account for the finer range resolution. We also checked again with a visual inspection that the typical size of tree canopy is of this order. Block size is intermediate between those used for the first and the second data sets. The block used is smaller than that of the first data set to cope with possible large spatial variability of the speckle shape parameter in the highly visually non stationary natural areas.

However, the results indicate that the SAR speckle in this image is basically Gaussian, as shown in Fig. 3.17 (as usual, blue codes bad fitting or non uniform phase).

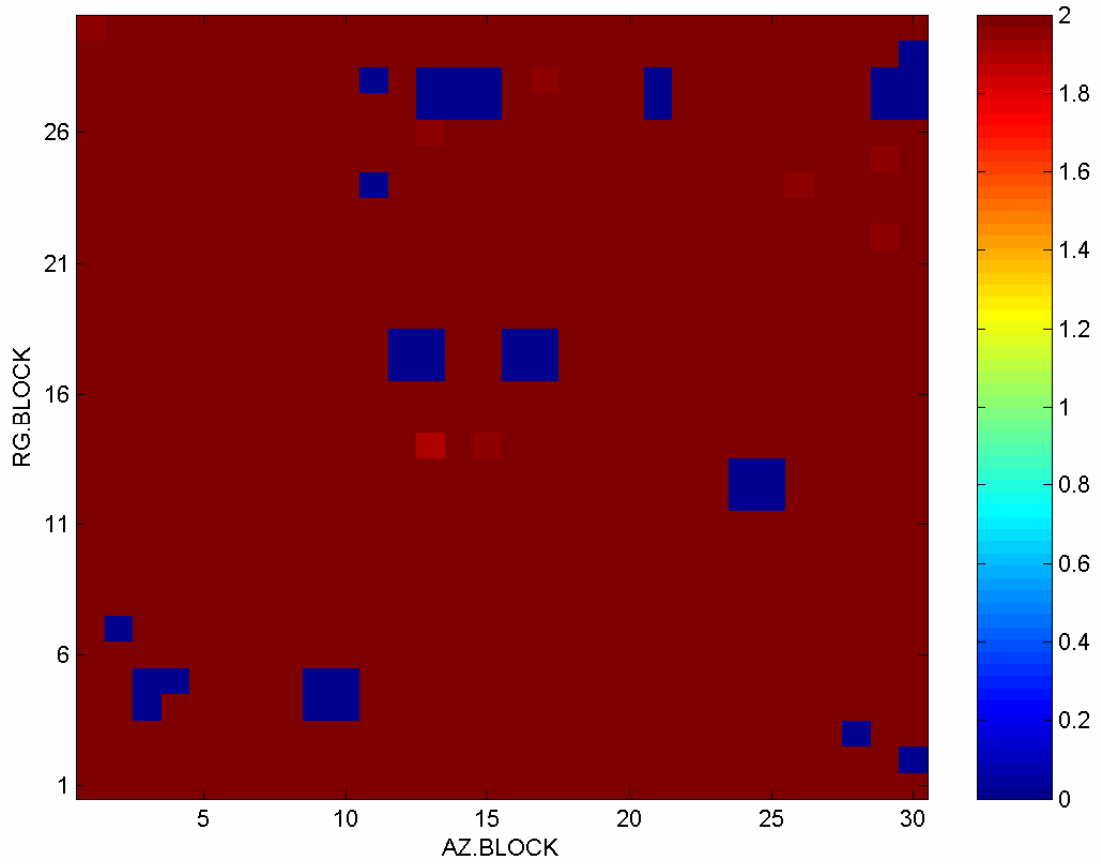


**Figure 3.17** - Shape parameter, patch: 17x17, block: 128x128.

The largest non Gaussian deviation in this portion of the image is given by  $\hat{c}=1.9$ , this deviation is very light and therefore it is not interesting.

Similar, slightly more interesting, results are got for the second portion of the image, shown in the next figure.





**Figure 3.18** - Second SAR scene portion (2000x2048 pixels, rg. x az.).

This portion is top adjacent to the previous portion. The corresponding estimated speckle shape parameter is shown in Fig. 3.19.

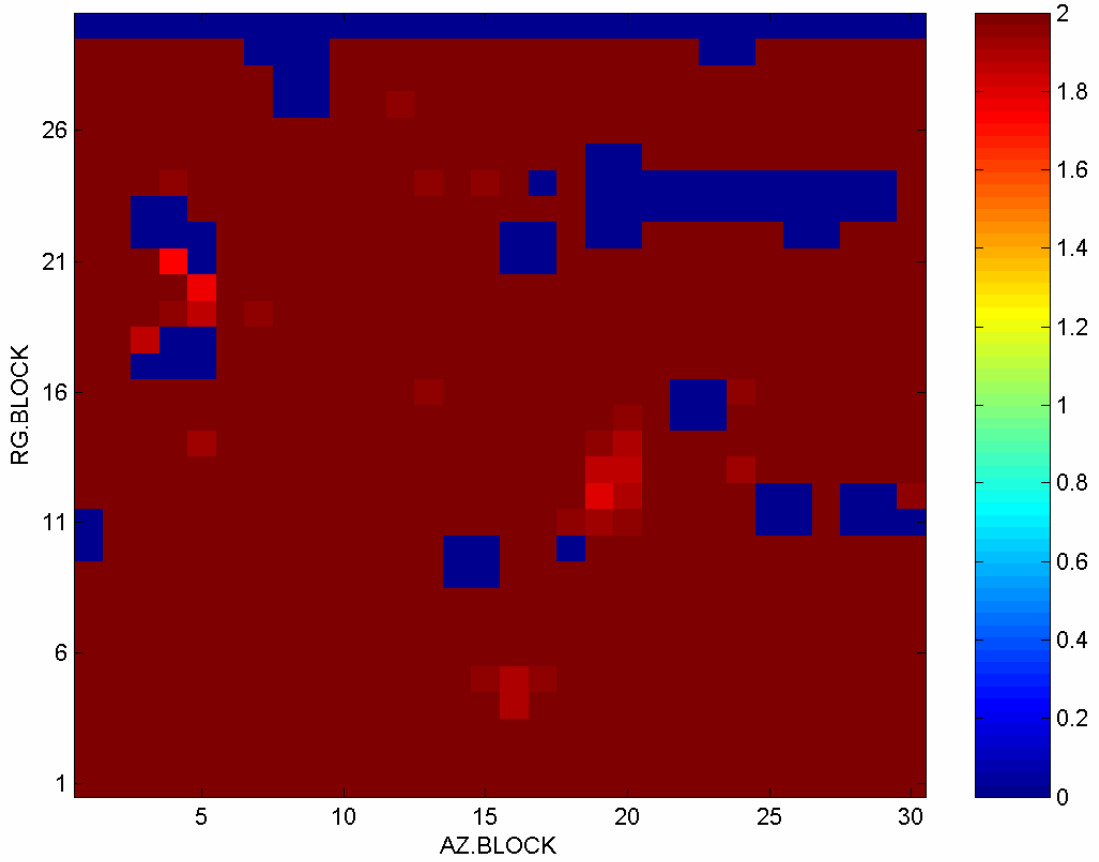


**Figure 3.19** - Shape parameter, patch: 17x17, block: 128x128.

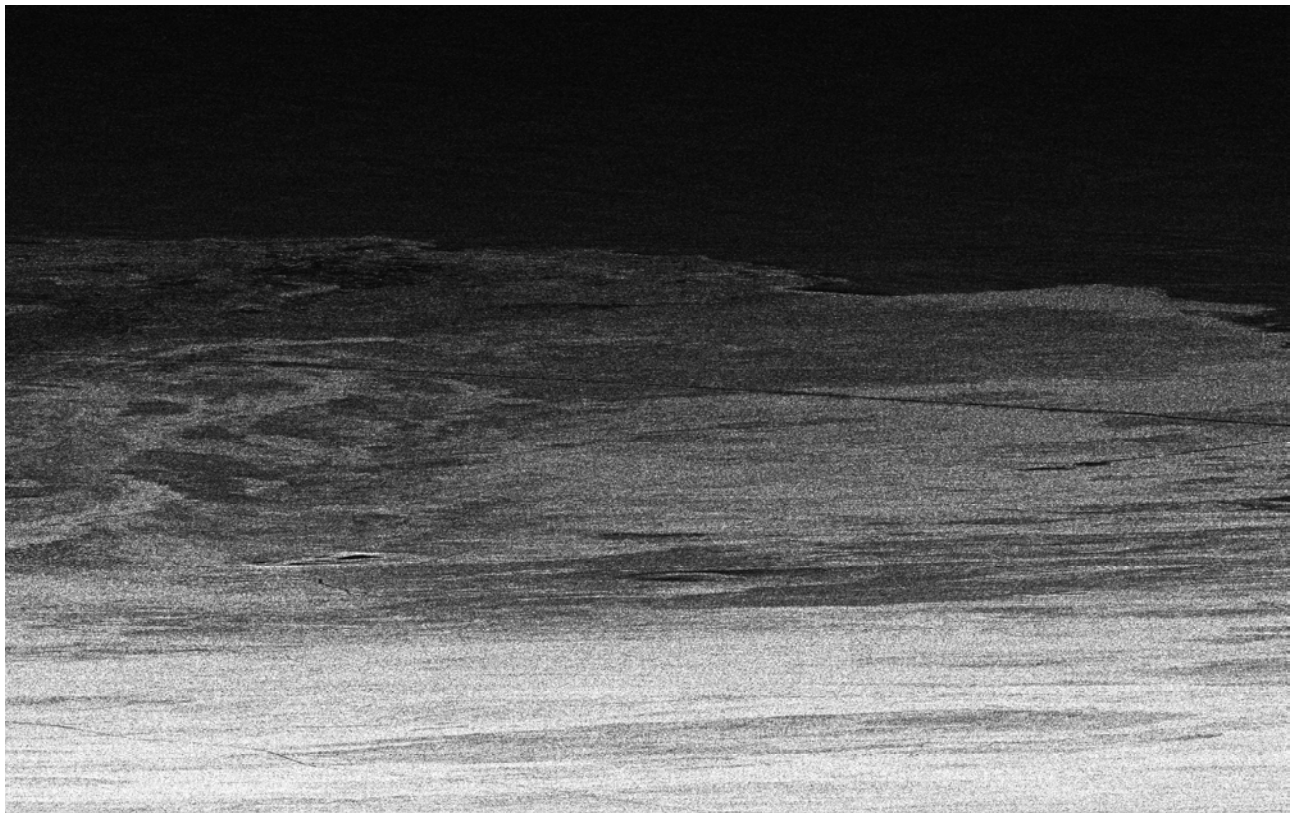
Values of  $\hat{c} \cong 1.7$  are found for blocks (21,4) and (20,5), but they are associated to areas that include strong artificial scatterers (buildings, pylons), thus the result is not interesting in the framework of our analysis. The next larger deviation from speckle Gaussianity is in block (12,19), corresponding to range from 704 to 832, azimuth from 1152 to 1280. Here,  $\hat{c}=1.8$  and the area is natural, seeming to contain trees. Summarizing, in the third data set only a light deviation from Gaussianity of the speckle regime is detected, in a not sensible percentage of areas.

### 3.7 Fourth data set

The data are from a littoral area in Kohala coast, Hawaii. The data have been acquired by the AIRSAR L-Band SAR from NASA Jet Propulsion Laboratory, 7.5m range resolution, incidence angle from  $70^\circ$  to  $30^\circ$ , VV polarization. In the SAR scene it is possible to see natural areas, roads, urbanized zones, an airport infrastructure, and the ocean. Because of its

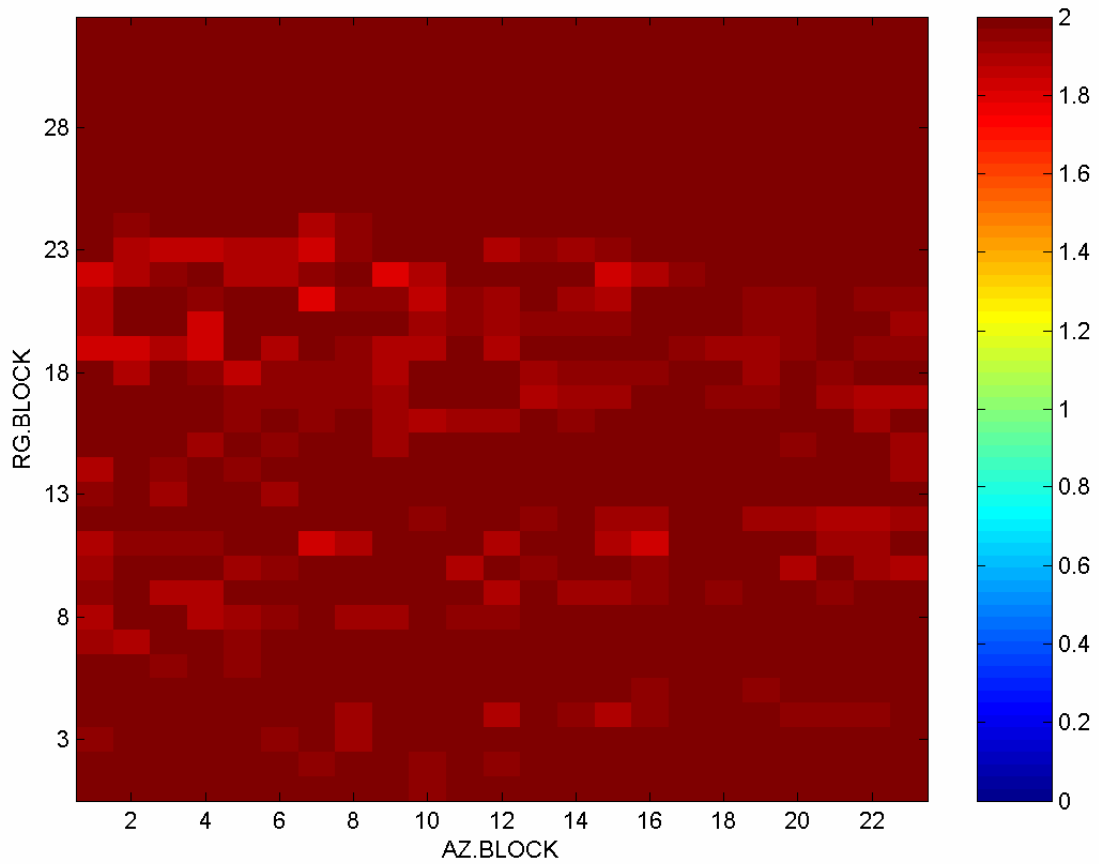
large dimension, this data set has been split in various sub-images for easier analysis, but only those producing the most interesting results will be reported here. In fact, speckle is mainly Gaussian in the reported and in all the other sub-images, as expected given the coarse SAR resolution. The total data set is composed of 2079x94000 pixels (rg. x az.), each sub-image is 2709x5000 pixels.

Fig. 3.20 shows the scene portion from azimuth pixel 20001 to 25000:



**Figure 3.20** - First SAR scene portion (2709x5000 pixels, rg. x az.).

The black area in far range is ocean, the land zone is natural areas; a road crosses horizontally the land area in mid range. Speckle analysis has been carried out with moving window patch size 11x25 and estimation on blocks 160x400, as for the first data set. The estimated speckle statistics are Gaussian on the ocean and mostly Gaussian on the land, as shown in the next figure:



**Figure 3.21** - Shape parameter, patch: 11x25, block: 160x400.

In fact, the minimum shape parameter estimate is 1.8. More than 96% of the image exhibits a shape parameter estimate greater or equal to 1.9.

Next figure shows the scene portion from azimuth pixel 25001 to 30000, i.e. the right adjacent portion to the previous one. The land area is again natural, apart from the presence of the littoral road.

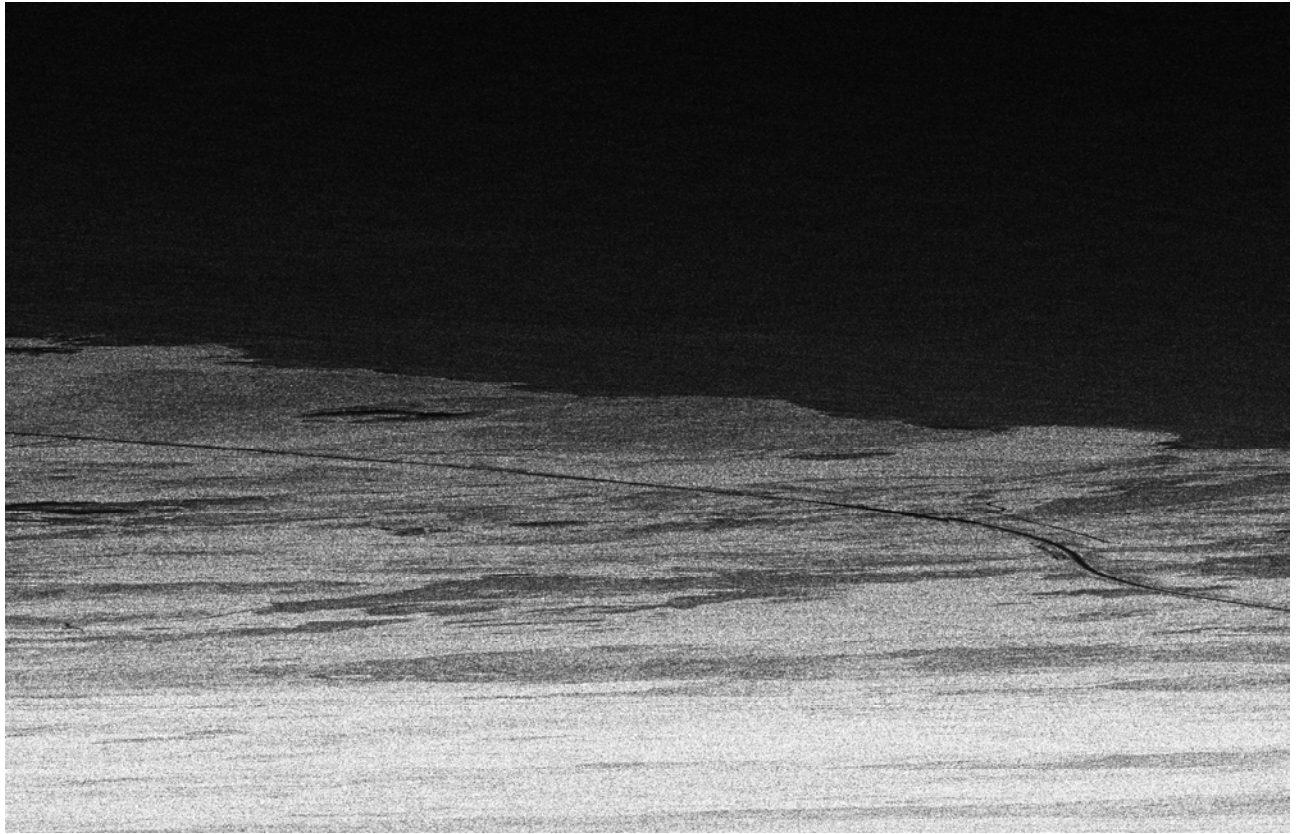


**Figure 3.22** - Second SAR scene portion (2709x5000 pixels, rg. x az.).

Figure 3.23 reports the corresponding speckle shape parameter estimates.

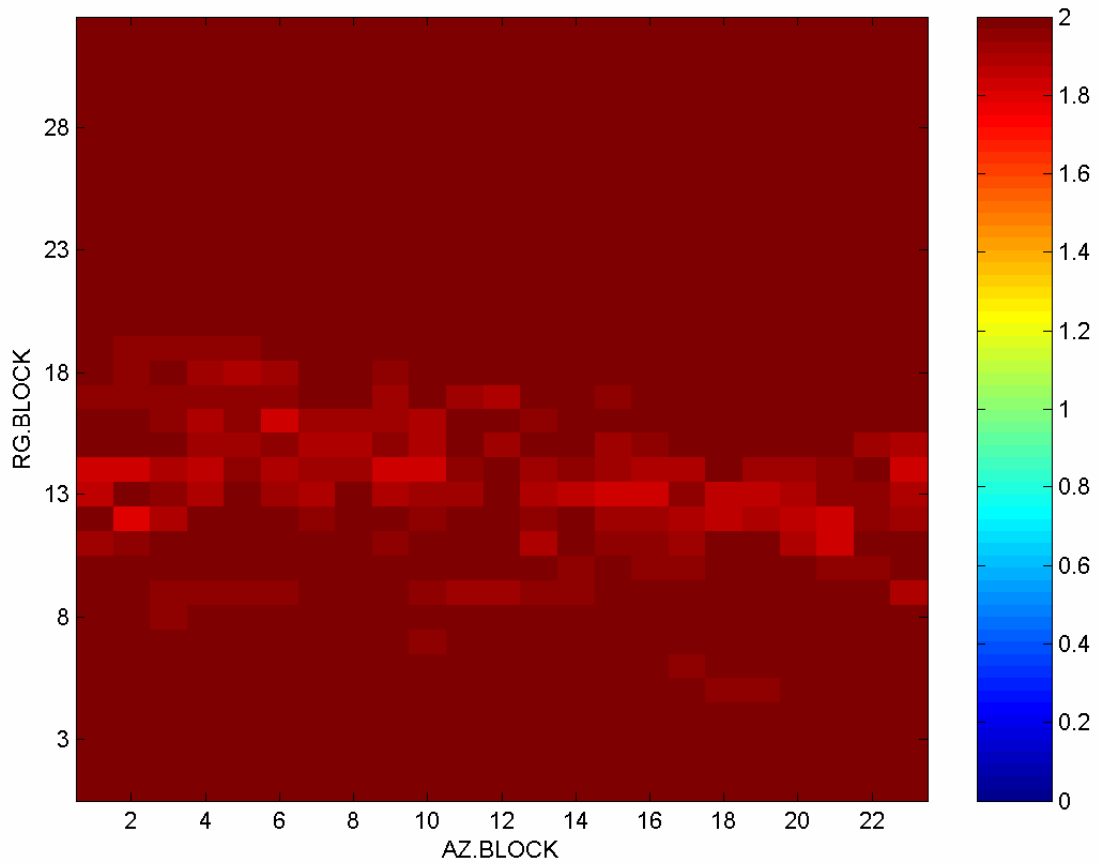


**Figure 3.23** - Shape parameter, patch: 11x25, block: 160x400.

Speckle in this image, like in the previous one, is mainly Gaussian. The minimum of  $\hat{c}$  is 1.8. Again, more than 96% of the image exhibits a shape parameter estimate greater or equal to 1.9.

The last image portion shown of this data set is the sub image from azimuth pixel 10001 to 15000, see Fig. 3.24:

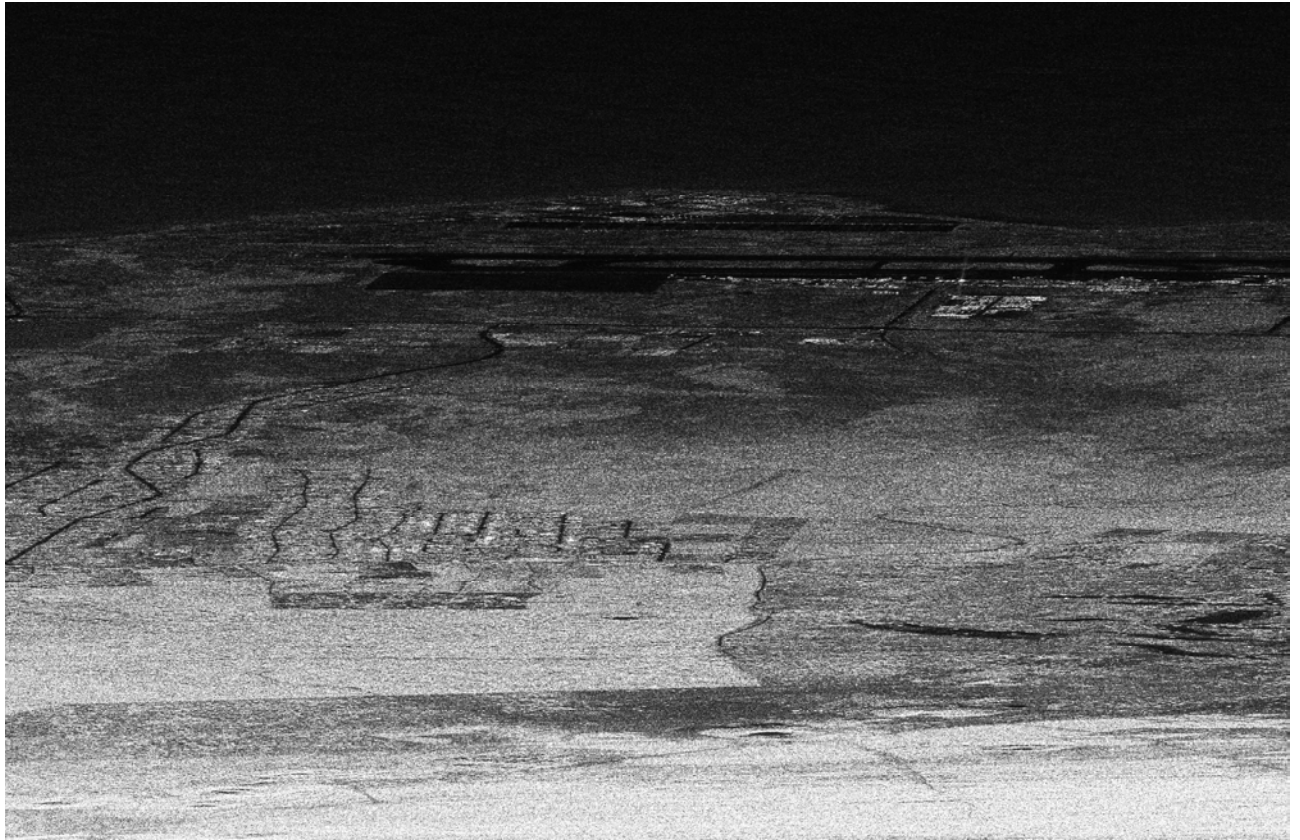


**Figure 3.24** - Third SAR scene portion (2709x5000 pixels, rg. x az.).

Unlike the two previous sub images, this one contains also many areas with artificial scatterers, like an urban agglomerate along the coastline, see the top image, an airport on the top center-right and another urbanized zone in correspondence of several roads in the central left part of the image. Blocks with shape parameter lower than 1.8 are found in correspondence of the central left urbanized zone, and of the buildings close to the airport lanes. Bad fitting is also detected for other blocks in the airport area and in the urban agglomerate along the coastline. The rest of the image exhibits almost Gaussian speckle.

### 3.8 Conclusions

The speckle analysis carried out on these four different data sets indicates, as expected, that deviations from the classical speckle regime on natural areas depend both on SAR system parameters and on the nature of the scattering surface. In particular, non negligible deviations from the Gaussian regime have been detected in meter resolution X-Band data at medium grazing angle (first data set) over some forest zones.

## **Acknowledgments**

Thanks to Prof. Joachim Ender from FGAN for providing the AER-II data set, to Dr. Alberto Moreira from DLR for providing the E-SAR data set, to Dr. Joao Moreira for providing the Aes-1 data set when at Aerosensing Radarsysteme, and to Dr. David Imel for providing the AIRSAR data set when at NASA.



# APPENDIX A

## A.1 Goodness-of-Fit Test

With the term “goodness-of-fit-test” we generally indicate a procedure to verify (through samples) whether a hypothesis regarding a probability distribution function of a variable is acceptable or not. Goodness-of-fit test is a hypothesis test where the hypothesis  $H_0$  and the alternative hypothesis are respectively:

$H_0$ : the data follow a specified distribution;

$H_1$ : the data do not follow the specified distribution;

Significance level  $\alpha$  indicates probability to refuse  $H_0$  when it is true (first type error). The quantity  $1-\alpha$  is the probability that hypothesis  $H_0$  is true. With  $\beta$  we indicate second type error; in other words, the probability to refuse hypothesis  $H_1$  when it is true. Obviously huge differences from reality for hypothesis  $H_0$  are easy to find, but small differences from reality are difficult to detect and these determine high values of  $\beta$ . It is possible to express  $\beta$  by  $\alpha$ .

Critical values for a hypothesis test are based on the statistic of test and on significance level  $\alpha$  which determines the sensibility of a test. For  $\alpha=0.05$   $H_0$  hypothesis is rejected with 5% when it is true. Choice of  $\alpha$  is arbitrary, common values are 0.1, 0.05 and 0.01. Critical regions include these values of test's statistic that cause the reject of hypothesis  $H_0$  with statistic test distribution and significance level  $\alpha$ ; it is possible to calculate cut-off value for test's statistic. Superior and inferior values (or both) of cut-off (in dependence on test direction) define the critical region.

Let  $x_1, x_2, \dots, x_n$  be  $n$  independent observations of a random variable with distribution function  $F(x)$  which is unknown. Suppose that we wish to test the hypothesis:

$$H_0: F(x)=F_0(x) \tag{A.1}$$

where  $F_0(x)$  is some particular distribution function, which may be continuous or discrete. The problem of testing (A.1) is called a *goodness-of-fit problem*. Any test of (A.1) is called a *test of fit*.  $H_0$  is a simple hypothesis if  $F_0(x)$  is completely specified. As instance, the

hypothesis that the  $n$  observations have come from a normal distribution with specified mean and variance is a simple hypothesis. On the other hand, we may wish to test whether the observations have come from a normal distribution whose parameters are unspecified, and this would be a composite hypothesis. Similarly, if the normal distribution has its mean, but not its variance, specified, the hypothesis remains composite. In the case of composite hypothesis parameters are estimated by using the observations. The composite hypotheses are more common since permit to decide if a sample comes from any distribution of specific type. Unfortunately, working with composite hypothesis is more difficult since the critical values are difficult to calculate and often we must resort to simulations methods (e.g. Monte Carlo) in order to determine the distribution of the test statistic.

### A.1.1 Kolmogorov-Smirnov Test

Kolmogorov-Smirnov (K-S) test is based on the empirical function (ECDF). Given  $N$  ordered data points  $Y_1, Y_2, \dots, Y_N$ , the ECDF is defined as  $E_N = n(i)/N$  where  $n(i)$  is the number of points less than  $Y_i$  and the  $Y_i$  are ordered from smallest to largest value. This is a step function that increases by  $1/N$  at the value of each ordered data point.

Figure A.1 is a plot of the empirical distribution function with a normal cumulative distribution function for 100 normal random numbers. The K-S test is based on the maximum distance between these two curves.

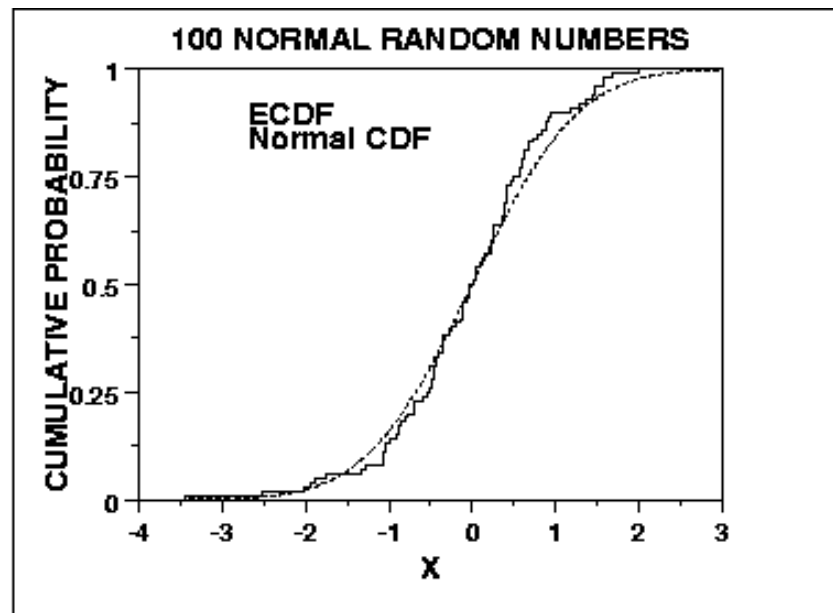


**Figure A.1** - Empirical distribution function (ECDF solid line) and normal distribution (dotted line).

An attractive feature of this test is that the distribution of the K-S test statistic itself does not depend on the underlying cumulative distribution function being tested. Another advantage is that it is an exact test (the chi-square goodness-of-fit test depends on an adequate sample size for the approximations to be valid) despite these advantages, the K-S test has several important limitations:

1. It only applies to continuous distributions.
2. It tends to be more sensitive near the center of the distribution than at the tails.
3. Perhaps the most serious limitation is that the distribution must be fully specified. That is, if location, scale, and shape parameters are estimated from the data, the critical region of the K-S test is no longer valid. It typically must be determined by simulation.

Due to limitations 2 and 3 above, many analysts prefer to use the Anderson-Darling goodness-of-fit test. However, the Anderson-Darling test is only available for a few specific distributions.

In the Table 1.1 we resume the characteristics of K-S test.

$H_0$	The data follow a specified distribution
$H_a$	The data do not follow a specified distribution
Test statistic	The Kolmogorov-Smirnov test statistic is defined as: $D = \max_{1 \leq i \leq N} \left  F(Y_i) - \frac{i}{N} \right $ where $F$ is the theoretical cumulative distribution of the distribution being tested, which must be a continuous distribution (i.e. no discrete distributions such as the binomial or Poisson), and it must be fully specified (i.e, the location, scale, and shape parameters cannot be estimated from the data).
Confidence level	$\alpha$
Critical region	The hypothesis regarding the distributional form is rejected if the test statistic, $D$ , is greater than the critical value obtained from a table. There are several variations of these tables in the literature that use somewhat different scaling for the K-S test statistic and critical regions. These alternative formulations should be equivalent, but it is necessary to ensure that the test statistic is calculated in a way that is consistent with how the critical values were tabulated.

**Table A.1** - Characteristics of K-S test.

The K-S test is applicable to unbinned distributions that are functions of a single independent variable, that is, to data sets where each data point can be associated with a single number. In such cases, the list of data points can be easily converted to an unbiased estimator  $S_N(x)$  of the cumulative distribution function of the probability distribution from which it was drawn. If the  $N$  events are located at values  $x_i$ ,  $i=1, \dots, N$ , then  $S_N(x)$  is the function giving the fraction of data points to the left of a given value  $x$ . This function is obviously constant between consecutive (i.e., sorted into ascending order)  $x_i$ 's, and jumps by the same constant  $1/N$  at each  $x_i$ .

Different distribution functions, or sets of data, give different cumulative distribution function estimates by the above procedure. However, all cumulative distribution function agree at the smallest allowable value of  $x$  (where they are zero), and at the largest allowable value of  $x$  (where they are unity). The smallest and largest values might of course be  $\pm\infty$ . So it is the behavior between the largest and smallest values that distinguishes distributions.

One can think of any number of statistics to measure the overall difference between two cumulative distribution functions: the absolute value of the area between them, for example, or their integrated mean square difference. The Kolmogorov-Smirnov  $D$  is a particularly simple measure: it is defined as the *maximum value* of the absolute difference between two cumulative distribution function. Thus for comparing one data set's  $S_N(x)$  to a known cumulative distribution function  $P(x)$ , the K-S statistic is:

$$D = \max_{-\infty < x < \infty} |S_N(x) - P(x)| \quad (\text{A.2})$$

while for comparing two different cumulative distribution functions  $S_{N_1}(x)$  and  $S_{N_2}(x)$ , the K-S statistic is:

$$D = \max_{-\infty < x < \infty} |S_{N_1}(x) - S_{N_2}(x)| \quad (\text{A.3})$$

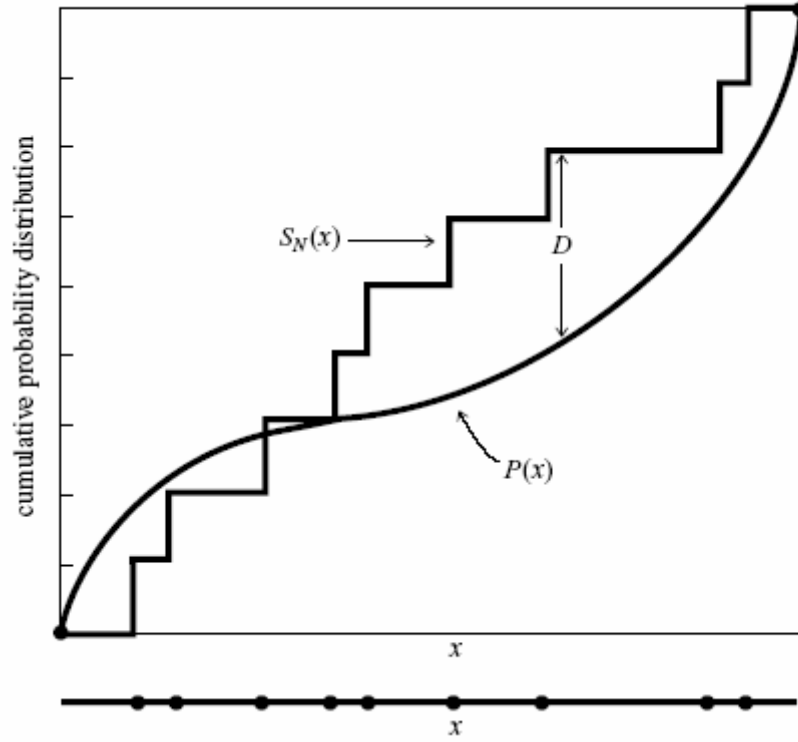


**Figure A.2** - Statistic D of K-S test.  $P(x)$  theoretical distribution,  $S_N(x)$  empirical distribution.

What makes the K-S statistic useful is that *its* distribution in the case of the null hypothesis (data sets drawn from the same distribution) can be calculated, at least to useful approximation, thus giving the significance of any observed nonzero value of  $D$ . A central feature of the K-S test is that invariant under reparametrization of  $x$ ; in other words, you can locally slide or stretch the  $x$  axis in figure 1.4, and the maximum distance  $D$  remains unchanged. For example, you will get the same significance using  $x$  as using  $\log x$ .

The function that enters into the calculation of the significance can be written as the following sum:

$$Q_{KS}(\lambda) = 2 \sum_{j=1}^{\infty} (-1)^{j-1} e^{-2j^2 \lambda^2} \quad (\text{A.4})$$

which is a monotonic function with the limiting values  $Q_{KS}(0) = 1$  and  $Q_{KS}(\infty) = 0$ .

In terms of this function the significance level of an observed value of  $D$  (as a disproof of the null hypothesis that the distributions are the same) is given approximately by the formula

$$\text{Prob}(D > \text{observed}) = Q_{KS} \left( \left[ \sqrt{N_e} + 0.12 + 0.11/\sqrt{N_e} \right] D \right) \quad (\text{A.5})$$

where  $N_e = N$  for the case (A.2) and  $N_e = \frac{N_1 N_2}{N_1 + N_2}$  for the case (A.3) of two distributions,

where  $N_1$  is the number of data points in the first distribution,  $N_2$  the number in the second. The nature of the approximation involved in (A.5) is that it becomes asymptotically accurate as the  $N_e$  becomes large, but is already quite good for  $N_e \geq 4$ , as small a number as one might ever actually use.

So, we have the following routines for the cases of one and two distributions (C language):

```
#include <math.h>
#include "nrutil.h"

void ksone(float data[], unsigned long n, float (*func)(float), float *d,
          float *prob)

Given an array data[1..n], and given a user-supplied function of a single variable
func which is a cumulative distribution function ranging from 0 (for smallest
values of its argument) to 1 (for largest values of its argument), this routine
returns the K-S statistic d, and the significance level prob. Small values of prob
show that the cumulative distribution function of data is significantly different
from func. The array data is modified by being sorted into ascending order.

{
    float probks(float alam);
    void sort(unsigned long n, float arr[]);
    unsigned long j;
    float dt,en,ff,fn,fo=0.0;

    sort(n,data);                                If the data are already sorted into
                                                ascending order, then this call can be omitted.

    en=n;
    *d=0.0;
    for (j=1;j<=n;j++) {
        fn=j/en;                                Loop over the sorted data points.
        ff=(*func)(data[j]);                    Data's c.d.f. after this step.
                                                Compare to the user-supplied
                                                function.
        dt=FMAX(fabs(fo-ff),fabs(fn-ff));        Maximum distance.
        if (dt > *d) *d=dt;
        fo=fn;
    }
    en=sqrt(en);
    *prob=probks((en+0.12+0.11/en)*(*d));        Compute significance.
}
```

```

#include <math.h>

void kstwo(float data1[], unsigned long n1, float data2[], unsigned long n2,
          float *d, float *prob)

Given an array data1[1..n1], and an array data2[1..n2], this routine returns the K-
S statistic d, and the significance level prob for the null hypothesis that the
data sets are drawn from the same distribution. Small values of prob show that the
cumulative distribution function of data1 is significantly different from that of
data2. The arrays data1 and data2 are modified by being sorted into ascending
order.

{
    float probks(float alam);
    void sort(unsigned long n, float arr[]);
    unsigned long j1=1,j2=1;
    float d1,d2,dt,en1,en2,en,fn1=0.0,fn2=0.0;

    sort(n1,data1);
    sort(n2,data2);
    en1=n1;
    en2=n2;
    *d=0.0;
    while (j1 <= n1 && j2 <= n2) {
        if ((d1=data1[j1]) <= (d2=data2[j2])) fn1=j1++/en1;      If we are not done...
                                                                Next step is in
                                                                data1.
        if (d2 <= d1) fn2=j2++/en2;                                Next step is in data2.
        if ((dt=fabs(fn2-fn1)) > *d) *d=dt;
    }
    en=sqrt(en1*en2/(en1+en2));
    *prob=probks((en+0.12+0.11/en)*(*d));      Compute significance.
}

```

Both of the above routines use the following routine for calculating the function  $Q_{KS}$  [Pre02]:

```

#include <math.h>
#define EPS1 0.001
#define EPS2 1.0e-8

float probks(float alam)
Kolmogorov-Smirnov probability function.
{
    int j;
    float a2,fac=2.0,sum=0.0,term,termbf=0.0;

    a2 = -2.0*alam*alam;
    for (j=1;j<=100;j++) {
        term=fac*exp(a2*j*j);
        sum += term;
        if (fabs(term) <= EPS1*termbf || fabs(term) <= EPS2*sum) return sum;
        fac = -fac;                                Alternating signs in sum.
        termbf=fabs(term);
    }
    return 1.0;                                Get here only by failing to converge.
}

```

### A.1.2 Variants of Kolmogorov-Smirnov test

The sensitivity of the K-S test to deviations from a cumulative distributions function  $P(x)$  is not independent of  $x$ . In fact, the K-S test tends to be most sensitive around the median

value, where  $P(x) = 0.5$ , and less sensitive at the extreme ends of the distribution, where  $P(x)$  is near 0 or 1. The reason is that the difference  $|S_N(x) - P(x)|$  does not, in the null hypothesis, have a probability distribution that is independent of  $x$ . Rather, its variance is proportional to  $P(x)[1 - P(x)]$ , which is largest at  $P = 0.5$ . Since the K-S statistic (A.2) is the maximum difference over all  $x$  of two cumulative distribution functions, a deviation that might be statistically significant at its own value of  $x$  gets compared to the expected chance deviation at  $P = 0.5$  and is thus discounted. A result is that, while the K-S test is good at finding shifts in a probability distribution especially changes in the median value, it is not always so good at finding spreads, which more affect the tails of the probability distribution, and which may leave the median unchanged.

One way of increasing the power of the K-S statistic out on the tails is to replace  $D$  by a so-called stabilized or weighted statistic, for example the Anderson-Darling statistic,

$$D^* = \max_{-\infty < x < \infty} \frac{|S_N(x) - P(x)|}{\sqrt{P(x)[1 - P(x)]}} \quad (\text{A.6})$$

Unfortunately, there is no simple formula analogous to equations (A.4) and (A.5) for this statistic. There are many other possible similar statistics, for example

$$D^{**} = \int_{P=0}^1 \frac{[S_N(x) - P(x)]^2}{\sqrt{P(x)[1 - P(x)]}} dP(x) \quad (\text{A.7})$$

which is also discussed by Anderson and Darling.

Another approach is due to Kuiper. We already mentioned that the standard K-S test is invariant under reparametrization of the variable  $x$ . An even more general symmetry, which guarantees equal sensitive at all values of  $x$ , is to wrap the  $x$  axis around into a circle (identifying the points at  $\pm\infty$ ), and to look for a statistic that is now invariants under all shifts and parametrizations on the circle. This allows, for example, a probability distribution to be “cut” at some central value of  $x$ , and the left and right halves to be interchanged, without altering the statistic or its significance.

Kuiper’s statistic, defined as



$$V = D_+ + D_- = \max_{-\infty < x < \infty} [S_N(x) - P(x)] + \max_{-\infty < x < \infty} [P(x) - S_N(x)] \quad (\text{A.8})$$

is the sum of the maximum distance of  $S_N(x)$  above and below  $P(x)$ . You should be able to convince yourself that this statistic has the desired invariance on the circle ( $D_+$  and  $D_-$  change individually but their sum is constant).

Furthermore, there is a simple formula for the asymptotic distribution of the statistic  $V$ , directly analogous to equations (A.4)-(A.5). The function  $Q$  is given by the follow formula:

$$Q_{KP}(\lambda) = 2 \sum_{j=1}^{\infty} (4j^2 \lambda^2 - 1) e^{-2j^2 \lambda^2} \quad (\text{A.9})$$

which is monotonic and satisfies  $Q_{KP}(0) = 1$   $Q_{KP}(\infty) = 0$ .

In term of this function the significance level  $(1-\alpha)$  is given by

$$\text{Prob}(V > \text{observed}) = Q_{KP} \left( \left[ \sqrt{N_e} + 0.155 + 0.24/\sqrt{N_e} \right] V \right) \quad (\text{A.10})$$

here  $N_e = N$  in the one-sample case, or is given by equation  $N_e = \frac{N_1 N_2}{N_1 + N_2}$  in the case of the two samples.

We report the matlab script of function for to calculate K-S probability:

```
function [D,n] = probks(Q)

% function D = PROBKS(Q) calculates for the Kolmogorov -Smirnov statistic d the
% significance level prob.
% See KSTWO. Adapted from Press, Teukolsky, Vetterling
% and Flannery, Numerical Recipes in Fortran p620.
% Checked using in XPROBKS in Numerical Recipes Example, Book p185

% Version 1.0 RHS 8/11/93

a2=-2.0*Q.^2;
factor=2;
D=0;
termbf=0;
term=1;
for n=1:100
    term=factor*exp(a2*n^2);
    D=D+term;
    if abs(term)<=0.001*termbf | abs(term)<=1e-8*D
        break
    end
end
```

```

end
factor=-factor;
termbf=abs(term);
end
probks=2; % get here by failing to converge

```

We report the matlab script of function for to calculate Kuiper probability

```

function [D,n] = probkp(Q)

a2=2.0*Q.^2;
factor=2;
D=0;
termbf=0;
term=1;
for n=1:100
    term=factor*(2*a2*n^2-1)*exp(-a2*n^2);
    D=D+term;
    if abs(term)<=0.001*termbf | abs(term)<=1e-8*D
        break
    end
    termbf=abs(term);
end
probkp=2; % get here by failing to converge

```

### A.1.3 Remarks

By observing the matlab scripts, we note that the `probks` function needs as input the test statistics. By using different test, test statistic changes. In the K-S test, the statistic is given by (A.2) (or by (A.3) if we are in the case of two distribution) while for the Kuiper test the statistic is given by (A.8). Expressions (A.5) and (A.10) show that the  $Q$  functions have similar statistics multiplied by two different factors for the case of K-S or Kuiper tests. In (A.5)-(A.10), the  $N_e$  term appears with different coefficients. Actually we used in our simulation the following expressions, defined as “modified statistic” of test

$$\left(\sqrt{N_e} + 0.12 + 0.11/\sqrt{N_e}\right) \cdot D \quad \text{and} \quad \left(\sqrt{N_e} + 0.155 + 0.24/\sqrt{N_e}\right) \cdot V \quad (\text{A.11})$$

We introduced this modified statistics because of the use of finite data points, as done in [Ste70].

## REFERENCES

- [Ana99] Anastassopoulos G., Lampropoulos G. A., Drosopoulos A., Rey M., “High Resolution Radar Clutter Statistics”, *IEEE Transactions on Aerospace and Electronic Systems*, Vol. 35, No. 1, January 1999.
- [Far97] Farina A., Gini F., Greco M., Verrazzani L., “High Resolution Sea Clutter Data: A Statistical Analysis of Recorded Live Data,” *IEE Proceedings-F*, Vol. 144, No. 3, pp. 121-130, June 1997.
- [Gin00] Gini F., Greco M., Diani M., Verrazzani L., “Performance Analysis of Two Adaptive Radar Detectors Against Non-Gaussian Real Sea Clutter Data”, *IEEE Transactions on Aerospace and Electronic Systems*, Vol. 36, No. 4, October 2000.
- [Gin02] Gini F., Greco M., “Texture Modelling, Estimation and Validation Using Measured Sea Clutter Data”, *IEE Proc., Radar Sonar Navig.*, Vol. 149, No. 3, June 2002.
- [Gre04] Greco M., Bordonì F., Gini F., “X-Band Sea Clutter Non-Stationarity: Influence of Long Waves,” *IEEE Journal of Oceanic Engineering*, Vol. 29, No. 2, April 2004.
- [Oli98] Oliver C., Quegan S., "*Understanding Synthetic Aperture Radar Images*", SciTech Publishing, 1998.
- [Pos93] Posner F., "Texture and Speckle in High Resolution Synthetic Aperture Radar Clutter", *IEEE Transactions on Geoscience and Remote Sensing*, Vol. 31, No. 1, January 1993.
- [Pre02] William H., Flannery B. P., Teukolsky S. A., Vetterling W. T., “*Numerical Recipes in C, The Art of Scientific Computing, second edition*”, Cambridge University Press, 2002, pp. 620-628.
- [Ste70] Stephens M. A., “*Journal of the Royal Statistical Society. Series B (Methodological)*” Vol. 32, No. 1, Royal Statistical Society, 1970, pp. 115-122.